

LEVEL

12

ADA 082884

WRIGHT
STATE
UNIVERSITY

DAYTON, OHIO

Brehm
Laboratory



DTIC
SELECTED
APR 9 1980
S E D

**Best
Available
Copy**

AIR FORCE
RESEARCH AND DEVELOPMENT
TECHNICAL INFORMATION OFFICE
AFOSR-TR-80-0200
Final Report for the Period
July 1, 1975 through Sept. 30, 1979
Submitted to:
A. F. Office of Scientific Research
Bolling Air Force Base, Bldg. 410
District of Columbia, 20332

AFOSR-TR- 80 - 0200
"COLLISIONAL EXCITATION AND IONIZATION"
AFOSR Contract No. F44620-76-C-0007
Final Report for the Period
July 1, 1975 through Sept. 30, 1979
Submitted to:
A. F. Office of Scientific Research
Bolling Air Force Base, Bldg. 410
District of Columbia, 20332

UNCLASSIFIED

SECURITY CLASSIFICATION OF THIS PAGE (When Data Entered)

REPORT DOCUMENTATION PAGE		READ INSTRUCTIONS BEFORE COMPLETING FORM			
1. REPORT NUMBER AFOSR/TR-80-0260	2. GOVT ACCESSION NO.	3. RECIPIENT'S CATALOG NUMBER			
4. TITLE (and Subtitle) Collisional Excitation and Ionization	5. TYPE OF REPORT & PERIOD COVERED Final Report - 1 Jul 75 - 30 Sep 79				
7. AUTHOR(s) Dr. T. O. Tiernan	6. PERFORMING ORG. REPORT NUMBER				
9. PERFORMING ORGANIZATION NAME AND ADDRESS Wright State University Department of Chemistry and The Brehm Laboratory Dayton, Ohio 45435	8. CONTRACT OR GRANT NUMBER(s) F44620-76-C-0007				
11. CONTROLLING OFFICE NAME AND ADDRESS AF Office of Scientific Research/NC Bldg, 410, Bolling AFB, DC 20332	10. PROGRAM ELEMENT, PROJECT, TASK AREA & WORK UNIT NUMBERS 61102F 2303/B1				
14. MONITORING AGENCY NAME & ADDRESS (if different from Controlling Office)	12. REPORT DATE 1979				
	13. NUMBER OF PAGES 215				
	15. SECURITY CLASS. (of this report) UNCLASSIFIED				
15a. DECLASSIFICATION/DOWNGRADING SCHEDULE					
16. DISTRIBUTION STATEMENT (of this Report) Approved for public release; distribution unlimited.					
17. DISTRIBUTION STATEMENT (of the abstract entered in Block 20, if different from Report)					
18. SUPPLEMENTARY NOTES					
19. KEY WORDS (Continue on reverse side if necessary and identify by block number) <table border="0"> <tr> <td>F2, Cl2, Br2, XeF2 and NF3 Ionization Processes Collisional Excitation Electron Transfer He+/Xe, He+/Kr, He+/H2, He+Cl2, He+/Br2, and He+I2</td> <td>Ionic Bond Dissociation Energies Heats of Formation</td> <td>Electron Affinities Ion Beam-fluorescence Mass Spectrometer Atmospheric Chemistry</td> </tr> </table>			F2, Cl2, Br2, XeF2 and NF3 Ionization Processes Collisional Excitation Electron Transfer He+/Xe, He+/Kr, He+/H2, He+Cl2, He+/Br2, and He+I2	Ionic Bond Dissociation Energies Heats of Formation	Electron Affinities Ion Beam-fluorescence Mass Spectrometer Atmospheric Chemistry
F2, Cl2, Br2, XeF2 and NF3 Ionization Processes Collisional Excitation Electron Transfer He+/Xe, He+/Kr, He+/H2, He+Cl2, He+/Br2, and He+I2	Ionic Bond Dissociation Energies Heats of Formation	Electron Affinities Ion Beam-fluorescence Mass Spectrometer Atmospheric Chemistry			
20. ABSTRACT (Continue on reverse side if necessary and identify by block number) <p>Ion-scattering apparatuses were utilized to investigate the kinetics, dynamics and energy transfer characteristics of selected positive- and negative-ion neutral reactions. Thresholds for endothermic electron transfer reactions involving O3, N2O, CO2, and other atmospheric molecules were determined, and these data were used to determine electron affinities of these species. Similarly, thresholds for collision-induced dissociation reactions of O3, CO3, NO3 ions, and other atmospheric negative ions were determined, and ionic bond dissociation energies, heats of formation and electron affinities were</p>					

DD FORM 1 JAN 73 1473

EDITION OF 1 NOV 65 IS OBSOLETE

410578 UNCLASSIFIED

1-1-12

UNCLASSIFIED

SECURITY CLASSIFICATION OF THIS PAGE (When Data Entered)

derived from these results. Cross sections for excitation of specific internal energy states in the ionic and neutral products of selected ion-neutral processes were determined by monitoring the radiation emitted upon decay of the excited species, using an ion beam-fluorescence apparatus. Among the systems examined were He⁺/Xe, He⁺/Kr, He⁺/He, He⁺/Cl₂, He⁺/Br₂, and He⁺/I₂. In still other experiments, the kinetics of attachment of low energy electrons to F₂, Cl₂, Br₂, XeF₂ and NF₃ were investigated using a flowing afterglow apparatus. In related studies, unique high-pressure negative ion sources were developed for a time-of-flight and a quadrupole mass spectrometer, and these instruments were utilized to investigate negative ion chemical ionization reactions of F ions with a wide variety of organic molecules.

Accession For	
NTIS GRA&I	<input checked="" type="checkbox"/>
DTIC TAB	<input type="checkbox"/>
Unannounced	<input type="checkbox"/>
Justification	
By	
Date	
Initials	
Special	
A	

UNCLASSIFIED

COLLISIONAL EXCITATION AND IONIZATION

AFOSR Contract No. F44620-76-C-0007

Department of Chemistry
and
The Brehm Laboratory
Wright State University
Dayton, Ohio 45435

Dr. T. O. Tiernan, Principal Investigator

Final Report
For the Period July 1, 1975 Through Sept. 30, 1979

Submitted to

Air Force Office of Scientific Research (AFSC)
Directorate of Chemical Sciences (Bldg. 410)
Bolling Air Force Base
District of Columbia 20332

Attention: Capt. Russell Armstrong

TABLE OF CONTENTS

	page
Table of Contents	i
I. ABSTRACT	1
II. BACKGROUND AND SUMMARY OF RESEARCH ACCOMPLISHED	2
A. Ion-Neutral Reactions	2
1. Endothermic Negative Ion Processes	2
2. Exothermic Reactions of Negative Ions Which Exhibit Small Rate Coefficients	7
3. Luminescence from Ion-Neutral Collisions	10
4. Crossed Ion-Molecular Beam Experiments	11
B. Electron-Molecule Reactions	14
C. Negative Ion-Chemical Ionization Studies	15
III. RELEVANCE OF RESEARCH ACCOMPLISHED TO THE AIR FORCE	16
IV. REFERENCES	18
V. PUBLICATIONS AND PRESENTATIONS RESULTING FROM RESEARCH SUPPORTED UNDER THIS CONTRACT	22
A. Publications	22

TABLE C - CONTENTS (cont'd.)

	page
B. Articles in Press	27
C. Manuscripts Submitted for Publication	28
D. Manuscripts in Preparation	29
E. Presentations at Technical Meetings	29
F. Graduate Theses	35
IV. Appendix	37

I. ABSTRACT

The objective of this research program was to accomplish fundamental investigations of certain collisional excitation and ionization processes which are relevant to highly energetic environments. In particular, these studies have provided chemical dynamics data which are needed in understanding the ion chemistry of the upper atmosphere and in the development of advanced technological devices of interest to the Air Force, such as lasers. Ion-scattering apparatuses were utilized to investigate the kinetics, dynamics and energy transfer characteristics of selected positive- and negative-ion neutral reactions. Thresholds for endothermic electron transfer reactions involving O_3 , N_2O , CO_2 , and other atmospheric molecules were determined, and these data were used to determine electron affinities of these species. Similarly, thresholds for collision-induced dissociation reactions of O_3^- , CO_3^- , NO_3^- , and other atmospheric negative ions were determined, and ionic bond dissociation energies, heats of formation and electron affinities were derived from these results. Cross sections for excitation of specific internal energy states in the ionic and neutral products of selected ion-neutral processes were determined by monitoring the radiation emitted upon decay of the excited species, using an ion beam-fluorescence apparatus. Among the systems examined were He^+/Xe , He^+/Kr , He^+/H_2 , He^+/Cl_2 , He^+/Br_2 , and He^+/I_2 . In still other experiments, the kinetics of attachment of low energy electrons to F_2 , Cl_2 , Br_2 , XeF_2 and NF_3 were investigated using a flowing afterglow apparatus. In related studies, unique high-pressure negative ion sources were developed for a time-of-flight and a quadrupole mass spectrometer, and these instruments were utilized to investigate negative ion chemical ionization reactions of F^- with a wide variety of organic molecules.

II. BACKGROUND AND SUMMARY OF RESEARCH ACCOMPLISHED

A. Ion-Neutral Reactions

Some of the major research accomplishments of this program are summarized below.

1. Endothermic Negative Ion Processes

Although many papers dealing with the kinetics and dynamics of ion-neutral collisions have appeared in the literature, in the past twenty years or so, relatively few of the studies on which these were based have dealt with endothermic processes. Endothermic processes of this type exhibit energy barriers, and their excitation functions therefore show energy thresholds. The potential energy surfaces which characterize the latter reactions are clearly different from the attractive type of surface which is typical of most of the exothermic reactions which have been studied by beam techniques thus far. It is clear, even from the limited studies of these processes accomplished thus far, that the utilization of ion beam techniques to investigate ion-neutral reactions, at collision energies in the neighborhood of threshold, can provide much important and previously unavailable information with respect to energy barriers to reaction, and the effectiveness of reactant translational energy in surmounting such barriers. Such data is of fundamental importance to theories of chemical kinetics in general, since many interesting chemical reactions (particularly those of neutral species) exhibit activation energies.

Prior to undertaking the work accomplished during the present AFOSR-supported program, there had been reports of several pioneering investigations, both from our own laboratory¹⁻⁶ and from others,⁷⁻⁹ in which beam-collision chamber apparatuses had been used to determine excitation functions for endothermic negative ion-neutral reactions. Among the negative ion processes examined using these methods were particle transfer and electron transfer reactions. The major emphasis in most of the latter investigations was placed on the determination of energy thresholds for various endothermic negative ion-neutral reactions, rather than on the microscopic mechanisms. The thresholds are of particular interest because, as we showed,²⁻⁶ these thresholds can be used, in conjunction with other known quantities, to derive thermochemical data for molecular negative ions which are of great interest, such as electron affinities, heats of formation, and bond dissociation energies. The data of this type which we obtained for a sizeable number of molecular species, using such techniques, were in good agreement with similar data obtained by other methods,^{2-6,10} although the interpretation of data obtained from our fixed-collector beam instrumentation was complicated by the lack of detailed data on product angular and velocity distributions. There was also the requirement that energy thresholds measured with the ion-beam-collision chamber apparatus be corrected for the Doppler broadening caused by the thermal motion of the target gas molecules. Because present theoretical knowledge with respect to most ion-molecule reactions is still inadequate to specify a priori the nature of the true threshold functions, trial functions were generally assumed and these were convoluted with the calculated energy distribution function, and then compared with or fit to the

experimental data.^{2,6} The uniqueness of this fitting procedure was difficult to demonstrate and generally resulted in increasing the error limits on the derived thresholds. Still, these experiments yielded highly useful electron affinity data, on a variety of molecular species, at a time when such data was generally unavailable. It is noteworthy that one of the papers from our laboratory which was published during this earlier period has recently been reprinted in a collection entitled "Benchmark Papers in Physical Chemistry, Ion-Molecule Reactions, Part I, Kinetics and Dynamics."¹¹

In the present research program, studies of the threshold behavior for endothermic ion-neutral collisions have been extended, but emphasis has been placed on collision-induced dissociation reactions of selected negative ions. Collision-induced dissociation processes were chosen because a theoretical description of the threshold function for such processes was developed and reported just prior to the initiation of our AFOSR program.¹² Thus, in deconvoluting the experimentally measured excitation functions for these reactions, it would no longer be necessary to assume the form of the threshold function and employ a "trial and error" fitting procedure. The small inorganic ions selected for study in this program (O_3^- , CO_3^- , NO_3^- , CO_2^- , N_2O^- , and others) were chosen primarily because of widespread scientific interest in their thermochemical properties, especially electron affinities and bond dissociation energies, and because of the relevance of this information to the formulation of accurate negative ion reaction schemes for the upper atmosphere.

Results of the negative ion studies just mentioned have been

documented in several publications and presentations which are listed in a later section of this report. This research has yielded electron affinities, bond dissociation energies and heats of formation for various negative ion and neutral species.¹³⁻¹⁷ In several instances where subsequent determinations, using other still more accurate techniques, provided analogous data on these species, the agreement with our ion-beam threshold data was excellent. This is true, for example, in the case of ozone,¹⁵ for which the electron affinity was later determined using laser photodetachment methods.¹⁸ Another highly significant result of the ion-beam experiments conducted in this program was the detection of excited states of O_3^- , CO_3^- and NO_3^- , and the determination of thermochemical data for the excited species. These were the first reports of such excited states, although the observation of a CO_3^{-*} state was subsequently confirmed by the photodissociation experiments of Vestal et al.¹⁹ These excited states were not apparent in other photodetachment¹⁸ and photodissociation²⁰ experiments, and are still the subjects of considerable controversy. The existence of long-lived states of these negative ions, and the possibility that there may be structurally different isomeric forms of these, has important consequences for atmospheric negative ion schemes. The involvement of excited negative ion species has not previously been considered.

Concurrent with the refinement in our laboratory of the ion-beam techniques described above, other new experimental methods have been developed and applied for determining molecular electron affinities and negative ion bond dissociation energies. The newer

techniques applicable for such purposes, including laser photo-detachment and photodissociation spectroscopy, ion-beam threshold measurements, chemical-bracketing techniques based on observation of the production or reaction of a given negative ion, and theoretical methods for calculating negative ion properties, were recently reviewed at a "Symposium on Electron Affinities and Negative Ion Stabilities," at the Tenth Annual Meeting of the Division of Electron and Atomic Physics (DEAP) of the American Physical Society.²⁰⁻²⁴ The important role of the ion-beam techniques for such applications was evident from the discussions at this conference.

Comparison of the experimental excitation functions for endothermic reactions, such as those obtained in the present program, with the theoretical predictions of Rebick and Levine¹² also reveals some important details of the collision process. For example, the theoretical model yields a threshold function of the form,

$$\sigma = A(E-E_0)^n/E \quad (1)$$

and the magnitude of the values of A and n which are required to obtain a calculated excitation function which "fits" the experimentally measured function are significant. It was observed in our studies, as expected, that the CID thresholds for excited species, such as O_3^{-*} , are lower than for the corresponding ground state ion. In addition, the A factor is higher for the former threshold. This is consistent with the conclusion from studies of collision-induced ion-pair formation in neutral-neutral interactions by other investigators,²⁵ which showed that the A factor increased with increasing internal energy of the reactants. Other observations relating to

the O_3^{-*} CID reaction led to the conclusion that the internal energy was probably in the form of vibrational excitation. The values of the n factor which were indicated for the O_3^{-} CID reactions from the present studies were in the range which the theoretical model predicted for so-called "direct" reactions.¹²

2. Exothermic Reactions of Negative Ions Which Exhibit Small Rate Coefficients

Most exothermic ion-neutral reactions which have been studied occur at essentially every collision (typical rate coefficients are 10^{-9} cm³/molecule sec), and exhibit decreasing cross sections with increasing translational energy of the reactants. However, some reactions of this type, in particular, proton transfer processes involving certain negative ions (D^- , NH_2^- and larger organic ions such as $CH_2CHCH_2^-$) have been found to be very slow. In the present program, the excitation functions of these and other similar reactions were determined, and energy thresholds were observed for these processes. The temperature dependence of these thresholds was also determined over a limited range. It was demonstrated that the deconvoluted excitation function for the ND_2^-/D_2 reaction is of the form $\sigma \propto (E_{rel} - E_0)^{1/2}/E_{rel}$, as required by theory, and that the measured translational energy threshold corresponds to the Arrhenius activation energy for this process. Relatively few measurements of such activation barriers for ion-neutral reactions have been reported.

The excitation functions observed for reactions of delocalized

enolate anions are of special interest because they reflect a complex dependence upon energy. These excitation functions do not exhibit translational energy thresholds, but show an initially decreasing cross section with increasing translational energy, followed by a sudden rise in the cross section, attaining a maximum and then again decaying. The effect of increasing the temperature of the reactants is to shift the translational energy at which the increase in the cross section begins. This is consistent with a model²⁶ which predicts that there are energy barriers in the potential surfaces which govern these reactions, but that the height of these barriers is lower than the potential energies of either the separated reactants or products. This barrier corresponds to the symmetrical transition state for proton transfer, the reaction proceeding via a three-step mechanism involving the formation of a nonsymmetrical intermediate, $[AH\cdots B]^-$, which lies in a potential well with respect to the reactants, $(AH + B^-)$, as well as with respect to the transition state, $(A\cdots H\cdots B)^-$. According to this model, it is the competition between two unimolecular decompositions of the intermediate, the back reaction forming $(AH + B^-)$ via a simple bond cleavage, and the forward rearrangement reaction, producing the symmetrical transition state, which determines the overall bimolecular rate coefficient at thermal energies. This model is well supported by the present results. We observe that the rate coefficient and its variation with translational energy are strongly dependent on the collision chamber temperature. At low translational energies, it is seen that an increase in the collision chamber temperature decreases the overall rate coefficient. A similar effect has been observed in certain hydride ion transfer reactions of large polyatomic positive ions.²⁷ Increasing the collision chamber

temperature results in an increase in the internal energy of the neutral reactant, and in turn, the internal energy of the intermediate, E^* , is increased. The larger internal energy of the intermediate favors the unimolecular channel having a high activation energy and a high entropy factor, that is, the simple bond cleavage, which corresponds to the back reaction yielding the original reactants. An increase in the cross section with increasing translational energy is observed at energies greater than ~ 1.5 eV in the laboratory system. This may reflect a change in the mechanism of the reaction, resulting from the fact that the long-lived intermediate can no longer be formed at the higher interaction energies. It is well known that the mechanism of an ion-neutral reaction can change from one involving formation of a persistent intermediate complex to a direct mechanism as the collision energy is increased. The lifetime of such an intermediate collision complex decreases with increasing internal energy E^* , and in turn the internal energy increases as the relative energy of the reactants is increased. When the interaction energy increases to the point that the intermediate is no longer formed, back reaction to give reactants can no longer compete effectively with the forward reaction, and an increase in the cross section (and of k) with increasing energy is then observed. This rationale is further supported by the fact that the point of onset of the rising portion of the plot of k as a function of ion energy shifts to lower relative energies as the temperature is increased. This demonstrates the equivalent role of internal and relative translational energy in reducing the lifetime of the intermediate complex. The second decrease in the cross section at still

higher energies is consistent with the behavior of many ion-molecule reactions at higher energies and presumably simply reflects a decrease in the collision cross section.

3. Luminescence from Ion-Neutral Collisions

A convenient method for assessing the role of internal energy in ion-neutral collisions involves the observation of luminescence which results from the radiative decay of internally excited products formed in these events. Prior to the pioneering observations of Tolk and coworkers²⁸ in 1965, it was generally assumed that the cross sections for radiative emissions from excited ion-neutral products would be too small to measure experimentally. In fact, for at least some reactions of this type, these cross sections proved to be quite large, and it has been realized in the past 3-5 years that such mechanisms may actually efficiently pump certain laser systems. Subsequent to the work of Tolk et al.,²⁸ more sophisticated experimental devices for measuring luminescence from ion-neutral processes were constructed in a few laboratories, including our own. At the outset of the present program, development of this apparatus was just being completed. During the course of the AFOSR-supported project, the apparatus was brought to the fully operational stage and several reaction systems were investigated in some detail. Most of the emphasis in this work has been on relatively low energy collisions of He^+ and other rare gas ions with rare gas and halogen (Cl_2 , Br_2 , I_2 , F_2) targets. Reactions of some dimeric species such as He_2^+ , have also been examined. As documented in several publications, this

work has revealed that the emission spectra resulting from many of these reactions are extremely complex and consist of many lines. Moreover, the cross section for radiative state production in some of these reactions is quite large in comparison to the cross section for total charge transfer. These experiments have also revealed important details with respect to the internal energy distribution of rare gas product ions. Another important outcome of this work is the determination of relative transition probabilities from individual excited levels to lower energy states. These are obtained here under conditions which minimize external perturbations, and some differences have been observed between our results and analogous transition probabilities derived from discharges (where there are substantial electric field perturbations). These results suggest the need to reevaluate many atomic transition probabilities obtained from other more conventional optical experiments. The experimental capability established under this program is expected to find extensive use in future studies of this type.

4. Crossed Ion-Molecular Beam Experiments

Prior to the initiation of the present research program, development of a crossed ion-molecular beam apparatus had been initiated in our laboratory. This apparatus was designed to yield information on the angular distributions, as well as on the masses and kinetic energies of the ionic products of low energy (down to ~ 0.5 eV, lab) ion-neutral reactions. Clearly, such an apparatus would markedly expand our capabilities to investigate in detail the

dynamics of these processes, and would complement our older tandem mass spectrometer, which utilizes a collision chamber, and which does not provide angular or energy distribution data on the product ions. Soon after the AFOSR-supported project began, construction of the apparatus was completed to the point of preliminary test and evaluation. Several exothermic ion-molecule reactions having large cross sections were examined (Ar^+/D_2 , Ar^+/H_2 , and others) and the scattering data obtained compared favorably to that reported earlier from other laboratories. It was intended, however, that the major focus of the experiments using the crossed ion-molecular beam apparatus would be on endothermic processes (charge transfer and collision-induced dissociation), and especially on the examination of these in the threshold energy regime. However, attempts to study several such endothermic processes (I^-/O_2 , O_2^-/Ar and others) using the apparatus indicated that under the conditions employed, reactions of this type, which exhibit very small cross sections, could not be observed in the translational energy region near threshold. This was attributable largely to the fact that the capillary array molecular beam source employed in the apparatus did not produce molecular beam densities of the magnitude anticipated from the design estimates. Consequently, it was decided to replace the capillary array with a nozzle beam source. This was a major modification affecting numerous other instrument systems. A nozzle beam assembly was designed and construction was undertaken in our machine shops. The nozzle and the associated skimmer and collimating slits were fabricated. Also constructed was a mechanical assembly to permit variation of the nozzle-to-skimmer distance during operation, (that is, adjustment is

possible by controls positioned outside of the vacuum chamber). A beam chopper assembly having a variable chopping frequency from 1 to 60 cycles/sec was fabricated and installed. Additional ionization gauges were installed to measure the molecular beam density produced by the nozzle. Because of the markedly larger volume of gas issuing from the nozzle beam source (as compared to the original capillary array) it was necessary to incorporate additional pumping capacity into the apparatus in order to maintain a sufficiently low pressure in the main vacuum housing and the collision region. Accordingly, the main cylindrical vacuum tank was modified and additional ports with flanges were added. One 6 in. diffusion pump and two smaller 2 in. pumps were added to provide additional pumping for the main vacuum chamber and for the several sections of the nozzle beam source (which are separately pumped). At this time, extensive improvements were also made to the electrical distribution system and the controlling electronic circuitry of the apparatus. A new servo system was installed to drive the rotating platform which holds the energy analyzer and the quadrupole mass filter. A potentiometer coupled directly to the servo drive shaft was installed so that the angular position of the platform could be precisely determined and controlled to less than 0.1 degree. This system was then calibrated. Finally, a new projectile ion beam monitor was fabricated and installed, with provision for external positioning.

At the time of completion of the present contract, the extensively modified crossed ion-molecular beam apparatus was completely assembled and operational. Preliminary tests indicated that the molecular beam densities attainable with the new nozzle beam source are an order

of magnitude or more larger than were obtained previously. The projectile ion beam currents which can be realized have also been significantly enhanced, and much greater beam stability has been achieved. Studies are now in progress to assess the capabilities of the new apparatus for investigating the dynamics of selected collisional dissociation processes in the threshold energy region, and the indications are highly favorable for such experiments at this time. AFOSR support of this program has therefore resulted in completion of a major new scattering apparatus which should permit investigation of endothermic ion-neutral reaction dynamics at lower translational energies than have previously been accessible.

B. Electron-Molecule Reactions

At the outset of the present program, there was a paucity of data in the literature relating to the kinetics of reactions of low-energy electrons (near-thermal) with halogenated molecules, and no data at all was available for fluorine. Such data is of considerable importance in developing hybrid laser devices, because processes of this type are potentially applicable for producing a uniform distribution of reacting chemical species in a laser cavity (for example, F atoms in the HF chemical laser using electron-beam initiation). Electron attachment data for relevant molecules such as F_2 was critically needed for reliable modeling of such laser systems.

In the course of the present AFOSR contract, development of a flowing afterglow apparatus was completed, and this facility was employed to

accomplish the first measurement of the rate coefficient for dissociative electron attachment to fluorine. Other halogenated molecules, including XeF_2 and NF_3 , were also investigated. The attachment rate coefficient for F_2 was found to be quite large, $3.1 \pm 1.2 \times 10^{-9} \text{ cm}^3/\text{molecule sec}$, at an electron temperature of 350°K , indicating that this process is a good source of F atoms for possible laser applications. The thermal energy electron attachment kinetic data for F_2 derived in our laboratory was subsequently shown to be consistent with electron attachment data measured more recently at higher energies by Nygaard et al.²⁹ Our results for F_2 are somewhat at variance with the still more recent data of Chantry³⁰, but other newer work suggests that the electron energy distribution in all such experiments is highly sensitive to the fluorine concentration.³¹ The latter factor may account for some of the observed inconsistencies. Obviously, this is still an area of continuing research activity and there is much scientific interest in data bearing on low energy electron attachment to halogens and halogenated molecules.

The results described above and similar data for XeF_2 and NF_3 have all been published, and reprints of these papers are attached. This work and these results were closely coordinated with scientists at the Air Force Weapons Laboratory, who initially prompted some of these studies.

C. Negative Ion-Chemical Ionization Studies

One of the objectives of the present research program was to establish the capability for conducting negative-ion chemical-ionization experiments. This was successfully realized by completion of a unique

high pressure ion source and other instrument adaptations for Time-of-Flight mass spectrometer. In addition, a negative-ion chemical-ionization source was designed and fabricated for another quadrupole mass spectrometer in our laboratory. Using these instruments, an extensive investigation was accomplished of the utility of F^- as a reagent ion for the production of negative-ion chemical-ionization (NICI) mass spectra of various organic compounds. NF_3 was used as the reagent gas in this instance since it is a very clean source of F^- . A systematic study of the reactions of F^- with a series of carboxylic acids, ketones, aldehydes, esters, alcohols, phenols, halides, nitrites, substituted benzenes, ethers, amines and hydrocarbons was conducted. The F^- reagent ion was shown to be useful for generating NICI spectra from a broad range of organic compound types. This work has been described in a paper currently in press (see attachments) and was presented at a Symposium on Negative Ion Chemical Ionization Mass Spectrometry. The capability established under this contract will be exploited to study reactions of other novel NICI reagent ions which have not yet been investigated.

III. RELEVANCE OF RESEARCH ACCOMPLISHED TO THE AIR FORCE

The research accomplished under the present contract was concerned with a somewhat broader array of topics than is perhaps usual in such programs. All of the "collisional excitation and ionization" processes investigated here however, are highly relevant to Air Force interests. Significant new fundamental data has been obtained with respect to the reactions and energy states of simple negative ions such as O_3^- , CO_3^- and NO_3^- , which are of major importance in upper atmospheric reaction schemes and models, and therefore bear directly on Air Force communication and detection and surveillance

requirements. More generally, the utility of ion beam threshold techniques, originally developed in our laboratory, in deriving thermochemical data for such negative ions has been firmly established, and all these methods can be applied to many other species of interest.

In a similar vein, new experimental capabilities developed in the course of this program, such as the crossed ion-molecular beam apparatus and the negative-ion chemical ionization mass spectrometric instruments are expected to have important future applications in the solution of fundamental problems of interest to the Air Force. In the case of the former apparatus, significant new data relative to fundamental reaction dynamics can be expected. This apparatus is expected to permit the first studies of the dynamics of endothermic ion-neutral reactions, which should be the most informative from the standpoint of understanding energy barriers to reaction and other features of the potential surfaces on which these reactions occur. These data, in turn, will provide tests and comparisons for theoretical computations of potential energy surfaces and will accelerate the development of reliable theoretical predictive capabilities.

Finally, the electron attachment data derived in this program have a significant bearing on hybrid laser development and modeling, as already noted; and should therefore have been of considerable interest to the Air Force.

The continuing development of high-technology Air Force weapons depends critically on the status of fundamental scientific knowledge such as that described herein. Hopefully, this program has contributed to this important objective.

IV. REFERENCES

1. C. Lifshitz, B. M. Hughes, and T. O. Tiernan, Chem. Phys. Letters 7, 469 (1970).
2. T. O. Tiernan, B. M. Hughes and C. Lifshitz, J. Chem. Phys. 55, (5692 (1971)).
3. B. M. Hughes, C. Lifshitz and T. O. Tiernan, J. Chem. Phys. 59, 3162 (1973).
4. C. Lifshitz, T. O. Tiernan and B. M. Hughes, J. Chem. Phys. 59, 3182 (1973).
5. T. O. Tiernan and R. P. Clow, Adv. Mass Spectrum 6, 295, (1974).
6. T. O. Tiernan, Chapter, "Reactions of Negative Ions," in "Interactions Between Ions and Molecules" P. Ausloos, Ed., Proceedings of the NATO Advanced Study Institute, Plenum Press, New York (1975), p. 353.
7. J. F. Paulson, Chapter in "Ion-Molecule Reactions," J. L. Franklin, Ed., Plenum Press, New York (1972).
8. W. A. Chupka, J. Berkowitz, and D. Gutman, J. Chem. Phys. 55, 2724 (1971).
9. W. A. Chupka, J. Berkowitz, and D. Gutman, J. Chem. Phys. 55, 2734 (1971).
10. It should also be noted that in several such cases, the data obtained by such methods in our laboratory was reported prior to the availability of more accurate data, such as that obtained by laser photodetachment, which provides further confidence in the ionic collision thresholds methods.

11. J. L. Franklin, Ed. "Ion-Molecule Reactions, Part I, Kinetics and Dynamics," Volume 3 in the series, "Benchmark Papers in Physical Chemistry and Chemical Physics (Dowden, Hutchinson & Ross, 1979).
12. C. Rebick and R. D. Levine, J. Chem. Phys. 58, 3942 (1973).
13. D. G. Hopper, T. O. Tiernan, A. C. Wahl and R. L. C. Wu, J. Chem. Phys. 65, 5474 (1976).
14. C. Lifshitz, R. L. C. Wu and T. O. Tiernan, Chem. Phys. Letters 51, 211 (1977).
15. C. Lifshitz, R. L. C. Wu, T. O. Tiernan and D. T. Terwilliger, J. Chem. Phys. 68, 247 (1977).
16. T. O. Tiernan and R. L. C. Wu, Adv. Mass Spec. 7A, 136 (1978).
17. R. L. C. Wu, T. O. Tiernan and C. Lifshitz, Argonne National Laboratory Report No. ANL-77-21, April, 1977, Proceedings of the Conference on High Temperature Sciences Related to Open-Cycle Coal-Fired MHD Systems.
18. S. E. Novick, P. C. Engelking, P. L. Jones, J. H. Futrell, and W. C. Lineberger, J. Chem. Phys. 70, 2652 (1979).
19. M. L. Vestal, private communication (1979); article submitted for publication in J. Chem. Phys.

20. J. T. Moseley, "Photon Interactions with Molecular Negative Ions," Abstract BA2, Bull. Am. Phys. Soc. 23, 1085 (1978).
21. W. C. Lineberger, "Laser Photodetachment Spectroscopy of Small Negative Ions," Abstract BA1, Bull. Am. Phys. Soc. 23, 1085 (1978).
22. T. O. Tiernan, "Applications of Ion Beam Experiments for Determination of Electron Affinities and Other Thermochemical Data," Abstract BA3, Bull. Am. Phys. Soc. 23, 1085 (1978).
23. D. L. Albritton, "Determination of Electron Affinities from Ion-Molecule Reactions," Abstract BA4, Bull. Am. Phys. Soc. 23, 1086 (1978).
24. W. A. Godard, "Theoretical Studies of Electron Affinities," Abstract BA5, Bull. Am. Phys. Soc. 23, 1086 (1978).
25. E. K. Parks, A. Wagner and S. Wexler, J. Chem. Phys. 58, 5502 (1973).
26. W. E. Farneth and J. I. Brauman, J. Am. Chem. Soc. 98, 7891 (1976).
27. J. J. Solomon, M. Meot-Ner and F. H. Field, J. Am. Chem. Soc. 96, 3727 (1974).
28. M. Lipeles, R. Novick and N. Tolk, Phys. Rev. Lett. 15, 815 (1965).
29. K. J. Nygaard, S. R. Hunter and S. R. Foltyn, "Electron Attachment in Fluorine-Rare Gas Mixtures," Paper FA-8, Bull. Am. Phys. Soc. 23, 141 (1978).

30. P. J. Chantry, "Dissociative Attachment Cross Section Measurements in F_2 and NF_3 ," Paper MA-5, Bull. Am. Phys. Soc. 24, 134 (1979).
31. C. A. Brau, A. E. Greene, S. D. Rockwood and B. I. Schneider, "Dissociative Attachment of Electrons to F_2 ," Paper MA-8, Bull. Am. Phys. Soc. 24, 134 (1979).

V. PUBLICATIONS AND PRESENTATIONS RESULTING FROM
RESEARCH SUPPORTED UNDER THIS CONTRACT

A. Publications

"Collision-Induced Dissociation of Molecular Negative Ions: Threshold Behavior," T. O. Tiernan and R. L. C. Wu, Abstracts of Papers of the IXth International Conference on the Physics of Electronic and Atomic Collisions, J. S. Risley and R. Geballe, Editors, University of Washington Press, Seattle, Washington (1975), p. 719.

"Formation of the Dimer Cation $(C_6H_6)_2^+$ in Gaseous Benzene," E. G. Jones, A. K. Bhattacharya and T. O. Tiernan, Int. J. Mass Spectrometry and Ion Physics 17, 147 (1975).

"A Case History in Computer Resource Sharing: ab initio Calculations via a Remote Control," D. G. Hopper, P. J. Fortune, A. C. Wahl and T. O. Tiernan, Chapter in ACS Symposium Series 19 Computer Networking and Chemistry, American Chemical Society, Washington (1975), p. 153.

"Collision-Induced Dissociation Reactions of N_2O^- , NO_2^- and CO_3^- ," R. L. C. Wu and T. O. Tiernan, Proceedings of the Twenty-third Annual Conference on Mass Spectrometry and Allied Topics, American Society for Mass Spectrometry (1975), p. 179.

"Measurement of Thermal Electron Dissociative Attachment Rates for Halogen Gases," G. D. Sides and T. O. Tiernan, Proceedings of the Twenty-Third Annual Conference on Mass Spectrometry and Allied Topics,

American Society for Mass Spectrometry (1975), p. 414.

"Crossed-Beam Studies of the Reactions of Ar^+/Kr^+ With CH_4 ,"

S. Y. Tang, R. L. C. Wu, E. G. Jones and T. O. Tiernan, Proceedings of the Twenty-third Annual Conference on Mass Spectrometry and Allied Topics, American Society for Mass Spectrometry (1975), p. 292.

"Low Energy He^+/H_2 Interactions," E. G. Jones, B. M. Hughes, D. G. Hopper and T. O. Tiernan, Proceedings of the Twenty-third Annual Conference on Mass Spectrometry and Allied Topics, American Society for Mass Spectrometry (1975), p. 305.

"Measurement of Thermal Electron Dissociative Attachment Rate Constants for Halogen Gases Using a Flowing Afterglow Technique," G. D. Sides, T. O. Tiernan and R. J. Hanrahan, J. Chem. Phys. 65, 1966 (1976).

"Dissociative Electron Attachment in Xenon Difluoride," G. D. Sides and T. O. Tiernan, J. Chem. Phys. 65, 3392 (1976).

"Theoretical and Experimental Studies of the N_2O^- and N_2O Ground State Potential Energy Surfaces. Implications for the $\text{O}^- + \text{N}_2 \rightarrow \text{N}_2\text{O} + \text{e}$ and Other Processes," J. Chem. Phys. 65, 5474 (1976).

"Luminescence from He^+/Cl_2 Collisions in the Energy Range 2-170 eV," K. E. Siegenthaler, B. M. Hughes, E. G. Jones and T. O. Tiernan, Proceedings of the Twenty-fourth Annual Conference on Mass Spectrometry and Allied Topics, American Society for Mass Spectrometry (1976), p. 370.

"Internal Energy Distribution in the Products of Charge-Transfer Between He^+ and Rare Gases," E. G. Jones, B. M. Hughes, D. C. Fee and T. O. Tiernan, Proceedings of the Twenty-fourth Annual Conference on Mass Spectrometry and Allied Topics, American Society for Mass Spectrometry (1976), p. 743.

"The $\text{N O}^-(X A)$ Potential Energy Surface," D. G. Hopper, A. C. Wahl, R. L. C. Wu and T. O. Tiernan, Proceedings of the Twenty-fourth Annual Conference on Mass Spectrometry and Allied Topics, American Society for Mass Spectrometry (1976), p. 744.

"Luminescence from Low-energy He^+/Xe Charge-transfer Reactions," E. G. Jones, B. M. Hughes, D. C. Fee, and T. O. Tiernan, Phys. Rev. A15, 1446 (1977).

"Mechanisms for the He^+/H_2 Reactive and Radiative Processes," D. G. Hopper, A. C. Wahl, E. G. Jones, B. M. Hughes, and T. O. Tiernan, Bull. Am. Phys. Soc. 22, 189 (1977).

"Thermodynamic Properties of Gas Phase Molecular Ions," R. L. C. Wu, C. Lifshitz and T. O. Tiernan, Proceedings of the Conference on High Temperature Sciences Related to Open-Cycle Coal-Fired MHD Systems," Argonne National Laboratory Report No. ANL-77-21, April, 1977, Argonne National Laboratory (U. S. ERDA), Argonne, Illinois.

"Application of Ion Equilibrium Measurements for Qualitative and Quantitative Analysis," C. Chang, C. C. Cheng, and T. O. Tiernan, Proceedings of the Twenty-fifth Annual Conference on Mass Spectrometry

and Allied Topics, American Society for Mass Spectrometry (1977), p. 128.

"Excitation Functions for Negative Ion-Molecule Reactions," C. Lifshitz, R. L. C. Wu and T. O. Tiernan, Proceedings of the Twenty-fifth Annual Conference on Mass Spectrometry and Allied Topics, American Society for Mass Spectrometry (1977), p. 269.

"Optical Emissions from Low Energy He^+/Br_2 , I_2 Reactions," K. E. Siegenthaler, B. M. Hughes, E. G. Jones and T. O. Tiernan, Proceedings of the Twenty-fifth Annual Conference on Mass Spectrometry and Allied Topics, American Society for Mass Spectrometry (1977), p. 400.

"Production of Radiative Excited States in Ion-Neutral Reactions," E. G. Jones, B. M. Hughes and T. O. Tiernan, Proceedings of the Twenty-fifth Annual Conference on Mass Spectrometry and Allied Topics, American Society for Mass Spectrometry (1977), p. 449.

"Associative Detachment Reactions of Negative Ions with O_3 ," C. Lifshitz, R. L. C. Wu, J. C. Haartz and T. O. Tiernan, J. Chem. Phys. 67, 238 (1977).

"Dissociative Electron Attachment in Nitrogen Trifluoride," G. D. Sides and T. O. Tiernan, J. Chem. Phys. 67, 2382 (1977).

"A Long-Lived Excited State of O_3^- ; Evidence from Collision-Induced Dissociation," R. L. C. Wu, T. O. Tiernan and C. Lifshitz, Chem. Phys. Letters 51, 211 (1977).

"Thermochemical Data for Molecular Negative Ions from Collisional-Dissociation Thresholds," T. O. Tiernan and R. L. C. Wu, Advances in Mass Spectrometry, Vol. 7A, p. 136, Heyden & Son, Ltd., London (1978).

"Negative Ion-Molecule Reactions of Ozone and Their Implications on the Thermochemistry of O_3^- ," C. Lifshitz, R. L. C. Wu, T. O. Tiernan and D. T. Terwilliger, J. Chem. Phys. **68**, 247 (1978).

"Excitation Functions of Slow Proton Transfer Reactions Involving Negative Ions," C. Lifshitz, R. L. C. Wu and T. O. Tiernan, J. Am. Chem. Soc. **100**, 2040 (1978).

"Characterization of the Luminescence from Low Energy He^+/Xe and He^+/Kr Reactions," E. G. Jones, B. M. Hughes, T. O. Tiernan, D. C. Fee and D. G. Hopper, Spectrochimica Acta **33B**, 787 (1978).

"The Bond Dissociation Energy of CO_3^- and the Electron Affinity of CO_3^- ," R. L. C. Wu and T. O. Tiernan, Proceedings of the Twenty-sixth Annual Conference on Mass Spectrometry and Allied Topics, p. 684 (American Society for Mass Spectrometry, 1978).

"Combined Theoretical and Experimental Studies of HeH_2^+ Potential Energy Surfaces Governing Several $He_2 + H_2$ Scattering Processes," D. G. Hopper, E. G. Jones, B. M. Hughes, R. L. C. Wu, and T. O. Tiernan, Proceedings of the Twenty-sixth Annual Conference on Mass Spectrometry and Allied Topics, p. 435 (American Society for Mass Spectrometry, 1978).

"Formation of Negative Ions," T. O. Tiernan, Proceedings of the Twenty-sixth Annual Conference on Mass Spectrometry and Allied Topics, p. 387 (American Society for Mass Spectrometry, 1978).

"Applications of Ion Beam Experiments for Determination of Electron Affinities and Other Thermochemical Data," T. O. Tiernan, Bull. Am. Phys. Soc. 23, 1085 (1978).

"Thermochemistry and Structure of the Molecular Negative Ion NO_3^- ," R. L. C. Wu and T. O. Tiernan, Proceedings of the Twenty-seventh Annual Conference on Mass Spectrometry and Allied Topics, p. 67 (American Society for Mass Spectrometry, 1979).

"Negative Ion Chemical Ionization Mass Spectrometry: Reactions of F^- Ion," C. C. Cheng, C. Chang and T. O. Tiernan, Proceedings of the Twenty-seventh Annual Conference on Mass Spectrometry and Allied Topics, p. 722 (American Society for Mass Spectrometry, 1979).

"Comment on 'Electron Affinities From Endothermic Negative-Ion Charge-Transfer Reactions. IV. SF_6 , Selected Fluorocarbons and Other Polyatomic Molecules'," C. Lifshitz, T. O. Tiernan and B. M. Hughes, J. Chem. Phys. 72, 789 (1980).

B. Articles in Press

"The Role of Excited States in Ion-Neutral Collisions," T. O. Tiernan and C. Lifshitz, Chapter in Vol. II. The Excited State in Chemical Physics, J. W. McGowan, Editor, A Volume in the Advances in Chemical Physics

Series, Wiley-Interscience Publishers, New York, in press, (1980).

"Distribution of Internal Energy in the Products of $\text{He}^+ + \text{Xe}$ Reactions," E. G. Jones, T. O. Tiernan, D. C. Fee and B. M. Hughes, J. Chem. Phys., in press, (1980).

"Formation and Reactions of Negative Ions Relevant to Chemical Ionization Mass Spectrometry. I. CI Mass Spectra of Organic Compounds Produced by F^- Reactions," T. O. Tiernan, C. Chang, and C. C. Cheng, Environmental Health Perspectives, in press (1980).

C. Manuscripts Submitted for Publication

"Experimental and Theoretical Investigation of the Excited State Potential Energy Surfaces of HeH_2^+ . Mechanisms for $\text{He}^+ + \text{H}_2$ Reactive and Radiative Processes," D. G. Hopper, E. G. Jones, T. O. Tiernan, R. L. C. Wu and B. M. Hughes, submitted to Journal of Chemical Physics.

"Investigation of Associative Detachment Reactions Using the SF_6 Scavenger Technique," C. Lifshitz, J. C. Haartz, T. O. Tiernan and R. L. C. Wu submitted to International Journal of Mass Spectrometry and Ion Physics.

"Thermochemical and Structural Information for CO_2^- and CO_2 From Collision-Induced Dissociation Threshold Measurements," R. L. C. Wu and T. O. Tiernan, submitted to Journal of Chemical Physics.

D. Manuscripts in Preparation

"Collision-Induced Dissociation of NO_3^- . Implications for the Structure and Thermochemistry of Ground and Excited State Ions," R. L. C. Wu and T. O. Tiernan, to be submitted to J. Chem. Phys.

"Negative Ion Reactions Involving CO_2 ," T. O. Tiernan, R. P. Clow and R. L. C. Wu, to be submitted to J. Chem. Phys.

"Luminescence from Low Energy Collisions of He^+ With Cl_2 , Br_2 and I_2 ," K. G. Siegenthaler, T. O. Tiernan, E. G. Jones, and B. M. Hughes, to be submitted to J. Chem. Phys.

E. Presentations at Technical Meetings

"Collision-Induced Dissociation of Molecular Negative Ions: Threshold Behavior," T. O. Tiernan and R. L. C. Wu, presented at the IXth International Conference on the Physics of Electronic and Atomic Collision, University of Washington, Seattle, Washington, July 29, 1975.

"A Case History in Computer Resource Sharing: ab initio Calculations via a Remote Control," D. G. Hopper, P. J. Fortune, A. C. Wahl, and T. O. Tiernan, Invited presentations at the Symposium on Computer Networking and Chemistry, sponsored by the Division of Computers in Chemistry, at the 170th Meeting of the American Chemical Society, Chicago, Ill., Aug. 26, 1975.

"Internal Energy Distribution in the Products of Charge Transfer Between He^+ and Rare Gases," E. G. Jones, B. M. Hughes, D. C. Fee and T. O. Tiernan, presented at the 24th Annual Conference on Mass Spectrometry and Allied Topics, San Diego, California, May 12, 1976.

"Luminescence from He^+/Cl_2 Collisions in the Energy Range 2-170 eV," B. M. Hughes, E. G. Jones, K. Siegenthaler and T. O. Tiernan, presented at the 24th Annual Conference on Mass Spectrometry and Allied Topics, San Diego, California, May 12, 1976.

"Experimental and Theoretical Characterizations of the $\text{N}_2\text{O}^-(X^2 A^1)$ Potential Energy Surface," D. G. Hopper, A. C. Wahl, R. L. C. Wu and T. O. Tiernan, presented at the 24th Annual Conference on Mass Spectrometry and Allied Topics, San Diego, California, May 13, 1976.

"Distribution of Internal Energy in Ion-Neutral Reaction Products," E. G. Jones, B. M. Hughes, D. C. Fee and T. O. Tiernan, Invited presentation at the Symposium on Mass Spectrometry, Annual Meeting of the Chemical Institute of Canada, London, Ontario, Canada, June 9, 1976.

"Cross Sections for Excited State Formation in $\text{He}^+/\text{Rare Gas}$ Collisions," E. G. Jones, D. C. Fee, B. M. Hughes, and T. O. Tiernan, presented at the 31st Symposium on Molecular Spectroscopy, The Ohio State University, Columbus, Ohio, June 17, 1976.

"The $\text{N}_2\text{O}^-(X^2 A^1)$ Potential Energy Surface," D. G. Hopper, A. C. Wahl, R. L. C. Wu and T. O. Tiernan, presented at the 31st Symposium on

Molecular Spectroscopy, The Ohio State University, Columbus, Ohio,
June 16, 1976.

"Thermochemical Data for Molecular Negative Ions from Collisional-Dissociation Thresholds," T. O. Tiernan and R. L. C. Wu, presented at the 7th International Mass Spectrometry Conference, Florence, Italy, September 2, 1976.

"Thermochemical Data for Molecular Negative Ions From Collisional-Dissociation Thresholds," T. O. Tiernan and R. L. C. Wu, presented at the 7th International Mass Spectrometry Conference, Florence, Italy, September 2, 1976.

"Mechanisms for He^+/H_2 Reactive and Radiative Processes," D. G. Hopper, A. C. Wahl, E. G. Jones, B. M. Hughes, and T. O. Tiernan presented at the Twenty-ninth Annual Gaseous Electronics Conference, Cleveland, Ohio, October 19, 1976.

"Thermodynamic Properties of Gas-Phase Molecular Ions," R. L. C. Wu, C. Lifshitz, and T. O. Tiernan, presented at the Conference on High Temperature Sciences Related to Open-Cycle, Coal-Fired MHD Systems, Argonne National Laboratories, Argonne, Illinois, April 4, 1977.

"Production of Radiative Excited States in Ion-Neutral Reactions," E. G. Jones, B. M. Hughes, and T. O. Tiernan, Invited presentation at the Symposium on Ionic Processes in Gaseous Lasers and High Temperature Plasmas, 25th Annual Conference on Mass Spectrometry and Allied Topics, Washington, D. C. , June 2, 1977.

"Optical Emission from Low Energy $\text{He}^+/\text{Br}_2, \text{I}_2$ Reactions," K. E. Siegenthaler, B. M. Hughes, E. G. Jones, and T. O. Tiernan, presented at the 25th Annual Conference on Mass Spectrometry and Allied Topics, Washington, D. C., June 1, 1977.

"Application of Ion Equilibrium Measurements for Qualitative and Quantitative Analysis," C. Chang, C. C. Cheng and T. O. Tiernan, presented at the 25th Annual Conference on Mass Spectrometry and Allied Topics, Washington, D. C., May 30, 1977.

"Excitation Functions for Negative Ion-Molecule Reactions," C. Lifshitz, R. L. C. Wu and T. O. Tiernan, presented at the 25th Annual Conference on Mass Spectrometry and Allied Topics, Washington, D. C., May 31, 1977.

"Electron and Ion Impact Processes Relevant to Lasers," T. O. Tiernan, Invited presentation at the Air Force Office of Scientific Research Contractors Meeting on Laser Research, Kirtland Air Force Base, New Mexico, May 16, 1977.

"Negative Ion-Neutral Reactions Involving Ozone, Implications on the Thermochemistry of O_3^- ," T. O. Tiernan, C. Lifshitz, R. L. C. Wu, and D. T. Terwilliger, Invited presentation at the Air Force Office of Scientific Research, Chemical Dynamics Meeting, Air Force Geophysics Laboratory, Hanscom Air Force Base, Massachusetts, October 26, 1977.

"Ground State Potential Energy Surface and Vertical Excitation Spectrum for Linear NO_2^+ ," D. G. Hopper, M. Krauss, A. C. Wahl and T. O. Tiernan, Presented at the 11th Midwest Theoretical Chemistry Conference, Columbus, Ohio, May 18, 1978.

"The Bond Dissociation Energy of CO_3^- and the Electron Affinity of CO_3 ," R. L. C. Wu, T. O. Tiernan, C. Lifshitz, Presented at the 26th Annual Conference on Mass Spectrometry and Allied Topics, St. Louis, Missouri, June 2, 1978.

"Combined Theoretical and Experimental Studies of HeH^+ Potential Energy Surfaces Governing Several $\text{He}^+ + \text{H}_2$ Scattering Processes," D. G. Hopper, T. O. Tiernan, E. G. Jones, B. M. Hughes and R. L. C. Wu, Presented at the 26th Annual Conference on Mass Spectrometry and Allied Topics, St. Louis, Missouri, June 1, 1978.

"Formation of Negative Ions," T. O. Tiernan, Invited presentation at the Symposium on Negative Ion Mass Spectrometry, 26th Annual Conference on Mass Spectrometry and Allied Topics, St. Louis, Missouri, May 31, 1978.

"Joint Theoretical and Experimental Studies of HeH_2^+ Potential Energy Surfaces for $\text{He}^+ + \text{H}_2$ Reactions," D. G. Hopper, E. G. Jones, R. L. C. Wu, B. M. Hughes and T. O. Tiernan, Presented at the 33rd Symposium on Molecular Spectroscopy; The Ohio State University, Columbus, Ohio, June 14, 1978.

"SCF Vertical Excitation Energies and Adiabatic State Correlation Diagram for Linear NO_2^+ ," D. G. Hopper, M. Krauss and T. O. Tiernan,

Presented at the 33rd Annual Symposium on Molecular Spectroscopy,
Ohio State University, Columbus, Ohio, June 14, 1978.

"Distribution of Internal Energy in the Products of Ion-Atom Charge
Transfer Reactions," E. G. Jones and T. O. Tiernan, Presented at the
National Meeting of the American Chemical Society, Miami Beach, Florida,
September 11, 1978.

"Evidence for Excited States of O_3^- and CO_3^- from Collision-Induced
Dissociation Processes," T. O. Tiernan, R. L. C. Wu and C. Lifshitz,
Presented at the Autumn Meeting of the Chemical Society, University
of Warwick, Coventry, England, September 19, 1978.

"Energetics and Structures of the Excited and Ground States of CO_3^- ,"
R. L. C. Wu and T. O. Tiernan, Presented at the Thirty-First Annual
Gaseous Electronics Conference, Buffalo, New York, October 18, 1978.

"Applications of Ion Beam Experiments for Determination of Electron
Affinities and Other Thermochemical Data," T. O. Tiernan, Invited
presentation at the Symposium on Electron Affinities and Negative Ion
Stabilities, Tenth Annual Meeting of the Division of Electron and Atomic
Physics, American Physical Society, University of Wisconsin, Madison,
Wisconsin, November 29, 1978.

"Formation and Reactions of Negative Ions Relevant to Chemical
Ionization Mass Spectrometry," T. O. Tiernan, Invited presentation
at the Second Conference on Negative Ion Chemical Ionization Mass
Spectrometry, University of North Carolina, Chapel Hill, N. C. ,
March 22, 1979.

"Thermochemistry and Structure of the Molecular Negative Ion, NO_3^- ,
R. L. C. Wu and T. O. Tiernan, Presented at the Twenty-Seventh Annual
Conference on Mass Spectrometry and Allied Topics, Seattle, Wash.,
June 4, 1979.

"Joint Experimental and Theoretical Study of CO_2 Potential Surfaces,"
D. G. Hopper, T. O. Tiernan, R. L. C. Wu and E. S. Sachs, Presented
at the Twenty-Seventh Annual Conference on Mass Spectrometry and Allied
Topics, Seattle, Wash., June 4, 1979.

"Negative Ion Chemical Ionization Mass Spectrometry: Reactions of F^-
Ion," C. Chang, C. C. Cheng and T. O. Tiernan, Presented at the Twenty-
Seventh Annual Conference on Mass Spectrometry and Allied Topics,
Seattle, Wash., June 4, 1979.

"Evidence for Excited States of CO_3^{*-} and NO_3^{*-} From Collisional
Dissociation Process," T. O. Tiernan, Presented at the Air Force Office
of Scientific Research Molecular Dynamics Conference, U. S. Air Force
Academy, Colorado Springs, Col., October 4, 1979.

"Formation and Energetics of the Excited and Ground States of NO_3^- ,"
R. L. C. Wu and T. O. Tiernan, Presented at the Thirty-Second Annual
Gaseous Electronics Conference, Pittsburgh, Pa., October 11, 1979.

F. Graduate Theses

Kenneth E. Siegenthaler, "Luminescence from He^+/Cl_2 , He^+/Br_2 , and He^+/I_2

Collisions in the Energy Range, 2-170 eV," Ph.D. Thesis, Air Force Institute of Technology, 1976.

Chih-Chyun Cheng, "Negative Ion Chemical Ionization Mass Spectrometry: Reactions of F^- Ion," MS. Thesis, Wright State University, 1979.

Reprints of many of the publications listed above are attached. Not included are the book chapter, the graduate theses, and the manuscripts of papers in press and submitted for publication. These are too lengthy to include here, but are available upon request.

VI. APPENDIX

REPRINTS AND PREPRINTS OF PUBLICATIONS

International Journal of Mass Spectrometry and Ion Physics, 17 (1975) 147-161
© Elsevier Scientific Publishing Company, Amsterdam - Printed in The Netherlands

FORMATION OF THE DIMER CATION $(C_6H_6)_2^+$ IN GASEOUS BENZENE

E. G. JONES*, A. K. BHATTACHARYA AND T. O. TIERNAN**

Aerospace Research Laboratories, Chemistry Research Laboratory, Wright-Patterson Air Force Base, Ohio 45433 (U.S.A.)

(Received 18 November 1974)

ABSTRACT

The formation of the dimer cation $(C_6H_6)_2^+$ in gaseous benzene has been investigated. Two distinct dimer species formed by different mechanisms are indicated. The ground state dimer cation is shown to be formed by a fourth order process involving the ground electronic state $C_6H_6^+$ ion as precursor. In addition, evidence is presented for an excited dimer cation formed bimolecularly by reaction of $C_6H_6^{+*}$ ions having an energy of 3.5 ± 0.5 eV above the ground state. It is suggested that the ground state dimer is in a sandwich configuration and the excited species has the form of a 1-substituted benzene.

INTRODUCTION

Dimers of aromatic systems are of basic interest because of the interactions of the π electronic systems [1]. Excimer fluorescence [2] observable in many aromatic systems has provided a method of studying neutral dimers (excimers). However, much less information concerning aromatic dimer cations is available.

In several of the early gas phase ionic studies of benzene [3-8], there was disagreement as to the relative importance of the dimerization process. More recently, Field et al. [9] and Tiernan and Bhattacharya [10] have shown that the temperature of the ion-source plays the dominant role in determining the relative importance of the dimer cation. Field et al. proposed that an equilibrium is established

* Present address: Systems Research Laboratories, Inc., 2800 Indian Ripple Road, Dayton, Ohio 45400.

** Author to whom reprint requests should be addressed.



and from van 't Hoff plots derived an enthalpy change of $-15 \text{ kcal mol}^{-1}$. In subsequent experiments, Wexler and Pobo [11] have obtained an enthalpy change of $-10 \text{ kcal mol}^{-1}$. They have also proposed a mechanism of dimer formation via a fourth order process, third order in benzene and first order in primary C_6H_6^+ ion abundance. The latter mechanism was supported by studies in our laboratory in which it was found that charge-transfer is the dominant reaction of C_6H_6^+ ions with benzene.

Friedman and Reuben [12] brought attention to the difficulties in resolving the early data; this prompted further studies [13, 14]. Using electron impact Stockdale [13] observed bimolecular formation of the dimer cation. Chupka [14] used photoionization to form C_6H_6^+ ions in the ground electronic and vibrational levels. He found dimer cation formation only after collisional stabilization. Similar results were obtained by Anicich and Bowers [15]. The present report concerns data obtained as a continuation of the experiments of Tiernan and Bhattacharya [10] in an effort to understand better the factors controlling the dimerization process.

EXPERIMENTAL

Studies of the equilibrium between C_6H_6^+ and $(\text{C}_6\text{H}_6)_2^+$ ions were made at relatively high pressures in a single-source, modified time-of-flight instrument described previously [16]. Ionizing voltages of 100 V were used and source temperatures, which were varied over the range from 300 to 500 K, were monitored with an iron-constantan thermocouple attached to the ion-source block. All other instrumental conditions were essentially as given in the detailed description of the instrument and operating techniques [16].

Other data relevant to the identification of the reaction sequences were obtained using the ARL tandem mass spectrometer [17, 18]. For these experiments the collision chamber pressure was varied over the range from 1 to 60 mtorr at temperatures from 300 to 500 K.

Reagents used in these experiments were research grade chemicals which were checked for purity by gas chromatographic-mass spectrometric analysis. Deuterated reagents were obtained from Merck, Sharp and Dohme, Ltd. of Canada. For experiments involving benzene- d_3 and benzene- d_6 , appropriate corrections were made to the observed product intensities to account for isotopic impurities.

RESULTS AND DISCUSSION

Pressure and temperature studies in the tandem mass spectrometer

To select reactant ions unambiguously and to follow the individual reac-

tion steps, the ARL tandem mass spectrometer was used in conjunction with isotopic labelling. The predominant channel for reaction of $C_6H_6^+$ ions with benzene is charge-transfer as represented by the labelled reaction (2).



At a collision chamber temperature of 300 K the ionic products of condensation reactions comprise less than 2% of the charge-transfer product. A value of $4.8 \cdot 10^{-10} \text{ cm}^3 \text{ molec}^{-1} \text{ s}^{-1}$ was measured for the rate coefficient of reaction (2) [19].

The pressure dependence of the bimolecular products is shown in Figs. 1 and 2. The bimolecularity is indicated by the initial linear rise. Deviations from linearity above 20 mtorr arise from further reactions with benzene- d_6 and from ion scattering. The condensation products include a stable bimolecular dimer ion $C_{12}D_6H_6^+$ and also $C_{12}D_6H_5^+$ and $C_{12}D_6H_4^+$ corresponding to the release of H and H_2 respectively.

In addition to the bimolecular products the ion $C_{12}D_{12}^+$ is formed by a higher order process. Its pressure dependence is shown in Fig. 3. Included in this Fig. is a plot of intensity as a function of the cube of the collision region pressure. Over a wide pressure range up to 60 mtorr the $C_{12}D_{12}^+$ ion is formed by a fourth

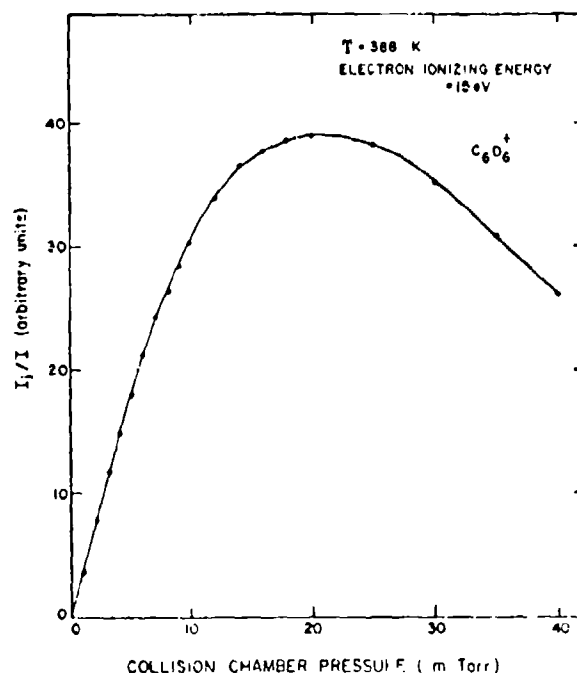


Fig. 1. Charge transfer $C_6H_6^+ + C_6D_6$: — pressure variation.

tion steps, the ARL tandem mass spectrometer was used in conjunction with isotopic labelling. The predominant channel for reaction of $C_6H_6^+$ ions with benzene is charge-transfer as represented by the labelled reaction (2).



At a collision chamber temperature of 300 K the ionic products of condensation reactions comprise less than 2% of the charge-transfer product. A value of $4.8 \cdot 10^{-10} \text{ cm}^3 \text{ molec}^{-1} \text{ s}^{-1}$ was measured for the rate coefficient of reaction (2) [19].

The pressure dependence of the bimolecular products is shown in Figs. 1 and 2. The bimolecularity is indicated by the initial linear rise. Deviations from linearity above 20 mtorr arise from further reactions with benzene- d_6 and from ion scattering. The condensation products include a stable bimolecular dimer ion $C_{12}D_6H_6^+$ and also $C_{12}D_6H_5^+$ and $C_{12}D_6H_4^+$ corresponding to the release of H and H_2 respectively.

In addition to the bimolecular products the ion $C_{12}D_{12}^+$ is formed by a higher order process. Its pressure dependence is shown in Fig. 3. Included in this Fig. is a plot of intensity as a function of the cube of the collision region pressure. Over a wide pressure range up to 60 mtorr the $C_{12}D_{12}^+$ ion is formed by a fourth

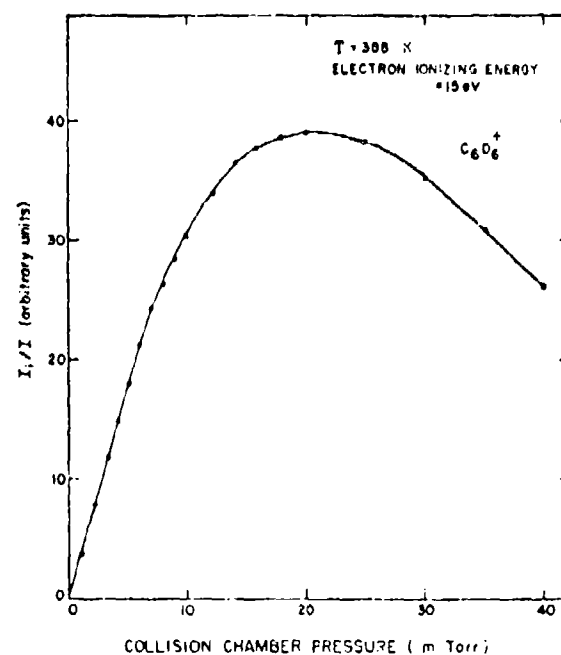


Fig. 1. Charge transfer $C_6H_6^+/C_6D_6$ - pressure variation.

order process in our instrument. The ion intensity was found to be extremely temperature dependent. For example, using $C_6H_6^+$ ions with 0.3-eV kinetic energy (laboratory system) impacted on 15 mtorr of benzene- d_6 at a temperature of 300 K, the $C_{12}D_{12}^+$ ion is the most abundant condensation product. Raising the collision region temperature to 380 K completely eliminates the $C_{12}D_{12}^+$ dimer cation. This can be contrasted with only minor changes in the intensity of the mixed dimer $C_{12}D_6H_6^+$ ion over the same temperature range. Clearly, the $C_{12}D_{12}^+$ and $C_{12}D_6H_6^+$ ionic products have important differences other than isotopic composition. The existence of two different dimeric cations formed by different mechanisms, (second and fourth order) is obviously quite important in the analysis of experiments in which unlabelled reactants are used.

Evidence concerning the origin of the difference in the two dimer ions is obtained by studying the pressure dependence plots for reactant ions formed at various electron impact energies. These experiments were carried out with unlabelled reactants at a collision chamber temperature of 300 K where both dimerization processes occur concurrently. The pressure variations are shown in Fig. 4 for reactant $C_6H_6^+$ ions formed by impact of 13, 25 and 80 V electrons. The initial linear portion indicates the bimolecular process, while at higher pressures the fourth order mechanism dominates under these conditions. The relative contribution of the bimolecular component decreases with a lowering of the electron bombarding energy. These results imply that a more energetic state of the $C_6H_6^+$ ion is responsible for the bimolecular dimer formation and establish the existence of an electron energy threshold below which the bimolecular process can no longer occur.

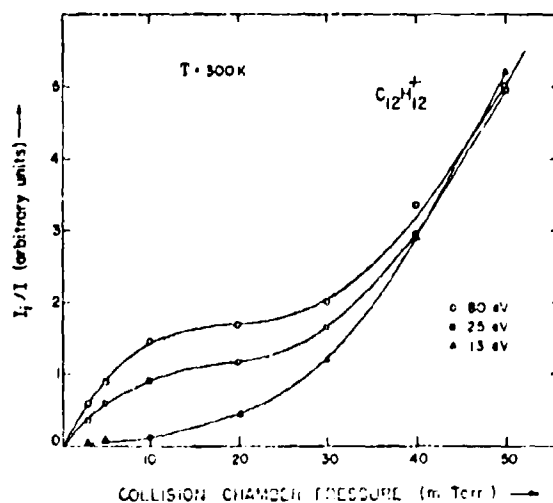


Fig. 4. Dimerization reaction: - pressure and electron energy variation.

Electron energy dependence studies in the tandem mass spectrometer

The existence of energy thresholds for various product ions was established by impacting $C_6H_6^+$ ions on benzene- d_6 at a collision chamber temperature of 360 K and a pressure of 20 mtorr. The intensities I_i/I were recorded for the product ions as a function of the electron energy. The results are plotted in Fig. 5 along with the variation of I with electron energy. The threshold of the $C_6H_6^+$ ion is taken as 9.24 eV [20]. Both the $C_{12}D_6H_6^+$ and $C_{12}D_6H_5^+$ ions are observed to exhibit the same energy dependence and the same threshold, the latter being 3.5 ± 0.5 eV above the benzene ionization potential. Within the experimental limits, the bimolecular dimer ion shows the same energy threshold for both the $C_6D_6^+/C_6H_6$ and the $C_6H_6^+/C_6D_6$ experiments.

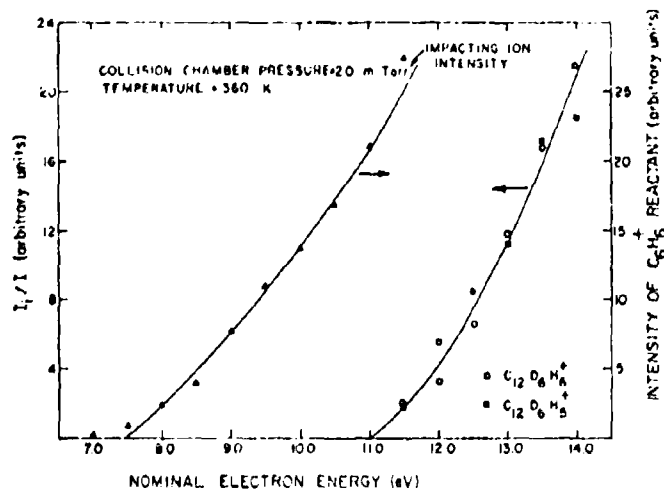


Fig. 5. Bimolecular dimer intensity: -- electron energy variation.

These results indicate that the formation of $C_{12}D_6H_6^+$, $C_{12}D_6H_5^+$ and also presumably $C_{12}D_6H_4^+$ requires the participation of an excited $C_6H_6^{+*}$ ion having internal energy ca. 3.5 eV above the benzene ionization threshold. On the other hand, the $C_{12}D_{12}^+$ product, as illustrated in Fig. 6, shows no sign of an energy threshold, apparently indicating its formation by ground state reactant $C_6H_6^+$ ions.

It should be mentioned at this point that the existence of an excited elec-

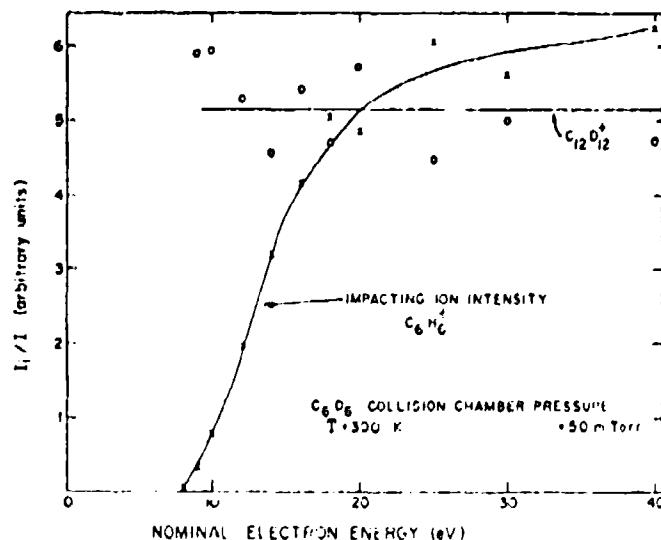


Fig. 6. Dimer intensity: --electron energy variation.

tronic state in the vicinity of 12.8 ± 0.5 eV is uncertain from photoelectron spectroscopy data [21-24]. Sampson [25] has detected states at 9.3, 11.5, 13.9 and 15.5 eV for benzene. In recent studies Lindholm and co-workers [26, 27] have found evidence for two states assigned $3e_{2g}$ and $1a_{2u}$ with onsets in the region 11-12 eV; these are somewhat below the limit determined for the reacting ions. According to the assignment, the former is weakly C-C bonding and the latter strongly C-C bonding. In view of the uncertain evidence, the $C_6H_6^+$ reacting ions cannot be definitely assigned to an electronic state. The identity of this species is considered further in a later section.

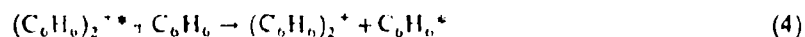
Summary of pressure and energy studies

Conclusions from the pressure and energy studies in the tandem instrument may be summarized as follows.

(a) The ground state benzene ion is the precursor of a benzene dimer ion product formed by an overall fourth order process. Experiments with labelled reagents indicate that the initial step is the charge-transfer reaction. (2). The function of this reaction is apparently twofold; it effectively relaxes the vibrational energy of the ions formed by electron impact and reduces their kinetic energy by as much as a factor of two for an intimate collision [28]. The next step in the dimer formation is best considered [5-7] as an associative equilibrium reaction

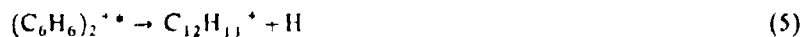


which forms an excited species $(\text{C}_6\text{H}_6)_2^{++}$ requiring collisional stabilization, (reaction 4).



in order to be observed as a stable ion. The occurrence of such a series of reactions depends critically on the lifetime of the excited dimer ion. If its internal energy is large compared to the depth in the potential energy surface along the direction of the reaction coordinate, then it will decompose unimolecularly within a few vibrational periods before a stabilizing collision can occur. The sensitivity of the lifetime to the internal energy of $(\text{C}_6\text{H}_6)_2^{++}$ is emphasized by the need for the initial vibrational relaxation step, (2). This is probably the reason why no fourth order dimer ions are observed at collision chamber temperatures ≥ 380 K. If C_6H_6^+ ions were formed in the lowest vibrational levels as is the case with the photoionization experiments, then the dimer cation would be observed to be formed by an overall third order process as observed by Chupka [14] and by Anicich and Bowers [15].

(b) An excited state of the benzene molecular ion having an energy threshold ca. 3.5 ± 0.5 eV above the ionization threshold, (but apparently not an electronic state), may also undergo an associative equilibrium reaction such as (3). Because of the extra internal energy, there are in addition to the back reaction, two other reaction channels, producing $\text{C}_{12}\text{H}_{11}^+$ and $\text{C}_{12}\text{H}_{10}^+$ products respectively.



Considering the energy sensitivity of the fourth order process and the magnitude of the energy threshold for the bimolecular reaction, it seems clear that the two mechanisms are forming quite different dimeric species. The existence of two distinct reaction mechanisms involving different states of the precursor ion accounts for reported observations of reaction mechanisms ranging from second to fourth order. In Stockdale's experiments [13] the bimolecular dependence was established for electron impact energies of 20 eV or greater. A glance at Fig. 4 indicates that at this electron energy appreciable amounts of excited $\text{C}_6\text{H}_6^{++}$ ions are present to undergo a bimolecular reaction. Furthermore, under the pressure conditions ($P < 1$ mtorr) the higher order process would make a negligible contribution. Further insight into understanding the ions involved is provided in the following isotopic study.

Isotopic study

The relative abundances of the bimolecular products from the benzene parent ion reactions were measured for various combinations of isotopically

TABLE I

BIMOLECULAR PRODUCT IONS FROM THE REACTIONS OF $C_6X_6^+$ IONS WITH C_6X_6 ($X = H, D$) IN THE TANDEM MASS SPECTROMETER^a

Reactant ion	Neutral	Product ion intensities (arbitrary units)					Apparent total cross section (\AA^2)
		Dimer (D)	(D-1)	(D-2)	(D-3)	(D-4)	
$C_6H_6^+$ ^b (benzene)	C_6H_6	101(1.00)	177(1.74)	28.5(0.28)	—	—	0.9
	C_6D_6	96.0(1.00)	146(1.52)	27.0(0.28)	—	—	0.9
$C_6D_3H_3^+$ ^b (<i>o</i> -d ₃ -benzene)	C_6H_6	61.1(1.00)	109(1.79)	66.6(1.09)	13.9(0.23)	11.8(0.19)	0.3
	$C_6D_3H_3$	59.6(1.00)	96.1(1.61)	57.9(0.97)	15.8(0.27)	10.2(0.17)	0.8
	C_6D_6	86.0(1.00)	77.1(0.90)	49.6(0.58)	14.7(0.17)	11.3(0.13)	0.8
$C_6D_6^+$ (benzene-d ₆)	C_6H_6	6.1(1.00)	—	157(25.6)	—	17.4(2.85)	0.6
	C_6D_6	18.9(1.00)	—	147(7.78)	—	20.3(1.07)	0.6

^a Collision chamber temperature, 300 K; ionizing voltage, 70 eV; collision chamber pressure, 10 μm ; ion kinetic energy ca. 0.3 eV.

^b The reactant ions ^{13}C $C_5H_6^+$ and ^{13}C $C_5D_3H_3^+$ were utilized to avoid $^{13}\text{C}^+$ interference in product identification.

^c Values in parentheses are relative intensities normalized to a value of 1.0 for the dimer ion.

labelled reactants. The collision chamber pressure was maintained at 10 mtorr to prevent the formation of any fourth order ionic products. The results are summarized in Table I.

The excited dimeric ion has several decomposition channels available. One of these paths, that leading to the original reactants, cannot be monitored with our in-line tandem experimental arrangement. Therefore, normalization of the observed intensities by the total ion current is not justified; the relative importance of the various fragmentation processes is best visualized by normalizing the spectra to unit dimer ion intensity. These quantities are shown in parentheses in Table I.

Since the collision rates are essentially the same for all cases considered, the magnitude of the apparent total reaction cross section in the last column of Table I provides some insight into the importance of the back reaction. It can be concluded from these data that the extent of back reaction increases with increasing deuterium substitution in the reacting ion.

An important observation from the dissociative product ions shown in Table I is that in the case of $C_6H_6^+$ reactions, only elimination of H and H₂ occurs, while in the corresponding reactions of $C_6D_6^+$, only D and D₂ are lost from the dimeric species. It is apparent that the mixed dimer product ion, $C_{12}D_nH_{6-n}^+$, retains some structural memory of the reacting ion in each case. To a first approximation, the product distribution is principally a function of the impacting ion, the role of the neutral being rather minor. This is further emphasized by the con-

stancy of the apparent total cross sections for the reactions of a given ion with various neutral targets.

The increased fragmentation of the dimer cation observed with decreasing deuterium substitution in the neutral reactant is likely related to internal energy differences in the neutral species. Certainly, in the energy range studied, the decomposition rates are rapidly changing functions of the internal energy. We are unable to specify the internal energy distributions of either the reactants or products from the present experiments. It seems clear, however, that elimination occurring only from the "ionic" portion of the dimer ion excludes the possibility of a symmetrical dimer structure such as two six membered rings attached appropriately. These results further suggest that the excited reactant ion probably does not have benzene-ring structure but is rather a structural isomer, possibly a linear chain or fulvene-structure. The former has been postulated [29] for excited benzene ions formed by electron impact. Recently Gross [30] has found significant differences in the bimolecular reactions of $C_6H_6^+$ isomers.

Equilibrium studies in the high pressure single-source mass spectrometer

There have been two reported measurements of the enthalpy change for the monomer-dimer cation equilibrium in benzene using mass spectrometric methods. Field et al. [9] and Wexler and Pobo [11] have obtained values of -15 and -10 kcal mol $^{-1}$ respectively, under conditions thought to be close to equilibrium. In view of the existence of two mechanisms for dimer ion formation established in the present study, the interpretation of van't Hoff plots and the existence of equilibrium under various source conditions should be discussed.

For the idealized equilibrium,



where B^+ and B_2^+ represent $C_6H_6^+$ and $(C_6H_6)_2^+$ ions respectively, the equilibrium constant can be expressed as,

$$K_P = \frac{[B_2^+]}{[B^+]} \cdot \left(\frac{1}{P}\right) \quad (8)$$

where P is the pressure of benzene. Provided that an equilibrium exists within the ion source and that collected ion currents represent the concentrations of the ions in the source, then van't Hoff plots of $\log K_P$ as a function of the reciprocal of the temperature can be made. From the slope of such plots the enthalpy change can be determined.

First, consider the bimolecular reaction sequence,

in Fig. 7, for several ion-source pressures and repeller field strengths in the high pressure Bendix instrument. The assumption is made there that the concentration of excited ions, $C_6H_6^{+*}$, is small relative to that of the ground state benzene ions. The plots are linear up to a temperature of ca. 370 K then are concave downwards. The average slope over the pressure range 100-200 mtorr and the temperature range 300-370 K at the lowest repeller field strengths yields an enthalpy difference ΔH of -8 ± 2 kcal mol $^{-1}$. This is in reasonably good agreement with the value of Wexler and Pobo [11] and about a factor of two lower than the value obtained by Field et al. [9]. The change in slope at 370 K coincides with the temperature at which the fourth order dimer was observed in the tandem experiments to become unstable, and at which the bimolecular process dominates. The plots in the higher temperature region are linear over the range from 390 K to 470 K, the latter being the maximum temperature investigated. Under our experimental conditions, no meaningful enthalpy difference can be determined from this high temperature region.

Formation of the fourth order dimer depends critically on the gas temperature and the ion energy. If the pressure is too low or the kinetic energy of the benzene ion is too high the lifetime of the associative product is too short to allow a stabilization collision. Under these conditions equilibrium cannot be achieved, as evidenced by the plots in Fig. 7 under conditions of low pressure and high repeller field strengths. Under conditions of the lowest field strengths and highest pressure, the benzene ions spend about 10 μ s in the ion source. Increasing the pressure from 150 to 200 mtorr produces essentially no change in the measured value for K_p over the low temperature region. The achievement of equilibrium is difficult to establish with certainty. However, the behavior of the observed K_p clearly indicates that the system is approaching equilibrium, and the measured enthalpy change is therefore a reasonable approximation of the equilibrium value.

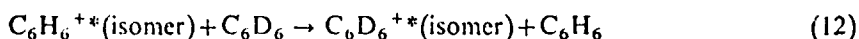
Ion structure ($C_6H_6^{+}$).* The results described previously indicate the participation of two states of the benzene parent ion. It is found that the ground electronic state ion having an ionization potential of 9.24 eV, and possibly other excited electronic states having a cyclic structure, react via a fourth order mechanism to form the dimer cation. The enthalpy change for this process (assuming that the charge-transfer and collisional stabilization steps have zero activation energies) is in the range $-(6 \rightarrow 10)$ kcal mol $^{-1}$.

In addition, our data demonstrate the existence of another $C_6H_6^{+*}$ species with an appearance potential of 12.8 ± 0.5 eV. The isotopic experiments suggest that this state is a non-cyclic isomer of the ground-state ion. If this is indeed the case, then the energy in excess of the ionization potential of benzene which is required to produce this species, that is, 3.5 ± 0.5 eV, should correspond to the activation energy for ring-opening. Taking $\Delta H_f(C_6H_6^{+*}) = 233$ kcal mol $^{-1}$ [32] for the cyclic form of the benzene parent ion therefore yields an upper limit of 314 ± 10 kcal mol $^{-1}$ for the linear form of the $C_6H_6^{+*}$ reactant. From studies of

linear C_6H_6 isomers, Momigny et al. [29] have determined $\Delta H_f(C_6H_6^+) = 307$ kcal mol $^{-1}$ for ionization of the structures CH-CCCH-CHCH-CH $_2$ and C_2H_5C -CC-CH. Thus, while we are unable to identify precisely the isomeric $C_6H_6^+$ ion in question from the present study, the results are clearly consistent with a linear chain structure formed by opening of the six-membered ring.

The existence of such a low activation energy for the ring opening may allow the isomerization to compete effectively with the loss of H and H $_2$ from the $C_6H_6^+$ ion. If the isomerization were the dominant process, then the loss of a hydrogen atom would take place via the linear $C_6H_6^+$ isomer and the observed appearance potential of $C_6H_5^+$ would be higher than predicted on the basis of benzyl ion formation [33].

The structural difference between the two benzene molecular ions may explain the failure to detect certain product ions at higher pressures. For example, no $C_{12}D_{11}^+$ or $C_{12}D_{12}^+$ products were observed at a temperature of ca. 400 K when bombarding benzene-d $_6$ with $C_6H_6^+$ ions in the tandem instrument. In view of the fast charge-transfer reaction observed for ground state benzene ions, and the existence of bimolecular products such as $C_{12}D_6H_6^+$, $C_{12}D_6H_5^+$ and $C_{12}D_6H_4^+$, one would expect formation of $C_{12}D_{12}^+$, $C_{12}D_{11}^+$ and $C_{12}D_{10}^+$ ions to occur following charge-transfer. The absence of such ions implies that the charge-transfer reaction,



does not occur. There are two possible reasons for this. First, the change in structure requires a much longer time than the charge-transfer process, so that the Franck-Condon factors for the latter reaction may be low. Secondly, the reaction might form a vibrationally excited ion with a cyclic structure which then requires an isomerization prior to undergoing a bimolecular dimerization reaction.

Ion structure $(C_6H_6^+)_2$. As already noted, two dimeric species are indicated from the present study. The first, formed by a fourth order reaction mechanism, has a binding energy in the range 6-10 kcal mol $^{-1}$, leading to the $C_6H_6^+$ ground state ion on decomposition. The second is formed bimolecularly, having some unknown binding energy, (but almost certainly >10 kcal mol $^{-1}$ because of its temperature stability and bimolecular formation requiring no collisional stabilization), and this yields the isomerized $C_6H_6^{+*}$ ion on decomposition. The isotopic studies and the conclusions concerning the $C_6H_6^{+*}$ ion suggest that the structure of the bimolecular dimer is non-symmetric, probably having the form of a 1-substituted benzene.

It may be noted that both experimental studies and theoretical calculations dealing with the structure of benzene excimers, $(C_6H_6)_2$, have been reported. The calculations of Jortner and co-workers [1] and of Chesnut et al. [34] as well as the experimental work of Birks and Conte [35], all of which treat the dimer as two benzene molecules in a sandwich configuration, are consistent with

shallow well depths (0.3–0.5 eV) and interplanar separations greater than 3 Å.

Badger and Brocklehurst [36] have discussed the form of dimer cations and from electron spin resonance experiments [37] have concluded that the benzene dimer cation has a symmetric sandwich structure. Studies by Hamlet [38] and Field et al. [9] have similarly concluded a sandwich structure for this dimer species. More recently, Chesnut [39] has performed Hückel molecular orbital calculations on the dimer cation in a sandwich configuration and again, the results indicate well depths on the order of 0.3–0.5 eV, and large (ca. 3 Å) interplanar separations. This theoretical well depth is in good agreement with the experimental binding energy of the dimer ion determined in the present work. Both theoretical and experimental evidence therefore point to a sandwich structure for the ground state dimer ion.

The structural similarities of the benzene excimer and the dimer cation make it reasonable to predict the ionization potential of the B₂ excimer. Since it has been shown that the ground state B⁺ ion reacts to form this structure, the total energy corresponding to the dimer ion in a relaxed state is ca. (9.2–0.3) eV. The corresponding energy for the excimer has been calculated by Chesnut [34] as ca. (4.1 + 0.2) eV at the equilibrium interplanar separation. Thus, a value of ca. 4.6 eV is predicted for the ionization potential of the benzene excimer. Experimental determinations of excimer ionization potentials, which would obviously be of interest for comparison, have not yet been reported.

ACKNOWLEDGEMENTS

The authors are greatly indebted to Dr. D. B. Chesnut and to Dr. W. A. Chupka for valuable discussions concerning the benzene dimer cation. Research performed by E. G. J. and A. K. B. while in the capacity of Ohio State University Research Foundation Visiting Research Associates under Contracts F33615-67-1758 and F33615-67-C-1758, respectively.

REFERENCES

- 1 M. T. Vala, Jr., I. H. Hillier, S. A. Rice and J. Jortner, *J. Chem. Phys.*, **44** (1966) 23
- 2 J. B. Birks, *Chem. Phys. Lett.*, **1** (1967) 304.
- 3 A. Henglein, *Z. Naturforsch. A*, **17** (1962) 44.
- 4 C. Lifshitz and B. G. Reuben, *J. Chem. Phys.*, **50** (1969) 951.
- 5 F. H. Field, P. Hamlet and W. F. Libby, *J. Amer. Chem. Soc.*, **89** (1967) 6035.
- 6 L. I. Virin, Yu. A. Safin and R. F. Dzhagatspanyan, *Khim. Vys. Energ.*, **1** (5) (1967) 417.
- 7 A. Giardini-Guidoni and F. Zocchi, *Trans. Faraday Soc.*, **64** (1968) 2342.
- 8 S. Wexler and R. P. Clow, *J. Amer. Chem. Soc.*, **90** (1968) 3940.
- 9 F. H. Field, P. Hamlet and W. F. Libby, *J. Amer. Chem. Soc.*, **91** (1969) 2839.
- 10 T. O. Tiernan and A. K. Bhattacharya, *Abstracts, 157th National Meeting of the American Chemical Society, Minneapolis, Minn., April 1969.*
- 11 S. Wexler and L. G. Pobo, *J. Phys. Chem.*, **74** (1970) 257.

- 12 L. Friedman and B. G. Reuben, *Advan. Chem. Phys.*, **19** (1971) 33.
- 13 J. A. D. Stockdale, *J. Chem. Phys.*, **58** (1973) 3881.
- 14 W. A. Chupka, unpublished work.
- 15 V. G. Anicich and M. T. Bowers, *J. Amer. Chem. Soc.*, **96** (1974) 1279.
- 16 J. H. Futrell, T. O. Tiernan, F. P. Abramson and C. D. Miller, *Rev. Sci. Instrum.*, **39** (1968) 340.
- 17 J. H. Futrell and C. D. Miller, *Rev. Sci. Instrum.*, **37** (1966) 1521.
- 18 B. M. Hughes and T. O. Tiernan, *J. Chem. Phys.*, **55** (1971) 3419.
- 19 Value obtained relative to $12 \cdot 10^{-10} \text{ cm}^3 \text{ molec}^{-1} \text{ s}^{-1}$ for principal reaction in methane; cf S. K. Gupta, E. G. Jones, A. G. Harrison and J. J. Myher, *Can. J. Chem.*, **45** (1967) 3107.
- 20 M. J. S. Dewar and S. D. Worley, *J. Chem. Phys.*, **50** (1969) 654.
- 21 M. I. Al-Joboury and D. W. Turner, *J. Chem. Soc., London*, (1964) 4434.
- 22 A. D. Baker, D. P. May and D. W. Turner, *J. Chem. Soc. B*, (1968) 22.
- 23 A. D. Baker, C. R. Brundle and D. W. Turner, *J. Mass Spectrom. Ion. Phys.*, **1** (1968) 443.
- 24 I. D. Clark and D. C. Frost, *J. Amer. Chem. Soc.*, **89** (1967) 244.
- 25 J. A. R. Sampson, *Chem. Phys. Lett.*, **4** (1969) 257.
- 26 B. Johnson and E. Lindholm, *Ark. Fys.*, **39** (1969) 65.
- 27 L. Asbrink, O. Edqvist, E. Lindholm and L. E. Selin, *Chem. Phys. Lett.*, **5** (1970) 192.
- 28 G. Gioumoussis and D. P. Stevenson, *J. Chem. Phys.*, **29** (1958) 294.
- 29 J. Momigny, L. Brakier and L. D'Or, *Bull. Cl. Sci. Acad. Roy. Belg.*, **48** (1962) 1002.
- 30 M. L. Gross, private communication.
- 31 H. S. Johnson, *Gas Phase Reaction Rate Theory*, Ronald Press, New York, 1966.
- 32 J. L. Franklin, J. G. Dillard, H. M. Rosenstock, J. T. Herron, K. Draxl and F. H. Field, *Ionization Potentials, Appearance Potentials and Heats of Formation of Gaseous Positive Ions*, NSRDS-NBS 26, 1969.
- 33 M. L. Vestal in P. Ausloos (Ed.), *Fundamental Processes in Radiation Chemistry*, Interscience, New York, 1968.
- 34 D. B. Chesnut, C. J. Fritchie and H. E. Simmons, *J. Chem. Phys.*, **42** (1965) 1127.
- 35 J. B. Birks and J. C. Conte, *Proc. Roy. Soc., Ser. A*, **303** (1968) 85.
- 36 B. Badger and B. Brocklehurst, *Nature (London)* **219** (1968) 263.
- 37 B. Badger, B. Brocklehurst and R. D. Russell, *Chem. Phys. Lett.*, **1** (1967) 122.
- 38 P. L. Hamlet, Ph.D. Thesis, University of California, Los Angeles, 1968.
- 39 D. B. Chesnut, private communication.

Measurement of thermal electron dissociative attachment rate constants for halogen gases using a flowing afterglow technique

G. D. Sides* and T. O. Tiernan

Department of Chemistry, Wright State University, Dayton, Ohio 45431

R. J. Hanrahan

Department of Chemistry, University of Florida, Gainesville, Florida 32611

(Received 10 May 1976)

A flowing afterglow apparatus was constructed and used to measure thermal electron attachment rate constants in the halogen gases fluorine, chlorine, and bromine. The operation of the afterglow system and the mathematical models applied in treating the data were tested by measuring the thermal attachment rate constant for electrons in sulfur hexafluoride. The average value obtained for this rate constant is $4.2 \pm 1.1 \times 10^{-8} \text{ cm}^3 \text{ molecule}^{-1} \text{ sec}^{-1}$ when a microwave discharge was used as the electron source and $3.6 \pm 1.8 \times 10^{-8} \text{ cm}^3 \text{ molecule}^{-1} \text{ sec}^{-1}$ when a filament was used as the electron source. The average electron temperature was estimated to be approximately 600°K for the microwave discharge source and approximately 350°K for the filament source. A charge transfer reaction between sulfur hexafluoride and the ion O_2^+ was also investigated in the present study to further assess the operation of the flowing afterglow apparatus in the microwave discharge source configuration. The average rate constant obtained for this reaction is $3.7 \pm 0.4 \times 10^{-11} \text{ cm}^3 \text{ molecule}^{-1} \text{ sec}^{-1}$ for an estimated ion temperature of 300–325°K. The average rate constants obtained for the dissociative attachment of electrons in fluorine are $4.6 \pm 1.2 \times 10^{-9} \text{ cm}^3 \text{ molecule}^{-1} \text{ sec}^{-1}$ for an electron temperature of approximately 600°K and $3.1 \pm 1.2 \times 10^{-9} \text{ cm}^3 \text{ molecule}^{-1} \text{ sec}^{-1}$ for an electron temperature of approximately 350°K. The average rate constants obtained for dissociative electron attachment in chlorine and bromine are $3.7 \pm 1.7 \times 10^{-9}$ and $1.0 \pm 0.9 \times 10^{-11} \text{ cm}^3 \text{ molecule}^{-1} \text{ sec}^{-1}$, respectively, for an electron temperature of approximately 350°K. The rate constant for the three-body attachment reaction $\text{Br}^- + \text{Br}_2 + \text{Ar}$ to form Br_2^- was also measured and found to be $1.9 \pm 0.5 \times 10^{-28} \text{ cm}^6 \text{ molecule}^{-2} \text{ sec}^{-1}$.

INTRODUCTION

The reaction rates for the attachment of thermal electrons to various molecules continue to be of considerable research interest. Applications of these data are important in the fields of aeronomy, laser physics, and spacecraft communication.^{1–3}

A survey of published literature data reveals that little information exists concerning thermal electron attachment in the halogen gases. Table I summarizes published thermal electron attachment rate constants for fluorine, chlorine, and bromine. The rate constant for fluorine, listed in Table I, was published in a preliminary report of this work.⁴ Prior to that publication, no rate constant for the dissociative attachment of low energy electrons in fluorine had been published. This article reports the final results of the measurement of that rate constant. A recent publication by Christodoulides *et al.*⁵ reports a rate constant for the attachment of thermal electrons in chlorine. Truby⁶

has measured the dissociative attachment rate constant for thermal electrons in bromine using a static afterglow technique. The results summarized in Table I not only illustrate the need for further halogen thermal electron attachment studies, but also suggest the desirability of a different approach for such measurements. Prior to the present work, none of the reported studies of these reactions involved measurements in which the product ions formed in the dissociative attachment reaction were monitored. Therefore, electron loss mechanisms other than the dissociative attachment reaction are also possible and may have caused the measured rate constant to be in error. The present work avoids this limitation by monitoring the product ions in order to determine the dissociative attachment rate constants.

In view of the absence of rate data for the attachment of thermal electrons to fluorine and the need to corroborate existing data for bromine and chlorine, an ap-

TABLE I. Thermal electron attachment rate constants for fluorine, chlorine, and bromine.

Molecule	$k (\text{cm}^3 \text{ molecule}^{-1} \text{ sec}^{-1})$	Technique	Electron temperature (°K)	Reference
F_2	7.5×10^{-9}	Flowing afterglow	~500	4
Cl_2	3.1×10^{-10}	Electron cyclotron resonance	293	5
Br_2	0.82×10^{-12}	Static afterglow	296	6

paratus was designed and constructed to obtain this information. A flowing afterglow technique was selected for these experiments after a review of the methods which have been used to measure thermal electron attachment rate constants. The flowing afterglow method was selected primarily due to the ease with which thermal electrons are produced in the afterglow. In addition, this technique has previously been used to measure a thermal electron attachment rate constant.⁷ Another reason for the selection of the flowing afterglow technique is its general applicability to the study of other kinetic processes such as ion-molecule⁸ and metastable atom-neutral molecule reactions.⁹

Another objective of the present work was the development of a flowing afterglow apparatus considerably smaller than those generally used in previous studies of electron-molecule and ion-molecule reactions.¹⁰ The smaller size decreases the cost and space requirements of such an apparatus.

The present experiments involved three stages: the design and construction of the flowing afterglow apparatus, the use of this apparatus to measure known reaction rate constants in order to assess the operation of the apparatus, and the use of the apparatus to measure thermal electron attachment rate constants for the halogens fluorine, chlorine, and bromine. The reactions studied in order to test the flowing afterglow apparatus were the electron attachment process

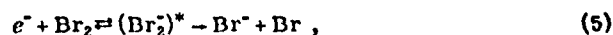
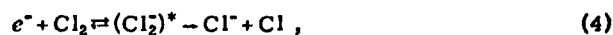


and the ion-molecule reaction



Both of these reactions were selected because their thermal rate constants have been measured previously

using a flowing afterglow technique.^{7,8} In addition, the thermal electron attachment rate constant for sulfur hexafluoride has been measured using several other experimental techniques.¹¹⁻¹⁴ Once the initial tests of the experimental technique were completed, the thermal electron attachment rate constants for



were determined. In addition, the rate constant for



was determined in the course of the present research.

EXPERIMENTAL

A schematic diagram of the flowing afterglow apparatus in the microwave discharge source configuration is shown in Fig. 1. Electrons are produced by a 2450 MHz microwave discharge (approximately 2 W total power) in argon buffer gas in a quartz discharge tube. The microwave power supply is coupled to the buffer gas by an Evenson cavity and monitored by a microwave power meter (not shown). Electrons produced in the active discharge are rapidly thermalized in the high pressure environment (1-3 torr buffer gas pressure) and flow past the reactant gas injection port, where a gas such as fluorine may be introduced into the afterglow. Negative ions formed in the reaction tube, 19.6 cm in length and 2.57 cm inside diameter, are sampled through an orifice, 0.23 mm in diameter and 0.076 mm in length, located on the tip of a stainless steel cone at the end of the reaction tube. The cone is maintained at +4 to +11 V with respect to ground in order to extract

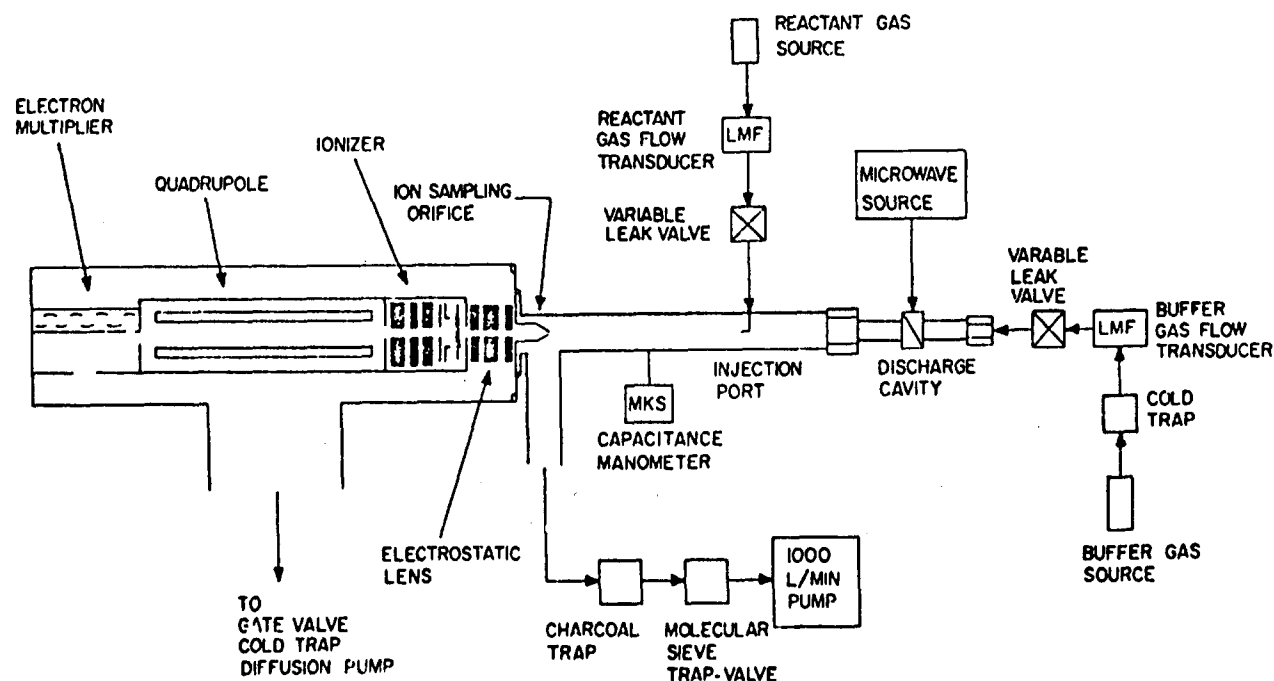


FIG. 1. Flowing afterglow apparatus in the microwave discharge source configuration.

negative ions from the flowing afterglow. The ions extracted are focused by a cylindrical electrostatic lens system into the lens elements of an ionizer. These elements then focus the ions into an Extranuclear voltage-scanned quadrupole mass spectrometer. The ions are then mass resolved and detected by an electron multiplier. A preamp-electrometer combination (not shown) amplifies the resulting signal and provides analog outputs for computer and oscilloscope inputs. The flow tube is pumped by a 1000 liter min^{-1} rotary pump. A charcoal trap in the pump line converts fluorine to carbon tetrafluoride¹⁵ in order to prevent mechanical pump degradation when fluorine is used as the reactant gas. A molecular sieve trap in the pump line prevents the back diffusion of hydrocarbons from the mechanical pump.

The flowing afterglow apparatus was also used in a filament source configuration. The basic difference between this configuration and that shown in Fig. 1 is the removal of the microwave discharge source and the substitution of a filament electron source. The filament is a thoriated-iridium ribbon which is spot welded to hermetic feedthroughs mounted in the flow tube walls. The anode is at ground potential and mounted approximately 1.3 mm from the filament. Also, at this point in time a sintered glass disc was installed upstream of the source in order to smooth the buffer gas flow in the reaction tube. In addition, an automatic flow control system was installed so that the reactant gas flow rate could be controlled by a computer.

The buffer gas generally used in these experiments was argon, trapped with a dry ice-acetone slush, the flow rate typically being 10–25 $\text{atm cm}^3 \text{sec}^{-1}$. A Hastings-Raydist linear mass flowmeter was used to measure the buffer gas flow rate for experiments presented in this article. This buffer gas flowmeter can be used to measure flow rates up to 155 $\text{atm cm}^3 \text{sec}^{-1}$ with an accuracy of approximately $\pm 0.1\%$ of full scale. The flowmeter provides a 5 V output signal at full scale for use with a readout device. The buffer gas linear mass flowmeter was calibrated for argon. The buffer gas flow rate is maintained constant by regulating the backing pressure behind a fixed leak. The stability of the buffer gas flow was found to be within $\pm 0.1\%$ of full scale per hour.

The reactant gas flow rate was monitored by a second Hastings-Raydist linear mass flowmeter for which full scale deflection corresponds to 0.64 $\text{atm cm}^3 \text{sec}^{-1}$ of argon. A monel transducer was used with this flowmeter in order to permit the monitoring of corrosive gases. The flowmeter was calibrated for argon since most of the reactant gas mixtures used in the present research consisted of at least 99.8% argon; thus, the thermal conductivity of the mixture is essentially that of argon. Conversion factors supplied by the manufacturer allow the calculation of gas flow rates for gases or mixtures of gases other than argon.

The number density of the reactant gas in the flow tube can be calculated from the measured reactant and buffer gas flow rates and the measured buffer gas pressure (measured at the center of the reaction tube with

a MKS Baratron capacitance manometer). As a check of this method of determining the reactant gas number density, the change in pressure in the reaction tube may be monitored as the reactant gas flow is varied; the number density of the reactant gas can then be calculated independently of the linear mass flowmeter signal. The agreement between the two techniques described above has been found to be within at least 9% over the full range of reactant gas flow. This indicates that the use of the linear mass flowmeter technique to determine the reactant gas number density is valid. The measurement of the partial pressure of the injected reactant gas during an actual experiment is not feasible, since this corresponds to only about 14 mtorr for full scale reactant gas flow; therefore, a small drift in the reaction tube pressure during an experiment would introduce considerable error. Such drift probably accounts for the difference observed in the two number density measurement techniques compared above, especially since the deviations observed correspond to a pressure of about 1 mtorr on a buffer gas pressure background of 3000 mtorr.

The data acquisition system ultimately developed during the course of this research is shown in Fig. 2. The system is designed around a Hewlett-Packard 24K, 16-bit minicomputer and its peripheral devices. Analog signals proportional to experimental parameters such as reactant and buffer gas flows, buffer gas pressure, ion signal, and ion mass are converted to digital signals by a 14-bit analog-to-digital converter. A relay register is used to advance the mass programmer-peak switching hardware. A 12-bit digital-to-analog converter provides the remote programmed input signal necessary to control the automatic flow system hardware. A cathode ray terminal is used to give the operator input/output capability. A storage oscilloscope allows the operator to display the ion signal as a function of the reactant gas flow at the end of each experiment. The raw data for each experiment is stored on a magnetic disc system to be reduced to a rate constant at a later time.

DATA ANALYSIS

Mathematical models for the analysis of experimental data, obtained using a flowing afterglow system, have been developed by several authors.^{9,10,17} The discussion presented below briefly outlines the development of the models used to calculate rate constants from the kinetic data obtained in the present research.

Simple model

The simplest analysis of reaction kinetics for a flowing afterglow system assumes that the buffer gas axial velocity v_0 is independent of radial or axial position in the reaction tube. In this simple model, it is also assumed that the neutral reactant gas is injected uniformly throughout the flow tube cross section at $z = 0$, where the z axis is the cylindrical axis of the reaction tube. In addition, the diffusion of reactants and products in the reaction tube is not considered. For net reactions of the type

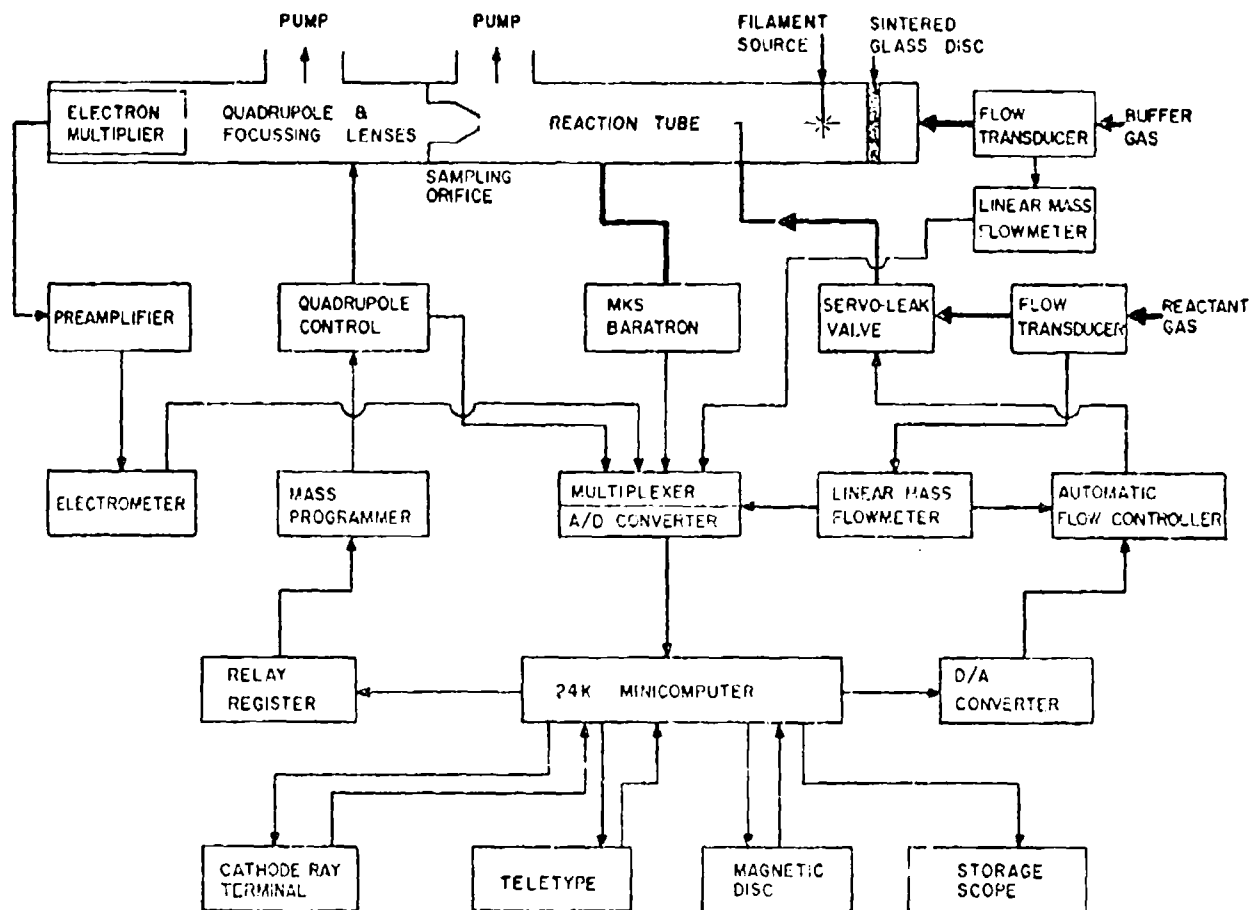
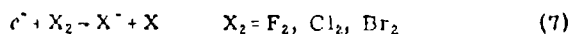


FIG. 2. Schematic of the computer-interfaced data acquisition system.



rate equations may be solved to give the desired expression for the product ion number density

$$[X^-] = [e^-]_0 \{1 - \exp(-k[X_2]t)\}, \quad (8)$$

where the bracketed symbols represent the number densities of reactants and product, k is the bimolecular rate constant, and $[e^-]_0$ is the electron density for $t > 0$ ($t=0$ at $z=0$, the reactant gas injection port location) and $[X_2] = 0$. It was assumed that $[X_2] = [e^-]$ for all t . Equation (8) shows that the measurement of $[X^-]$ at the end of the reaction tube as a function of $[X_2]$ results in the determination of the rate constant k if the reaction time t is known.

Radial velocity profile

If the planar velocity profile assumption made above is true, then the time required by any species to transit the reaction tube is given by

$$t = \pi a^2 L / F = L / v_0, \quad (9)$$

where a is the reaction tube radius, L is the reaction tube length, and F is the buffer gas volume flow rate. Due to frictional forces at the walls, the radial velocity profile for the viscous flow of gas in a cylindrical tube

is not planar but parabolic.⁹ Neglecting the axial velocity gradient (near zero in the present research), the radial velocity profile is given by

$$v(r) = 2v_0(1 - r^2/a^2), \quad (10)$$

where v_0 is the planar profile axial velocity.

In order to determine whether the radial velocity profile in the flow tube used in the present research is parabolic, the time required for ions to traverse the distance (19.6 cm) from the reactant gas injection port to the ion sampling orifice was determined. In the field freq. high pressure afterglow, ions (and electrons) should travel down the flow tube at the same rate as the buffer gas. A comparison of measured ion transit times with buffer gas transit times, calculated (assuming a parabolic radial velocity profile) from measured buffer gas flow rates, was used to indicate the validity of the parabolic velocity profile assumption. Ions, extracted from the afterglow, were monitored as a function of time after the application of a positive potential to a platinum probe inserted between the microwave discharge and the reactant gas injection port for the microwave discharge source configuration, or after the application of a positive potential to the filament for the filament source configuration. The time required for charged species at $r=0$ to travel down the flow tube

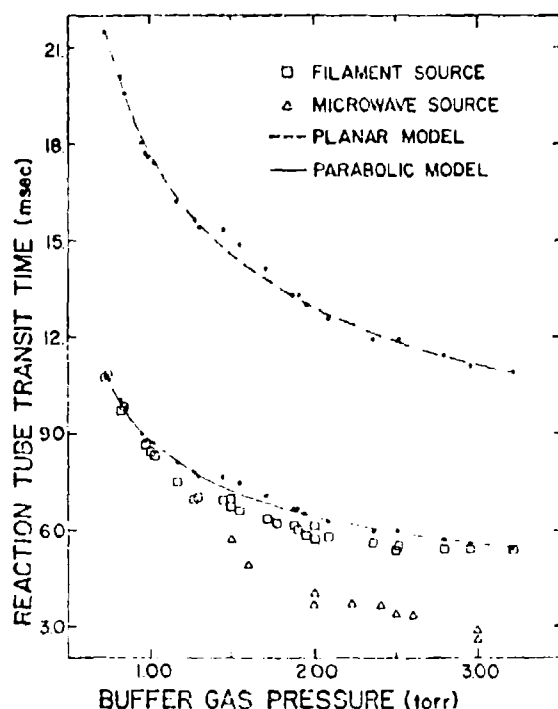


FIG. 3. Measured ion transit times as a function of buffer gas pressure.

from the point of disturbance to the ion sampling orifice was determined by noting the time at which the ion signal decreased sharply due to the depletion of charged species by the positive potential applied to the probe or filament. Figure 3 shows the results of a series of ion transit time measurements versus buffer gas pressure for the flowing afterglow in the filament and microwave discharge source configurations. The expected ion transit times for the two radial velocity profiles discussed above are represented by a dashed line for the planar profile and a solid line for the parabolic profile. These expected ion transit times were calculated using Eq. (9) for the planar profile and

$$t = L/r(r-0) - \frac{1}{2} \pi a^2 L/F \quad (11)$$

for the parabolic profile. The measured ion transit times are much smaller than those expected for even a parabolic radial velocity profile with the flowing afterglow apparatus in the microwave discharge source configuration. This may be attributed to the geometry of the present flow tube when in the microwave discharge source configuration. The microwave discharge produces ions and electrons in the buffer gas in a quartz tube with an inner diameter of less than 1.12 cm. The buffer gas is pumped through this tube into the flow tube, which has an inner diameter of 2.57 cm. Due to this arrangement the buffer gas tends to stream through the center of the flow tube at a velocity higher than predicted by a parabolic velocity profile. In addition, the velocity of the buffer gas outside this central filament will be less than predicted from the parabolic radial velocity profile model. At this point the development of a

mathematical model for the flowing afterglow apparatus in the microwave discharge configuration could no longer be pursued, since the radial profile for the buffer gas velocity could not be determined. Therefore, the equation used to reduce data obtained with the microwave discharge source was

$$[X^-] = [e^-]_0 \{1 - \exp(-k[X_2]t')\}, \quad (12)$$

where t' is the measured ion reaction tube transit time. In order to avoid the flow problem described above, previous researchers have found it necessary to make their flow tubes long enough to allow a parabolic velocity profile to develop¹⁰ or to smooth the buffer gas flow with a sintered glass disc placed in the flow channel upstream of the reaction region.⁹ The latter solution was employed in the present research. This necessitated the location of the electron source downstream from the sintered glass disc. Thus, at this point the apparatus was converted to the filament electron source previously described. As shown in Fig. 3, ion transit times calculated, assuming a parabolic velocity profile, from measured buffer gas volume flow rates are in good agreement with measured ion transit times for the flowing afterglow apparatus in the filament source configuration. This indicates that the sintered glass disc installed in the flow tube is effective in smoothing the buffer gas flow (that is, in establishing a parabolic velocity profile in the flow tube).

Radial diffusion

In order to include the radial diffusion of the product ions in the mathematical model being developed, the transport equation¹² for these ions, produced by dissociative electron attachment in the flowing afterglow reaction tube, must be solved.

$$2r_0(1 - r^2/a^2) \partial[X^-]/\partial z = (D_e/r) \partial(r \partial[X^-]/\partial r) + \partial r - k[e^-][X_2], \quad (13)$$

where the left side represents the time rate of change of the negative ion concentration, the first term on the right represents the negative ion concentration change due to radial diffusion, and the second term the negative ion production rate from the attachment reaction. D_e is the negative ion diffusion coefficient. However, before a solution for this equation can be found, a similar transport equation for the electron density must be solved:

$$2r_0(1 - r^2/a^2) \partial[e^-]/\partial z = (D_e/r) \partial(r \partial[e^-]/\partial r) + \partial r - k[e^-][X_2], \quad (14)$$

where the left side represents the time rate of change of the electron density, the first term on the right represents the electron concentration change due to radial diffusion, and the second term represents the electron loss rate due to the electron attachment reaction. D_e is the electron diffusion coefficient. Equation (14) has been solved by Cher and Hollingsworth,⁹ and its solution is given by

$$[e^-] = C \exp \left\{ - (D_e X_2^2 / a^2 + k[X_2] z / 2r_0) \right. \\ \left. \times \exp(-\beta X r^2 / 2a^2) {}_1F_1 \left(\frac{1}{2} - \frac{1}{2} \beta X r^2 / a^2; \frac{1}{2} - \beta X r^2 / a^2 \right) \right\}, \quad (15)$$

where

$$\lambda^2 = \lambda_0^2 + \epsilon_1 k a^2 [X_2] / D_e - \epsilon_2 k^2 a^4 [X_2]^2 / D_e^2, \quad (16)$$

$$\beta = 1 + k a^2 [X_2] / D_e^2, \quad (17)$$

where $\lambda_0^2 = 7.3428$, $\epsilon_1 = 0.2372$, $\epsilon_2 = 0.00150$, ${}_1F_1(\frac{1}{2}; \frac{3}{2}; -\frac{1}{2}\lambda/\beta, 1; \beta a r^2/a^2)$ is a confluent hypergeometric function, and C is a constant. Now that a solution has been obtained for the electron density in the flow tube, this solution must be substituted into Eq. (13) and an expression for $[X^*]$ found. It is obvious at this point that obtaining an exact analytical expression for the negative ion number density is impossible due to the intractability of Eq. (13) upon substitution of the expression derived for the electron number density. Therefore, the assumption is made that since the present experiments measure only the axial variation of the products, only the solution of Eq. (14) at $r=0$ is necessary. The axial variation of the electron density may now be

$$[e^-] = [e^-]_0 \{\exp(-0.619 [X_2] z / v_0)\}, \quad (18)$$

where $[e^-]_0$ is the electron density at $r=0$ and $z=L$ (at the ion sampling orifice) for $[X_2]=0$. The third term in Eq. (16) has been dropped since it is not significant in the present experiments. Equation (18) applies only to the electron density at $r=0$, that is, on the flow tube axis. Therefore, the substitution of Eq. (18) into Eq. (13) and the subsequent solution of Eq. (13) to yield an expression $[X^*] = f(r, z)$ is meaningless. Therefore, it is further assumed that

$$[X^*] = [e^-]_0 - [e^-], \quad (19)$$

i. e., that the difference between the electron number density at $r=0$ and $z=L$ with $[X_2]=0$ (that is, $[e^-]_0$) and the electron number density at $r=0$ and $z=L$ with $[X_2] \neq 0$ (that is, $[e^-]$) is due to the formation of negative ions which undergo negligible radial diffusion in their transit through the reaction tube. Substitution of Eq. (19) and $z=L$ into Eq. (18) then yields

$$[X^*] = [e^-]_0 \{1 - \exp(-0.619 [X_2] L / v_0)\}, \quad (20)$$

which is applicable to the flowing afterglow apparatus in the filament source configuration. The validity of this equation was tested by measuring known reaction rates.

The mathematical models derived above do not take into account pressure gradients in the flow tube or the axial diffusion of charged species. These factors would result in only small corrections to Eq. (20). Other factors which may be significant in the analysis of experimental data include corrections for nonuniform reactant gas injection and variation of the electron diffusion coefficient (assumed to be constant above) with the reactant gas number density.¹⁷

Data reduction

In the present experiments Eqs. (12) and (20) were used to reduce experimental data, obtained with the microwave discharge and filament source configurations, respectively, to dissociative attachment rate constants. The data were fit to these equations using the technique discussed in the first section of a paper by Curl,¹⁸ in which the nonlinear parameters (b in this case) are linearized by using a Taylor series approximation. With this procedure, initial guesses must be made for unknown parameters; through successive iterations, the values of these parameters converge to the true values. However, if the initial guesses for these parameters are not reasonable, the successive iterations may diverge and no solution will be found. In order to overcome this limitation and to curve fit data to more complex equations, where the Taylor series approximation requires the initial guesses to be quite near the true values (for example, in the case of several nonlinear parameters), the technique of Beesey *et al.*¹⁹ was used. This technique uses a grid search method to locate the values of the unknown parameters which yield the minimum sum of the squares of the deviation.

RESULTS

As previously mentioned, experiments using the flowing afterglow apparatus with both a microwave discharge electron source and a filament electron source have been completed. Thus, the experimental results will be presented under these two headings. The rate constants measured in the present research are summarized in Table II.

TABLE II. Rate constants determined in the present experiments.

Net reaction	k (cm ³ molecule ⁻¹ sec ⁻¹)	Source ^a	Buffer gas pressure (torr)	Comments
$e^- + \text{SF}_6 \rightarrow \text{SF}_6^-$	$4.6 \pm 1.3 \cdot 10^{-14}$	microwave	2.08–2.17	with metastable quenchant
	$3.9 \pm 0.9 \cdot 10^{-14}$	microwave	2.66–2.16	without metastable quenchant
	$4.2 \pm 1.1 \cdot 10^{-14}$	microwave		average
	$3.6 \pm 1.8 \cdot 10^{-14}$	filament	0.96–2.32	
$\text{SF}_6 + \text{O}_2 \rightarrow \text{SF}_6^- + \text{O}_2$	$3.7 \pm 0.4 \cdot 10^{-11}$	microwave	2.00–2.03	
$e^- + \text{F}_2 \rightarrow \text{F}^- + \text{F}$	$4.6 \pm 1.2 \cdot 10^{-10}$	microwave	2.30–2.50	
	$3.1 \pm 1.2 \cdot 10^{-10}$	filament	1.28–2.08	
$e^- + \text{Cl}_2 \rightarrow \text{Cl}^- + \text{Cl}$	$3.7 \pm 1.8 \cdot 10^{-9}$	filament	1.01–2.35	³⁵ Cl ⁻ isotope monitored
	$3.7 \pm 1.7 \cdot 10^{-9}$	filament	1.01–2.35	³⁷ Cl ⁻ isotope monitored
$e^- + \text{Br}_2 \rightarrow \text{Br}^- + \text{Br}$	$1.0 \pm 0.9 \cdot 10^{-11}$	filament	1.02–1.11	
$\text{Br}^- + \text{Br}_2 + \text{Ar} \rightarrow \text{Br}_3^- + \text{Ar}$	$1.9 \pm 0.5 \cdot 10^{-24}$	filament	1.86–2.01	k in units of cm ³ molecule ⁻² sec ⁻¹

^a Average electron temperatures for the microwave and filament electron sources are approximately 600 and 350°K, respectively.

Microwave discharge electron source

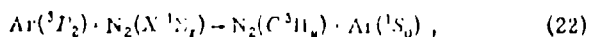
Several authors have shown that electrons are rapidly thermalized in a flowing afterglow environment.^{7,20} In the present research the only experimental procedure used to actually estimate the electron temperature in the flowing afterglow, downstream of the electron source, was based on the measurement of the ratio of SF_5^+ to SF_6^+ ion currents when sulfur hexafluoride was injected at the neutral reactant port. This ratio has been shown by other investigators to be strongly dependent on electron energy.^{7,20,21} The SF_5^+/SF_6^+ ratio (~ 0.2) measured here indicates an average electron temperature of approximately 600°K when the ratio is compared to the data of Fehsenfeld,⁷ who determined this ratio as a function of electron temperature in a flowing afterglow apparatus.

In order to determine whether attachment rate constants measured with the flowing afterglow system in the microwave discharge electron source configuration were reliable, the total attachment rate constant for electrons in sulfur hexafluoride was measured. The rate constant for this attachment reaction is so large that pure sulfur hexafluoride cannot be injected into the afterglow without quenching it, that is, immediately attaching all free electrons. Thus, mixtures of sulfur hexafluoride with argon, which were in the concentration range 0.1 to 0.991% sulfur hexafluoride, were used in these experiments. These mixtures were made using a MKS Baratron capacitance manometer to measure the partial pressure of sulfur hexafluoride and the total pressure of the gas mixture. In the experiments utilizing the microwave discharge source, the total product ion signal (the sum of SF_5^+ and SF_6^+) was monitored as a function of the sulfur hexafluoride flow rate into the afterglow. The average value obtained for the total attachment rate constant is $4.2 \pm 1.1 \times 10^{-9} \text{ cm}^3 \text{ molecule}^{-1} \text{ sec}^{-1}$ for an electron temperature of about 600°K.

In order to make accurate kinetic measurements in a flowing afterglow system, downstream sources of electrons must be removed to ensure that all electrons in the flow tube have the same time to react with the injected gas; that is, no electrons should be produced downstream of the reactant gas injection port. One possible source of electrons in the reaction tube is Penning ionization. This is not a problem in the sulfur hexafluoride reaction studies, since the energies of the argon metastable atoms (11.54 and 11.72 eV²²) are less than the ionization potential of sulfur hexafluoride (16.15 eV²³). Another possible mechanism for the production of electrons by metastable atoms has been suggested by Biondi.^{24,25} The reaction



is energetically possible, since $2E(Ar^m) > 2E(Ar^+)$. Because of the possibility of this metastable-metastable reaction, experiments were conducted in which nitrogen was injected into the afterglow, upstream of the reaction tube. The added nitrogen removes metastable atoms by the reaction



followed by radiative emission of the excited nitrogen product ($C^3\Pi_u \rightarrow B^3\Pi_g$). The rate constant for this quenching reaction has been measured²² ($0.3 \times 10^{-10} \text{ cm}^3 \text{ molecule}^{-1} \text{ sec}^{-1}$) and found to be large enough that the injection of even a few mtorr of nitrogen into the afterglow should deplete the metastable atom concentration by several orders of magnitude before the reactant gas is injected. The results listed in Table II for sulfur hexafluoride include experiments in which nitrogen was injected as a metastable atom quenchant. Considering the scatter in the data, there is no significant difference between the average electron attachment rate constant for experiments using the quenchant ($k = 4.6 \pm 1.3 \times 10^{-9} \text{ cm}^3 \text{ molecule}^{-1} \text{ sec}^{-1}$) and that for experiments not using a quenchant ($k = 3.9 \pm 0.9 \times 10^{-9} \text{ cm}^3 \text{ molecule}^{-1} \text{ sec}^{-1}$). Thus, it does not appear that the metastable-metastable reaction is an important source of electrons in the present research.

As previously stated, electrons undergo a dissociative attachment reaction in fluorine to form a negative ion and an atom [see Eq. (3)]. A 0.065% fluorine in argon gas mixture was injected into the afterglow in order to determine the dissociative electron attachment rate constant for fluorine. This gas mixture, nominally 0.1%, was purchased from Matheson Gas Products and analyzed using a triphenyl tin fluoride technique.²⁶ The average value obtained for the bimolecular rate constant for the dissociative attachment of electrons in fluorine is $4.6 \pm 1.2 \times 10^{-9} \text{ cm}^3 \text{ molecule}^{-1} \text{ sec}^{-1}$ for an electron temperature of approximately 600°K. Since the ionization potential of fluorine (16.6 eV²⁷) is greater than the energy of the argon metastable atoms, Penning ionization will not be a possible downstream source of electrons. Therefore, no metastable atom quenchant was injected into the afterglow for the fluorine experiments.

In the process of determining whether the present flowing afterglow system could be used to obtain reliable kinetic data, the rate constant for the charge transfer reaction between SF_5^+ and O_2^+ was measured. This charge transfer reaction is particularly suitable for testing the flowing afterglow system, since the reaction rate is so slow that pure sulfur hexafluoride may be injected into the afterglow in order to study the reaction. This eliminates possible errors which arise in making reactant/diluent mixtures. In addition, the rate constant for this reaction has been measured previously using a flowing afterglow technique.⁸ In making these measurements, helium was used as the buffer gas and oxygen was injected into the afterglow both to remove helium metastable atoms and to produce O_2^+ ions. Under these conditions, the helium metastable atoms are removed by the Penning ionization reaction



The O_2^+ ions are formed by the three-body attachment reaction



Sulfur hexafluoride was injected into the afterglow downstream of the oxygen inlet port and the decay of the O_2^+ ion signal was monitored as a function of the sulfur

hexafluoride flow rate as determined by a linear mass flowmeter. The average value obtained for the bimolecular rate constant k for the SF_6/O_2^+ charge transfer reaction is $3.7 \pm 0.4 \times 10^{-11} \text{ cm}^3 \text{ molecule}^{-1} \text{ sec}^{-1}$ for an O_2^+ ion temperature of about 300–325 °K (approximately the temperature of the buffer gas in the flow tube).

Filament electron source

When sulfur hexafluoride was injected into the flowing afterglow apparatus in the filament source configuration, the SF_6^+ signal levels were so low that they could not be extracted from the noise ($\sim 5 \text{ mV}$). Even for experiments in which the system sensitivity was fairly high ($\sim 5 \text{ V SF}_6^+$ signal), no SF_6^+ signal could be observed. Therefore, it is assumed that the $\text{SF}_6^+/\text{SF}_6$ ratio is less than 10^{-3} (the smallest detectable ratio). This corresponds to an average electron energy of less than 350 °K when this ratio is compared to the data of Fehsenfeld.⁷ The lower electron energy estimate for the filament electron source configuration compared to the microwave discharge electron source configuration is not unreasonable, since a microwave discharge results in a greater heating of the buffer gas with which the electrons are in equilibrium.¹⁰ In addition, the incidence of superelastic collisions, which tend to increase the average electron energy, between electrons and metastable atoms is greater in a microwave discharge afterglow due to the higher metastable atom densities.²⁸

A series of nineteen determinations of the rate constant for the attachment of thermal electrons in sulfur hexafluoride were made using the flowing afterglow system in the filament source configuration. The average value obtained for the rate constant k is $3.6 \pm 1.8 \times 10^{-9} \text{ cm}^3 \text{ molecule}^{-1} \text{ sec}^{-1}$ for an electron temperature of about 350 °K. It has been shown that flowing afterglows with a filament electron source have a lower metastable atom density than those with a microwave discharge source.²⁸ Therefore, no experiments were done in

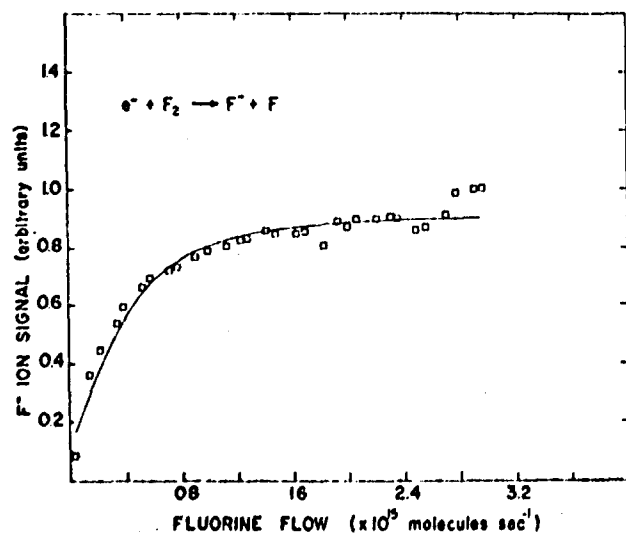


FIG. 4. Fluoride ion signal as a function of fluorine injection rate for dissociative electron attachment in fluorine (filament source).

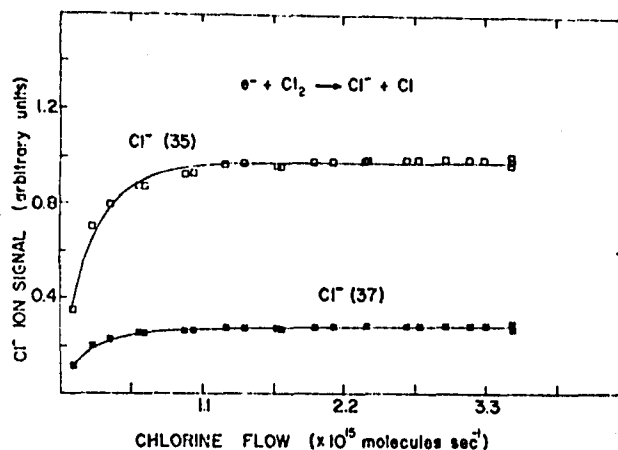


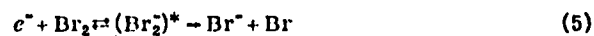
FIG. 5. Chloride ion signal as a function of chlorine injection rate for dissociative electron attachment in chlorine (filament source).

which a metastable atom quenchant was injected into the afterglow, since the experiments with a microwave discharge source configuration indicated that argon metastable atoms were not a significant downstream source of electrons.

The study of dissociative electron attachment in fluorine, using the filament source, yielded a rate constant k equal to $3.1 \pm 1.2 \times 10^{-9} \text{ cm}^3 \text{ molecule}^{-1} \text{ sec}^{-1}$. A sample of the data obtained is shown in Fig. 4; the solid line is the least squares curve fit.

The dissociative attachment rate constant for electrons in chlorine was also measured using the filament electron source. Both the Cl^- ($m/e = 35$) and the Cl^- ($m/e = 37$) isotopes were monitored in these experiments. The rate constants obtained for this reaction are $3.7 \pm 1.8 \times 10^{-9} \text{ cm}^3 \text{ molecule}^{-1} \text{ sec}^{-1}$ for the mass 35 isotope and $3.7 \pm 1.7 \times 10^{-9} \text{ cm}^3 \text{ molecule}^{-1} \text{ sec}^{-1}$ for the mass 37 isotope for an electron temperature of approximately 350 °K. Figure 5 illustrates the results of a typical chlorine experiment. The solid lines are the curve fits. The chlorine/argon ratio in mixtures made for these experiments was determined by measuring the chlorine pressure and the total pressure of the mixture during preparation with a capacitance manometer.

The study of dissociative electron attachment in bromine



is complicated by the occurrence of three other reactions when bromine is injected into the afterglow



The injection of a metastable atom quenchant, such as nitrogen, into the afterglow eliminates the Penning ionization and pair production processes (represented by Eqs. (25) and (26), respectively). The data obtained in the present experiments then depend only on the two re-

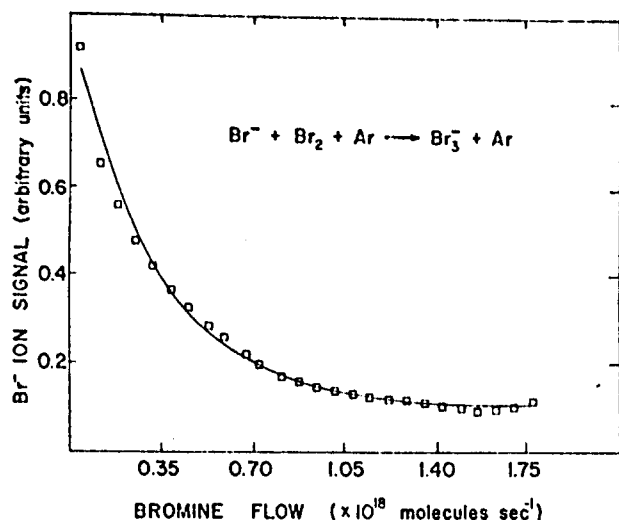


FIG. 6. Bromide ion signal as a function of bromine injection rate for Br_3^- formation in bromine (filament source).

actions represented by Eqs. (5) and (6). The study of this system was then conducted under two different conditions: the injection of a high concentration of bromine so that only the reaction represented by Eq. (6) had to be considered in the reduction of data and the injection of dilute bromine so that only the dissociative electron attachment reaction represented by Eq. (5) is important. For the high concentration experiments, pure bromine was injected into the afterglow. For the low concentration experiments, bromine/argon mixtures were injected. These mixtures were prepared using a MKS Baratron capacitance manometer to measure the bromine pressure and the total pressure of the mixture during preparation. Figure 6 illustrates the data obtained when pure bromine was injected into the afterglow. The solid line represents a least squares curve fit of the Br^- signal. The rate of bromine injection was so rapid that only the reaction represented by Eq. (6) was observed. The average rate constant obtained for the formation of Br_3^- , determined by monitoring the disappearance of the Br^- signal, is $1.9 \pm 0.5 \times 10^{-28} \text{ cm}^6 \text{ molecule}^{-2} \text{ sec}^{-1}$ for a Br^- ion temperature of about 300°K (approximately the buffer gas temperature). Br_3^- was not monitored since its mass exceeded the upper mass limit of the mass spectrometer used in these experiments. Figure 7 illustrates the data obtained in an experiment for which the bromine injection rate was so small that only the reaction represented by Eq. (5) occurs. The average rate constant, obtained in the present research, for the dissociative attachment of thermal electrons in bromine is $1.0 \pm 0.9 \times 10^{-11} \text{ cm}^3 \text{ molecule}^{-1} \text{ sec}^{-1}$ for an electron temperature of about 350°K.

The rate constants listed in Table II were measured at various buffer gas pressures. No buffer gas pressure dependence was observed for any of the bimolecular rate constants determined in the present research. This is expected in view of the limited pressure range and relatively high pressures of the present experiments.

DISCUSSION

The first two reactions listed in Table II were investigated in order to determine whether rate constants measured in the present flowing afterglow apparatus are reliable. The rate constant $(3.6 \pm 1.8 \times 10^{-8} \text{ cm}^3 \text{ molecule}^{-1} \text{ sec}^{-1})$ for an electron temperature of about 350°K measured for the attachment of electrons to sulfur hexafluoride is approximately a factor of 5 to 8 smaller than the rate constant measured by Fehsenfeld⁷ ($2.21 \times 10^{-7} \text{ cm}^3 \text{ molecule}^{-1} \text{ sec}^{-1}$ for an electron temperature of 289°K) in a flowing afterglow apparatus and by other researchers¹¹⁻¹⁴ using various techniques ($2.14\text{--}3.1 \times 10^{-7} \text{ cm}^3 \text{ molecule}^{-1} \text{ sec}^{-1}$ for an electron temperature of 300°K). This agreement indicates that electron attachment rate constants measured in the present research are reasonable. The discrepancy between the present result and other reported data may be attributed to several factors not considered in the model used in the present study to reduce experimental data to rate constants. Such factors include the variation of the electron diffusion coefficient with changes in the reactant gas injection rate, nonuniform reactant gas injection, and product ion radial diffusion.

As noted previously, prior to the present work, no electron attachment rate data had been reported for fluorine. The present results represent the first measurement of the rate constant for dissociative attachment of thermal electrons in fluorine. The fact that this reaction is rapid has significant implications for the development of hybrid chemical lasers utilizing fluorine. One important application of this data is in the modeling of an electron-beam initiated HF chemical laser system. Recent work has suggested that the production of F atoms by the dissociative attachment of thermal electrons to fluorine is the most important F atom generation mechanism for such a laser device.²⁰ The present results confirm the importance of this reaction.

The rate constant measured in the present research

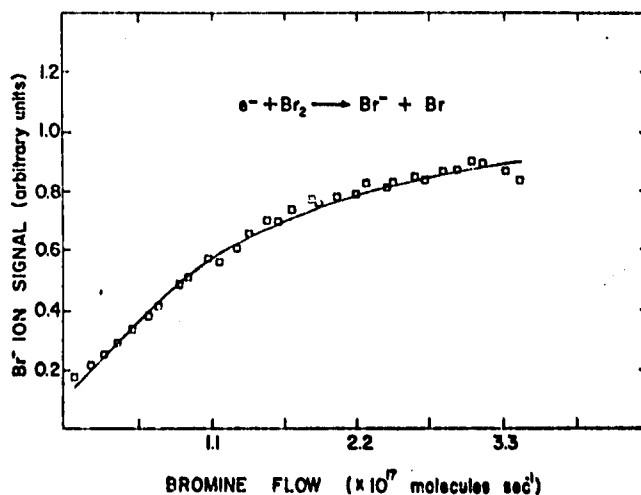


FIG. 7. Bromide ion signal as a function of bromine injection rate for dissociative electron attachment in bromine (filament source).

for the dissociative attachment of near thermal electrons in chlorine is approximately a factor of 12 larger than the result reported by Christodoulides *et al.*⁵ shown in Table I. However, the values of the rate constant measured for this reaction by those authors range from 0.27×10^{-9} to 2.2×10^{-9} cm³ molecule⁻¹ sec⁻¹ for thermal energy electrons. In view of this scatter and the spread in the rate constant measured in the present research ($3.7 \pm 1.8 \times 10^{-9}$ cm³ molecule⁻¹ sec⁻¹), the agreement between the two measurements is considered to be reasonable.

The thermal electron attachment rate constant measured for bromine in the present research is a factor of 13 larger than that obtained by Truby⁶ in a static afterglow experiment (shown in Table I). However, the standard deviation for the rate constant measured in the present research is large. In addition, the rate constant for electron attachment in bromine has been shown to increase with increasing electron temperature.³⁰ Thus, since the electron temperature in the present flowing afterglow (350°K) is larger than the electron temperature in Truby's static afterglow (296°K), the measured rate constant is expected to be larger than Truby's result. The rate of the three-body formation of Br₃ in which argon is the third body has not been reported. The rate constant measured in the present research ($1.9 \pm 0.5 \times 10^{-28}$ cm⁶ molecule⁻¹ sec⁻¹) is larger than that measured by Truby³¹ for the corresponding reaction in which bromine is the third body (2.9×10^{-29} cm⁶ molecule⁻¹ sec⁻¹).

The relatively large rate constants determined for the attachment reactions in fluorine and chlorine obviously indicate that these molecules are efficient scavengers of thermal electrons. Recent studies of the energy dependence of electron attachment in chlorine by other workers³² have demonstrated the existence of a broad maximum in the attachment cross section at ~0.25 eV. Christodoulides *et al.*⁵ suggest that the low energy attachment process involves formation of a vibrationally excited temporary negative ion state, Cl₂⁻(²Σ_u⁺), lying about 1.1 eV below the ground state of the neutral molecule. This state then leads to the dissociative products. This picture is consistent with the potential energy curves for Cl₂ calculated by Gilbert and Wahl³³ which show the Cl₂⁻(²Σ_u⁺) curve crossing the Cl₂(¹Σ_g⁺) curve in the region of the well minimum of the neutral. Presumably a similar situation exists for the F₂ and the F₂⁻ potential curves, but little potential energy curve data is available for either the F₂ or for the Br₂ system.

ACKNOWLEDGMENTS

A portion of this work was accomplished while the authors were located at the Aerospace Research Laboratories, Wright-Patterson Air Force Base, Ohio. This research was sponsored in part by the Air Force Office of Scientific Research (AFSC), United States Air

Force, under Contract No. F44620-76-C-0007. The authors are grateful for the advice of F. C. Fehsenfeld and E. E. Ferguson of the National Oceanic and Atmospheric Administration in this research.

⁴Work published as this author's doctoral dissertation (1975) at the Department of Chemistry, University of Florida, Gainesville, FL 32611.

¹P. M. Banks and G. Kockarts, *Aeronomy* (Academic, New York, 1973).

²D. I. Rosen, R. N. Silco, and T. A. Cool, *IEEE J. Quantum Electron.* QE-9, 163 (1973).

³National Aeronautics and Space Administration Report No. SP-252, 1971.

⁴G. D. Sides and T. O. Tiernan, ARL Report No. 74-0105, 1974.

⁵A. A. Christodoulides, R. Schumacher, and R. N. Schindler, *J. Phys. Chem.* 79, 1904 (1975).

⁶F. K. Truby, *Phys. Rev. A* 4, 613 (1971).

⁷F. C. Fehsenfeld, *J. Chem. Phys.* 53, 2000 (1970).

⁸F. C. Fehsenfeld, *J. Chem. Phys.* 54, 438 (1971).

⁹M. Cher and C. S. Hollingsworth, *Adv. Chem. Ser.* 80, 118 (1969).

¹⁰E. E. Ferguson, F. C. Fehsenfeld, and A. L. Schmeltekopf, *Adv. At. Mol. Phys.* 5, 1 (1969).

¹¹B. H. Mahan and C. E. Young, *J. Chem. Phys.* 44, 2192 (1966).

¹²C. E. Young, UCRL Report No. UCRL-17171, 1966.

¹³E. Chen, R. O. George, and W. E. Wentworth, *J. Chem. Phys.* 49, 1973 (1968).

¹⁴F. J. Davis and D. R. Nelson, *Chem. Phys. Lett.* 3, 461 (1969).

¹⁵H. W. Schmidt, NASA Rept. No. SP-3037, 1967.

¹⁶R. C. Bolden, R. S. Hemsworth, M. J. Shaw, and N. D. Twiddy, *J. Phys. B* 2, 45 (1969).

¹⁷F. Kaufman, *Adv. Chem. Ser.* 80, 29 (1969).

¹⁸R. F. Curl, Jr., *J. Comput. Phys.* 6, 367 (1970).

¹⁹J. C. Becsey, L. Berke, and J. R. Callan, *J. Chem. Educ.* 45, 728 (1968).

²⁰C. L. Chen and P. J. Chantry, *Bull. Am. Phys. Soc.* 15, 418 (1970).

²¹W. M. Hickam and R. E. Fox, *J. Chem. Phys.* 25, 642 (1950).

²²M. Bourene and J. LeCalve, *J. Chem. Phys.* 58, 1452 (1973).

²³J. L. Franklin, J. G. Dillard, H. M. Rosenstock, K. Draxil, and F. H. Field, *Natl. Bur. Stand. Ref. Data Ser.* 26, 1 (1969).

²⁴M. A. Blondi, *Phys. Rev.* 82, 453 (1951).

²⁵M. A. Blondi, *Phys. Rev.* 88, 660 (1952).

²⁶N. Allen and N. H. Furman, *J. Am. Chem. Soc.* 54, 4625 (1932).

²⁷R. Thorburn, *Proc. Phys. Soc. London*, 73, 122 (1959).

²⁸D. Smith, C. V. Goodall, and M. J. Copsey, *J. Phys. B* 1, 660 (1968).

²⁹Aerosp. Rept. No. TR-0074 (9240-05)-1, 1973.

³⁰J. P. Blewett, *Phys. Rev.* 49, 900 (1936).

³¹F. K. Truby, *Phys. Rev. A* 4, 114 (1971).

³²E. Schults, A. A. Christodoulides, and R. N. Schindler, *Chem. Phys.* 8, 354 (1975).

³³T. L. Gilbert and A. C. Wahl, *J. Chem. Phys.* 55, 5247 (1971).

Dissociative electron attachment in xenon difluoride

G. D. Sides and T. O. Tiernan

Department of Chemistry, Wright State University, Dayton, Ohio 45431
(Received 2 July 1976)

The rate constant for the dissociative attachment of thermal electrons (300–350 °K) to xenon difluoride has been measured using a flowing afterglow technique, which was described in a previous publication.¹ The data presented here have possible applications in the development of discharge-sustained, rare gas-halide lasers^{2–4} and in the development of electron-beam initiated HF laser systems.^{5,6}

Xenon difluoride is a white, crystalline solid at room temperature and has a vapor pressure of 3.10 torr at 293.2 °K.⁷ The xenon difluoride used in the present experiments was analyzed using mass spectrometric techniques. No significant impurities were detected.

The results of the present rate constant measurement are shown in Table I. The average rate constant obtained for the reaction



is $2.4 \pm 1.1 \times 10^{-9} \text{ cm}^3 \text{ molecule}^{-1} \text{ sec}^{-1}$.

During the course of the present experiments, sampling problems arose with the use of a stainless steel cone through which ions are sampled from the afterglow. The ion signals obtained from the flow tube were somewhat unstable and sensitive to the contamination of the stainless steel surface. The stainless steel cone was then replaced with a molybdenum cone as suggested by Ferguson *et al.*⁸ The data shown in Table I include experiments performed using both sampling cone materials. The improvement in the standard deviation of the results with the molybdenum cone is obvious.

After the replacement of the stainless steel cone with the molybdenum cone, it was found that the maximum ion signal from the afterglow was obtained for a buffer gas pressure of approximately 0.8 torr instead of the previously observed maximum at approximately 2 torr. After the reinstallation of the stainless steel cone, the maximum ion signal remained at approximately 0.8 torr. This phenomenon cannot be explained at present. However, it is felt that this change in the ion signal maximum does not affect any measured

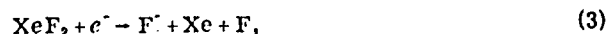
rate constants since the same rate constant, within experimental error, was obtained at 0.8 torr and 2 torr for the reaction reported here.

In several experiments, an argon metastable atom quenchant, nitrogen, was injected into the afterglow in order to determine whether metastable atoms might be interfering with the measurement of the electron attachment reaction by acting as a downstream source of electrons.¹ There is no significant difference between rate constants measured with a quenchant and those measured without a quenchant. Therefore, metastable atoms did not interfere with the present rate constant measurement.

The present data does not indicate whether the reaction studied is



or



since the neutral products could not be observed with the experimental technique utilized. XeF is known to be weakly bonded ($\sim 0.48 \text{ eV}^9$); however, the exoergicity ($-2.28 \text{ eV}^{10,11}$) of Reaction (2) is certainly sufficient to break the XeF bond, provided that this energy goes into internal modes of vibration.

The only thermal energy attachment product observed in the present experiments is F^- even though XeF^- and XeF_2^- have been observed by other workers.¹² This fact may be explained in terms of the hypothetical potential energy diagram shown in Fig. 1. Thermal electrons attach near the minimum in the XeF_2 potential curve, and the molecular negative ions are formed at energies well above the XeF_2^- dissociation limit. The energetic XeF_2^- formed then dissociates within one vibration to XeF and F^- . The potential curve representing an F-XeF^- bond apparently crosses the neutral

TABLE I. Dissociative electron attachment rate constants measured for xenon difluoride.

Number of experiments	Rate constant ($\text{cm}^3 \text{ molecule}^{-1} \text{ sec}^{-1}$)	Buffer gas pressure (torr)	Comments
9	$1.8 \pm 1.2 \times 10^{-9}$	2.0	stainless steel cone
12	$2.9 \pm 0.6 \times 10^{-9}$	0.8	molybdenum cone
21	$2.4 \pm 1.1 \times 10^{-9}$		all experiments

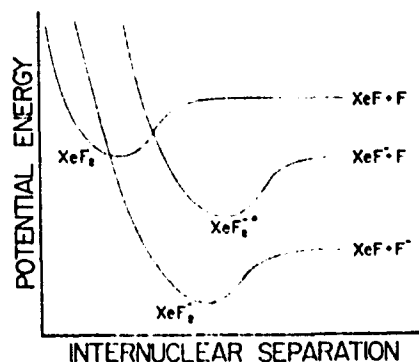


FIG. 1. Hypothetical potential energy diagrams for XeF_2 and XeF_2^- .

molecule surface above the potential well minimum, and thus the XeF^- cannot be formed by thermal energy electrons. If the XeF_2^+* surface crossed the XeF_2 surface near the potential minimum, then one would expect to observe either XeF_2^+ or XeF^- as products. Since this is not the case, the XeF_2^+* curve apparently crosses the XeF_2 curve above the potential energy minimum.

Very little information exists concerning the negative ion chemistry of the rare gas halides. The current rate constant measurement is believed to be the first electron attachment rate constant measured for this class of molecules. In view of the current interest in rare gas-halide lasers and fluorine-containing chemical-laser systems, there is obviously a need for further research on these molecules.

The authors gratefully acknowledge the gift of a sample of xenon difluoride from the Rocket Propulsion Laboratory, Edwards Air Force Base, California, and the helpful discussions with Dr. D. G. Hopper at Wright State University, Dayton, Ohio. This research was sponsored by the Air Force Office of Scientific

Research (AFSC), United States Air Force, under Contract No. F44620-76-C-0007.

- ¹G. D. Sides, T. O. Tiernan, and R. J. Hanrahan, *J. Chem. Phys.* **65**, 1966 (1976).
- ²J. A. Mangano and J. H. Jacob, *Appl. Phys. Lett.* **27**, 495 (1975).
- ³R. Burnham, N. W. Harris, and N. Djen, *Appl. Phys. Lett.* **28**, 86 (1976).
- ⁴E. D. Hinkley, K. W. Nill, and F. A. Blum, *Laser Focus* **12**, 18 (1976).
- ⁵D. Brabson, Air Force Weapons Laboratory, Albuquerque, New Mexico (private communication).
- ⁶Air Force Report No. SAMS0-TR-74-16 (1973).
- ⁷F. Schreiner, G. N. McDonald, and C. L. Chernick, *J. Phys. Chem.* **72**, 1162 (1968).
- ⁸E. L. Ferguson, F. C. Fehsenfeld, and A. L. Schmeltekopf, *Adv. At. Molec. Phys.* **5**, 1 (1969).
- ⁹H. S. Johnston and R. Woolfolk, *J. Chem. Phys.* **41**, 269 (1964).
- ¹⁰B. Weinstock, E. E. Weaver, and C. P. Krep, *Inorg. Chem.* **5**, 2189 (1966).
- ¹¹H. O. Pritchard, *Chem. Rev.* **52**, 529 (1953).
- ¹²G. M. Begun and R. N. Compton, *J. Chem. Phys.* **51**, 2367 (1969).

Theoretical and experimental studies of the N_2O^- and N_2O ground state potential energy surfaces. Implications for the $\text{O}^- + \text{N}_2 \rightarrow \text{N}_2\text{O} + e$ and other processes*

Darrel G. Hopper and Arnold C. Wahl

Chemistry Division, Argonne National Laboratory, Argonne, Illinois 60439

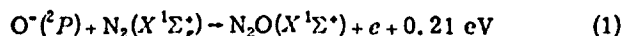
Richard L. C. Wu and Thomas O. Tiernan

Department of Chemistry, Wright State University, Dayton, Ohio 45431
(Received 14 July 1976)

The ground state potential energy surface of the nitrous oxide negative ion is characterized and related to that of the neutral molecule by a synergetic theoretical-experimental approach. *Ab initio* multiconfiguration self-consistent-field/configuration interaction (MCSCF/CI) and other calculations for $\text{N}_2\text{O}^-(X^2A')$ yield the minimum energy geometry ($R_{\text{NN}}^e, R_{\text{NO}}^e, A_{\text{NNO}}^e$) = (1.222 ± 0.05 Å, 1.375 ± 0.10 Å, 132.7 ± 2°), the vibrational frequencies (ν_1, ν_2, ν_3) = (912 ± 100 cm⁻¹, 555 ± 100 cm⁻¹, 1666 ± 100 cm⁻¹), the dipole moment μ = 2.42 ± 0.3 D, and other properties. The N_2O^- molecular ion in the X^2A' state is found to have a compact electronic wavefunction—one with very little diffuse character. The MCSCF/CI bending potential energy curve from 70° to 180° for the $X^1\Sigma^+(1^1A')$ state of N_2O as well as the bending curve for the X^2A' state of N_2O^- are also reported. The dissociation energy $D(\text{N}_2\text{O}^-)$ = 0.43 ± 0.1 eV and, thus, the adiabatic electron affinity $\text{E.A.}(\text{N}_2\text{O})$ = 0.22 ± 0.1 eV and the dissociation energy $D(\text{N-NO}^-)$ = 5.1 ± 0.1 eV are determined from beam-collision chamber experiments. Corrections are made for both the dispersion in the ion beam and the translational motion of each target gas. The combined theoretical and experimental results yield a vertical electron affinity $\text{V.E.A.}(\text{N}_2\text{O})$ of -2.23 ± 0.2 eV and enable the construction of angular dependent Morse functions to represent the neutral and ionic surfaces. This construction leads to the determination of the minimum intersection locus as ($V^*, R_{\text{NN}}^*, R_{\text{NO}}^*, A_{\text{NNO}}^*$) = (0.67 ± 0.1 eV, 1.18 ± 0.05 Å, 1.28 ± 0.10 Å, 154 ± 3°). The predicted activation energy of this critical point with respect to the asymptote O^-, N_2 - 0.21 ± 0.1 eV—and the position of the critical point with R_{NN}^* well outside of the N_2 ($\nu=0$) outer turning point imply that the reaction $\text{O}^- + \text{N}_2 \rightarrow \text{N}_2\text{O} + e$ will be strongly facilitated by reagent vibrational excitation.

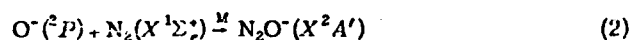
I. INTRODUCTION

The relationship of the potential energy surface for the X^2A' ground state of the nitrous oxide negative ion N_2O^- to the potential energy surface for the $X^1\Sigma^+(1^1A')$ ground state of the neutral molecule N_2O has been of some concern in recent years.¹⁻¹³ This relationship is interesting partly because the possible ionospheric associative detachment reaction

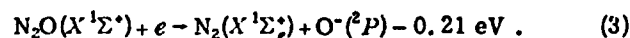


is not observable in laboratory experiments conducted at 300 °K.^{2-6,11,13} An upper bound to the thermal rate coefficient has been placed at about 10⁻¹²–10⁻¹³ cm³ s⁻¹ by various experimenters.^{2,3,5,13} There are conflicting reports of reactivity¹¹ or a lack of it¹³ above 0.3 eV relative collision energy for N_2 ($\nu=0$). The low thermal rate for this exothermic reaction and the effects of reagent translational or vibrational excitation are determined by the characteristics of the aforementioned potential energy surfaces. The $\text{N}_2\text{O}^-(X^2A')$ surface connects adiabatically to the reagent asymptote for Reaction (1) and passes in some regions above the $\text{N}_2\text{O}(X^1\Sigma^+)$ surface.¹² Characterization of these potential energy surfaces and their intersection should make it possible to predict the effects of increased translational or vibrational temperature on the rate of Reaction (1). Vibrational excitation of nitrogen is common in the ionosphere but has been little investigated in laboratory experiments. Lastly, a knowledge

of the $\text{N}_2\text{O}^-(X^2A')$ potential energy surface and its relationship to that for $\text{N}_2\text{O}(X^1\Sigma^+)$ can contribute to the understanding of other interesting processes, including the recombination reaction



and the dissociative attachment reaction



This paper presents both experimental and theoretical studies conducted to characterize the $\text{N}_2\text{O}^-(X^2A')$ potential energy surface and to relate it to that for $\text{N}_2\text{O}(X^1\Sigma^+)$. Bond dissociation energies and the adiabatic electron affinity are derived from collision-induced dissociation experiments with N_2O^- , which are the subject of Sec. II. Correlated *ab initio* and other theoretical calculations which yield the $\text{N}_2\text{O}^-(X^2A')$ and $\text{N}_2\text{O}(X^1\Sigma^+)$ bending potential curves and the $\text{N}_2\text{O}^-(X^2A')$ equilibrium geometry, force constants, vibrational frequencies, and dipole moment are presented in Sec. III. The neutral and negative ion potential energy surfaces are related and the minimum energy intersection locus determined by representing each by an angle-dependent Morse function as described in Sec. IV. The potential surface features which are determined by these data are summarized, and discussed in terms of their implications for the above noted collision processes in Sec. V. Conclusions are drawn in Sec. VI.

II. COLLISION-INDUCED DISSOCIATION EXPERIMENTS WITH N_2O^+

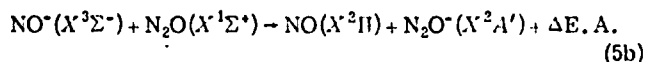
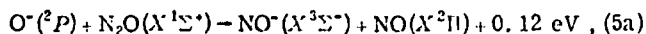
A. Apparatus and cross section determination

An in-line tandem mass spectrometer was utilized in this study. The instrument has been described previously.^{14,15} Briefly, it is a beam-collision chamber apparatus which provides mass analysis of the product ions. The collection stage is fixed at 0° (LAB) scattering angles. The projectile ion is formed in the electron-impact ion source of the first stage mass spectrometer which produces a mass and energy analyzed beam which is impacted upon the target gas in the collision chamber. The energy spread of the projectile ion beam entering the collision cell is about 0.3 eV (LAB) over the ion energy range 0.3 to about 180 eV (LAB).^{14,15} Pulse counting techniques are used to measure the product ion current. The product (secondary) ion intensity $I_s(E_{i0})$ is converted to an observed apparent cross section¹⁶

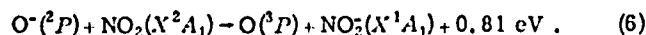
$$\sigma_{app}^{obs}(E_{i0}) = C[I_s(E_{i0})/P_t]/I_p(E_{i0}), \quad (4)$$

where $I_p(E_{i0})$ is the primary ion intensity, E_{i0} is the nominal reactant ion energy in the laboratory frame, P_t is the target gas pressure, and C is a conversion factor.

In the present study the projectile ion, N_2O^+ , was formed by electron impact on nitrous oxide gas at a pressure of $\sim 0.1 \mu$. Under these conditions N_2O^+ is most probably formed by Reaction (3) followed by Reactions (5a) and (5b):



It is estimated that the N_2O^+ ion undergoes approximately 30 collisions within the source chamber and, therefore, it is assumed that the exiting N_2O^+ is predominately in the ground vibrational state. The temperature of the collision chamber was maintained at 160°C . The target gas pressure was 40μ ; it was established that single collision conditions prevail at this pressure. The conversion factor C in Eq. (4) was determined at $E_{i0} = 0.3 \text{ eV}$ using the previously reported¹⁷ cross section of 63 \AA^2 and the product ion intensity observed in the present study for the charge transfer reaction



B. Threshold behavior and corrections for the ion energy distribution and Doppler motion

The threshold behavior of the total cross section σ for collision-induced dissociation reactions



is known from theoretical considerations¹⁸ and experimental studies¹⁹⁻²² to be well approximated by the functional form

$$\sigma_{abs}^{cid}(E_{rel}) = A(E_T - E_0)^n/E_{rel}, \quad (8)$$

where E_{rel} is the relative translational energy (c.m.),

A is a function of the internal energy in the reagent molecule RS , E_T is the total energy (c.m.) less the average internal energy of the reactant molecules, and E_0 is the threshold value of E_T . The exponent n depends upon the mechanism of Reaction (7), with the range $1.9 < n < 2.2$ implying a direct process and the range $1.5 < n < 1.8$, an indirect process.¹⁸

In the present beam-collision chamber experiments the apparent cross section is related to the absolute cross section via the equation

$$\sigma_{app}^{calc}(E_{i0}) = \int_0^\infty dE_i \int_{-\infty}^\infty du_m f(E_i|E_{i0}) f(u_m) \sigma_{abs}(E_{rel}), \quad (9)$$

where E_{i0} is the nominal and E_i is actual laboratory energy of ions moving along the axis directed through the collision chamber, u_m is the speed of the target molecule M along this same axis, and E_{rel} is the relative collision energy determined by E_i and u_m . The distribution function $f(E_i|E_{i0})$ for the RS ion energy about the nominal value E_{i0} is assumed to be a Gaussian function in the variable $(E_i - E_{i0})$ determined by the requirement that the full width at half-maximum be 0.3 eV.^{15,16} It is further assumed in Eq. (9) that $f(u_m)$ is the one-dimensional Maxwellian distribution and that $\sigma_{abs}(E_{rel})$ has the form $\sigma_{abs}^{cid}(E_{rel})$ given in Eq. (8). In the present application E_T has reduced to E_{rel} since the internal energy distribution is well approximated by a delta function centered at the zero-point (i.e., average) level for thermal molecular ions RS . Because of this identity E_0 may be identified as the dissociation energy $D(R-S)$. With this consideration and a change of variable to transform E_{rel} and E_0 to the laboratory energy scale, Eq. (8) becomes^{22,23}

$$\sigma_{abs}^{cid}(E_i) = A_{LAB}(E_i - E_0)^n/E_i. \quad (10)$$

Optimum values of the parameters E_0 and n are determined for each target gas by a grid search procedure. For each trial set of values for E_0 and n , A_{LAB} is found from the approximation $\sigma_{app}^{obs} \approx \sigma_{abs}^{cid}$ at the highest ion energy included in the fit procedure. The optimum set of parameter values is the one which causes $\sigma_{app}^{calc}(E_{i0})$ to best fit $\sigma_{app}^{obs}(E_{i0})$ over the desired range. For the present study the best fit was ascertained by visual comparisons. Further details on this data reduction procedure and on the applicability of Eq. (8) when RS in Eq. (7) is a negative molecular ion will be given elsewhere.²²

C. Results for $D(N_2-O^+)$, $D(N-NO^+)$, and $E.A.(N_2O)$

In the course of the present experiments a steady signal for $m/e = 44$ negative ions (N_2O^-) was detected in the second stage mass spectrometer when the collision chamber contained no target gas. This result implies that the lifetime of N_2O^+ is $> 50 \mu\text{sec}$, the transit time through the apparatus. Such a lifetime implies stability with respect to dissociation and is a precondition for stability with respect to electron detachment (i.e., for a positive electron affinity).

Quantitative determinations of the bond dissociation energy $D(N_2-O^+)$ were made from studies of Reaction (7), where $R = N_2$ and $S = O^+$, for $M = He, Ne, Ar, Kr$,

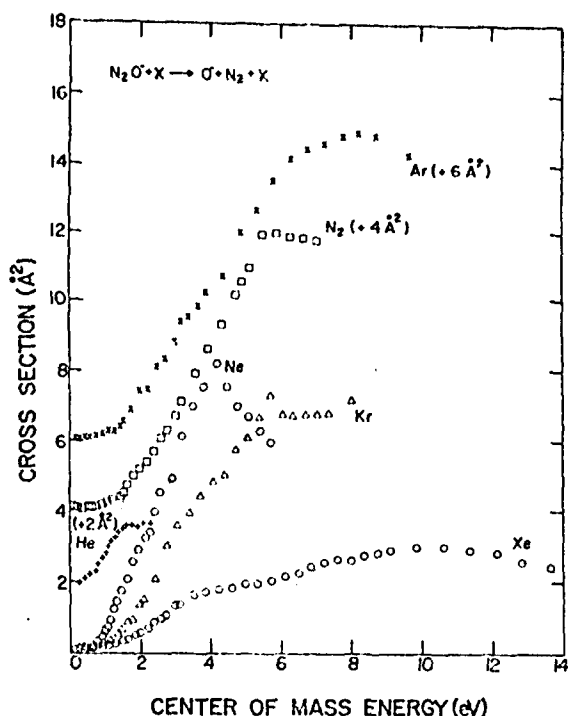


FIG. 1. Observed apparent cross sections $\sigma_{app}^{obs}(E_{I0})$ for O^- production from the collision-induced dissociation reactions $\text{N}_2\text{O}^+ + \text{M} \rightarrow \text{N}_2 + \text{O}^- + \text{M}$, where $\text{M} = \text{He}, \text{Ne}, \text{Ar}, \text{Kr}, \text{Xe}, \text{N}_2$. For plotting purposes E_{I0} has been converted to the center-of-mass coordinate system, and the cross sections for He, Ne, and Ar have been shifted upwards by 2, 4, and 6 \AA^2 , respectively.

Xe, N_2 . The observed apparent cross sections $\sigma_{app}^{obs}(E_{I0})$ are shown in Fig. 1. All of the six reactions observed exhibit thresholds and thus may be assumed to be endo-ergic. The cross sections all show exponential increase in the threshold region, followed by a linear rise towards a maximum, and then a gradual decrease. The true energy threshold for each reaction was obtained from the observed apparent cross sections by means of the convolution procedure outlined above. The application of this procedure is illustrated in Fig. 2, where the calculated apparent cross sections $\sigma_{app}^{calc}(E_{I0})$ for the production of O^- from the reaction of N_2O^+ with Ne are shown (solid lines) for various combinations of E_0 and n . Comparisons with the data— $\sigma_{app}^{obs}(E_{I0})$ represented by solid circles—show that the computed curve with $E_0 = 0.4$ eV (COM) = 1.27 eV (LAB) and $n = 2.3$ is the best fit. The uncertainty in the values of E_0 (COM) and n is on the order of ± 0.1 . These errors are estimated from the ranges of E_0 and n which yield a good fit to the experimental data. Figure 3 compares the calculated best fit curves $\sigma_{app}^{calc}(E_{I0})$ [Eq. (9)] and the corresponding absolute cross sections $\sigma_{abs}^{calc}(E_I)$ [Eq. (10)] to the experimental data $\sigma_{app}^{obs}(E_{I0})$ [Eq. (4)] for the other five reactions studied. The values of E_0 and n which correspond to these best fits are listed in Table I. The dashed lines in Figs. 2 and 3 are the (unconvoluted) absolute cross sections $\sigma_{abs}^{calc}(E_I)$ from Eq. (10). Comparison of these curves with the solid curves $\sigma_{app}^{calc}(E_{I0})$ for each target gas and for given values of E_0 and n shows the importance of taking the ion and neutral translational energy distributions into consideration in

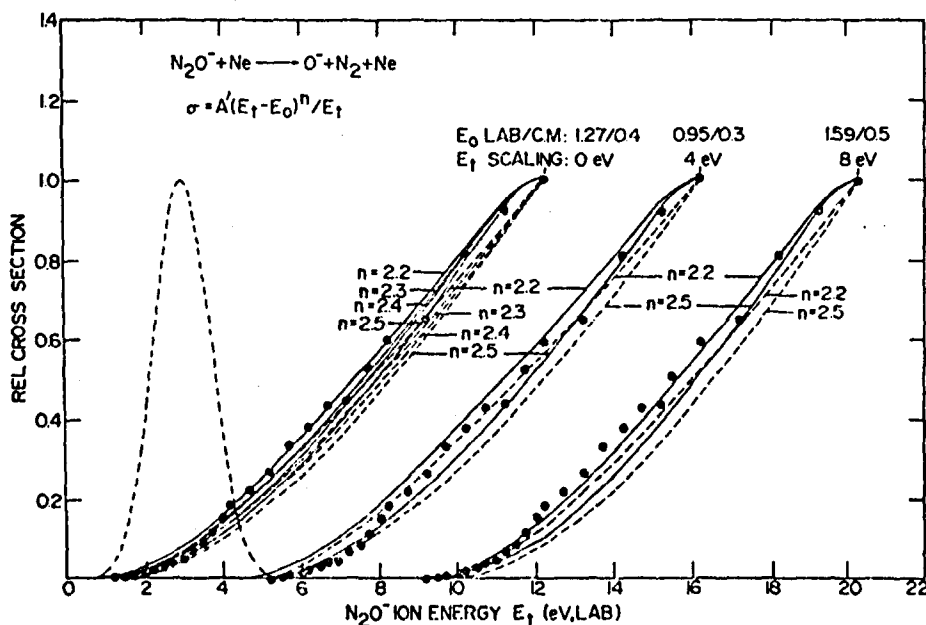


FIG. 2. Optimization of the parameters E_0 and n for $\text{M} = \text{Ne}$. The effect of the variation of n is shown for three values at E_0 . The curves for which $E_0 = 0.3$ or 0.5 eV (COM) are offset 4 or 8 eV (LAB) on the energy scale for clarity of presentation. The circles are the data points $\sigma_{app}^{obs}(E_{I0})$. Each solid line represents the calculated apparent cross section $\sigma_{app}^{calc}(E_{I0})$ which results from the use of a given pair of parameter values. Shown for comparison (as dashed lines) are the absolute cross section functions $\sigma_{abs}^{calc}(E_I)$ with which the calculated apparent cross sections are computed. The near Gaussian distribution curve drawn for $E_{I0} = 3$ eV illustrates the combined distribution function $f(E_I, u_m | E_{I0}) = f(E_I | E_{I0}) f(u_m)$ with which $\sigma_{abs}^{calc}(E_I)$ is convoluted to compute $\sigma_{app}^{calc}(E_{I0})$. Note 1: E_I in the figure alternatively represents E_{I0} or E_I , and A' in the figure is A_{LAB} from the text.²³ Note 2: All cross sections have been normalized to the highest energy data point $\sigma_{app}^{obs}(E_{I0}^{max})$ which is included in the fit procedure. Note 3: A_{LAB} is found for each set of values for the other parameters, E_0 and n , by the assumption that $\sigma_{app}^{calc} = \sigma_{abs}^{calc} \cdot \sigma_{app}^{obs}$ and $E_{I0} = E_I$ at the data point $\sigma_{app}^{obs}(E_{I0}^{max})$.

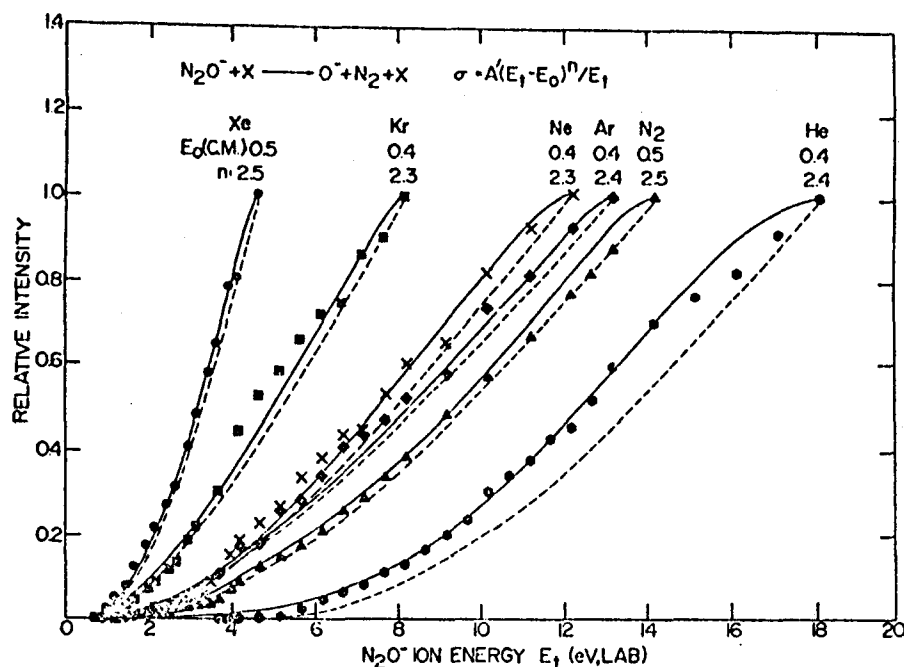


FIG. 3. Comparisons of the optimized, calculated apparent cross sections $\sigma_{app}^{calc}(E_{10})$ (—) with the observed data $\sigma_{app}^{obs}(E_{10})$ for the target gases Xe, Kr, Ne, Ar, N₂, and He. The optimized values for E_0 and n are shown for each reaction; the absolute cross sections $\sigma_{abs}^{calc}(E_1)$ (---) determined by these values are also shown. Comparison of the solid and dashed lines provides a visual indication of the importance of the combined effects on the cross section of thermal motion of the collision gas and dispersion of the nominally monoenergetic ion beam. For symbol clarification and plotting details, see the notes in the caption to Fig. 2.

fitting the experimental data.

As indicated earlier (Sec. II, B), the threshold E_0 in the present experiments corresponds to the dissociation energy $D(R-S)$, where $R-S$ is N_2-O^+ . From Table I the average value for $D(N_2-O^+)$ for the six reactions studied is 0.43 ± 0.1 eV. This result is based upon the assumption noted above (Sec. II, B) that neither reagent molecule is internally excited at the threshold. The assigned uncertainty of ± 0.1 eV (COM) arises from the limiting resolution assessed in the present study to the optimization of the parameter E_0 . The accuracy of the present method has been established to be ± 0.1 eV by comparisons with results from more accurate methods for the O_2 , $NO-O^+$, and CO_2-O^+ bond dissociation energies.²²

The value determined for the dissociation energy $D(N_2-O^+)$ enables the construction of thermodynamic Hess cycles to evaluate the nitrous oxide adiabatic electron affinity E. A. (N_2O) and the dissociation energy $D(N-NO^+)$:

$$E. A. (N_2O) = -D(N_2-O) + E. A. (O) + D(N_2-O^+), \quad (11a)$$

$$D(N-NO^+) = +E. A. (N_2O) + D(N-NO) - E. A. (NO). \quad (11b)$$

The use of known values for $D(N_2-O) = 1.68$ and $D(N-NO) = 4.93$ from Ref. 24, for $E. A. (O) = 1.47$ from Ref. 25, and for $E. A. (NO) = 0.02$ from Ref. 26 yields $E. A. (N_2O) = 0.22 \pm 0.1$ and $D(N-NO^+) = 5.13 \pm 0.1$ in the present work. All values are in electron volts, and the uncertainties given for the latter two values result from the predominating uncertainty of ± 0.1 in the value for $D(N_2-O^+)$.

III. AB INITIO AND OTHER THEORETICAL CALCULATIONS

A. Ab initio method of calculation

The *ab initio* calculations were performed with single configuration (SCF), multiconfiguration (MCSCF), and

configuration interaction (MCSCF/CI) self-consistent-field molecular wavefunctions. The MCSCF method employed in this study has been presented in detail elsewhere.^{27,28} Previous applications of the MCSCF and MCSCF/CI methods to first row triatomics have been reported.²³⁻²² The calculations were made with BISON-MC and its associated-computer codes.^{29,33,34}

In brief, and to establish terminology, the MCSCF wavefunction Ψ_{MC}^s for a molecular state s ,

$$\Psi_{MC}^s = \sum_{k=1}^{N_{MC}} C_{MC,k}^s \Phi_k^s, \quad (12)$$

is obtained by the iterative optimization of the weighting coefficients $C_{MC,k}^s$ of the N_{MC} configurations Φ_k^s

$$\Phi_k^s = \alpha \prod_{j=1}^{N_{so}} \delta_{kj}^s \phi_{MC,j}^s, \quad (13)$$

TABLE I. Best-fit values of A , E_0 , and n for Eq. (8) as obtained by convoluting $\sigma_{abs}^{calc} = A_{LAB}(E_1 - E_0)^n/E_1$ with the combined ion and neutral translational distribution and comparing to the observed apparent cross section for the reaction $N_2O^+ + M \rightarrow N_2 + O^+ + M$.

Best-fit parameter values ^a			
M	A ($\text{\AA}^2(\text{eV})^{1-n}$)	E_0 (eV, c.m.)	n
Xe	0.56	0.5	2.5
Kr	1.46	0.4	2.3
Ar	1.18	0.4	2.4
Ne	2.75	0.4	2.3
He	2.70	0.4	2.4
N ₂	1.26	0.5	2.6
Averages	...	0.43	2.40

^aThe values for E_0 and n are accurate to ± 0.1 ; see text. For the relationship of A to A_{LAB} , see Ref. 22 and 23 and Sec. II, B. of the text.

and of the expansion coefficients C_{ji}^s of the N_{so} spin orbitals $\phi_{MC,j}^s$

$$\phi_{MC,j}^s = \sum_{i=1}^{N_{bf}} C_{ji}^s \chi_i \eta_j \quad (14)$$

until a stationary variational solution to the energy eigenvalue problem is achieved. In the present study the convergence criterion was 10^{-6} a.u. In Eq. (13), α is the antisymmetrization operator and the quantity δ_{kj}^s is unity if spin orbital j is occupied in configuration k for state s and zero otherwise. In Eq. (14) the basis $\{\chi_i\}$ in which the spatial component of the spin orbitals are expanded is, in practice, always finite and usually spans a limited cartesian space about the nuclear framework. Also, in Eq. (14) η_j is the spin component of spin orbital j . Because of the optimization of both the configurational and the orbital expansion coefficients, the MCSCF wavefunction is a compact wavefunction, consisting of the orbitals and a relatively few (about 15–20 for a triatomic) configurations. These configurations are chosen to allow the wavefunction to describe dissociation to the formally correct atom-diatomic asymptotic states and to contain most of those electron correlation effects necessary to determine potential surface characteristics in the triatomic regions.

The MCSCF/CI wavefunction Ψ_{CI}^s for molecular state s ,

$$\Psi_{CI}^s = \sum_{k=1}^{N_{CI}} C_{CI,k}^s \Phi_k^s, \quad (15)$$

is constructed from the MCSCF orbitals $\phi_{MC,j}^s$ according to Eq. (13). This relatively small CI wavefunction (N_{CI} is on the order of 100 for a first row triatomic) is a helpful aid in the process of determining an appropriate set of MCSCF configurations $\{\Phi_k^s\}_{MC}$ and is used to pick up additional correlation energy from the hundreds or thousands of configurations whose effect upon the MCSCF orbitals is too small to warrant their inclusion in $\{\Phi_k^s\}_{MC}$. The MCSCF/CI configuration set $\{\Phi_k^s\}_{CI}$ may be chosen from the complete configuration set $\{\Phi_k^s\}$ for state s by the criterion of a threshold contribution to the total energy eigenvalue for Ψ_{CI}^s of, say, 10^{-5} a.u. Experience has shown, however, that one can, for convenience and with some confidence, usually make the assumption that this energy selection criterion can be met by retaining those configurations for which $|C_{CI,k}^s|$ is greater than a numerical threshold ϵ_{CI} of, e.g., 0.001–0.002.

The choice of orbital $\{\chi_i\}$ and wavefunction $\{\Phi_k^s\}_{MC}$ expansion bases is crucial to the success of the MCSCF method. Aspects of these choices peculiar to the present application will be discussed below.

B. Basis set and accuracy considerations

The orbital expansion basis functions for nitrogen and oxygen were taken to be the atom-optimized 9s5p Gaussian basis sets of Huzinaga³⁵ as contracted to 4s3p sets by Dunning.³⁶ No attempt was made to reoptimize these basis sets for the calculations reported in this paper. Since the positive experimental electron affinity indicates stability of N_2O^+ towards electron de-

tachment in the vicinity of its minimum and since preliminary SCF calculations showed no Rydberg character³⁷ in the X^2A' wavefunction, this basis set should be sufficient to predict the equilibrium geometry and the shape of the surface in the minimum region. The use of a fixed basis, furthermore, enables the extension of the X^2A' surface scan into regions in which the ion surface passes above the neutral surface. In the latter regions the computed results for $N_2O^+(X^2A')$ are to be interpreted as estimates of the $N_2O + e$ resonance energy. Lastly, test calculations are described below in which the 4s3p basis was complemented with diffuse s , p or with polarization d functions. The results tend to indicate the sufficiency of the 4s3p basis for the present survey in the triatomic interactive region.

From previous studies an accuracy of about 5% for the geometric parameters and about 10% for the vibrational frequencies and electric moments can be expected with the 4s3p basis set and with the MCSCF treatment of correlation effects.^{29,31,32} The sophistication of the presently applied level of *ab initio* methodology has not, however, proven sufficient for the reliable prediction of either triatomic dissociation energies or adiabatic electron affinities.^{31,32} Since these latter quantities are provided by the experimental portion of the present paper, no attempt is made here to go to the additional expense and effort which would be required to compute them reliably. Such a more sophisticated computation would involve improvements in the orbital expansion basis set $\{\chi_i\}$, such as exponent reoptimization plus the addition of polarization functions, and in the wavefunction expansion basis set $\{\Phi_k^s\}$, such as the consideration of configurations involving excitations to nonvalence virtual orbitals.³⁸

C. Development of optimum wavefunction expansion bases $\{\Phi_k^s\}_{MC}$ and $\{\Phi_k^s\}_{CI}$

1. General considerations

Throughout the present study, the selection of configurations Φ_k^s for the MCSCF and MCSCF/CI wavefunctions was restricted to a valence subset of the full basis $\{\Phi_k^s\}$. For a first row triatomic this valence subset, $\{\Phi_k^s\}_{valence}$, consists of the main, so-called SCF, configuration(s) and those configurations obtainable from it via spin orbital excitations among the valence orbitals 4–9 σ , 1–3 π_x , 1–3 π_y .³⁸ The rational and general manner by which configurations are selected from $\{\Phi_k^s\}_{valence}$ are embodied in the optimized valence configuration (OVC) scheme discussed by Das and Wahl.³⁹ Aspects of the selection procedure peculiar to the present applications of this scheme to first row triatomics are discussed briefly below and more extensively elsewhere.³²

It should be noted that the present selection subset $\{\Phi_k^s\}_{valence}$ may be somewhat deficient in that it does not include any configuration in which nonvalence virtual orbitals are occupied. The relatively small but cumulatively significant correlation energy obtainable from such configurations has been documented in diatomic OVC-MCSCF calculations.^{39,40} In the present triatomic

work on the $X^1\Sigma^+$ state of N_2O and the $1^2\Pi$ state of N_2O^- it is significant that the SCF wavefunction for the ion but not the neutral involves occupancy of the 3π orbital. For this reason, no quartically and relatively few doubly and triply excited configurations can be constructed in the valence π -orbital space for $N_2O^-(1^2\Pi)$. Such configurations have been shown to be important for $N_2O(X^1\Sigma^+)$.^{41,42} Thus, the lowest unoccupied nonvalence virtual orbitals, e.g., 4π , 5π , 10σ , must be considered in order to provide an orbital space for correlating the $1^2\Pi$ ion state which is as flexible as the 15 orbital (valence) space is for $N_2O(X^1\Sigma^+)$. It is fully intended to incorporate the 4π and higher orbitals in future calculations on vertical excitation spectra of the N_2O neutral and ionic systems. For the present we confine ourselves to pointing out the problem. This differential sufficiency of the valence orbital space results in a correlated vertical excitation energy from $N_2O(X^1\Sigma^+)$ to $N_2O^-(1^2\Pi)$ which tends to be too high. Correspondingly, the adiabatic electron affinity tends to be underestimated. The quantitative amount of this underestimate—a measure of the differential sufficiency of the valence configuration space $\{\Phi_k^s\}_{\text{valence}}$ for the ion versus the neutral—will be deduced by comparing the experimental adiabatic electron affinity from Sec. II to the computational results presented in this section.

2. $N_2O^-(1^2\Pi)$

Initially, the MCSCF wavefunction Ψ_{MC}^s , $s=1^2\Pi$, for N_2O^- was developed at the $N_2O(X^1\Sigma^+)$ experimental equilibrium geometry by the sequential consideration of configurations which differed by two spin orbitals from (i.e., doubly excited wrt) the SCF configuration,

$$1\sigma^2 2\sigma^2 3\sigma^2 4\sigma^2 5\sigma^2 6\sigma^2 7\sigma^2 1\pi^4 2\pi^4 3\pi^0. \quad (16)$$

The configurations for $N_2O^-(1^2\Pi)$ were selected for examination upon the basis of experience with the N_2O system.^{41,42} After some testing, 15 configurations were incorporated.

3. $N_2O(X^2A')$

The 15 configuration $N_2O^-(1^2\Pi)$ wavefunction (15 MC) was then used to scan the $X^2A'(1^2\Pi)$ potential energy surface. Most of the effort was applied in the neighborhood of the minimum located in an extensive preliminary scan with the SCF wavefunction, Φ_1^s ,

$$(1a')^2 \dots (9a')^2 (10a')^2 (1a'')^2 (2a'')^2. \quad (17)$$

Most of the SCF results have been recorded in Ref. 31. The minimum energy nuclear conformation located in the 15 MC scan is $(R_{NN}, R_{NO}, A_{NNO}) = (2.3045 \text{ a.u.}, 2.6051 \text{ a.u.}, 130.2^\circ)$.

Then $\{\Phi_k^s\}_{MC}$, $s=X^2A'$, was reoptimized near the 15 MC minimum but with $A_{NNO} = 130.0^\circ$. In addition to configurations doubly excited with respect to Φ_1^s , those configurations which become allowed upon bending from $C_{\infty v}$ to C_s symmetry and all triply excited configurations were considered. A CI configuration set was simultaneously determined. The Φ_k^s were considered for inclusion in $\{\Phi_k^s\}_{MC}$ or $\{\Phi_k^s\}_{CI}$ on the basis of the magnitude of their weighting coefficient $C_{CI,k}^s$ in Ψ_{CI}^s . The CI wave-

function was optimized to include all singly but only those doubly and triply excited configurations for which $|C_{CI,k}^s| > 0.00155$. The corresponding cutoff for Ψ_{MC}^s was $|C_{MC,k}^s| > 0.02$. Alternating MCSCF and CI calculations led to an 18 configuration MCSCF wavefunction (18 MC) and a ninety-one configuration CI wavefunction. Seven configurations for which $0.00100 < |C_{CI,k}^s| < 0.00155$ were added to obtain a final, 98 configuration CI wavefunction (98 CI). The 18 MC configurations and their weighting coefficients at a few geometries are displayed in Table II. It is noted that $\{\Phi_k^s\}_{MC}$ contains none of the triply excited configurations from $\{\Phi_k^s\}_{\text{valence}}$. It is also noted that none of the MCSCF orbitals exhibits significant Rydberg character³⁷ in the vicinity of the minimum.

4. $N_2O(X^1\Sigma^+)$

The MCSCF and MCSCF/CI configuration sets for $N_2O(X^1\Sigma^+)$ were optimized at the experimental equilibrium geometry. The optimization was conducted in much of the same fashion as just described for $N_2O^-(X^2A')$.^{41,42} The MCSCF configuration set is listed in Table III and the orbitals (for a slightly different configuration set) in Ref. 43. There are several triply and one quartically excited configurations in Ψ_{MC}^s . The CI configuration set consists of the SCF configuration, all single excitations with respect to it, and all doubly, triply, and quartically excited configurations for which $|C_{CI,k}^s| > 0.001$.

D. *Ab initio* results for $N_2O^-(X^2A')$

1. Stability with respect to electron detachment

Test calculations have been made in which the $4s3p$ basis set was augmented with diffuse s and p functions. The information that such an augmentation provides with regard to the stability toward electron detachment of $N_2O^-(X^2A')$ is of primary interest. However, for comparison purposes, calculations are also reported at the experimental neutral equilibrium geometry for $N_2O(X^1\Sigma^+)$ and for the N_2O^- resonant states $1^2\Pi$ and $1^2\Sigma^+$. The results are summarized in Table IV and Fig. 4.

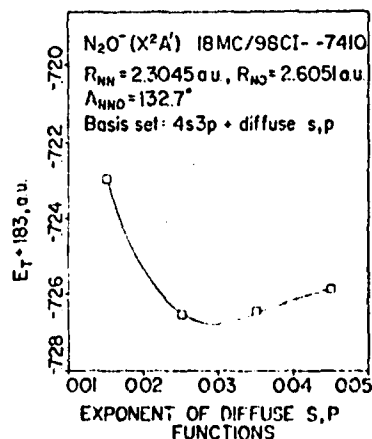


FIG. 1. Optimization of the 18 MC/98 CI total energy of $N_2O^-(X^2A')$ with respect to the exponent of diffuse s , p functions added to the $4s3p$ basis set.

TABLE II. Configurations of the 18 MC-7510 MCSCF wavefunction for N_2O^- in its X^2A' ($1^2\Pi$) state and their weighting coefficients at selected geometries; total energies for the SCF, MCSCF, and MCSCF/CI wavefunctions at these geometries.

Conf. No.	Orbital occupancy ^a												Spin coupling sequence ^b	Weighting coefficients at $R_{\text{NN}}/R_{\text{NO}}/A_{\text{NNO}}$				
	$1a'$	$5a'$	$6a'$	$7a'$	$8a'$	$9a'$	$10a'$	$11a'$	$12a'$	$1a''$	$2a''$	$3a''$		2.3045	2.3045 ^c	2.1320	2.1320	2.3045
	1σ	5σ	6σ	$1\pi_x$	7σ	$2\pi_x$	$3\pi_x$	8σ	9σ	$1\pi_y$	$2\pi_y$	$3\pi_y$		2.6051	132.73°	130°	180°	180°
1.	2	2	2	2	2	2	1	0	0	2	2	0	D	0.962	0.962	0.971	0.973	0.963
2.	2	2	2	2	2	1	0	0	2	2	2	0	D	0.000	0.002	0.000	-0.002	0.000
3.	2	2	2	2	2	2	1	0	0	0	2	2	D	-0.207	-0.170	-0.144	-0.143	-0.167
4.	2	2	2	2	2	2	1	0	0	2	0	2	D	-0.019	-0.029	-0.015	-0.039	-0.021
5.	0	2	2	2	2	2	1	0	2	2	2	0	D	-0.116	-0.095	-0.068	-0.071	-0.105
6.	2	2	2	2	0	2	1	2	0	2	2	0	D	-0.073	-0.063	-0.053	-0.051	-0.058
7.	2	2	2	2	2	1	2	0	0	2	1	1	SD	-0.011	-0.017	-0.023	-0.024	-0.015
8.	2	2	2	2	2	1	2	0	0	2	1	1	TD	0.021	0.023	0.027	0.031	0.021
9.	2	2	2	1	2	2	2	0	0	1	2	1	SD	-0.053	-0.105	-0.097	-0.081	-0.091
10.	2	2	2	1	2	2	2	0	0	1	2	1	TD	0.017	0.095	0.097	0.094	0.100
11.	2	2	0	2	2	2	1	0	0	2	2	2	D	-0.027	-0.029	-0.025	-0.027	-0.031
12.	1	2	2	2	2	1	2	0	1	2	2	0	SD	-0.055	-0.053	-0.012	-0.055	-0.061
13.	2	2	2	2	1	1	2	0	1	2	2	0	SD	0.099	-0.022	0.015	0.012	0.018
14.	2	2	2	1	1	2	2	1	0	2	2	0	SD	-0.033	-0.057	-0.050	-0.053	-0.062
15.	2	2	2	2	1	2	1	1	0	2	1	1	SDTD	-0.024	-0.020	-0.029	-0.025	-0.015
16.	2	2	2	2	2	2	0	0	1	2	1	1	SD	0.011	0.020	0.011	0.000	0.000
17.	2	2	2	2	2	2	0	0	1	2	1	1	TD	-0.024	-0.042	-0.020	0.000	0.000
18.	2	2	2	2	2	2	0	0	1	1	2	1	TD	-0.020	-0.033	-0.030	0.000	0.000
Total energy ^c 183, a.u.																		
SCF																-0.6032	-0.5661	-0.5181
MCSCF (18 MC)																-0.6102	-0.7078	-0.6576
MCSCF/CI (18 MC/98 CI)																-0.6510	-0.7159	-0.6652

^aThe core $1a'^2 2a'^2 3a'^2$ is assumed.^bCumulative spin coupling from the left. Abbreviations: S, singlet; D, doublet; T, triplet.^cThe geometry at which the final optimization of the MCSCF configuration list was performed, (2.3045/2.6051/130°), is associated with weighting coefficients which are within 0.001 of these 132.73° values. The atomic one-electron bases were the $4s3p$ sets from Ref. 36.

Calculations were made at the geometry $R_{\text{NN}} = 2.3045$ a.u., $R_{\text{NO}} = 2.6051$ a.u., $A_{\text{NNO}} = 130^\circ$. Figure 4 is a plot of the 18 MC/98 CI total energy of $\text{N}_2\text{O}^-(X^2A')$ as a function of the exponent of the diffuse s and p type functions. The same exponent has been used for all 12 functions added to the basis set. A minimum occurs at a total energy of -183.726753 a.u. for an exponent value of 0.0291. The occurrence of this minimum is evidence that the negative molecular ion is stable with respect to electron detachment in the vicinity of its equilibrium geometry. As shown in Table IV, the minimum is not an artifact of the correlation energy: it occurs also in the results with the 18 MC and the single configuration wavefunctions. Also, the augmentation of the basis set with 12 diffuse functions having the optimized exponent lowers the 18 MC/98 CI total energy for $\text{N}_2\text{O}^-(X^2A')$ by just 0.0112 a.u. (0.304 eV). The corresponding change in the dipole moment is also small. See the last two columns of Table IV. Examination of the 18 MC wavefunction shows that none of the MCSCF orbitals may be described as diffuse, let alone as Rydberg, in character. From these results $\text{N}_2\text{O}^-(X^2A')$ appears to have a compact electronic structure. The "extra" electron resides in an orbital which is bonding between the terminal nitrogen and the oxygen atom. This orbital, the $10a'(3\pi)$ orbital, is unoccupied in the SCF configuration for the neutral molecule.

Comparisons with calculations made at the neutral experimental equilibrium geometry provide perspective.

From these calculations it is seen that the addition of diffusion functions effects a lowering of less than 0.002 a.u. (0.05 eV) in the total energy of $\text{N}_2\text{O}^-(X^1\Sigma^+)$. See Table IV. The corresponding lowering for the $\text{N}_2\text{O}^-(1^2\Pi)$ resonance state is about 0.02 a.u. (0.5 eV). By contrast, the SCF total energy for the $\text{N}_2\text{O}^-(1^2\Sigma^+)$ resonance state decreases by 0.1940 a.u. (5.28 eV) with the addition of diffuse s functions. The large difference in the effect of diffuse functions for the two resonance states correlates with the valence character assumed by the $10a'(3\pi)$ orbital and the diffuse/Rydberg character assumed by the $8\sigma(11a')$ orbital upon occupancy in the main (SCF) configuration in a wavefunction.

The improvements in the $\text{N}_2\text{O}^-(X^2A')$ wavefunction which result from the addition of diffuse functions are small enough that the neglect of these functions is not expected to have much effect on the shape and location of the potential surface minimum. Hence, they have been left out of the calculations described below.

2. Equilibrium geometry and force constants

The points computed for the $\text{N}_2\text{O}^-(X^1A')$ potential energy surface with the 18 MC and 18 MC/98 CI wavefunctions are given in Table V. Variation of the angle A_{NNO} from 125° to 140° for the 18 MC wavefunction with the 15 MC equilibrium bond lengths showed a minimum total energy E_T at 132.73° . Sequential reoptimization of the bond lengths at this angle with the 18 MC wavefunction gave $R_{\text{NN}}^e = 2.3047$ a.u. and $R_{\text{NO}}^e = 2.5900$ a.u.

Conf. No.	Orbital occupancy ^b										Spin coupling sequence ^c	Weighting coefficients at $R_{NN}/R_{NO}/A_{HNO}$		
	6σ	7σ	8σ	9σ	1π _x	2π _x	3π _x	1π _y	2π _y	3π _y		2.132 2.238 90°	2.132 2.238 130°	2.132 2.238 180°
	6a'	7a'	8a'	9a'	7a''	9a'	10a'	1a''	2a''	3a''				
1	2	2	0	0	2	2	0	2	2	0		0.955	0.919	0.956
2	2	2	0	0	2	2	0	2	0	2		-0.090	-0.127	-0.126
3	2	2	0	0	2	0	2	2	2	0		-0.188	-0.158	-0.126
4	2	0	2	0	2	2	0	2	2	0		-0.019	-0.020	-0.018
5	2	0	0	2	2	2	0	2	2	0		-0.052	-0.018	-0.051
6	2	2	0	0	2	2	0	0	2	2		-0.058	-0.050	-0.048
7	2	2	0	0	0	2	2	2	2	0		-0.044	-0.053	-0.048
8	2	2	0	0	2	1	1	2	1	1	SDS	-0.140	-0.146	-0.145
9	2	2	0	0	2	1	1	2	1	1	TDS	-0.048	-0.055	-0.043
10	2	2	0	0	2	1	1	2	1	1	SDS	-0.005	-0.075	-0.071
11	2	1	1	0	2	2	0	2	1	1	SDS	0.048	0.051	0.050
12	2	1	1	0	2	1	1	2	2	0	SDS	0.054	0.052	0.050
13	2	1	0	1	2	2	0	1	2	1	SDS	-0.078	-0.069	-0.071
14	2	1	0	1	1	2	1	2	2	0	SDS	-0.000	-0.067	-0.071
15	2	2	0	0	2	0	2	2	0	2		0.047	0.054	0.045
16	2	2	0	0	0	2	2	2	1	1	S	0.011	-0.022	-0.018
17	2	2	0	0	2	1	1	0	2	2	S	-0.012	-0.019	-0.018
18	2	2	0	0	1	2	1	1	1	2	SDS	-0.000	0.028	0.027
19	2	2	0	0	1	1	2	1	2	1	SDS	-0.003	0.033	0.027
Total energy + 183, a.u.														
SCF												-0.4156	-0.5310	-0.6019
MCSCF (19 MC)												-0.5592	-0.7015	-0.7716
MCSCF/CI (19 MC/99 CI)												-0.5727	-0.7105	-0.7819

^cCumulative spin coupling from the left. Abbreviations: S, singlet; D, doublet; T, triplet.

The results for all SCF, MCSCF, and MCSCF/CI calculations made of the minimum in the $\text{N}_2\text{O}^+(\text{X}^2\text{A}')$ potential energy surface are summarized and compared to $\text{N}_2\text{O}(\text{X}^1\Sigma^+)$ in Table VI. From Table VI it can

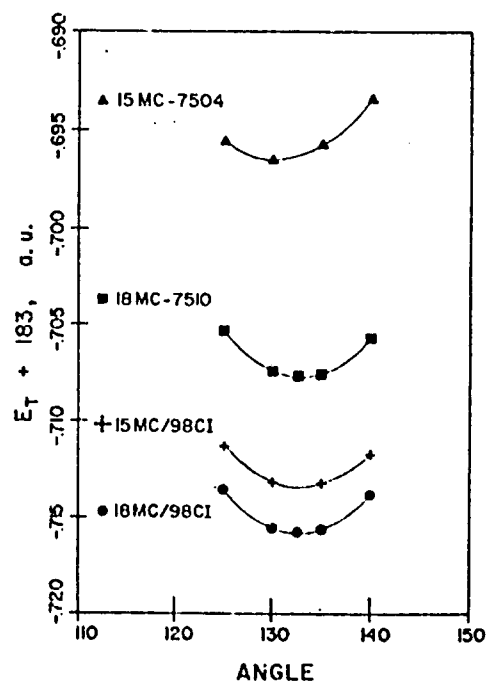


FIG. 5. Bending potential curves for $\text{N}_2\text{O}^+(\text{X}^2A')$ near the minimum with the 15 MC, 15 MC/98 CI, 18 MC, and 18 MC/98 CI wavefunctions. The bond lengths are $R_{\text{NN}} = 2.3015$ a.u. and $R_{\text{NO}} = 2.6051$ a.u.

TABLE III. Configurations of the 19 MC-7410 MCSCF wavefunction of the $X^1\Sigma^+(1^1A')$ state of N_2O and their weighting coefficients at selected geometries.^{a,b}

Conf. No.	Orbital occupancy ^b										Spin coupling sequence ^c	Weighting coefficients at $R_{NN}/R_{NO}/A_{NNO}$		
	6 σ	7 σ	8 σ	9 σ	1 π_x	2 π_x	3 π_x	1 π_y	2 π_y	3 π_y		2.132	2.132	2.132
	6a'	8a'	11a'	12a'	7a'	9a'	10a'	1a''	2a''	3a'		2.238	2.238	2.238
												90°	130°	180°
1	2	2	0	0	2	2	0	2	2	0		0.955	0.949	0.956
2	2	2	0	0	2	2	0	2	0	2		-0.090	-0.127	-0.126
3	2	2	0	0	2	0	2	2	2	0		-0.188	-0.158	-0.126
4	2	0	2	0	2	2	0	2	2	0		-0.019	-0.020	-0.018
5	2	0	0	2	2	2	0	2	2	0		-0.052	-0.048	-0.054
6	2	2	0	0	2	2	0	0	2	2		-0.058	-0.050	-0.048
7	2	2	0	0	0	2	2	2	2	0		-0.044	-0.053	-0.048
8	2	2	0	0	2	1	1	2	1	1	SDS	-0.140	-0.146	-0.145
9	2	2	0	0	2	1	1	2	1	1	TDS	-0.018	-0.055	-0.043
10	2	2	0	0	2	1	1	2	1	1	SDS	-0.005	-0.075	-0.071
11	2	1	1	0	2	2	0	2	1	1	SDS	0.048	0.051	0.050
12	2	1	1	0	2	1	1	2	2	0	SDS	0.051	0.052	0.050
13	2	1	0	1	2	2	0	1	2	1	SDS	-0.078	-0.069	-0.071
14	2	1	0	1	1	2	1	2	2	0	SDS	-0.000	-0.067	-0.071
15	2	2	0	0	2	0	2	2	0	2		0.047	0.054	0.045
16	2	2	0	0	0	2	2	2	1	1	S	0.011	-0.022	-0.018
17	2	2	0	0	2	1	1	0	2	2	S	-0.012	-0.019	-0.018
18	2	2	0	0	1	2	1	1	1	2	SDS	-0.000	0.028	0.027
19	2	2	0	0	1	1	2	1	2	1	SDS	-0.003	0.033	0.027
Total energy +183, a.u.														
SCF												-0.4156	-0.5310	-0.6019
MCSCF (19 MC)												-0.5592	-0.7015	-0.7716
MCSCF/CI (19 MC/99 CI)												-0.5727	-0.7105	-0.7819

^aThe configuration list was optimized at $(R_{NN}, R_{NO}, A_{NNO}) = (2.132 \text{ a.u.}, 2.238 \text{ a.u.}, 180^\circ)$, the experimental equilibrium geometry. The atomic-one electron bases were the $4s3p$ sets from Ref. 36.

^bA core $1\sigma^2 2\sigma^2 3\sigma^2 4\sigma^2 5\sigma^2$ is assumed.

^cCumulative spin coupling from the left. Abbreviations: S, singlet; D, doublet; T, triplet.

The corresponding energy minimum for the 98 CI wavefunction with the 18 MC orbitals (18 MC/98 CI) was found to be $(R_{NN}^e, R_{NO}^e, A_{NNO}^e) = (2.3085 \text{ a.u.}, 2.5979 \text{ a.u.}, 132.68^\circ)$.

Figures 5 and 6 illustrate the potential energy dependence upon each internal coordinate at the minimum located with each correlated wavefunction. The total energies at the minima illustrated in the R_{NN} , R_{NO} , and A_{NNO} curves for the 18 MC and 18 MC/98 CI wavefunctions are within 0.00001 a.u. ($< 0.0003 \text{ eV}$) of one another. Thus, the 18 MC (18 MC/98 CI) minimum given above is indeed optimized in all three coordinates.

Each potential curve minimum was located by a numerical search of a function fitted to the computed points $E_T(X)$, where X is R_{NN} , R_{NO} , or A_{NNO} . The form of the fit function $V(X)$ was a polynomial of degree $n-1$ in X . The curve drawn through each set of computed points in Figs. 5, 6, and 8 represents $V(X)$ fitted to those points. The force constants were then computed from the second derivatives $V''(X^e) = [\partial^2 V(X)/\partial X^2]_{X=X^e}$ of the fit function: $k_{NN} = V''(R_{NN}^e)$, $k_{NO} = V''(R_{NO}^e)$, $k_{NNO} = V''(A_{NNO}^e)/R_{NN}^e R_{NO}^e$.

The results for all SCF, MCSCF, and MCSCF/CI calculations made of the minimum in the $N_2O^+(X^1\Sigma^+)$ potential energy surface are summarized and compared to $N_2O(X^1\Sigma^+)$ in Table VI. From Table VI it can

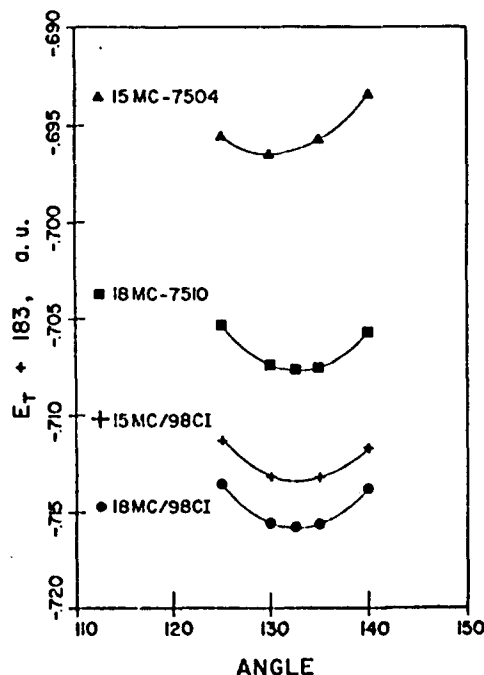


FIG. 5. Bending potential curves for $N_2O^+(X^1\Sigma^+)$ near the minimum with the 15 MC, 15 MC/98 CI, 18 MC, and 18 MC/98 CI wavefunctions. The bond lengths are $R_{NN} = 2.3045 \text{ a.u.}$ and $R_{NO} = 2.6051 \text{ a.u.}$

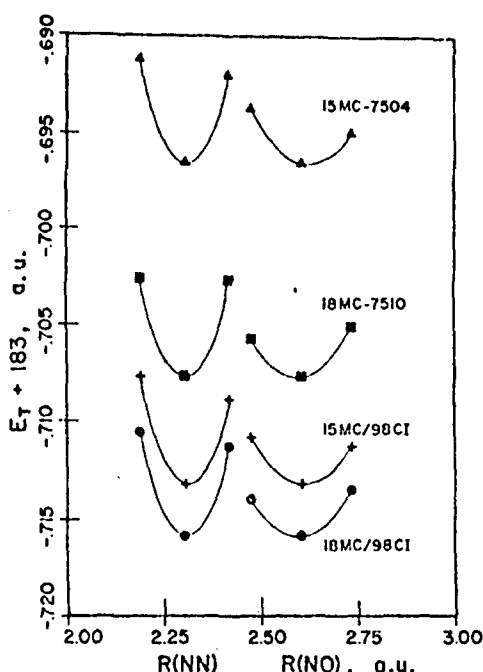


FIG. 6. Bond stretching potential curves for N_2O . The curves for the 15 MC and 15 MC/98 CI wavefunctions were computed at 130° . The curves for the 18 MC and 18 MC/98 CI wavefunctions were computed at 132.73° . The unvaried bond length was, alternatively, $R_{\text{NN}} = 2.3015$ a.u. and $R_{\text{NO}} = 2.6051$ a.u.

be seen that the bond lengths and their associated force constants change little as correlation is added to the wavefunction. The bond angle, however, increases 8.9° . The last three configurations of the 18 MC wavefunction (see Table II) account for 2.5° of the increase. These configurations involve the excitation of an electron out of the $10a'$ ($3\pi_u$) orbital. It is the occupancy of this orbital in the SCF configuration which causes N_2O^- to be bent in the X^2A' state. The remaining 6.4° of the increase is attributable to Configurations 3–15 of Table II.

With regard to the optimization of the MCSCF configuration set it is notable that the 18 MC wavefunction contains all correlation components of the 98 CI wavefunction necessary to represent the equilibrium bond angle and other quantities defining the location and shape of the minimum.

A comparison is made of the 18 MC/98 CI results for $\text{N}_2\text{O}^-(X^2A')$ with the experimental equilibrium geometry for $\text{N}_2\text{O}(X^1\Sigma^+)$ in Table VI. The results show the N–N and N–O bond lengths of the ion to be about 8% and 16% greater, respectively, than the neutral values. The corresponding bond force constants k_{NN} and k_{NO} in the ion are but $\frac{2}{3}$ and $\frac{1}{3}$, respectively, of those in N_2O . The ion equilibrium angle is, of course, much less than 180° and its associated bending force constant is 31% greater than for the neutral.

The accuracy of the geometry predicted here for $\text{N}_2\text{O}^-(X^2A')$ can be assessed by reference to other MCSCF/CI calculations for the ground states of N_2O and NO_2 . Comparisons to experiment can be made for the latter two molecules. As shown in Table VI,

the MCSCF/CI calculations⁴² for $\text{N}_2\text{O}(X^1\Sigma^+)$ with the same basis set as used here for the ion give the N–N and N–O equilibrium bond lengths to be about 2% and 5% greater, respectively, than the experimental values. The equilibrium bond angle for $\text{NO}_2(X^2A_1)$, which is isoelectronic with N_2O^- , is found in an MCSCF/CI calculation by Gillispie *et al.*³² to be within 0.5° of the experimental value of 134.1° .²⁴ The basis set for the latter calculations was augmented with d functions. From these considerations the error in the minimum located here for $\text{N}_2\text{O}^-(X^2A')$ is estimated to be 0.05 Å in R_{NN}^e , 0.10 Å in R_{NO}^e , and 2° in A_{NNO}^e .

The error in the predicted force constants for $\text{N}_2\text{O}^-(X^2A')$ can be assessed by analogy to the MCSCF/CI calculations for $\text{N}_2\text{O}(X^1\Sigma^+)$.⁴² In the latter calculations the force constants were found to be uniformly less than their experimental counterparts—less by about 4% for k_{NN} , by 12% for k_{NO} , and by 16% for k_{NNO} . The comparison is made in Table VI. In the absence of further information 4%–13% errors must be expected in the ion force constants. Errors of ± 0.8 , ± 0.8 , and ± 0.2 mdyn/Å are estimated for k_{NO} , k_{NN} , and k_{NNO} , respectively.

3. Vibrational frequencies

The vibrational frequencies for $\text{N}_2\text{O}^-(X^2A')$ may be predicted from the computed force constants. These force constants determine a potential V of the form

$$V(R_{\text{NN}}, R_{\text{NO}}, A_{\text{NNO}}) = \frac{1}{2}(k_{\text{NN}}R_{\text{NN}}'^2 + k_{\text{NO}}R_{\text{NO}}'^2 + \frac{1}{2}k_{\text{NNO}}R_{\text{NN}}^e R_{\text{NO}}^e A_{\text{NNO}}'^2), \quad (18)$$

where $X' = (X - X^e)$ in the neighborhood of the potential surface minimum. The solution of the Schrödinger equation for nuclear motion subject to this potential for nonlinear triatomics has been made and recorded by Wilson, Decius, and Cross.⁴⁴ The expanded secular equation given by these authors was programmed for numerical location of roots and, in turn, solved with the force constants from each electronic wavefunction. The results are included in Table VI.

A calculation of the frequencies of neutral N_2O from the experimentally determined force constants⁴⁴ gives values for ν_1 , ν_2 , and ν_3 which are 32 cm^{-1} higher, 14 cm^{-1} lower, and 38 cm^{-1} lower, respectively, than the experimental frequencies. These discrepancies may be taken as estimates of the error inherent in the assumption of Eq. (18) to represent the potential energy surface near the minimum. On the other hand, computation of the N_2O frequencies determined by the MCSCF/CI equilibrium geometry and force constants gives values for ν_1 , ν_2 , and ν_3 which are 62, 65, and 41 cm^{-1} (or 5%, 11%, and 2%) lower, respectively, than the experimental values. See Table VI. Thus, the error in the potential shape determined by MCSCF/CI calculations for N_2O with the present, $4s3p$, one-electron basis set exceeds the error introduced by the use of the approximate potential form of Eq. (18).

From the neutral molecule results one might reasonably expect that the frequencies ν_1 , ν_2 , and ν_3 re-

TABLE VI. Computed potential energy surface characteristics for $\text{N}_2\text{O}^-(X^2A')$ with a $4s3p$ basis set^a and comparisons to $\text{N}_2\text{O}(X^1\Sigma^+)$.

Parameter	SCF	$\text{N}_2\text{O}^-(X^2A')$ wavefunction				$\text{N}_2\text{O}(X^1\Sigma^+)$	
		15 MC	15 MC/98 CI	18 MC	18 MC/98 CI	MCSCF/CI ^b	Exptl.
E_T^0 (a.u.)	-183.6070	-183.6965	-183.7136	-183.7078	-183.7159	-183.7819	...
R_{NN}^e (Å)	1.204	1.219	1.223	1.220	1.222	1.147	1.128 ⁱ
R_{NO}^e (Å)	1.376	1.379	1.383	1.374	1.375	1.240	1.184 ⁱ
A_{NNO}^e (deg)	123.6	130.19	132.72	132.73	132.68	180.00	180.0 ⁱ
k_{NN} (mdyn/Å)	11.54	11.52	11.56	11.78	11.49	17.21	17.68 ^j
k_{NO} (mdyn/Å)	3.93	4.04	3.94	4.16	3.83	9.99	11.39 ^j
k_{NNO} (mdyn/Å)	0.645	0.576	0.593	0.658	0.643	0.41	0.49 ^j
ΔE_T^{bend} (eV) ^b	1.41	1.16	1.05	1.15	1.10
$\Delta E_T^{\text{contract}}$ (eV) ^c	1.00	1.42	1.41	1.38	1.40
ν_1 (cm ⁻¹) ^d	915	934	919	946	912	1223	1285 ⁱ
ν_2 (cm ⁻¹) ^d	535	524	537	563	555	524	589 ⁱ
ν_3 (cm ⁻¹) ^d	1660	1667	1672	1690	1666	2183	2224 ⁱ
ϵ (eV) ^d	0.196	0.195	0.195	0.199	0.195	0.245	0.254
μ (D)	3.03	2.78	2.67	2.52	2.42	0.157	0.166 ^k
A_μ (deg) ^e	97.2	98.5	95.1	95.5	93.3	180.0	...
E.A. (eV) ^f	0.20	-1.98	-1.80	-1.68	-1.74	...	0.22 ± 0.1 ^l
V.E.A. (eV) ^g	-2.38	-4.51	-4.21	-4.15	-4.18	...	-2.2 ^m

^aThe basis set is from Ref 36.^bEnergy rise upon bending from A_{NNO}^e to 180° at the computed equilibrium bond lengths.^cEnergy rise upon contraction of both bond lengths to the neutral experimental bond lengths at 180°.^dThe atomic masses used were $m_{\text{N}} = 14.00751$ and $m_{\text{O}} = 16.0000$.^eSee footnote d of table IV.^fAdiabatic electron affinity of $\text{N}_2\text{O}(X^1\Sigma^+)$, computed as $\text{E.A.}(\text{N}_2\text{O}) = E_T^0(\text{N}_2\text{O}) - E_T^0(\text{N}_2\text{O}^-) + \epsilon(\text{N}_2\text{O}) - \epsilon(\text{N}_2\text{O}^-)$. The SCF, MCSCF, and MCSCF/CI total energies for $\text{N}_2\text{O}(X^1\Sigma^+)$ at its experimental equilibrium geometry are -183.60187 a.u., -183.771558 a.u., and -183.781931 a.u., respectively.^gVertical electron affinity of $\text{N}_2\text{O}(X^1\Sigma^+)$ to the $1^2\Pi$ state of N_2O^- , computed as $\text{V.E.A.}(\text{N}_2\text{O}) = -[E_T(1^2\Pi) - E_T^0(X^2\Sigma^+)] + \epsilon(\text{N}_2\text{O}^-) - \epsilon(\text{N}_2\text{O})$ at the $\text{N}_2\text{O}(X^1\Sigma^+)$ experimental equilibrium geometry. The zero-point energy for $\text{N}_2\text{O}^-(1^1\Pi)$ is estimated to be that of N_2 , 0.146 eV, since $\text{N}_2\text{O}^-(1^1\Pi)$ is bound only with respect to the N-N coordinate.^hFrom Ref. 42.ⁱFrom Ref. 24.^jFrom Ref. 44.^kFrom Ref. 45.^lFrom the experimental section of the present work.^mThere is a broad, strong feature in the electron scattering results for N_2O which peaks at an electron energy of approximately 2.2-2.3 eV. See Ref. 47 and other works quoted therein.

corded for the $\text{N}_2\text{O}^-(X^2A')$ ion in Table VI are accurate to within about 100 cm⁻¹.

4. Dipole moment

The dipole moment μ at the equilibrium geometry is found to depend strongly upon the addition of correlating configurations. As shown in Table VI, the SCF value is 25% greater than the final 18 MC/98 CI value of 2.42 D. The direction angle A_μ for the position of the center of negative charge places it inside the bond angle A_{NNO}^e and adjacent to the N-O bond.

The MCSCF/CI dipole moment for $\text{N}_2\text{O}(X^1\Sigma^+)$ is 0.16 D with the oxygen atom negative.⁴² The experimental value is 0.17 D. On the basis of the 6% error in the neutral computation, the MCSCF/CI dipole moment for $\text{N}_2\text{O}^-(X^2A')$ is expected to be accurate to within ± 0.3 D.

The $\text{N}_2\text{O}^-(X^2A')$ dipole moment as a function of geometry is shown in Table V for the 18 MC/98 CI wavefunction. A positive (negative) entry for μ indicates that the polarity is $\text{N}_2\text{O}^-(\text{N}_2\text{O}^+)$. The angle A_μ is the angle subtended by $\bar{\mu}$ on the vector $(\bar{R}_{\text{N1}} - \bar{R}_{\text{N2}})$, where N1 is the terminal and N2 the central nitrogen atom. See Fig. 7. Notice that $A_\mu \leq A_{\text{NNO}}$.

5. Adiabatic and vertical electron affinities

As noted in Sec. III.B, the *ab initio* calculations reported upon here were performed only to a degree of sophistication which has proven sufficient for the reliable determination of equilibrium geometries and properties. The greater sophistication required to compute accurate electron affinities or dissociation energies was avoided for the present since these quantities have

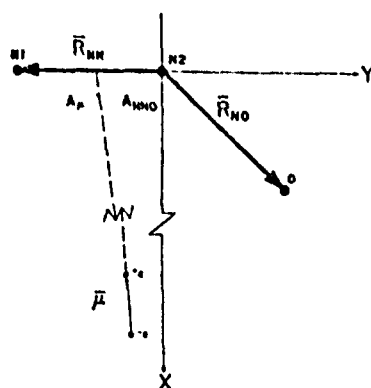


FIG. 7. Coordinant system and definition of the dipole direction angle A_μ .

been determined to within ± 0.1 eV from the collision-induced dissociation experiments reported in Sec. II. It is of interest, however, to compare the computed adiabatic electron affinity of $N_2O(X^1\Sigma^+)$ to the experimental result. From this comparison it is possible to document the degree to which the differential one-electron basis set sufficiency for $N_2O(X^1\Sigma^+)$ vs $N_2O^+(X^2A')$ is balanced by the differential wavefunction correlation energy. The degree of balancing is obtained here as a function of the extent of correlation for the fixed, $4s3p$, one-electron basis set. The dependence is shown in Table VI. For the SCF wavefunction the adiabatic electron affinity, after zero-point vibrational energies have been considered, is 0.20 eV. This value agrees very well with the experimental value of 0.22 ± 0.1 eV from Sec. II. This agreement at the SCF level is fortuitous. The value computed from the 18 MC/98 CI wavefunction is -1.74 eV, or about 2.0 eV below experiment. The agreement at the SCF level is, thus, the result of a cancellation of the correlation energy by the one-electron basis set truncation error.

The accidental agreement at the SCF level allows one to conclude that the 2.0 eV difference in the correlation energy recovered by the 18 MC/98 CI wavefunction for $N_2O^+(X^2A')$ and by the 19 MC/99 CI wavefunction for $N_2O(X^1\Sigma^+)$ is an indication of the insufficiency of the valence orbital space for the construction of correlated MCSCF/CI wavefunctions for the two systems. The two electron volt estimate is only indicative, rather

than predictive, of this differential valence space sufficiency since the correlation energy for these two particular ion and neutral states will probably not be equally affected by basis set improvements.

The vertical electron affinity of $N_2O(X^1\Sigma^+)$ to the $1^2\Pi$ state of N_2O^+ is computed to be -2.38 eV in the SCF and -4.18 eV in the 18 MC/98 CI calculations. Zero-point vibrational energies have been considered. See Table VI. From the above comparison of the adiabatic electron affinity to experiment it is seen that the error bracket for the present ($4s3p$ valence space) *ab initio* electron affinities is at least 2 eV.

6. Barriers to linearity and bond length contraction

The barrier to linearity at the optimized bond lengths, ΔE_T^{bend} , is given in Table VI for the SCF, 15 MC, 15 MC/98 CI, 18 MC, and 18 MC/98 CI wavefunctions. All of the correlated wavefunctions give a value of about 1.1 eV. The somewhat larger value given by use of the SCF wavefunction correlates with the location of the equilibrium SCF valence angle at several degrees below the correlated equilibrium angle.

The barrier to the contraction at 180° of the bond lengths from the equilibrium ion values (calculated) to the equilibrium neutral (experimental) values is also shown in Table VI for the various wavefunctions listed above. The value for the final correlated wavefunctions is about 1.4 eV. The SCF value is lower, which suggests that the correlation effects which are stabilizing at the relatively longer ion bond lengths are destabilizing at the neutral bond lengths.

It is interesting to note that the sum of the bending and contraction barriers, about 2.5 eV, is roughly independent of correlation in the wavefunction.

7. Initial consideration of polarization functions

A partial consideration of the effects of polarization functions upon the results reported above has been made. The $4s3p$ basis set was augmented with a full set of six Cartesian d functions with exponent 1.00. The MCSCF/CI results for N_2O^+ and N_2O at their respective equilibrium geometries are given in Table VII. The $4s3p1d$ basis set yields total energies which are several electron volts lower than their $4s3p$ counterparts. Not

TABLE VII. Effect of polarization functions on the adiabatic electron/affinity of N_2O and the dipole moments of N_2O^+ and N_2O .^a

Molecule (state)	Geometry (a.u., deg.)			$E_T + 183$ (a.u.)		ΔE_T (eV)	E.A. ^b (eV) basis		μ (D) ^c basis	
	R_{NN}	R_{NO}	A_{NNO}	Basis			$4s3p$	$4s3p1d$	$4s3p$	$4s3p1d$
				$4s3p$	$4s3p1d$					
$N_2O^+(X^2A')$	2.3045	2.6051	132.7	-0.715867	-0.782449	-1.81	2.12	2.481
$N_2O(X^1\Sigma^+)$	2.1320	2.2378	180.0	-0.781931	-0.88291	-2.75	-1.74	-2.68	0.157	0.051

^aFor $N_2O^+(X^2A')$, the 18 MC/98 CI wavefunction was used. For $N_2O(X^1\Sigma^+)$, the 19 MC/99 CI wavefunction was used. The d -function exponent was 1.00.

^bThe adiabatic electron affinity is computed as $E.A.(N_2O) = E_T(N_2O) - E_T(N_2O^+) + \epsilon(N_2O) - \epsilon(N_2O^+)$. The zero-point energies ϵ are given in Table VI.

^cIn all entries the polarity is N_2O^+ .

TABLE VIII. Bending potential curve and dipole moment function for $N_2O(X^1\Sigma^+)$.

A_{NNO} (deg)	SCF	E_T 183 (a.u.) 19 MC	19 MC/99 CI	$\mu(D)^c$ 18 MC/99 CI	A_{NNO} (deg)
180	-0.601871	-0.771588	-0.781931	0.157 ^d	180.0
175	-0.601373	-0.771118 ^b	-0.781457 ^b		
170	-0.599817	-0.769778	-0.779991	0.187	116.1
150	-0.580170	-0.751868	-0.761365	0.379	113.3
130	-0.531015	-0.701527	-0.710515	0.721	102.6
110	-0.455168	-0.591661	-0.601653	1.214	103.5
100		-0.551466	-0.566623	1.302	101.8
90	-0.415559	-0.559239	-0.572735	0.675	75.5
80		-0.539909	-0.553218	0.616	59.6
70		-0.486782	-0.502735	0.568	66.1

^aBasis set—4s3p Dunning, Ref. 36. Experimental bond lengths; Ref. 24. MCSCF wavefunction 19 MC-7410.

^bInterpolated.

^cSee footnote d of Table V.

^dThe experimental value is 0.166 D. See Ref. 45.

unexpectedly, there is a different lowering for the ionic surface (-1.81 eV) than for the neutral surface (-2.75 eV). It is interesting that it is the neutral for which polarization functions have the greater effect.

The MCSCF/CI 4s3p_{ad} adiabatic electron affinity, -2.68 eV, is 0.94 eV below the 4s3p MCSCF/CI result and 2.9 eV below the experimental value from Sec. II. This comparison shows that the valence orbital space is even less adequate for the correlation of the ion (versus the neutral) than suspected from the discussion of the 4s3p results in Sec. III. D. 5. It is apparent that a further optimization of the MC and CI configuration lists to include excitations to nonvalence virtuals would be at least if not more important than the inclusion of polarization functions in any attempt at a reliable *ab initio* calculations of the adiabatic electron affinity. However, the addition of *d* functions effects dipole moment changes which are less than the 0.3 D uncertainty assigned to the 4s3p results.

E. MCSCF/CI *ab initio* bending potential for $N_2O(X^1\Sigma^+)$

The bending potential curve for $N_2O(X^1\Sigma^+)$ from 180° to 70° was computed with the SCF, 19 MC, and 19 MC/99 CI wavefunctions for use in the next section. The bond lengths for these calculations were the experimental values. The results are presented in Table VIII and Fig. 8. The metastable minimum near 90° in the correlated wavefunctions is yet to be confirmed by calculations involving a reoptimization of the configuration lists at 90° . It probably is real and derives from an avoided adiabatic intersection with the $^1A'(1^1\Delta)$ surface. The dipole moment function $\mu(A_{NNO})$ is also reported in Table VIII.

IV. INTERSECTION LOCUS OF THE $N_2O(X^2A')$ AND $N_2O(X^1\Sigma^+)$ POTENTIAL ENERGY SURFACES

A. Hypersurface representation by a two-dimensional function $V(R_{AB}, A_{ABC})$

If one treats one bond length parametrically, the full dimensional potential energy hypersurface for a triatomic, $V(R_{AB}, R_{BC}, A_{ABC})$, can be represented by two

dimensional cuts $V(R_{AB}, A_{ABC}|R_{BC})$. If one relaxes the parametric dependence upon R_{BC} to an implicit dependence, then a two dimensional function $V(R_{AB}, A_{NNO})$ results. In the latter case R_{BC} assumes the equilibrium diatomic value at $R_{AB} = \infty$ but the equilibrium triatomic value R_{BC}^e at $R_{AB} = R_{AB}^e$. The bonds AB and BC can be treated interchangeably and comparisons made to establish the extent to which such a two dimensional treatment is valid. A possible functional form for $V(R_{AB}, A_{ABC})$ is

$$V(R_{AB}, A_{ABC}) = -2D_{AB}^e \exp[-\beta_{AB}^e(R_{AB} - R_{AB}^e)] f(A_{ABC}) + D_{AB}^e \exp[-2\beta_{AB}^e(R_{AB} - R_{AB}^e)] + D_{AB}^e + V_{scale}, \quad (19)$$

where $f(A_{ABC})$ is determined from the condition $f(A_{NNO}^e) = 1$ and a known bending potential function

$$g(A_{ABC}) = V(R_{AB}^e, R_{BC}^e, A_{ABC}) - V_{scale} \quad (20)$$

as

$$f(A_{ABC}) = 1 - [g(A_{ABC}) - g(A_{ABC}^e)] / [2D_{AB}^e]. \quad (21)$$

Rationalizations for the placement of the angular dependence in only the attractive term have been given previously.⁴⁶ The parameter V_{scale} is used to adjust the energy origin from zero at the hypersurface minimum as desired. The conditions

$$D_{AB}^0 = V(R_{AB} = \infty) - V_{scale} = D_{AB}^e, \quad (22a)$$

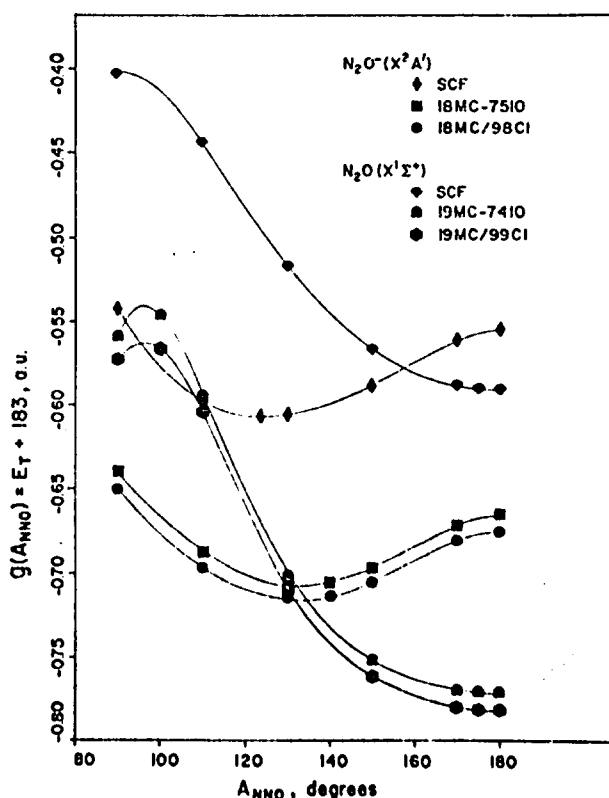


FIG. 8. MCSCF/CI, MCSCF, and SCF bending potential curves from 90° to 180° for $N_2O(X^2A')$ and $N_2O(X^1\Sigma^+)$. The ion bond lengths (R_{NN} , R_{NO}) in a.u. are (2.2745, 2.6011) for the SCF and (2.3045, 2.6061) for the correlated wavefunctions. The neutral bond lengths are the experimental equilibrium values.

$$0 = V(R_{AB}^e, R_{BC}^e, A_{ABC}^e) - V_{\text{scale}} = -2D_{AB}^a + D_{AB}^r + D_{AB}^d, \quad (22b)$$

$$0 = \left[\frac{\partial V(R_{AB}, R_{BC}, A_{ABC})}{\partial R_{AB}} \right]_e = 2(D_{AB}^a \beta_{AB}^a - D_{AB}^r \beta_{AB}^r), \quad (22c)$$

$$k_{AB} = \left[\frac{\partial^2 V(R_{AB}, R_{BC}, A_{ABC})}{\partial R_{AB}^2} \right]_e = -2D_{AB}^a \beta_{AB}^a + 4D_{AB}^r \beta_{AB}^r, \quad (22d)$$

$$V(R_{AB}^r, R_{BC}^e, A_{ABC}^e) - V(R_{AB}^e, R_{BC}^e, A_{ABC}^e) = -2D_{AB}^a \{\exp[-\beta_{AB}^a(R_{AB}^r - R_{AB}^e)] - 1\} + D_{AB}^r \{\exp[-2\beta_{AB}^r(R_{AB}^r - R_{AB}^e)] - 1\} \quad (22e)$$

can be used to determine the values of the parameters D_{AB}^a [Eq. (22a)], D_{AB}^r [to satisfy Eq. (22c)], D_{AB}^d [Eq. (22b)], and β_{AB}^a and β_{AB}^r [from Eqs. (22c) and (22d)] so as to establish the desired surface features. These features are the potential binding energy D_{AB}^a , the stretching force constant k_{AB} , the equilibrium geometry ($R_{AB}^e, R_{BC}^e, A_{ABC}^e$), the bending potential function $g(A_{ABC})$ at $R_{AB} = R_{AB}^e$ and $R_{BC} = R_{BC}^e$, and the value of the potential energy at a point ($R_{AB}^r, R_{BC}^e, A_{ABC}^e$) with respect to the value at the equilibrium geometry. The distance R_{AB}^r should be considerably less than R_{AB}^e in order to improve the representation of the repulsive region. If Condition (22e) is replaced by the assumption that $D_{AB}^r = D_{AB}^d$, then D_{AB}^r becomes $D_{AB}^d = D_{AB}^0$ and β_{AB}^r becomes equivalent to β_{AB}^a with the result that $V(R_{AB}, A_{ABC}^e)$ becomes a Morse function in R_{AB} .

With the latter assumption, all of the features required to parameterize Eq. (19) for the ground state energy surface of either N₂O⁺ or N₂O are available from the results presented in Secs. II and III along with some literature values for N₂O. Either bond length, AB=NN or AB=NO, can be treated. The value of the scaling parameter V_{scale} may be set to zero for N₂O⁺ and determined for N₂O from the adiabatic electron affinity (from Sec. II) and the zero-point energies (from Sec. III).

B. Harmonic Morse representations

Wentworth, Chen, and Freeman⁸ proposed the assumptions that $g(A_{ABC})$ is the harmonic bending potential

$$g_H(A_{ABC}) = \frac{1}{2} k_{ABC} (A_{ABC} - A_{ABC}^e)^2, \quad (23)$$

and that $D_{AB}^r = D_{AB}^d$ in Eq. (19). They wrote one such resulting harmonic Morse representation $V_{HM}(R_{AB}, A_{ABC})$, AB=NO, for N₂O and one for N₂O⁺. The parameters were determined for N₂O from literature values and for N₂O⁺ by a series of admittedly crude assumptions. However, k_{NNO} for N₂O⁺ in Eq. (23) was treated as a calibration parameter. Its value was determined from the requirement that the lowest energy crossing point $V(R_{NO}^*, A_{NNO}^*)$ of the neutral and negative surfaces occur at an energy 0.45 ± 0.02 eV above the zero-point energy of N₂O. The latter energy is the activation energy which they obtained from their measurement of the rate of Reaction (3) as a function of temperature over the range -66 to 215 °C. The objective of Wentworth, Chen, and Freeman was the

estimation of the adiabatic electron affinity. However, it is interesting to note for later comparison that they reported a value of 160° for A_{NNO}^* .

The results of the present study may be used to establish all of the parameters in the harmonic Morse function without any assumptions or calibrations to reaction thresholds. The minimum energy crossing locus (R_{NO}^*, A_{NNO}^*) and its activation energy with respect to N₂O⁺(0, 0, 0) may, thus, be predicted. Comparisons with the experimental activation energy and the vertical electron affinity will serve to check the appropriateness of the harmonic Morse functional form. The values for the parameters are given in Table IX. The minimum energy surface intersection is shown in the harmonic section of Table X for the SCF, 18 MC, and 18 MC/98 CI N₂O⁺ wavefunctions. The vertical surface separation at the N₂O equilibrium geometry is also listed in Table X. The latter energy quantity is some 7.0–9.8 eV. The *ab initio* vertical excitation (resonance) energy for N₂O⁺(1²Π) above N₂O(X¹Σ⁺) is 2.3–3.9 eV, depending upon the degree of wavefunction correlation. See Table VI. The main source of this rather large discrepancy is the assumption of a harmonic bending potential. This source of error can be removed by replacing Eq. (23) with an anharmonic representation of $g(A_{ABC})$. A direct way of providing the anharmonic potential is taken in the next subsection. It is noted that the crossing angle A_{NNO}^* is about 6° below the value reported by Wentworth, Chen, and Freeman.⁸

C. Anharmonic Morse representations

The shape of the anharmonic bending potential, $g_A(A_{ABC}) - g_A(A_{ABC}^e)$, is reliably given if

$$g_A(A_{ABC}) = \sum_{i=1}^n C_i A_{ABC}^{i-1}, \quad (24)$$

where the expansion coefficients C_i are determined by an exact-matching fit of Eq. (24) to *n ab initio* potential energy surface points $V(R_{AB}^e, R_{BC}^e, A_{ABC})$. The *n* values of A_{ABC}^e are chosen in this study to span the range 90°–180°. Wherever necessary a point at 175° is included to ensure that $g_A'(180°) = 0$.

The bending potential energy curves for N₂O⁺(X²A') and N₂O(X¹Σ⁺) are shown in Fig. 8 for selected SCF, MCSCF, and MCSCF/CI wavefunctions. Note that only the shape of these curves enters into Eq. (21) and, thence, their placement on the energy scale does not. The anharmonic Morse representation $V_{AM}(R_{AB}, A_{ABC})$ is, then, Eq. (19) with the approximation that $D_{AC}^r = D_{AB}^r$ and with $f(A_{ABC})$ given by Eqs. (21) and (24).

The anharmonic section of Table X displays the results obtained with $V_{AM}(R_{AB}, A_{ABC})$. For AB=NO, the separation of the N₂O and N₂O⁺ surfaces at the equilibrium geometry (R_{ABC}^e, A_{ABC}^e) of the former is lowered to 3.8–4.8 eV, which slightly overlaps the 2.3–3.9 eV *ab initio* range given in Table VI. Thus, the anharmonic modification is a necessary improvement which greatly increases the faithfulness with which the shape of *ab initio* potential surface is represented.

TABLE IX. Parameters for the angular-dependent Morse function $V_M(R_{AB}, A_{ABC})$.

Parameter ^{a-c}	Units	Molecule (state)			
		N ₂ O($X^1\Sigma^+$) ^d (Exptl)	SCF	N ₂ O(X^2A') ^e MCSCF (18 MC)	MCSCF/CI (18 MC/98 CI)
D_{NN-O}^0	eV	3.758	0.480	0.483	0.479
β_{NO}	\AA^{-1}	3.076	5.055	5.183	4.993
R_{NO}^0	\AA	1.1842	1.3764	1.3739	1.3747
k_{NNO}	eV/deg ²	0.001245	0.002062	0.002101	0.002051
A_{NNO}^0	deg	180.0	123.6	132.7	132.7
V_{scale}	eV	0.16	0.00	0.00	0.00
D_{N-NO}^0	eV	5.066	5.157	5.160	5.156
β_{NN}	\AA^{-1}	3.3188	2.643	2.669	2.637
R_{NN}^0	\AA	1.1282	1.2036	1.2197	1.2216

^a $D_{AB-C}^0 = D_{AB-C} + \epsilon_{ABC} - \epsilon_{AB}$, where D_{AB-C} is the experimental dissociation energy and the ϵ are the zero-point vibrational energies whose value in eV are 0.251 (N₂O), 0.195–0.199 (N₂O⁺), 0.146 (N₂), 0.118 (NO), and 0.169 (NO⁺). See Ref. 21.

^b $\beta_{AB} = 1.76655 (k_{AB}/D_{AB}^0)^{1/2}$, where k_{AB} is in mdyn/ \AA and D_{AB}^0 is in eV to give β_{AB} in \AA^{-1} .

^c $V_{scale} = E.A.(N_2O) - \epsilon(N_2O) + \epsilon(N_2O^+)$ positions the potential minimum of the neutral surface with respect to the negative.

^dThe experimental quantities required to compute these parameters are listed and referenced in Table VI.

^eComputed from the results presented in Tables I and VI.

Further improvement can be made by removing the assumption that $D_{AB}^0 = D_{AB}^+$. The most important result of this improvement would be the treatment of the repulsive portion of $V(R_{AB}, A_{ABC})$ for AB=NO. This can

be seen as follows. The anharmonic Morse function for AB=NN places the vertical excitation energy at 1.6 eV. See Table X. This result is in better agreement with the more reliable, lower end of the *ab initio*

TABLE X. Minimum potential energy crossing point $V^*(R_{NN}^*, R_{NO}^*, A_{NNO}^*)$ and equilibrium geometry vertical surface separations for the ground state energy surfaces of N₂O and N₂O⁺ as given by various angular-dependent Morse functions $V(R_{AB}, A_{NNO})$.^a

Character of the angular dependence	Minimum in the intersection locus					Surface separation $V(N_2O^+) - V(N_2O)$ eV at the equilibrium geometry	
	AB	Wave function ^b	V^* (eV)	R_{AB}^* (\AA)	A_{NNO}^* (deg)	N ₂ O ⁺	N ₂ O
Harmonic	NO	SCF	0.9629	1.295	146.8	-2.01	9.80
		MCSCF	0.7881	1.282	151.7	-1.68	7.47
		MCSCF/CI	0.7749	1.279	151.7	-1.68	7.00
	NN	SCF	0.7681	1.175	149.3	-1.95	4.09
		MCSCF	0.6265	1.175	151.1	-1.54	3.23
		MCSCF/CI	0.6221	1.176	151.2	-1.51	3.18
Anharmonic	NO	SCF	0.9110	1.310	152.6	-2.35	4.85
		MCSCF	0.7491	1.286	153.0	-1.81	4.25
		MCSCF/CI	0.7536	1.284	153.1	-1.82	3.89
	NN	SCF	0.6991	1.180	153.7	-2.44	1.81
		MCSCF	0.5795	1.178	155.3	-1.72	1.69
		MCSCF/CI	0.5911	1.179	155.6	-1.71	1.64

^aSee Eqs. (19)–(21) and (23) and, for the anharmonic only, Eq. (21) as well.

^bThe neutral surface is determined completely from the experimental quantities in the harmonic Morse representation. In the anharmonic Morse representation the *ab initio* bending potential replaces the harmonic for both neutral and the ion. All of the parameters for the ion surface are determined from the experimental and theoretical surface features reported in Secs. II and III of this paper. See Table VI. The neutral geometry at equilibrium is experimental. The ion geometry and potential parameters are computed and vary with the wavefunction employed.

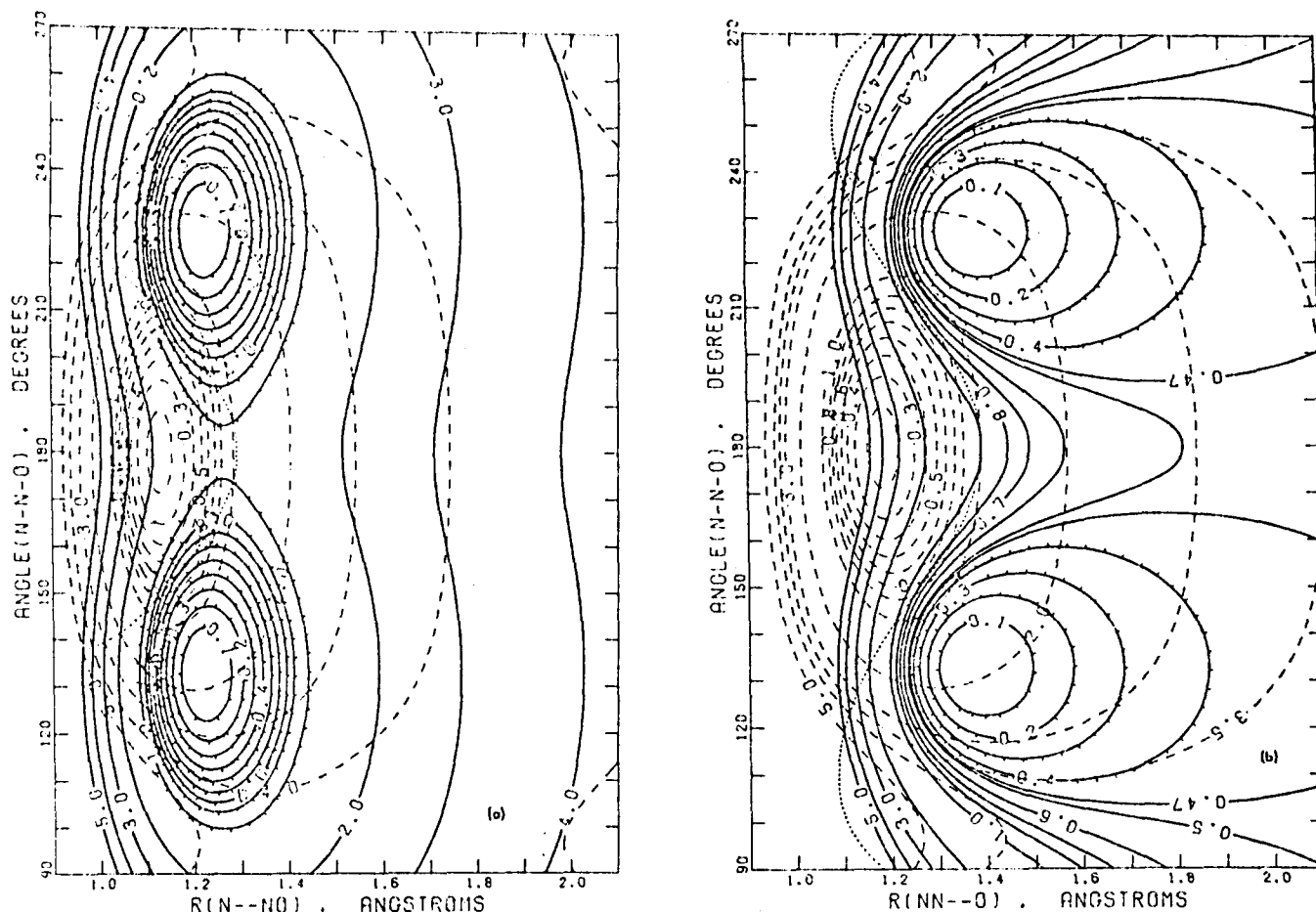


FIG. 9. Overlaid $\text{N}_2\text{O}^+(\text{X}^2\text{A}')$ and $\text{N}_2\text{O}(\text{X}^1\Sigma^+)$ contour plots of the angular dependent Morse function $V_M(R_{AB}, A_{\text{NNO}})$ with the *ab initio* MCSCF/CI bending potential energy curves. The intersection locus of the ionic surface (shown as solid contours) with the neutral surface (shown as long-dashed contours) is illustrated by the short-dashed line. The surface contours are identified in electron volts with respect to the minimum in the negative surface. The neutral surface is positioned in accordance to the adiabatic electron affinity and zero-point energies. (a) $R_{AB} = R_{\text{NN}}$; (b) $R_{AB} = R_{\text{NO}}$.

viewing the N_2O^+ plots one should keep in mind that near linearity there may be an avoided intersection between the $1^2\Sigma^+(\text{X}^2\text{A}')$ Rydberg state and the $2^2\text{A}'(1^2\Pi)$ valence state.⁴² The solid contours represent the $2^2\text{A}'$ ion surface with valence character even near 180° . Thus, it is the diabatic, valencelike $2^2\text{A}'$ surface that is being represented. In viewing the plot for N_2O in Fig. 9(b) one should note that although the surface is drawn for adiabatic dissociation to the asymptote $\text{O}(^1\text{D})$, $\text{N}_2(\text{X}^1\Sigma^+)$, the molecule is predissociated to the ground state asymptote $\text{O}(^3\text{P})$, $\text{N}_2(\text{X}^1\Sigma^+)$ by repulsive triplet surfaces. However, as shown elsewhere, the singlet-triplet surface intersection occurs outside of the present plot range at $R_{\text{NO}} \approx 3.1 \text{ \AA}$.⁴² A similar situation exists for the N-N bond for N_2O .

The various collisional processes which involve the N_2O^+ and N_2O ground state surfaces may be readily visualized from these overlaid contour plots. The plots clearly show the great disparity in the location of the minimum regions and the potential barriers between them. A comparison of Figs. 9(a) and 9(b) shows the strong difference between the weak $\text{N}_2\text{-O}^+$ bond vs the strong N-NO bond.

V. SUMMARY AND DISCUSSION

A. Final results

A summary of the final results from Secs. II, III, and IV is made in Table XI. These combined results constitute a detailed characterization of the $\text{N}_2\text{O}^+(\text{X}^2\text{A}')$ potential energy surface and its relationship to that of $\text{N}_2\text{C}(\text{X}^1\Sigma^+)$. Further explanation of the values entered is unnecessary except for the vertical electron affinity. This explanation is given below. A discussion of several of the quantities entered in Table XI in the context of the literature is in order. Discussion is given for the adiabatic and vertical electron affinities of nitrous oxide and for the role that surface effects play in Reactions (1) and (3).

B. Electron affinities of nitrous oxide

1. Adiabatic

The adiabatic electron affinity of the N_2O molecule in its ground electronic state has been determined experimentally by various groups using different techniques. A tabulation of these studies is made in Table

TABLE XI. Summary of the quantities determined in the present study to characterize the $X^2A'(^2\Pi)$ ground state potential energy surface of N_2O^+ and to relate it to the $X^1\Sigma^+$ energy surface of N_2O .

Parameters	Value	Section
$N_2O^+(X^2A')$ hypersurface characteristics		
$D(N_2-O^+)$	0.43 ± 0.1 eV	II
$D(N-NO^+)$	5.13 ± 0.1 eV	II
R_{NN}^e	1.222 ± 0.05 Å	III
R_{NO}^e	1.375 ± 0.10 Å	III
A_{NNO}^e	132.7 ± 2 deg	III
k_{NN}	11.49 ± 0.8 mdyne/Å	III
k_{NO}	3.83 ± 0.8 mdyne/Å	III
k_{NNO}	0.64 ± 0.2 mdyne/Å	III
ν_1	912 ± 100 cm ⁻¹	III
ν_2	555 ± 100 cm ⁻¹	III
ν_3	1666 ± 100 cm ⁻¹	III
$\epsilon(N_2O^+)$	0.195 ± 0.02 eV	III
μ	2.42 ± 0.3 D	III
ΔE_T^{bead} (barrier to linearity at R_{NN}^e, R_{NO}^e)	1.10 eV	III
$\Delta E_T^{\text{contract}}$ (barrier to bond length contraction to the neutral values at 180°)	1.40 eV	III
Electron affinities		
E. A. (N_2O)	0.22 ± 0.1 eV	II
V. E. A. (N_2O)	-2.23 ± 0.2 eV	II and III as combined in V
Minimum energy point in the crossing locus of the neutral and ion ground state hypersurfaces		
$V^* - V^e(N_2O^+)$	0.67 ± 0.1 eV	IV
R_{NN}^*	1.18 ± 0.05 Å	IV
R_{NO}^*	1.28 ± 0.10 Å	IV
A_{NNO}^*	154 ± 3 deg	IV
Reaction thresholds		
E_a [Reaction (3)]	0.40 ± 0.1 eV	IV
E_a [Reaction (3)]	0.21 ± 0.1 eV	IV

XII. That the adiabatic electron affinity might be positive while the vertical electron affinity remained negative was suggested in 1967 by Ferguson, Fehsenfeld, and Schmeltekopf.⁴ Bardsley⁷ concurred in his molecular orbital analysis in 1969. In 1971 Wentworth, Chen, and Freeman reported a value of 0.3 ± 0.2 eV which they deduced from a thermal electron attachment rate experiment. Nalley *et al.*⁹ subsequently reported a lower bound for the electron affinity of -0.15 ± 0.1 eV from their cesium collisional ionization experiments in 1973. Tiernan and Clow¹⁰ reported E. A. (N_2O) = 0.6 eV on the basis of collisional-induced dissociation experi-

ments, but they made no correction of the data to take into account the velocity distributions of the ion beam and the target gas. The present collision-induced dissociation result of 0.22 ± 0.1 eV, which is based upon data which have been corrected for the ion and neutral velocity distributions, is perhaps the most reliable measurement reported to date.

The estimate of the adiabatic electron affinity reported by Wentworth, Chen, and Freeman⁸ is in good agreement with the determination reported here, but it appears that this agreement may be fortuitous. Wentworth *et al.* made their estimate from the difference in the potential minima of the harmonic Morse function discussed in Sec. IV as parametrized for N_2O and N_2O^+ . This parameterization was based in part on experimental information but involves some gross assumptions. These assumptions—e.g., the value of $D(N_2-O^+)$, the harmonic form of $g(A_{NNO})$, and the value of $R_{NO}^e(N_2O^+)$ —are shown by the present study to be markedly incorrect.

As noted in Sec. III, the theoretical calculations were not performed at the level of sophistication necessary to produce accurate adiabatic electron affinities. The good agreement at the SCF level is happenstance. An error bracket of ~ 3 eV is assigned to the present ($4s^2p$ valence space) *ab initio* adiabatic electron affinity on the basis of the 0.2 ± 0.1 eV experimental value.

2. Vertical

The vertical electron affinity (resonance energy) for $N_2O(X^1\Sigma^+)$ going to the $^2A'(1^2\Pi)$ state can be reliably obtained from combining the experimental and theoretical results of the present paper with the following computational cycle:

$$\begin{aligned} \text{V. E. A. } (X^1\Sigma^+ - 1^2\Pi) \\ = \text{E. A. } (N_2O) - \epsilon(X^1\Sigma^+) + \epsilon(X^2A') \\ - \Delta E_T^{\text{bead}} - \Delta E_T^{\text{contract}} + \epsilon(X^1\Sigma^+) - \epsilon(1^2\Pi). \end{aligned} \quad (29)$$

This cycle may be expected to yield a reliable result since it is written so as to depend upon those areas of the present study which have been established to be of predictive quality—*ab initio* surface shape features in the interactive, triatomic region and the experimental adiabatic electron affinity. All of the quantities needed to evaluate Eq. (29) are listed in Table X, except for $\epsilon(N_2O)$, which is 0.254 eV (Ref. 24), and $\epsilon(1^2\Pi)$, which may be estimated, for reasons given earlier, as that of nitrogen, 0.146 eV. The resulting vertical electron affinity is

$$\text{V. E. A. } (X^1\Sigma^+ - 1^2\Pi) = -2.23 \pm 0.2 \text{ eV}. \quad (30)$$

This value is to be compared with the broad experimental electron scattering feature centered at about 2.2 eV. See Zecca *et al.*¹⁷

Comparison can also be made to the vertical electron affinity to the $1^2\Sigma^+$ state of the negative ion V. E. A. ($X^1\Sigma^+ - 1^2\Sigma^+$). An MCSCF/CI calculation of the V. E. A. ($X^1\Sigma^+ - 1^2\Sigma^+$) as -1.8 ± 0.5 eV by Hopper *et al.*

TABLE XII. Adiabatic electron affinity of $N_2O(X^1\Sigma^+)$.

Paper	Electron affinity (eV)	Method
Wentworth, Chen, Freeman (1971) ^a	0.3 ± 0.2	Deduced from the activation energy for thermal electron attachment rate
Nalley <i>et al.</i> (1973) ^b	$> -0.15 \pm 0.1$	Collisional ionization of Cs
Tiernan and Clow (1975) ^c	0.6	Linear extrapolation of collision-induced dissociation cross section
Present work	0.22 ± 0.1	Section II—Levine model fit to collision-induced cross section with corrections for Doppler motion of target gas and for ion velocity speed
	0.20	Section III— <i>ab initio</i> SCF calculations with a $1s3p$ orbital expansion basis. The good agreement is happenstance.
	> -1.7	Section III— <i>ab initio</i> MCSCF/CI calculations with a $1s3p$ orbital basis and restriction of correlating configurations to those constructable from the valence space. This is a lower limit; see text.

^aReference 8.^bReference 9.^cReference 10.

*al.*⁴² is probably reliable since it included a diffuse s basis function to describe the Rydberg character of the 8σ orbital in $N_2O^-(X^2\Sigma^+)$ and since differential correlation effects to the 3π orbital play no significant role as they do for $V.E.A. (X^1\Sigma^+ - 1^2\Pi)$. Thus, the broad resonance in the electron scattering spectrum centered near 2.2 eV can probably be attributed to both the valence $1^2\Pi$ and the Rydberg $1^2\Sigma^+$ molecular ion resonance states.

C. Threshold for the $e + N_2O$ dissociative attachment reaction

The activation energy predicted from the present study for the dissociative attachment Reaction (3) is 0.40 ± 0.1 eV. This value is in agreement with the experimental value of 0.45 ± 0.02 eV obtained by Wentworth, Chen, and Freeman⁸ by a least-squares fitting of the rate expression $K = AT^{-3/2} \exp(-E_a/kT)$ to their rate-temperature data for Reaction (3) over the range -36 to 215°C . The location reported in this paper for the minimum intersection energy at $25 \pm 3^\circ$ from linearity requires that, in the harmonic approximation, the bending mode ν_2 in N_2O be excited to at least the $\nu_2 = 4$ state. The energy required for the latter excitation, 0.40 eV, may be just sufficient for reaction to proceed. However, given the extended values of both bond lengths at the minimum intersection energy (see Table XI), it is likely that excitation of the symmetric stretch mode would greatly facilitate reaction.

D. Implications of the potential energy surfaces for the kinetics of the $O^- + N_2$ associative detachment reaction

There is at present a controversy concerning the reactivity of O^- with N_2 . Comer and Schulz¹⁸ impacted an O^- ion beam onto nitrogen gas in such a manner that the effective interaction region was 0.5 mm in diameter. They determined the cross section as a function of the relative collision energy from 0.32 ± 0.5 to 14.7 ± 0.5 eV by following the detached electron intensity. The cross section scale was calibrated against the $O^- + CO$ results of McFarland *et al.*¹⁹ From their results the cross section falls from 0.62 \AA^2 at 0.32 ± 0.5 eV to a

minimum of 0.10 \AA^2 at 2.0 ± 0.5 eV before beginning a monotonic rise to 1.52 \AA^2 at 14.7 ± 0.5 eV. Comer and Schulz report no observable reactivity at thermal collision energies. Thus, the cross section is expected to rise from zero to a peak located at a collision energy between 0.03 and 0.32 eV. Their cross section at 0.32 eV corresponds to a rate coefficient of $1.5 \times 10^{-11} \text{ cm}^3 \text{ s}^{-1}$.

Lindinger *et al.*⁵⁰ performed a flow-drift experiment in which they followed an effective rate constant for O^- depletion as a function of the N_2 concentration in the ion drift region of their flow tube. Their effective rate constant is averaged over internal energy distributions but not over the relative collision energy. They report no observable reaction for relative collision energies from about 0.03 eV to about 1 eV. From this observation they suggest that the reaction rate for the entire range is less than $10^{-12} \text{ cm}^3 \text{ s}^{-1}$. Lindinger *et al.* attempted to reconcile their results with those of Comer and Schulz¹⁸ by folding the latter authors' cross section into a displaced Maxwellian distribution applicable to the field-drift environment. The assumption was made that the Comer and Schulz cross section was zero below 0.32 eV. The resulting effective rate coefficient, $7 \times 10^{-12} \text{ cm}^3 \text{ s}^{-1}$ for relative drift energies of 0.5–1 eV, was taken by Lindinger *et al.* to indicate that the two experiments are irreconcilable.

From the present paper the energy threshold to Reaction (1) is established as 0.21 ± 0.1 eV. This result implies a very, very low thermal rate coefficient as reported both by Comer and Schulz¹⁸ and by Lindinger *et al.*⁵⁰ The magnitude of the predicted threshold and the restricted region of the minimum energy in the intersection locus of the ground state surfaces [see Table XI and Figs. 9(a) and 9(b)] are in accord with the observation of reactivity and an inverse temperature dependence of that reactivity from 0.32 to 2.0 eV. However, the present results also strongly suggest that reagent N_2 must be vibrationally excited to at least the first vibrational state for reaction to proceed for collision energies below several eV. This last conclusion follows from the value of R_{NN}^* being definitely greater than that of the outer classical turning point of $N_2(v$

$=0$) but approximately equal to that of $N_2(\nu=1)$. Also, the statistically favored collision angle is 90° and, as illustrated in Fig. 9(b), a collision energy of about 5 eV is required to reach the crossing locus at this angle. The crossing locus is less than 1 eV above the reagents only for angles greater than about 140° . This situation may be aptly termed a dynamic hindrance to Reaction (1) and because of it translational excitation is not expected to promote reactivity for thermal N_2 . This dynamic hindrance suggested by the potential surface studies of the present paper is in accord with the lack of reactivity for thermal N_2 for relative energies up to 1 eV or well above the energy threshold to Reaction (1). The present results also indicate that the results of Comer and Schulz could be explained if some N_2 vibrational excitation is effected in their experiment by collisions of the electrons being released in the collision cell of their apparatus.

VI. CONCLUSION

The potential energy surface of the $X^2A'(1^2\Pi)$ state of N_2O^+ is stable in its equilibrium region with respect to either dissociation or detachment. This conclusion is supported by both the experimental and the theoretical studies which have been described in this report. The quantities required to characterize this surface and to relate it to the neutral ground state surface have been determined and are summarized in Table XI.

An experimental value of 0.22 ± 0.1 eV is established for the adiabatic electron affinity of N_2O . It is concluded from this study that it is an electron correlation effect which causes the adiabatic electron affinity to be positive. In the *ab initio* calculations reported here the augmentation of the one-electron basis set with neither diffuse *s* and *p* functions nor polarization *d* functions significantly improves the *ab initio* adiabatic electron affinity value. In fact, the discrepancy with the experimental value becomes greater with some of these basis set augmentations. The truncation of the orbital basis to the valence shell is, thus, primarily responsible for the large, negative theoretical adiabatic electron affinity. Work is currently underway to test this conclusion by including nonvalence orbitals in the orbital basis from which correlating configurations are constructed.

A presentation and discussion of the potential energy surfaces of the $X^2A'(1^2\Pi)$ and $X^1\Sigma^+(1^1A')$ states of N_2O^+ and N_2O , respectively, shows why the associative detachment Reaction (1) is immeasurably slow for thermal N_2 . First, there is a potential barrier of some 0.21 eV that the reagents $O(^2P) + N_2(X^1\Sigma_g^+)$ must overcome to reach the minimum energy intersection locus. Secondly, given the threshold energy, the collisions are subject to a dynamic hindrance: only those which approach the minimum energy intersection locus with $A_{NNO} = 154^\circ$ and expanding while $R_{NO} = 1.28$ contracting can react. The X^2A' energy minimum with $A_{NNO} = 132.7^\circ$ tends to cause A_{NNO} to be contracting or R_{NO} expanding as O^+ approaches N_2 near the minimum in the intersection locus. More importantly, collision at an angle of 154° is statistically much less likely than

collision at 90° where the barrier to reaction is several electron volts. And, lastly, given threshold energy and a collision angle $A_{NNO} = 154^\circ$, the extended value of R_{NN}^* suggests that vibrational excitation of reagent N_2 will be necessary to reaction.

That Reaction (2) is slow at thermal energies is at least partially understandable in terms of the limited angular range $110^\circ - 160^\circ$ over which short-range attractive forces exist between O^+ and N_2 . See Fig. 9(b). The probability of ensnarlment of the N_2O^+ potential well long enough for collisional stabilization is also low owing to the remarkably low N_2-O^+ dissociation energy.

Reaction (3), unlike Reactions (1) and (2), is not subject to a dynamic hindrance. The N_2O molecule must be at least in the (0, 4, 0) vibrational state in order that the outer turning points reach the critical geometry (R_{NN}^* , R_{NO}^* , A_{NNO}^*). The threshold energy, however, is sufficient to populate N_2O vibrational levels up to and including (0, 6, 0), (1, 5, 0), (2, 4, 0), and (0, 4, 1). Because the N_2O outer turning point nuclear separations for $\nu_1 = \nu_3 = 0$ only just reach the critical bond lengths, levels with ν_1 or $\nu_3 \geq 1$ may be expected to be the most reactive.

ACKNOWLEDGMENTS

Doctor R. P. Hosteny and Doctor P. J. Fortune assisted in the establishment of a CDC 6600 version of BISON-MC and its associated codes. Dr. A. Hinds provided much helpful information on the use of the IBM version of BISON-MC. The *ab initio* calculations reported here were performed mostly on the CDC 6600 computer at Wright-Patterson AFB. The remainder were performed on the IBM 360/195 at Argonne or the IBM 370/155 at Wright-Patterson AFB. We thank the Applied Mathematics Division, Argonne National Laboratory, and the ASD Computer Center, Wright-Patterson AFB, for the computer resources which they made available to us for this study.

*Research supported in part by the Air Force Office of Scientific Research under Contract F44620-76-C-007 with Wright State University and Contract P7510A with Argonne National Laboratory (U.S.E.R.D.A.) and supported in part by the Aerospace Research Laboratories, Wright-Patterson AFB, under Contracts F33615-72-M-5015 and MIPRS9947400117 with Argonne National Laboratory (U.S.E.R.D.A.).

¹J. F. Paulson, *Adv. Chem. Ser.* **58**, 28 (1966).

²F. C. Fehsenfeld, E. E. Ferguson, and A. L. Schmeltekopf, *J. Chem. Phys.* **45**, 1844 (1966).

³F. Kaufman, *J. Chem. Phys.* **46**, 2449 (1967).

⁴E. E. Ferguson, F. C. Fehsenfeld, and A. L. Schmeltekopf, *J. Chem. Phys.* **47**, 3085 (1967).

⁵J. L. Moruzzi, J. W. Ekin, and A. V. Phelps, *J. Chem. Phys.* **48**, 3070 (1968).

⁶P. J. Chantry, *J. Chem. Phys.* **51**, 3380 (1969).

⁷J. N. Bardsley, *J. Chem. Phys.* **51**, 3384 (1969).

⁸W. E. Wentworth, E. Chen, and R. Freeman, *J. Chem. Phys.* **55**, 2075 (1971).

⁹S. J. Nalley, R. N. Compton, H. C. Schweinler, and V. E. Anderson, *J. Chem. Phys.* **59**, 4125 (1973).

¹⁰T. O. Tiernan and R. P. Clow, *Adv. Mass. Spectrom.* **6**, 295 (1974).

- ¹¹J. Comer and G. J. Schulz, *Phys. Rev. A* **10**, 2100 (1974).
- ¹²M. Krauss, D. G. Hopper, P. J. Fortune, A. C. Wahl, and T. O. Tiernan, "Potential Energy Surfaces for Air Triatomics. Volume I. Literature Review," ARL (AFSC) Tech. Rep. 75-0202, Vol. I, June 1975. Available from NTIS, Springfield, VA 22161.
- ¹³W. Lindinger, D. L. Albritton, F. C. Fehsenfeld, and E. E. Ferguson, *J. Chem. Phys.* **63**, 3238 (1975).
- ¹⁴T. O. Tiernan and R. E. Marcotte, *J. Chem. Phys.* **3**, 2107 (1970).
- ¹⁵B. M. Hughes and T. O. Tiernan, *J. Chem. Phys.* **55**, 3419 (1971).
- ¹⁶T. O. Tiernan, in *Interaction Between Ions and Molecules*, edited by P. Ausloos (Plenum, New York, 1974), pp. 601-604.
- ¹⁷The value of 63 \AA^2 has been deduced from the thermal rate constant of $1.2 \times 10^{-9} \text{ cm}^3 \text{ s}^{-1}$ reported in Ref. 1 from the equation $k = \bar{v} \bar{\sigma}$. The $^{16}\text{O}^+$ velocity was computed as $\bar{v} = (2E/m)^{1/2}$ at $E = 0.3 \text{ eV}$ (LAB).
- ¹⁸C. Rebick and R. D. Levine, *J. Chem. Phys.* **58**, 3912 (1973).
- ¹⁹W. B. Maier II, *J. Chem. Phys.* **41**, 2174 (1964).
- ²⁰W. B. Maier II, *J. Chem. Phys.* **42**, 1790 (1965).
- ²¹E. K. Parks, A. F. Wagner, and S. Wexler, *J. Chem. Phys.* **58**, 5502 (1973).
- ²²T. O. Tiernan and R. L. C. Wu, *J. Chem. Phys.* (to be submitted).
- ²³The conversion $E(\text{LAB}) = cE(\text{COM})$, $c = (m_i + m_m)/m_m$, effects the result $A_{\text{LAB}} = c^{-1}A$. See Ref. 22 for details.
- ²⁴G. Herzberg, *Electronic Spectra and Electronic Structure of Polyatomic Molecules* (Van Nostrand Reinhold, New York, 1966).
- ²⁵R. S. Berry, *Chem. Rev.* **69**, 533 (1969).
- ²⁶R. Celotta, R. Bennett, J. Hall, M. W. Siegel, and J. Levine, *Bull. Am. Phys. Soc.* **15**, 1515 (1970).
- ²⁷G. Das and A. C. Wahl, "BISON-MC: A FORTRAN Computing System for Multiconfiguration Self-Consistent-Field (MCSCF) Calculations on Atoms, Diatoms, and Polyatoms," Argonne National Laboratory, Tech. Rep. ANL-7955, 1972. Available from NTIS, Springfield, VA 22161.
- ²⁸G. Das and A. C. Wahl, *J. Chem. Phys.* **56**, 1769, 3532 (1972).
- ²⁹A. Karo, M. Krauss, and A. C. Wahl, *Int. J. Quantum Chem.* **7S**, 143 (1973).
- ³⁰D. G. Hopper, *Chem. Phys. Lett.* **31**, 446 (1975).
- ³¹P. J. Fortune, D. G. Hopper, B. J. Rosenberg, W. B. England, G. Das, A. C. Wahl, and T. O. Tiernan, "Potential Energy Surfaces for Air Triatomics. Volume II. Results of SCF and Preliminary OVC Calculations," ARL (AFSC) Tech. Rep. 75-0202, Vol. II, June 1975. Available from NTIS, Springfield, VA 22161.
- ³²G. D. Gillispie, A. U. Kahn, A. C. Wahl, R. P. Hosteny, and M. Krauss, *J. Chem. Phys.* **63**, 3425 (1975).
- ³³D. Neuman *et al.*, "POLYATOM (Version 2)," Quantum Chemistry Program Exchange, Indiana University, Bloomington, IN. PA300 was modified and linked to BISON-MC by A. Hinds of Argonne National Laboratory. The modified version generates canonical lists of integrals and no labels.
- ³⁴A small (100-configuration) configuration interaction program was developed by G. Das from BISON-MC to perform CI calculations with the MCSCF orbitals.
- ³⁵S. Huzinaga, *J. Chem. Phys.* **42**, 1293 (1964).
- ³⁶T. H. Dunning, Jr., *J. Chem. Phys.* **55**, 3958 (1971).
- ³⁷Rydberg character is not manifested in the $N_2O^+(X^2A')$ wavefunction with the $4s3p$ contracted Gaussian bases (Ref. 36) in the sense that in no orbital does the expansion coefficient for the most diffuse s or p basis functions dominate the orbital. A list of the SCF and/or MCSCF orbitals will be provided upon request.
- ³⁸The valence orbitals for a first row triatomic are taken to be the 15 orbitals $1-\sigma$, $1-3\pi_x$, $1-3\pi_y$ in $C_{\infty v}$ symmetry (or $1-12a'$, $1-3a''$ in C_s symmetry) which can be constructed from the $2s1p$ minimal atomic bases, less the $1-\sigma$ ($1-3a'$) orbitals containing the $1s$ electrons.
- ³⁹G. Das and A. C. Wahl, *J. Chem. Phys.* **56**, 3533 (1972).
- ⁴⁰F. P. Billingsley II and M. Krauss, *J. Chem. Phys.* **60**, 4130 (1974).
- ⁴¹D. G. Hopper (unpublished preliminary MCSCF results on N_2O).
- ⁴²D. G. Hopper *et al.* (to be submitted).
- ⁴³D. G. Hopper, P. J. Fortune, A. C. Wahl, and T. O. Tiernan, in *ACS Symposium Series, Number 19, Computer Networking and Chemistry*, edited by P. Lykos (American Chemical Society, Washington, 1975), pp. 153-182.
- ⁴⁴E. B. Wilson, J. C. Decius, and P. C. Cross, *Molecular Vibrations. The Theory of Infrared and Raman Vibrational Spectra* (McGraw-Hill, New York, 1955).
- ⁴⁵A. L. McClellan, *Tables of Experimental Dipole Moments* (Freeman, San Francisco, 1963).
- ⁴⁶W. E. Wentworth, R. George, and H. Keith, *J. Chem. Phys.* **61**, 1791 (1969).
- ⁴⁷A. Zecca, I. Lazzizzera, M. Krauss, and C. E. Kuyatt, *J. Chem. Phys.* **61**, 4560 (1974).
- ⁴⁸J. Comer and G. J. Schulz, *Phys. Rev. A* **10**, 2100 (1974).
- ⁴⁹M. McFarland, D. L. Albritton, F. C. Fehsenfeld, E. E. Ferguson, and A. L. Schmeltzke, *J. Chem. Phys.* **59**, 6629 (1973).
- ⁵⁰W. Lindinger, D. L. Albritton, F. C. Fehsenfeld, and E. E. Ferguson, *J. Chem. Phys.* **63**, 3238 (1975).

Luminescence from low-energy He^+/Xe charge-transfer reactionsE. G. Jones, B. M. Hughes,* D. C. Fee,[†] and T. O. Tiernan

Department of Chemistry, Wright State University, Dayton, Ohio 45431

(Received 1 November 1976)

Optical emissions produced by collision of 100-eV He^+ ions with Xe atoms have been studied over the spectral range from 40 to 900 nm. All of the major lines in the emission spectrum can be assigned to transitions in XeII resulting from charge-transfer reactions. Emission cross sections for the major lines in the vacuum-ultraviolet and visible spectral regions are reported and the importance of cascading is assessed. The kinetic energy dependence is discussed for several of these lines.

INTRODUCTION

Charge transfer has recently been shown to be an efficient pumping mechanism for certain laser systems.^{1,2} In this laboratory, luminescence from ion-neutral reactions having potential laser applications has been investigated. Part of this study has focused on reactions of He^+ with rare gases.³⁻⁵ These reactions are of particular interest because of the earlier reports by Lipeles *et al.*⁶ of vacuum-ultraviolet (VUV) and visible emissions from these reactions at relatively low interaction energies. However, no spectral assignments or cross-section measurements for the production of specific states were made by these authors for the He^+/Xe system. In this communication, we will report assignments and cross sections for some of the major lines in the visible and vacuum ultraviolet regions.

EXPERIMENTAL

A. Apparatus

The emission spectra and the translational energy dependences of selected spectral lines were obtained using a previously described³ beam-spectrometer apparatus constructed in our laboratory. Briefly, the apparatus consists of a single focusing mass spectrometer with conventional electron impact source which is utilized to produce a mass-resolved ion beam and transmit it into a collision chamber. The apparatus incorporates differential pumping in order to minimize collisions of the projectile ion beam in the region between the ion source and the collision chamber. The energy and focal point of the ion beam are controlled by a decelerating lens positioned immediately ahead of the collision chamber. This is a four-element slot lens which slows the ions from 170 eV, as they exit the mass spectrometer, to the desired interaction energy, as low as 1.0 eV (lab) with uncertainty represented by an energy spread of 1 eV (FWHM). Some of the photons produced in the

collision chamber pass through the ion exit slit and enter a McPherson 1-m VUV monochromator. The monochromator is equipped with a variety of gratings and photomultiplier detectors to permit monitoring a broad spectral region. The output from the photomultiplier detectors is pulse counted using an SSR Model 1110 photon counter.

With the experimental configuration described, the monochromator views along the axis of the ion beam, and some of the radiation collected originates from collisions occurring in the region of the decelerating lens, where the He^+ ion energy is higher than at the collision chamber. To determine an appropriate background correction factor, the ion beam is deflected immediately in front of the collision region, thereby eliminating reaction in the collision chamber, however, not affecting reactions occurring within the deceleration lens. The resulting photon count is then subtracted from the total photon count observed while the ion beam is traversing the collision chamber. This correction varies from 10 to 30% depending on the energy dependence of the emission.

B. Operating conditions

The He^+ ion flux was 2.5×10^{11} ions $\text{cm}^{-2} \text{sec}^{-1}$ (current of 40 nA cm^{-2}) and Xe atom density was 1.6×10^{14} atoms cm^{-3} (5-mTorr pressure at room temperature) in the interaction region. The pressure was measured using an MKS Baratron capacitance manometer directly coupled to the collision region. For isotropic photon emission, typically 1 out of 2000 photons strikes the monochromator grating.

C. Calibration

In the VUV region, cross sections were calculated using the best available data for detector quantum efficiency. Both Bendix Channeltron⁷ and EMR 541-F⁸ detectors were used. Namioka and Hunter⁹ have reported an absolute reflectance of 4% at 121.6 nm for a gold-coated grating. Samp-

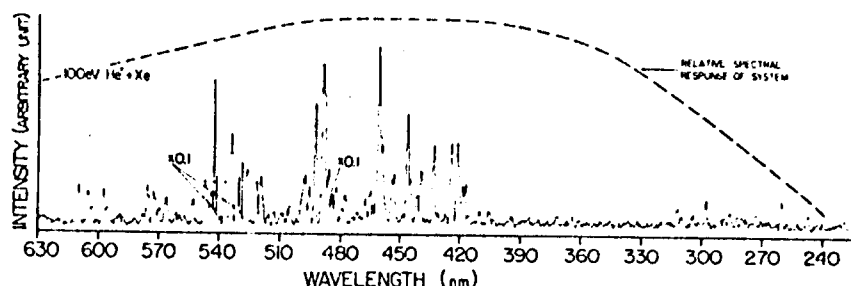


FIG. 1. Optical emissions observed in the visible spectral region from the reaction of 100-eV He^+ ions with Xe. Optical resolution is 2 nm. Note: When output from the digital counter exceeds full scale on the recorder, it is automatically reduced by a factor of 10 for plotting.

son¹⁰ has shown platinum to have a reflectance of about 1.4–1.5 times that of gold. On this basis and consistent with reports of Zaidel and Shreider¹¹ we have estimated a reflectance of 6% at 121.6 nm. Using these assumptions we find that the calculated cross section of 0.60 \AA^2 for Lyman- α production (121.6 nm) from impact of a 100-eV He^+ ion beam on hydrogen compares favorably with the accepted value of 0.44 \AA^2 derived by Dunn, Geballe, and Pretzer.¹² The relative spectral reflectances were interpolated from the data of Namioka and Hunter at 121.6, 58.4, and 30.4 nm.

An absolute calibration of the monochromator was made in the 450–900 nm region for each grating, using an NBS-calibrated tungsten strip lamp, based on the method outlined by Kostkowski and Lee.¹³ Below 450 nm, the internally reflected light was equal to or greater than the light emitted by the tungsten lamp. Therefore, the relative grating reflectance¹⁴ and photomultiplier quantum efficiency¹⁵ between 250 and 450 nm were used to determine a relative instrument function. This function was normalized at 450 nm to the absolute value obtained from the NBS-calibrated lamp.

Errors are estimated to amount to $\pm 30\%$ uncertainty in the relative values of the emission cross section and a factor of 2 to 3 in the absolute values.

RESULTS AND DISCUSSION

Emission spectra observed in the visible and VUV regions from impact of 100-eV He^+ ions on Xe are shown in Figs. 1 and 2. These were obtained with the monochromator slits adjusted for a spectral resolution of about 2 nm. Higher-resolution spectra (0.2 nm) have also been obtained for most of the intense lines. The raw data were reduced using a computer program which compares the observed spectral lines with transitions expected on the basis of known energy levels in the HeI , XeI , and XeII systems.¹⁰ About 95% of the emissions observed in the VUV can be unequivocally assigned to specific transitions, but many of the lines observed with high resolution in the visible can be assigned to more than one transition. In assigning the states listed in Tables I

and II, all wavelengths calculated by the computer search routine for Xe II transitions which do not violate the selection rule $\Delta J = 0, \pm 1$ or Laporte's rule, are included. None of the observed lines could be positively identified with HeI or XeI transitions.

The dependences of the cross sections for several of the major emissions upon He^+ translational energy were also determined. The major line observed in the visible region ($484.6 \pm 0.2 \text{ nm}$), was found to exhibit an energy threshold which is below 10 eV (c.m.). Only one transition can be identified which is consistent with this threshold, that is, $6s^4P_{5/2} - 6p^4D_{7/2}^o$. Other J combinations within this band can be recognized among the possible assignments that are summarized in Table I. Table I includes all possible transitions for the five wavelengths listed, consistent with the spectral resolution. From relative emission cross sections¹⁷ and relative transition probabilities,¹⁸ we infer that the transition $6s^4P - 6p^4D^o$ is the major contributor to the emission cross section at these wavelengths. The same five transitions (J combinations) have also been observed in this laboratory in the analogous He^+/Kr system. It is interesting to note that of the five assigned transitions listed in Table I, two are among the strong-

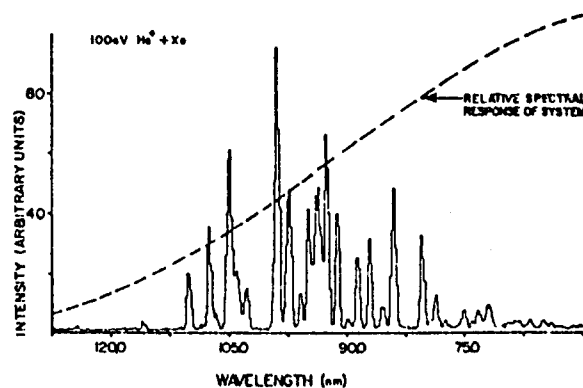


FIG. 2. Optical emissions observed in the VUV from the reaction of 100-eV He^+ ions with Xe. Optical resolution is 2 nm.

TABLE I. Xe II transitions observed in the visible spectral region from the reaction of 100-eV He⁺ with Xe.

Observed wavelength ^a λ_0 (nm)	Total cross section for observed emission ^b (10 ⁻¹⁸ cm)	Possible assignments, Xe II		$\lambda_T - \lambda_0$ ^c (nm)	ΔH ^c (eV)
		Lower	Upper		
484.6 ₃ ± 0.2	6.4	6s ⁴ P _{3/2}	6p ⁴ D _{1/2} ^o	-0.06	1.64
542.1 ₈ ± 0.2 ^d	5.6	6s ⁴ P _{3/2}	6p ⁴ D _{5/2} ^o	-0.11	1.62
421.5 ₃ ± 0.2	1.9	6s ⁴ P _{3/2}	6p ⁴ D _{3/2} ^o	0.10	2.02
		5d ² P _{1/2}	6p' ² P _{3/2} ^o	0.01	3.62
		6p ⁴ D _{1/2} ^o	6d ⁴ P _{3/2}	-0.10	5.41
		6s ⁴ P _{3/2}	6p ⁴ D _{3/2} ^o	-0.05	2.02
460.4 ₈ ± 0.2 ^d	4.2	5d ⁴ F _{3/2}	6p ² P _{3/2} ^o	-0.05	2.83
		6s ⁴ P _{1/2}	6p ⁴ D _{1/2} ^o	-0.05	2.47
519.3 ₃ ± 0.4	1.1	5d ² P _{3/2}	6p ² P _{1/2} ^o	-0.06	2.99
		6p ⁴ P _{1/2} ^o	2 _{1/2}	0.31	4.02
		6p ⁴ S _{3/2} ^o	6d ⁴ P _{1/2}	0.03	5.01
		6p ² D _{5/2} ^o	7s ² P _{3/2}	-0.38	5.20

^a Calculated in vacuum.^b The calculation of these values assumes isotropic photon emission and neglects possible polarization effects.^c λ_T , calculated from levels listed in Ref. 16, is the wavelength corresponding to the assigned transition.^d These are among the strongest lines observed in the xenon ion laser (see Ref. 19).^e Enthalpy change for the reaction He⁺ + Xe → He + Xe⁺.TABLE II. Major emissions observed in the VUV from reaction of 100-eV He⁺ with Xe.

Observed wavelength ^a λ_0 (nm)	Total cross section for observed emission ^b (10 ⁻¹⁸ cm ²)	Possible assignments, Xe II		$\lambda_T - \lambda_0$ ^c (nm)
		Lower	Upper	
93.13 ± 0.1	5.2	5p ⁵ 2P _{3/2} ^o	5d ⁴ P _{3/2}	0.00
93.52 ± 0.1	7.8	5p ⁵ 2P _{3/2} ^o	5d ⁴ P _{1/2}	0.02
93.95 ± 0.1	9.5	5p ⁵ 2P _{3/2} ^o	5d ⁴ P _{3/2}	-0.03
94.42 ± 0.1	5.4	5p ⁵ 2P _{3/2} ^o	5d ² P _{1/2}	-0.03
94.98 ± 0.1	9.4	5p ⁵ 2P _{3/2} ^o	5d ² P _{3/2}	-0.03
98.90 ± 0.1	28.5	5p ⁵ 2P _{3/2} ^o	6s ⁴ P _{1/2}	-0.04
103.25 ± 0.2	1.7	5p ⁵ 2P _{3/2} ^o	5d ⁴ D _{1/2}	-0.01
		5p ⁵ 2P _{1/2} ^o	5d ⁴ P _{3/2}	0.01
103.81 ± 0.1	4.7	5p ⁵ 2P _{1/2} ^o	5d ⁴ P _{1/2}	-0.04
104.83 ± 0.1	25.3	5p ⁵ 2P _{3/2} ^o	5d ⁴ D _{3/2}	0.00
		5p ⁵ 2P _{1/2} ^o	5d ² P _{1/2}	-0.01
105.22 ± 0.1	10.4	5p ⁵ 2P _{3/2} ^o	6s ⁴ P _{3/2}	-0.03
107.47 ± 0.1	16.5	5p ⁵ 2P _{3/2} ^o	6s ⁴ P _{5/2}	-0.02

^a Calculated in vacuum.^b The calculation of these values assumes isotropic photon emission and neglects possible polarization effects.^c λ_T , calculated from levels listed in Ref. 16, is the wavelength corresponding to the assigned transition.

est lines observed in the cw xenon-ion laser.¹⁹

The VUV emissions shown in Fig. 2 can all be assigned to XeII transitions. Table II is a summary of some of the more intense lines. This includes all of the observed transitions from $6s\ ^4P$, $5d\ ^4P$, and $5d\ ^2P$ states. The cross section of the most intense line in the VUV (98.90 nm) was found to be constant over the energy range 20–140 eV. In contrast, emissions monitored over the interval 97.3 ± 1 nm as shown in Fig. 3 exhibit a strong kinetic energy dependence. There are two lines, 97.34 nm ($5p\ ^5\ ^2P_{3/2}^o - 6s\ ^2P_{3/2}$) and 97.70 nm ($5p\ ^5\ ^2P_{1/2}^o - 6s\ ^2D_{3/2}$) contributing to this curve. The maximum, occurring at 12 eV (lab), corresponds to a cross section of $\sim 0.4\ \text{\AA}^2$. Lipeles *et al.*⁶ observed a similar dependence in the total cross section for photon production in the range 20–120 nm. The total cross section obtained by summing the emission cross sections (100-eV He⁺ ion impact) of all individual lines in this interval is $2.4\ \text{\AA}^2$ which is about one-half the apparent cross section observed by Lipeles *et al.*⁶ De Heer and co-workers^{20,21} have studied this reaction at higher energies and have obtained a total cross section²¹ of $3.6\ \text{\AA}^2$ over this interval for impact of 300-eV He⁺ ions.

A detailed study of the excitation mechanism for the $6s\ ^4P$, $5d\ ^4P$, and $5d\ ^2P$ states is summarized in Table III. The energetics of formation of each of the possible J levels of the 4P and 2P states of XeII from ground-state He⁺ and Xe reactants are listed. In addition, the total emission cross section for radiation to the $5p\ ^5\ ^2P_{3/2}^o$ and $5p\ ^5\ ^2P_{1/2}^o$ ground ionic states (determined from VUV emission cross sections) is shown, along with the total

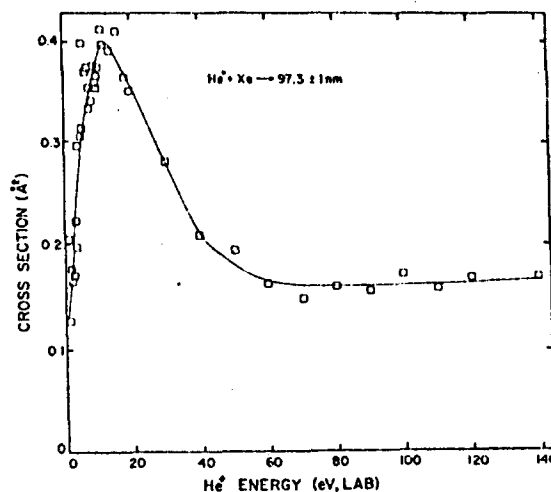


FIG. 3. Emission cross section for XeII radiation observed within the interval 97.3 ± 1 nm from impact of He⁺ ions on Xe.

cascading cross section from high-energy states to those individual states (determined from visible emission cross sections). The last column is the difference between the measured emission cross section in the VUV and the measured cascading cross sections in the visible region for each individual state populated and thus is the cross section for direct formation of the states indicated in Table III formed in the original ion-neutral collision. As can be seen, the first two states listed in Table III are formed mainly by populating higher-energy states, followed by cascading, rather than directly in the ion-neutral collision. This is in agreement with the findings of De Heer

TABLE III. Total emission and cascading cross sections for the major XeII 4P and 2P states observed in the He⁺/Xe reaction.

State, XeII	ΔH^a (eV)	Cross sections ($10^{-18}\ \text{cm}^2$)		
		Total emission	Cascading	Direct formation
$6s\ ^4P_{5/2}$	-0.92	16.5	15.1	1.4
$6s\ ^4P_{3/2}$	-0.67	10.4	12.0	-1.6
$6s\ ^4P_{1/2}$	0.09	28.5	1.2	27.4
$5d\ ^2P_{3/2}$	0.60	9.4	0.4	9.05
$5d\ ^2P_{1/2}$	0.68	18.1 (12.7) ^b	...	18.1
$5d\ ^4P_{5/2}$	0.74	9.5	4.6	4.9
$5d\ ^4P_{1/2}$	0.80	12.5	0.6	12.0
$5d\ ^4P_{3/2}$	0.86	6.1 (0.9)	...	6.1

^a Enthalpy change for the reaction $\text{He}^+ + \text{Xe} \rightarrow \text{He} + \text{Xe}^{++}$.

^b There is an uncertainty on the order of ± 12.7 in this value because of unknown contribution of the unresolved transition $5p\ ^5\ ^2P_{3/2}^o \leftarrow 5d\ ^4P_{3/2}$. Tabulated value assumes approximately equal contribution from each transition.

and co-workers²¹ at 300-eV He⁺ ion energy. However, in contrast, the $6s\ ^4P_{1/2}$ state is almost entirely formed directly in the ion-neutral collision. Radiation from this state constitutes more than 7% of the total radiation produced in the reaction. Similarly, the remaining states listed in Table III, which are also populated by processes which are endoergic for ground-state reactants, are formed directly in the ion-neutral collision. The total cross section for those emissions listed in the table approaches one-third of the total cross section for radiation produced by impact of 100-eV He⁺ ions on Xe. While cascading effects must be assessed for each state on an individual basis, overall cascading contributions account for about 30% of the total observed radiation (visible and VUV) in the He⁺/Xe reaction at 100-eV ion energies.

De Heer and co-workers²¹ have extensively studied this system at impact energies above 300 eV. The highest ion energy attainable on our instrument is 150 eV preventing a *direct* comparison with the data of De Heer and co-workers.^{20,21} Nevertheless, one might expect many similarities in the results of these two studies; however, some gross disparities exist in the states populated and in their total emission cross sections. De Heer and co-workers²¹ make no mention of transitions from $6s\ ^4P_{1/2}$, $5d\ ^4P_{1/2}$, or $5d\ ^2P_{1/2}$ levels. It is presumed, therefore, that transitions from these three levels are relatively unimportant under their experimental conditions, although these are the three most intense lines observed in the present study. No XeI resonance lines were observed in this investigation, yet De Heer and co-workers report large apparent emission cross sections for XeI resonance lines ($\sigma > 0.15\ \text{\AA}^2$ at 147 nm).

While a detailed comparison of the experimental methods of De Heer *et al.*^{20,21} with those of the present study will not be presented here, it is appropriate to note some obvious differences which may account for this discrepancy. One important difference is the ion beam flux. De Heer *et al.* used a plasma ion source which resulted in a much larger flux of He⁺ ions in the collision region than is realized in the present experiments (typically larger by a factor of 10^3). This very

large density of He⁺ ions may permit the occurrence of neutral-neutral excitation processes in the collision region. De Heer *et al.*²¹ find that the cross sections for the resonance atomic lines do not vary linearly with pressure in the collision region. This indicates that some of the radiative states may be formed by competitive processes in their experiments, and these authors suggest that fast He atoms may be involved. In the experiments reported here, the cross sections of all major emissions were found to depend linearly upon collision chamber pressure, up to pressures of 8 mTorr. These emissions therefore result only from bimolecular He⁺/Xe reactions with little possibility of their formation by He-atom reactions or other processes.

It is noteworthy that Tanaka *et al.*²² have recently observed a strong emission line of XeII, corresponding to the transition $5p^5\ ^2P_{3/2}^o - 6s\ ^4P_{1/2}$, from the excitation of a mixture of He and Xe in an ac pulsed discharge at a total pressure of about 10 Torr. As shown in Tables II and III, this line is one of the major emissions observed in the present study. Tanaka *et al.*²² detected only very weak emission bands from the (HeXe)⁺ diatomic ion.

The results of the present investigation indicate that the production of radiative states of XeII in the reaction of He⁺ (100 eV, lab) with Xe is quite efficient. The total cross section for direct excitation measured in this study constitutes about 25% of the total He⁺/Xe charge-transfer cross section ($10\ \text{\AA}^2$ at 100 eV).²³ A complete reporting of all lines observed in this and other He⁺ rare gas systems is in preparation.

ACKNOWLEDGMENTS

The authors would like to acknowledge C. D. Miller for his extensive efforts in the design and fabrication of the instrument and D. G. Hopper for developing the computer search programs used in this study. This research was supported by the Air Force Office of Scientific Research (AFSC), United States Air Force, under Contract No. F44620-76-C-0007.

*Present address: Flammability Research Center, University of Utah, Salt Lake City, Utah 84103.

†Present address: Chemical Engineering Division, Argonne National Laboratory, Argonne, Ill. 60439.

¹A. R. Turner-Smith, J. M. Green, and C. E. Webb, *J. Phys. B* **6**, 114 (1973).

²C. B. Collins, A. J. Cunningham, S. M. Curry, B. W.

Johnson, and M. Stockton, *Appl. Phys. Lett.* **24**, 477 (1974).

³B. M. Hughes, E. G. Jones, and T. O. Tiernan, *Abstracts of the Eighth International Conference on the Physics of Electronic and Atomic Collisions* (Institute of Physics, Belgrade, 1973), Vol. I, p. 223.

⁴B. M. Hughes, E. G. Jones, and T. O. Tiernan, *Bull.*

- Am. Phys. Soc. **19**, 156 (1974).
- ⁵B. M. Hughes *et al.* (unpublished).
- ⁶M. Lipeles, R. Novick, and N. Tolk, Phys. Rev. Lett. **15**, 815 (1965).
- ⁷K. C. Schmidt, Technical Applications Note 9803, Bendix Electro-Optics Division, Ann Arbor, Mich. (unpublished); M. C. Johnson and J. Svenson, Technical Note, Bendix Corp., Research Laboratories Division, Southfield, Mich.
- ⁸EMR photoelectric data for calibration of 541F-03-18-03900 photomultiplier tube that was used in this study.
- ⁹T. Namioka and W. R. Hunter, Opt. Commun. **8**, 229 (1973).
- ¹⁰J. A. R. Sampson, *Techniques of Vacuum Ultraviolet Spectroscopy* (Wiley, New York, 1967).
- ¹¹A. N. Zaidel and E. Ya. Shreider, *Vacuum Ultraviolet Spectroscopy*, translated by Z. Lerman (Ann Arbor-Humphrey Science Publishers, London, 1970).
- ¹²G. H. Dunn, R. Geballe, and D. Pretzer, Phys. Rev. **128**, 2200 (1962).
- ¹³H. J. Kostkowski and R. D. Lee, Natl. Bur. Stand. (U.S.) Monogr. No. 41 (1962).
- ¹⁴Reflectance data for grating of serial number 2659-1 blazed at 500 nm was provided by Bausch and Lomb, Analytical Systems Divisions, Rochester, N.Y.
- ¹⁵Quantum efficiency data for C31034 A photomultiplier tube was provided by RCA, Electronic Components Division, Lancaster, Pa.
- ¹⁶C. E. Moore, *Atomic Energy Levels*, NBS Circ. No. 467 (U.S. GPO, Washington, D.C., 1949, 1952, 1958), Vols. I, II, and III.
- ¹⁷A. R. Striganov and N. S. Sventitskii, *Tables of Spectral Lines of Neutral and Ionized Atoms* (Plenum, New York, 1969).
- ¹⁸M. H. Miller, R. A. Roig, and R. D. Bengston, Phys. Rev. A **8**, 480 (1973).
- ¹⁹W. B. Bridges and A. N. Chester, Appl. Opt. **4**, 573 (1965).
- ²⁰D. Jaceks, F. J. De Heer, and A. Salop, Physica **36**, 606 (1967).
- ²¹F. J. De Heer, B. F. J. Luyken, D. Jaceks, and L. Walterbeek Muller, Physica **41**, 588 (1969).
- ²²Y. Tanaka, K. Yoshino, and D. E. Freeman, J. Chem. Phys. **62**, 4484 (1975).
- ²³W. B. Maier II, Phys. Rev. A **5**, 1256 (1972).

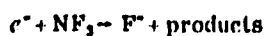
Dissociative electron attachment in nitrogen trifluoride

G. D. Sides and T. O. Tiernan

Department of Chemistry, Wright State University, Dayton, Ohio 45431
(Received 28 April 1977)

The chemical physics of the gas nitrogen trifluoride is currently of interest owing to its applicability in the development of HF/DF chemical lasers and its use in the rare gas-halide laser systems.¹⁻⁸ Since these lasers are electron-beam or discharge initiated, the reaction of electrons with NF_3 is of particular interest.⁹

The rate constant for the dissociative attachment of thermal energy electrons (300–350 °K) to nitrogen trifluoride has been measured using a flowing afterglow technique described in a previous publication.¹⁰ The rate constant obtained for the reaction



(1)

is $2.1 \pm 0.8 \times 10^{-11} \text{ cm}^3 \text{ molecule}^{-1} \text{ sec}^{-1}$. This rate constant was obtained using a filament electron source, and with an argon buffer gas pressure of 0.3 torr.

The rate constant for thermal energy electron attachment in nitrogen trifluoride has previously been measured by Mothes *et al.*¹¹ using an electron cyclotron resonance technique. The current measurement agrees well with the value, $2.4 \times 10^{-11} \text{ cm}^3 \text{ molecule}^{-1} \text{ sec}^{-1}$ at 300 °K, obtained by Mothes *et al.* In addition, the current research establishes the identity of the ionic attachment products.

The only product ion observed in the present study is

F⁻. This result contradicts a previous publication¹² citing the formation of NF⁻, F₂⁻ and F⁻ by thermal electron attachment. However, that work was performed using a time-of-flight mass spectrometer, in which it was not possible to obtain a thermal electron beam, which is necessary to determine thermal energy electron attachment products. No evidence was obtained in the present experiments for the formation of the ions NF⁻ or F₂⁻ at thermal energy.

Reactions which may be proposed to occur at thermal energy include



Each of these reactions may be discussed using available thermochemical data (in kcal mole⁻¹ at 298 °K) $\Delta H_f(\text{N}) = 112.979$,¹³ $\Delta H_f(\text{F}) = 18.88$,¹³ $\Delta H_f(\text{NF}) = 57$,¹⁴ $\Delta H_f(\text{F}^-) = -60.0$,¹⁵ $\Delta H_f(\text{NF}^-) = 43.2$,¹⁶ $\Delta H_f(\text{F}_2^-) = 68.6$,¹⁷ $\Delta H_f(\text{NF}_2) = 10.3$,¹³ $\Delta H_f(\text{NF}_3) = -29.8$,¹³ and $\Delta H_f(\text{NF}_2^-) = -28.4$.¹⁸ Using these data, Reaction (2a) may be shown to be exoergic by 19.9 kcal mole⁻¹ while Reactions (2b) and (2c) are endoergic by 45.7 and 120.5 kcal mole⁻¹, respectively. Reactions (3a) and (3b) are endoergic by 73.0 and 110.8 kcal mole⁻¹, respectively. Reactions (4a), (4b), and (5) are also endoergic (by 18.2, 93.1, and 20.3 kcal mole⁻¹, respectively). Thus, a thermochemical analysis of the proposed Reactions (2)–(5) indicates that Reaction (2a) is the only process expected to occur in the reaction of thermal energy electrons with NF₃. To the authors' knowledge, the formation of NF₃⁻ has not been reported and is not observed in the present experiments [$k < 10^{-20}$ cm⁶ molecule⁻² sec⁻¹ for Reaction (6)].

The present experiments were performed at NF₃ densities approximately three orders of magnitude greater than in Thynne's experiments. Thus, the possibility of ion-molecule reactions disguising the direct thermal electron attachment products must be considered. Reactions (2b)–(5) are thermochemically forbidden. However, the electron affinity of NF has not been measured experimentally, and reaction (3a) would be exoergic if the electron affinity of NF is > 86.8 kcal mole⁻¹, which falls within the known range of electron affinities for small molecules.¹⁹ However, the charge transfer reaction



would be endoergic by 66.0 kcal mole⁻¹, and NF⁺ would be observed in the afterglow. Thus, it is unlikely that

the electron affinity of NF is as large as 86.8 kcal mole⁻¹.

If NF₃⁻ is formed by Reaction (6), then the reaction



may occur if the electron affinity of NF₃ is less than or equal to 19.9 kcal mole⁻¹. However, even in experiments where the NF₃ density was $\sim 5 \times 10^{11}$ molecules cm⁻³, no NF₃⁻ was observed. Under the present experimental conditions, the rate constant for Reaction (8) would have to be $\geq 10^{-9}$ cm³ molecule⁻¹ sec⁻¹ in order for NF₃⁻ not to be observed.

The results of the present research show that only one product ion, F⁻, is formed in the thermal energy attachment of electrons to NF₃. The rate constant has been found to be quite slow but significant for high pressure NF₃ mixtures.

The authors gratefully acknowledge the contribution of the nitrogen trifluoride to our laboratory by Dr. E. A. Dorko of the Air Force Institute of Technology. This work was sponsored by the Air Force Office of Scientific Research (AFSC), United States Air Force, under Contract No. F44620-76-C-0007.

¹M. C. Lin, J. Phys. Chem. 75, 284 (1971).

²W. H. Green and M. C. Lin, IEEE J. Quantum Electron. 7, 98 (1971).

³D. W. Gregg, B. Krawetz, R. K. Pearson, B. R. Schleicher, S. J. Thomas, E. B. Huss, K. J. Pettipiece, J. R. Creighton, R. E. Niver, and Y.-L. Pan, Chem. Phys. Lett. 8, 609 (1971).

⁴W. H. Green and M. C. Lin, J. Chem. Phys. 54, 3222 (1971).

⁵E. R. Ault, R. S. Bradford, Jr., and M. L. Bhaumik, Appl. Phys. Lett. 27, 413 (1975).

⁶M. L. Bhaumik, R. S. Bradford, Jr., and E. R. Ault, Appl. Phys. Lett. 28, 23 (1976).

⁷R. Burnham, N. W. Harris, and N. Djcu, Appl. Phys. Lett. 28, 86 (1976).

⁸J. A. Mangano, J. H. Jacob, and J. B. Dodge, Appl. Phys. Lett. 29, 426 (1976).

⁹J. Hsia, Appl. Phys. Lett. 30, 101 (1977).

¹⁰G. D. Sides, T. O. Tiernan, and R. J. Hanrahan, J. Chem. Phys. 65, 1966 (1976).

¹¹K. G. Mothes, E. Schultes, and R. N. Schindler, J. Phys. Chem. 76, 3758 (1972).

¹²J. C. J. Thynne, J. Phys. Chem. 73, 1586 (1969).

¹³D. D. Wagman, W. H. Evans, V. B. Parker, I. Halow, S. M. Bailey, and R. H. Schumm, NBS Tech. Note 270-3, U.S. Government Printing Office, Washington, D. C. 20402 (1968).

¹⁴J. L. Franklin, J. G. Dillard, H. M. Rosenstock, J. T. Herron, K. Draxl, and F. H. Field, Natl. Stand. Ref. Data Syst., NBS 26, U. S. Government Printing Office, Washington, D. C. 20402 (1969).

¹⁵Based on the heat of formation of F given in Ref. 13 and the electron affinity of F (78.9 kcal mole⁻¹) obtained from an average of the values given in: F. M. Page and G. C. Goode, *Negative Ions and the Magnetron*, (Wiley, New York, 1969); R. S. Berry and C. W. Reinmann, J. Chem. Phys. 38, 1540 (1963); H. P. Popp, Z. Naturforsch. Teil A20, 642 (1965); H. P. Popp, Z. Naturforsch. Teil A22, 251 (1967); R. Mihalstein and R. S. Berry, J. Chem. Phys. 55, 1146 (1971).

¹⁶Based on the heat of formation of NF given in Ref. 14 and the estimated electron affinity of NF (13.8 kcal mole⁻¹) given in:

P. A. G. O'Hare and A. C. Wahl, *J. Chem. Phys.* **54**, 4563 (1971).

¹⁷Average of the values given in: J. J. DeCorpo and J. L. Franklin, *J. Chem. Phys.* **54**, 1885 (1971); P. W. Harland and J. L. Franklin, *J. Chem. Phys.* **61**, 1621 (1974); W. A. Chupka, J. Berkowitz and D. Gutman, *J. Chem. Phys.* **55**,

2724 (1971).

¹⁸Based on the heat of formation of NF_2 given in Ref. 13 and the electron affinity of NF_2 (38.7 kcal mole⁻¹) given in P. W. Harland and J. L. Franklin, *J. Chem. Phys.* **61**, 1621 (1974).

¹⁹J. L. Franklin and P. W. Harland, *Ann. Rev. of Phys. Chem.* **25**, 485 (1974).

Associative detachment reactions of negative ions with O₃

C. Lifshitz,^{a)} R. L. C. Wu, J. C. Haartz,^{b)} and T. O. Tiernan

Department of Chemistry and The Brehm Laboratory, Wright State University, Dayton, Ohio 45431
(Received 16 May 1977)

Associative detachment reactions of the type $A^- + B \rightarrow AB + e$ have been studied recently¹ using flow-drift techniques. These experiments yield rate coefficients based on observations of the disappearance of the negative ion reagent as the concentration of B is increased. Neither electrons nor neutral products are directly monitored in such experiments. It is difficult to determine branching ratios for other negative-ion reaction channels from measurements of this type. An alternative method which has been utilized to study associative detachment processes employs an ion beam-collision chamber apparatus² in which electrons produced in the detachment reaction are directly observed. Other channels producing negative ions are not monitored, however. A third method, recently developed in our laboratory³ is also based on ion beam-collision chamber experiments, but both negative ion products and electrons from the negative ion-neutral collision can be readily monitored. Cross sections for negative ion products are obtained as previously described,⁴ while detached slow electrons are monitored by using SF₆ as a scavenger in the collision chamber, and measuring the resultant SF₆⁻ currents. The wide translational energy range accessible to the tandem mass spectrometer used for these experiments (0.3–180 eV in the laboratory system) facilitates studies of the energy dependences of the reactions. At the lowest energies employed (~0.3 eV), cross sections for associative detachment reactions determined by this method are quite reliable, since the direct reaction of most simple negative ions (for example, O⁻ or S⁻) with SF₆ is endoergic, and the observed SF₆⁻ can be formed only by capture of the electrons released in the detachment reaction. At higher translational energies, contributions to the SF₆⁻ signal from the direct reaction become more important and must be subtracted from the total SF₆⁻ current to obtain a measure of the associative detachment channel.

In the present experiments, we have employed the SF₆ scavenger technique to observe associative detachment reactions of several negative ions with O₃ which have not previously been reported. Table I summarizes the reaction rate coefficients determined for these reactions. These rate coefficients k are related to the experimentally determined cross sections σ via the relation, $k = \sigma \bar{v}$, where \bar{v} is the average incident ion velocity at the corresponding laboratory energy employed.

Of particular interest is the associative detachment reaction



for which the rate approaches the gas kinetic collision rate. This reaction is highly exoergic, and apparently the reactants approach each other along attractive potential surfaces which lead into the autodetaching region.

A fairly long-lived collision complex must be formed in order to permit the extensive rearrangement which is necessary for the sulfur atom insertion to occur. It is also interesting to note that one of the fastest associative detachment reactions previously observed,^{1b,3} $O^- + SO_2 \rightarrow SO_3 + e$ yields the same final products as Reaction

TABLE I. Rate coefficients for various negative ion reactions with O₃.^a

Reaction	10 ⁻¹⁰ cm ³ /molecule · sec
O ⁻ + O ₃ → 2O ₂ + e + 2.65 eV ^b	3 ± 1 ^c
→ O + O ₃ ⁻ + 0.7 eV	2 ± 0.4 ^d
→ O ₂ ⁻ + O ₂ + 3.1 eV	0.1 ± 0.05
OH ⁻ + O ₃ → O ₂ + HIO ₂ + e - 0.16 eV	< 0.01 (not observed)
→ OH + O ₃ ⁻ + 0.3 eV	5 ± 0.2
→ HO ₂ ⁻ + O ₂	0.3 ± 0.1
→ O ₂ ⁻ + HIO ₂ + 0.28 eV	0.1 ± 0.05
S ⁻ + O ₃ → SO ₃ + e + 6.4 eV	11 ± 2
→ S + O ₃ ⁻ + 0.1 eV	0.9 ± 0.3
→ SO ⁻ + O ₂ + 3.5 eV	0.3 ± 0.1
→ O ₂ ⁻ + SO + 2.8 eV	0.08
→ SO ₂ + O ⁻ + 4.3 eV	0.01
→ SO ₂ ⁻ + O + 3.9 eV	0.02
SH ⁻ + O ₃ → (OH + SO ₂) + e + 3.3 eV	5.5 ± 1
→ SH + O ₃ ⁻ - 0.15 eV	0.6 ± 0.3
→ HSO ⁻ + O ₂	1.0 ± 0.4
→ SO ⁻ + HO ₂ + 1.5 eV	0.2 ± 0.1
→ SO + HIO ₂	0.06
→ SO ₂ ⁻ + OH + 4.4 eV	0.02
→ SO ₂ + OH ⁻ + 5.1 eV	0.01
→ S ⁻ + ?	0.09
→ O ⁻ + ?	0.01

^aMeasured with reactant ions of ~0.3 eV laboratory energy.

^bExoergies were calculated using known heats of formation (Ref. 5) and electron affinities, EA(O) = 1.462 eV; EA(OH) = 1.825 eV; EA(S) = 2.077 eV; EA(SH) = 2.319 eV, EA(O₂) = 0.44 eV; EA(SO) = 1.1 eV; EA(SO₂) = 1.097 eV, Refs. 6–12], and from the recently obtained electron affinity of ozone EA(O₃) = 2.15 ± 0.15 eV (Ref. 13).

^cAll associative detachment rate coefficients were determined relative to the rate, $k = 1.4 \times 10^{-10}$ cm³/molecule · sec for the reaction O⁻ + NO → NO₂ + e.

^dAll charge transfer and particle transfer rate coefficients were determined relative to the rate $k = 1.2 \times 10^{-9}$ cm³/molecule · sec for the reaction O⁻ + NO₂ → NO₂⁻ + O.

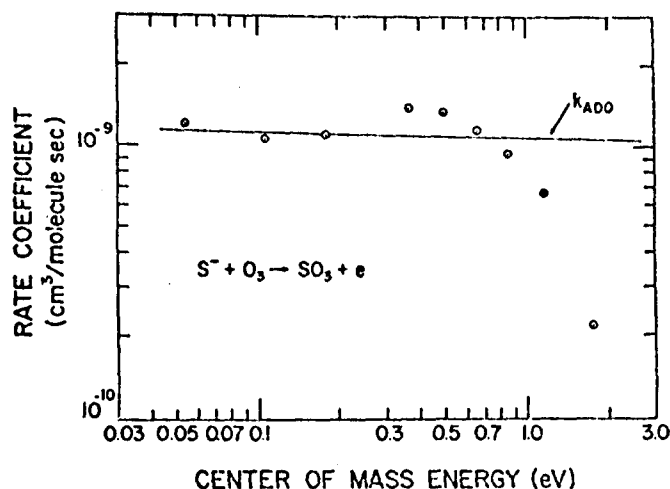


FIG. 1. Rate coefficients for $S^- + O_3 \rightarrow SO_3 + e$ as a function of relative kinetic energy. The predictions of the average dipole orientation (ADO) theory¹⁵ are given. (A polarizability, $\alpha = 4 \times 10^{-24} \text{ cm}^3$, was employed for ozone.¹⁶)

(1). Apparently, both of these associative detachment reactions are quite rapid, in spite of the fact that more than three atoms are involved, because none of the alternative charge transfer or particle transfer channels is more exoergic.¹⁴ The final products of Reaction (1) may however be SO_2 and O , since SO_3 carries away most of the reaction exoergic energy as internal energy and is therefore likely to dissociate.

The rate coefficient for Reaction (1) as a function of relative kinetic energy has also been determined in the present study, as shown in Fig. 1. The decreasing rate with increasing energy is typical of that previously observed for other associative detachment reactions.¹

This work was supported by the Air Force Office of Scientific Research under Contract No. F44620-76-C-0007 with Wright State University. The authors ac-

knowledge helpful discussions with Dr. F. C. Fehsenfeld and Professor J. Heicklen.

^aOn sabbatical leave from The Hebrew University of Jerusalem, 1976-77.

^bPresent address: National Institute for Occupational Safety and Health, Cincinnati, Ohio 45226.

¹(a) M. McFarland, D. L. Albritton, F. C. Fehsenfeld, E. E. Ferguson, and A. L. Schmeltekopf, *J. Chem. Phys.* **59**, 6629 (1973); (b) W. Lindinger, D. L. Albritton, F. C. Fehsenfeld, and E. E. Ferguson, *J. Chem. Phys.* **63**, 3238 (1975).

²(a) J. Comer and G. J. Schulz, *J. Phys. B* **7**, L249 (1974); (b) J. Comer and G. J. Schulz, *Phys. Rev. A* **10**, 2100 (1974).

³T. O. Tiernan, "Interactions Between Ions and Molecules," edited by P. Ausloos (Plenum, New York, 1975), p. 353.

⁴D. G. Hopper, A. C. Wahl, R. L. C. Wu, and T. O. Tiernan, *J. Chem. Phys.* **65**, 5474 (1976).

⁵J. L. Franklin, J. G. Dillard, H. M. Rosenstock, J. T. Herron, K. Draxl, and F. H. Field, *Natl. Stand. Ref. Data Ser. Natl. Bur. Stand.* **26**, (1969).

⁶R. S. Berry, *Chem. Rev.* **69**, 533 (1969).

⁷H. Hotop, T. A. Patterson, and W. C. Lineberger, *J. Chem. Phys.* **60**, 1806 (1974).

⁸W. C. Lineberger and B. W. Woodward, *Phys. Rev. Lett.* **25**, 424 (1970).

⁹B. Steiner, *J. Chem. Phys.* **49**, 5097 (1968).

¹⁰M. W. Siegel, R. J. Celotta, J. L. Hall, J. Levine, and R. A. Bennett, *Phys. Rev. A* **6**, 603 (1972).

¹¹J. L. Franklin and P. W. Harland, *Annu. Rev. Phys. Chem.* **25**, 485 (1974).

¹²R. J. Celotta, R. A. Bennett, and J. L. Hall, *J. Chem. Phys.* **60**, 1740 (1974).

¹³C. Lifshitz, R. L. C. Wu, and T. O. Tiernan (to be published).

¹⁴F. C. Fehsenfeld, "Interactions Between Ions and Molecules," edited by P. Ausloos (Plenum, New York, 1975), p. 337.

¹⁵M. T. Bowers and T. Su, "Interactions Between Ions and Molecules," edited by P. Ausloos (Plenum, New York, 1975), p. 163.

¹⁶M. J. Weiss, J. Berkowitz, and E. H. Appelman, *J. Chem. Phys.* **66**, 2049 (1977).

A LONG-LIVED EXCITED STATE OF O_3^- ; EVIDENCE FROM COLLISION-INDUCED DISSOCIATION

R.L.C. WU, T.O. TIERNAN and C. LIFSHTZ *

*Department of Chemistry, Wright State University,
Dayton, Ohio 45431, USA*

Received 27 June 1977

Translational energy thresholds were determined for collision-induced dissociation of O_3^- formed by two alternative reactions. The different thresholds observed for these two processes, 0.96 eV and 1.80 eV respectively, suggest the existence of a long-lived ($> \mu s$) excited state or isomeric form of O_3^- .

1. Introduction

Ozone and its ions play an important role in the chemistry of the atmosphere [1]. Yet there is still considerable controversy and uncertainty regarding such basic thermochemical quantities as the electron affinity of O_3 and the bond dissociation energy of the O_3^- negative ion. The purpose of this communication is to present new experimental results bearing on these topics. These results suggest the existence of two stable forms of O_3^- , a fact which may serve to resolve some of the current experimental discrepancies. The experimental procedures employed here involve measurements of the threshold for collision-induced dissociation (CID) of O_3^- ions upon impact with various target gases. The CID method has previously been shown to be useful in detecting the presence of excited states in positive ion beams [2], but to our knowledge, no application of this method which indicates the presence of a long-lived excited negative ion state has yet been reported. The derivation of reliable energy thresholds from CID measurements has also been facilitated by the recent development of an adequate theoretical model, which predicts the energy dependence of the cross section in the threshold region [3].

2. Experimental

An in-line tandem mass spectrometer, previously described [2,4], was utilized for these studies. The projectile ion is formed in the electron-impact ion source of the first stage mass spectrometer, which produces a mass and energy resolved beam. This beam is then decelerated in a retarding lens and impacted upon the target gas in the field free collision chamber maintained at a temperature of $30^\circ C$. The energy spread of the projectile ion beam entering the collision cell is ± 0.3 eV (lab). Pulse counting techniques are used to measure the product ion current.

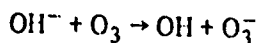
The gases used in these studies were reagent grade and were obtained from the Matheson Co. Ozone was produced by a Tesla coil discharge through oxygen at low pressure (≈ 10 torr) in a vacuum system which was free of hydrocarbon grease or mercury [5]. The ozone was condensed at $-196^\circ C$ and residual oxygen was removed by pumping on the trapped O_3 . The latter was then vaporized immediately into the ion source of the first stage mass spectrometer.

The projectile ion, O_3^- , was formed by electron impact on gaseous mixtures of O_3 and N_2O , and of O_3 and H_2O . Under these conditions O_3^- is most probably formed by the ion-molecule reaction



in the first gaseous mixture, and the reaction

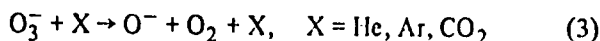
* On sabbatical leave from The Hebrew University of Jerusalem, 1976-77.



in the latter mixture.

3. Data treatment

The measured primary ion intensity, and target gas pressure were employed to convert the product ion intensity to an observed apparent cross section for the CID reactions



as a function of projectile ion translational energy. Corrections for the ion energy distribution and Doppler motion of the target gas were applied as previously described [4,6]. A statistical model for the threshold behavior of the CID reaction was assumed to be applicable [3]. With this model, the threshold dependence of the cross section is well approximated by the functional form,

$$\sigma(E_{\text{rel}}) = A(E_T - E_0)^n / E_{\text{rel}}, \quad (4)$$

where E_T is the total energy available from the collision,

E_0 is the threshold energy, and E_{rel} is the relative translational energy of the colliding pair. A is a function of the internal energy in the reagent ion. The exponent n depends upon the mechanism of the CID reaction, with the range $1.9 < n < 2.2$ implying a direct process and the range $1.5 < n < 1.8$, an indirect process [3]. A computer fitted excitation function based on these energy corrections, calculated using an assumed threshold function, was compared in each case with the experimental data. Assuming that the products are in their ground states at threshold, the bond dissociation energy $D(\text{O}^- - \text{O}_2)$ is then determined from the best fit value of E_0 .

4. Results and discussion

Typical excitation functions for the O_3^-/He reactions are illustrated in fig. 1. Table 1 summarizes the translational energy thresholds derived from these curves and from similar data obtained using Ar and CO_2 as target gases. The uncertainty in the values of E_0 is ± 0.1 eV in the center of mass system, and the uncertainty in n is on the order of ± 0.1 . These errors

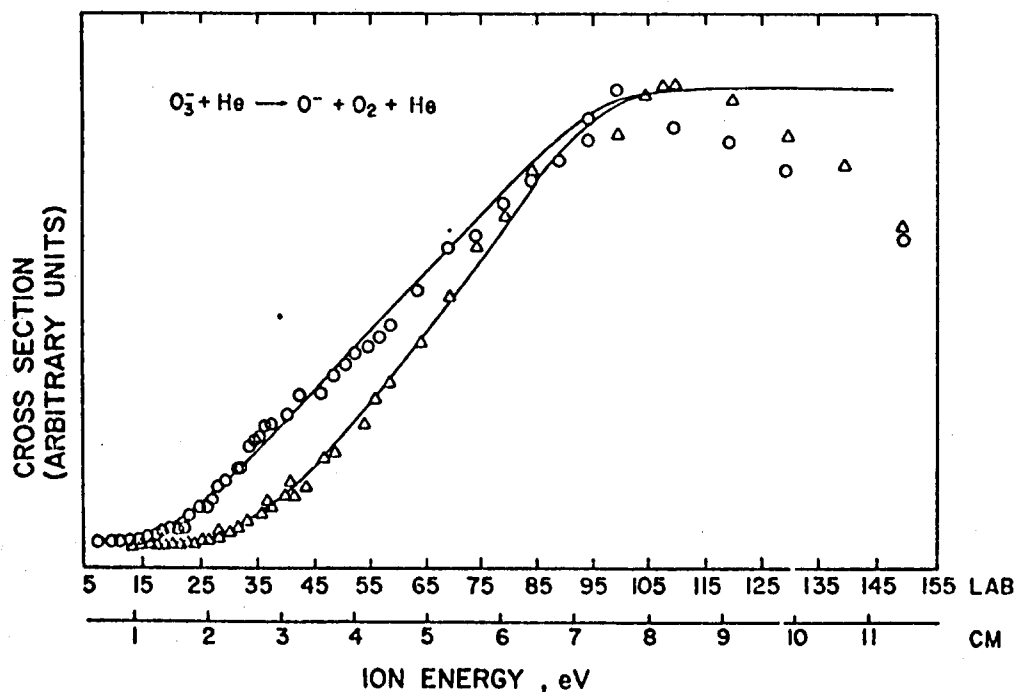


Fig. 1. Cross section for the reaction $\text{O}_3^- + \text{He} \rightarrow \text{O}^- + \text{O}_2 + \text{He}$ as a function of translational energy. Δ - experimental data for O_3^- from $\text{OH}^+(\text{O}_3, \text{OH})\text{O}_3^-$; \circ - data for O_3^- from $\text{O}^-(\text{O}_3, \text{O})\text{O}_3^-$. Solid lines are the calculated "best-fit" excitation functions.

Table 1

Best fit values of E_0 and n obtained by convoluting $\sigma = A(E_T - E_0)^n/E_{rel}^{2n}$ with the energy distribution for the collision-induced dissociation reactions, $O_3^- + X \rightarrow O^- + O_2 + X$

Target gas X	O_3^- from $O^-(O_3, O)O_3^-$		O_3^- from $OH^-(O_3, OH)O_3^-$	
	n	E_0 (eV, c.m.)	n	E_0 (eV, c.m.)
He	2.1	1.08	2.1	1.77
Ar	2.1	0.95	2.0	1.82
CO ₂	2.0	0.86		
	average 0.96		average 1.80	

a) E_T was actually equated with E_{rel} (or $E_{c.m.}$) in these computer fit calculations.

are estimated from the ranges of E_0 and n which yield a good fit to the experimental data.

Two different threshold energies were obtained depending upon the method of formation of O_3^- , but irrespective of the target gas employed for CID. O_3^- produced via reaction (1) gave in each case a lower threshold than the one produced via reaction (2). These thresholds apparently represent the bond dissociation energies of two different states of O_3^- . The average values for $D(O^- - O_2)$ are calculated to be 0.96 ± 0.1 eV and 1.80 ± 0.1 eV, respectively.

Taking $D(O^- - O_2) = 1.8$ eV, in conjunction with the known electron affinity of the oxygen atom, 1.462 eV [7] and the bond dissociation energy of neutral ozone, 1.05 eV [8], one can calculate the electron affinity of ozone to be $EA(O_3) = 2.2$ eV. This value is in very good agreement with recent results obtained from endoergic charge transfer [9] and collisional ionization [10] experiments.

The enthalpy changes for reactions (1) and (2) are $\Delta H_1 = -0.75$ eV and $\Delta H_2 = -0.37$ eV, respectively (the electron affinity of the OH radical is 1.825 eV [11]). Reaction (1) is thus more exoergic than (2) and the results described above indicate that, within experimental error, the total exoergicity of this reaction appears as internal excitation energy of the O_3^- product, since the ion must be formed with an energy of $(1.80 \pm 0.1) - (0.96 \pm 0.1) = 0.84 \pm 0.2$ eV above the energy of the most stable ground state configuration of O_3^- . On the basis of the pressures existing in the ion source ($P \leq 0.1$ torr), the rate coefficient for collisional deactivation of the excited O_3^- must be $< 10^{-11}$ cm³/s in order for the excited O_3^- to survive.

The transit time required for O_3^- to reach the collision chamber is such that the lifetime of this species must be on the order of several microseconds.

The excess energy of O_3^- produced from reaction (1) may be in the form of vibrational excitation, as has been suggested to be the case for NO_2^- [12]. Vibrational excitation of positive ions in the electronic ground state is known to cause a reduction in the translational energy thresholds for CID by an amount equal to the degree of excitation [13]. Alternatively, the excited O_3^- may be formed in an electronically excited state which correlates to ground state fragments. The only possible candidate for such an electronic state is the 2A_1 state, for which the exact energy above the ground 2B_1 state is still unknown [14]. This state has not yet been observed spectroscopically, but by analogy with a similar state in SO_2 [15] (the 1B_1 state) the lifetime should be quite long. Still another possibility is that the O_3^- formed in reaction (1) is a cyclic isomer of the open-chain O_3^- formed in reaction (2). Recent theoretical calculations [16,17] have indicated that the ground state potential surface of neutral $O_3(^1A_1)$ has two minima occurring at bond angles of 117° and 60° respectively, with the 60° configuration corresponding to a metastable ring structure. Similar behavior for O_3^- is quite plausible [18].

The present CID data provide information relative to the structure, excited states, and reactivities of the O_3^- ion which is complementary to that which has been obtained from photodissociation [19] and flow-drift [20] experiments. The latter are less suitable for the detection of excited states owing to the high pressures and long ion residence times which characterize the experiments and which dictate that reactant ions are usually fully relaxed.

Acknowledgement

This work was supported by the Air Force Office of Scientific Research under Contract No. F44620-76-C-0007 with Wright State University. The authors are grateful for the invaluable assistance of C.D. Miller with the tandem mass spectrometer, and for the assistance of D.T. Terwilliger in programming the computer fit calculations. We are indebted to D.L. Albritton for providing us a preprint of the manuscript describing studies of the O_3^-/CO_2 reaction conducted at the NOAA laboratories.

References

- [1] E.F. Ferguson, *Accounts Chem. Res.* 3 (1970) 402.
- [2] T.O. Tiernan and R.E. Marcotte, *J. Chem. Phys.* 53 (1970) 2107;
R.P. Clow, T.O. Tiernan and B.M. Hughes, 22nd Conference of the American Society of Mass Spectrometry (ASMS), Philadelphia (1974).
- [3] R.D. Levine and R.B. Bernstein, *Chem. Phys. Letters* 11 (1971) 552;
C. Rebeck and R.D. Levine, *J. Chem. Phys.* 58 (1973) 3942.
- [4] C. Lifshitz, B.M. Hughes and T.O. Tiernan, *Chem. Phys. Letters* 7 (1970) 469;
T.O. Tiernan, B.M. Hughes and C. Lifshitz, *J. Chem. Phys.* 55 (1971) 5692;
T.O. Tiernan, in: *Interactions between ions and molecules*, ed. P. Ausloos (Plenum Press, New York, 1975) pp. 353, 601--604.
- [5] S. Braslavsky and J. Heicklen, *Intern. J. Chem. Kinetics* 8 (1976) 801.
- [6] T.O. Tiernan and R.L.C. Wu, *Advan. Mass Spectrom.* 7, to be published;
D.G. Hopper, A.C. Wahl, R.L.C. Wu and T.O. Tiernan, *J. Chem. Phys.* 65 (1976) 5474.
- [7] R.S. Berry, *Chem. Rev.* 69 (1969) 533.
- [8] J.L. Gole and R.N. Zare, *J. Chem. Phys.* 57 (1972) 5331.
- [9] C. Lifshitz, R.L.C. Wu and T.O. Tiernan, to be published.
- [10] E.W. Rothe, S.Y. Tang and G.P. Reck, *J. Chem. Phys.* 62 (1975) 3829.
- [11] H. Hotop, T.A. Patterson and W.C. Lineberger, *J. Chem. Phys.* 60 (1974) 1806.
- [12] B.A. Huber, P.C. Cosby, J.R. Peterson and J.T. Moseley, *J. Chem. Phys.* 66 (1977) 4520.
- [13] W.A. Chupka, in: *Ion-molecule reactions*, ed. J.L. Franklin (Plenum Press, New York, 1972) pp. 70--73;
T. Baer, L. Squires and A.S. Werner, *Chem. Phys.* 6 (1974) 325.
- [14] M.F. Jacox and D.E. Milligan, *J. Mol. Spectry.* 43 (1972) 148.
- [15] K.F. Greenough and A.B.F. Duncan, *J. Am. Chem. Soc.* 83 (1961) 555.
- [16] P.J. Hay, T.H. Dunning Jr. and W.A. Goddard III, *Chem. Phys. Letters* 23 (1973) 457; *J. Chem. Phys.* 62 (1975) 3912.
- [17] P.G. Burton and M.D. Harvey, *Nature* 266 (1977) 826.
- [18] P.G. Burton, private communication, May 1977.
- [19] P.C. Cosby, R.A. Bennett, J.R. Peterson and J.L. Moseley, *J. Chem. Phys.* 63 (1975) 1612;
P.C. Cosby, J.H. Ling, J.R. Peterson and J.T. Moseley, *J. Chem. Phys.* 65 (1976) 5267.
- [20] I. Dotan, J.A. Davidson, G.E. Streit, D.L. Albritton and F.C. Fehsenfeld, A Study of the Reaction $O_3 + CO_2 \rightleftharpoons CO_3 + O_2$ and its Implication on the Thermochemistry of CO_3 and O_3 and their Negative Ions, *J. Chem. Phys.*, submitted for publication.

Thermochemical Data for Molecular Negative Ions From Collisional-Dissociation Thresholds

Thomas O. Tiernan and Richard L. C. Wu

Department of Chemistry, Wright State University, Dayton, Ohio 45431, U.S.A.

Previously reported experiments¹ conducted in our laboratory demonstrated that thresholds measured for collision-induced dissociation reactions of positive molecular ions could be used in conjunction with other thermodynamic data to obtain ionic bond dissociation energies. In the earlier beam-collision chamber experiments, the thresholds determined for these reactions were not corrected for the effects of energy broadening resulting from the velocity distributions of the incident ion beam and the target gas. In the present study of collision-induced dissociation reactions of the molecular negative ions, NO^- , NO_2^- , N_2O^- , O_2^- and CO_3^- , the experimental excitation functions (that is, the cross-sections as a function of energy) have been treated to take account of energy broadening and the thresholds have been more reliably deduced. These thresholds yield the enthalpy of formation of the reactant negative ions, which in turn can be used to calculate electron affinities for the corresponding neutral molecules. Comparison of the threshold behavior with the predictions of a statistical theory of the dissociation process also provides insights into the dissociation mechanism.

EXPERIMENTAL

Instrumentation and Procedures

The apparatus utilized for these experiments is an in-line tandem mass spectrometer which has been described previously.^{1, 2} The reactant ion beam, produced in an electron impact source is mass- and energy-analyzed by a double-focusing mass spectrometer, retarded by a slot lens which controls the collision energy, and impacted on the target gas in a collision chamber. The energy distribution of the projectile ion beam is ± 0.3 eV (Lab) over the entire accessible energy range of 0.3–180 eV. Product ions, produced by reactions in the shielded field-free collision chamber, exit from the reaction zone, are reaccelerated, and enter a second double-focusing mass spectrometer where mass analysis occurs. The ion detector is an electron multiplier coupled to a pulse counter. The collector stage of the apparatus is fixed and preferentially accepts product ions scattered in the forward direction (0° scattering angle). Possible discrimination effects have been discussed in other publications.¹ For the experiments reported herein,

the temperature of the collision chamber was maintained at 160°C, and collision chamber pressure was typically 4×10^{-2} Torr. Pressure-dependence studies were conducted over the range of collision chamber pressures, 0.5×10^{-2} – 4×10^{-2} Torr, to ensure that the observed product ions result from single bimolecular collision events. Cross-sections for the observed reactions were calculated relative to the cross-section for the O^-/NO_2 charge-transfer reaction, which is 63 Å^2 at 0.3 eV (Lab) ion energy.³

Reactant negative ions were formed by electron impact on various pure gases or mixtures. These ions and the respective molecules from which they were derived were as follows: NO^- , N_2O ; NO_2^- , mixture of N_2O and NO_2 ; N_2O^- , N_2O ; O_2^- , mixture of N_2O and O_2 ; CO_3^- , mixture of CO_2 and N_2O .

Determination of Dissociation Thresholds

Endoergic collision-induced dissociation reactions of the type



exhibit translation energy thresholds which may be assumed to correspond to the ionic bond dissociation energy. According to the statistical model for such processes developed by Rebick and Levine,⁴ the energy dependence of the cross-section in the post-threshold region has the form

$$\sigma(E_{\text{rel}}) = \frac{A_0(E_t - E_0)^n}{E_{\text{rel}}} \quad (2)$$

where E_t is the total energy available from the collision (c.m.), E_0 is the threshold energy, and E_{rel} is the relative energy for the colliding pair. The value of the exponent n depends upon the mechanism of the reaction. The statistical theory⁴ predicts that $1.9 < n < 2.2$ for a direct process, where in the final state all three particles are unbound, and $1.5 < n < 1.8$ for an indirect process, where two of the three particles are *quasi*-bound in the final state. The coefficient A_0 is a function of the internal energy of the reactant ion. In the present study, however, the reactants and products are assumed to be in their ground states and A_0 is thus independent of the internal states. When it is converted to the laboratory system of energy, Eqn (2) reduces to

$$\sigma(E_l) = \frac{A'_0(E_l - E_0)^n}{E_l} \quad (3)$$

where E_l is the effective energy for the reacting ion-neutral pair.

In the actual experiments, E_l represents a distribution of energies, owing to the translational energy spread of the incident ion beam and the velocity distribution of the target molecules which leads to Doppler broadening.^{5,6} The experimentally measured cross-section is therefore related to the absolute cross-section by the expression

$$\sigma_{\text{exp}}(E_{l0}) = \int_0^\infty \sigma(E_l) (\omega E_l | E_{l0}) dE_l \quad (4)$$

where $\sigma(E_i)$ is given by Eqn (3) and $\omega(E_i|E_{i0})$, the effective energy-distribution function for the collision, is given by

$$\omega(E_i|E_{i0}) dE_i = \left\{ (a\Pi^{1/2})^{-1} \exp \left[-\frac{(E'_i - E_{i0})^2}{a^2} \right] \right\} \left\{ (\Pi)^{-1/2} \Delta^{-1} \exp \left[-\frac{(E_i - E'_i)^2}{\Delta^2} \right] \right\} dE'_i dE_i \quad (5)$$

The first bracketed term in Eqn (5) is the energy distribution for the incident ion translational energy about the set point E_{i0} , where E'_i is the particular ion energy in the laboratory frame and the parameter a is computed to be 0.2 from the fact that the full-width at half-maximum of the reactant ion translational energy distribution is 0.3 eV. The second bracketed term in Eqn (5) is the energy distribution arising from the thermal motion of the target molecules and Doppler broadening,^{5,6} where Δ , the Doppler width, is given by $\Delta = 2(m_i E'_i kT/m_n)^{1/2}$, and m_i and m_n are the masses of the ion and neutral species respectively. The Doppler width is the half-width of the probability distributions at $1/e$ of the maximum height.

In order to enable one to deduce thresholds from the experimental data, the following procedures were employed. The cross-section as a function of energy for a given reaction was calculated using Eqn (4) for various assumed values of n and E_0 . The calculated curves are then fitted to the experimental data points in the energy region from onset up to the energy at which the experimentally measured cross-section attained a maximum. The optimum values of n and the threshold E_0 were then obtained from the calculated cross-section curve which gives the best fit to the experimental data.

Thermochemistry

The energy threshold determined as described above for a particular collision-induced dissociation process is taken to correspond to ΔH_r , the enthalpy of the dissociation reaction (Reaction 1). If it is assumed that the reactants and products are in their ground states at threshold, the heat of formation of the molecular ion, AB^+ , is given by

$$\Delta H_f^\circ(AB^+) = \Delta H_f^\circ(A^+) + \Delta H_f^\circ(B) - \Delta H_r \quad (6)$$

or

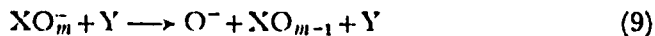
$$\Delta H_f^\circ(AB^+) = \Delta H_f^\circ(A^+) + \Delta H_f^\circ(B) - E_{th} \quad (7)$$

If the heat of formation of the neutral molecule AB is known, the electron affinity of AB can then be calculated from the expression

$$E.A.(AB) = \Delta H_f^\circ(AB) - \Delta H_f^\circ(AB^+) \quad (8)$$

RESULTS AND DISCUSSION OF RESULTS

Cross-sections were measured as a function of incident ion translational energy for the collisional dissociation reactions of NO^+ , NO_2^+ , N_2O^+ , O_2^+ and CO_2^+ impacted on various atomic and molecular targets (Xe, Kr, Ar, Ne, He, N_2 , O_2 , NO and CO). These processes, which are of the general form



are all endoergic and exhibit energy thresholds. The effective energy distribution for such collisions, calculated using Eqn (5), is illustrated for the case of the NO^-/Xe reaction in Fig. 1. Figure 2 shows typical experimental cross-section data as a function of translational energy for dissociation of NO^- upon impact with several different targets. Figure 3 presents excitation functions calculated for the NO^-/CO collisional-dissociation reaction using Eqn (4) for various combinations of n and E_0 . Figure 3 also demonstrates the fitting of these calculated functions to the experimental data points for this reaction. The sensitivity of this procedure is such that the best values of n and E_0 can be

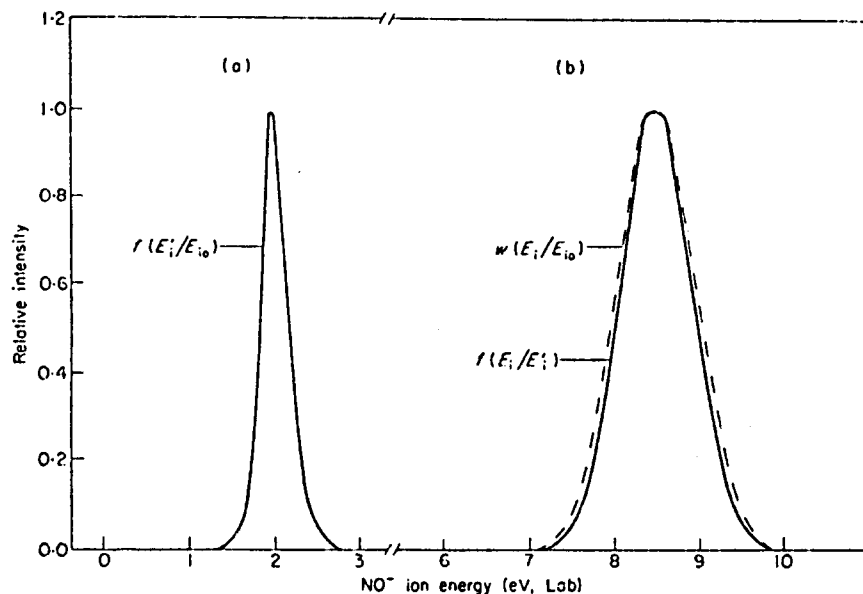


Fig. 1. (a) Energy distribution of the NO^- incident ion beam. (b) Calculated relative energy distribution functions for the reaction pair NO^-/Xe at 8.5 eV NO^- laboratory energy and a temperature of 443 K. The solid line represents the calculated function for a mono-energetic ion beam and a Boltzmann distribution of target molecules. The dashed line represents the calculated function incorporating both the ion translational energy distribution and the neutral velocity distribution.

deduced to within ~ 0.1 and ~ 0.1 eV respectively. When such energy corrections are made, the energy thresholds determined from the reactions of NO^- with Xe, Kr, N_2 , CO and NO are identical (within the experimental error), and indicate an $\text{N}-\text{O}^-$ bond dissociation energy of 5.0 ± 0.1 eV. When this value is used in Eqn (7), it leads to an electron affinity value of 0.02 ± 0.1 eV for NO. Table 1 summarizes the bond dissociation energies derived similarly for all the negative ions investigated in the present study, and the electron affinities calculated for the corresponding neutral molecules. As is also indicated in Table 1, these values are in good agreement with recently reported electron affinity data obtained by several other techniques, including laser photodetachment, collisional ionization and endoergic charge transfer. It appears, therefore, that the collisional dissociation methods applied here yield generally reliable ionic bond dissociation energies. This technique should be particularly useful

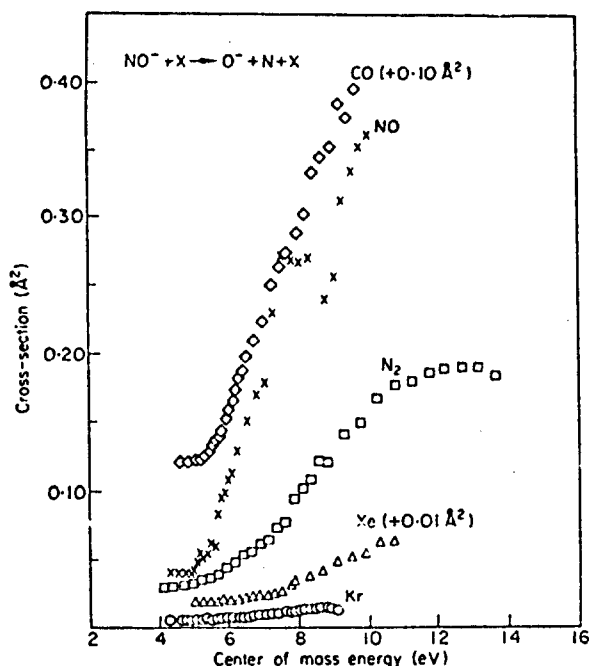


Fig. 2. Energy dependence of the cross-section for the collision-induced dissociation of NO^- on various atomic and molecular targets. Where noted, the curves have been scaled by the indicated factors.

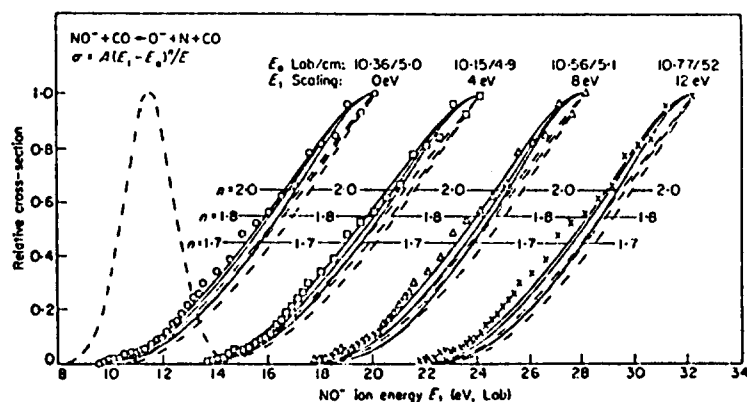


Fig. 3. Effects of varying n and E_0 on the calculated excitation functions (solid curves) for the NO^-/CO collisional-dissociation reaction. Dotted-line curves are the threshold functions predicted by the statistical theory. The dotted-line curve at left of figure is the calculated energy distribution function for the reaction, which is convoluted with the threshold functions to obtain the solid-line curves. Points are experimental data. Where noted, the curves are shifted by the indicated scaling factors.

for more complex negative molecular ions (such as hydrates) which may be less amenable to photodetachment, and for many of which the corresponding neutral species are unstable.

In Figure 3, it is seen that a value of $n=1.7$ is determined from the curve fitting procedure for the NO^-/CO reaction. According to the statistical model of the dissociation process,⁴ this is indicative of an indirect process in which two of the three particles in the final state are *quasi*-bound (in the present case, the target is considered to be a single particle even if it is diatomic as in the case of CO). For the negative ions of interest here, such *quasi*-bound final states would be more likely expected in the case of reactions with N_2 , CO , O_2 and NO targets, than for the reactions with rare gas targets. Indeed, all negative ion reactions

TABLE 1

Bond dissociation energies for molecular negative ions obtained from collisional-dissociation thresholds and calculated electron affinities

Ion (XO_m^-)	$\text{O}^- - \text{XO}_{m-1}$ bond dissociation energy (eV)	Electron affinity of XO_m (eV)	Electron affinity obtained from other experiments ^a
NO^-	5.0 ± 0.1	0.02 ± 0.1	0.024 ± 0.010 (PD); ⁷ 0.1 ± 0.1 (CI); ⁸ $\geq 0.015 \pm 0.1$ (CT) ⁹
O_2^-	4.1 ± 0.1	0.44 ± 0.1	0.44 ± 0.01 (PD); ¹⁰ $\geq 0.45 \pm 0.1$ (CT) ⁶
NO_2^-	4.0 ± 0.1	2.4 ± 0.1	2.5 ± 0.1 (CI); ^{8, 11} 2.3 ± 0.1 (CT) ⁹
N_2O^-	0.43 ± 0.1	0.22 ± 0.1	$> -0.1 \pm 0.1$ (CI); ⁸ 0.6 (CT) ¹²
CO_2^-	2.0 ± 0.1	3.1 ± 0.2	> 2.7 (PD) ¹³

^a Symbol following the data designates the type of experiment: PD=photodetachment; CI=collisional ionization; CT=endoergic charge transfer.

with rare gas targets which were observed in the present study yielded values of $n > 1.9$, as the statistical theory⁴ predicts for direct processes, in which the final states are unbound.

The reactions of N^{16}O^- and $^{16,16}\text{O}_2^-$ with N^{18}O were also studied to determine if the O^- product originates entirely from the projectile ion. In both reactions, $^{16}\text{O}^-$ and $^{18}\text{O}^-$ products were observed, again indicating that some *quasi*-bound intermediate state is formed which results in isotopic scrambling. The thresholds for production of $^{16}\text{O}^-$ and $^{18}\text{O}^-$ were found to be identical, and the relative cross-sections at the maximum are in the ratio, $\sigma_{^{16}\text{O}^-} : \sigma_{^{18}\text{O}^-} \sim 1:1$ and $2:1$ respectively.

The collision-induced dissociation reactions of the larger negative ions studied here (NO_2^- , N_2O^- , CO_2^-) are characterized by values of n which generally exceed the limits predicted by the Reibick-Levine model,⁴ and the distinction between reactions with rare gas and molecular targets is less evident.

ACKNOWLEDGEMENT

This work was supported by the Air Force Office of Scientific Research under Contract No. F44620-76-C-0007 with Wright State University.

References

1. T. O. Tiernan and R. E. Marcotte, *J. Chem. Phys.* **53**, 2107 (1970).
2. B. M. Hughes and T. O. Tiernan, *J. Chem. Phys.* **55**, 3419 (1971).
3. J. F. Paulson, *Adv. Chem. Ser.* **58**, 28 (1966).
4. C. Rebick and R. D. Levine, *J. Chem. Phys.* **58**, 3942 (1973).
5. P. J. Chantry, *J. Chem. Phys.* **55**, 2746 (1971).
6. T. O. Tiernan, B. M. Hughes and G. Lifshitz, *J. Chem. Phys.* **55**, 5692 (1971).
7. M. W. Siegel, R. J. Celotta, J. L. Hall, J. Levine and R. A. Bennett, *Phys. Rev.* **A6**, 607 (1972).
8. S. J. Nalley, R. N. Compton, H. C. Schweinler and W. E. Anderson, *J. Chem. Phys.* **59**, 4125 (1973).
9. B. M. Hughes, G. Lifshitz and T. O. Tiernan, *J. Chem. Phys.* **59**, 3162 (1973).
10. M. W. Siegel, R. J. Celotta, J. L. Hall, J. Levine and R. A. Bennett, *Phys. Rev.* **A6**, 603 (1972).
11. G. B. Lefert, W. M. Jackson and E. W. Rothe, *J. Chem. Phys.* **58**, 5801 (1973).
12. T. O. Tiernan and R. P. Clow, *Adv. Mass Spectrom.* **6**, 295 (1974).
13. J. P. Moseley, P. C. Cosby, R. A. Bennett and J. R. Peterson, *J. Chem. Phys.* **62**, 4826 (1975).

Discussion

R. W. Rozett (Fordham University, New York): Your experimental curve near threshold showed a slight shoulder. Isn't there a danger that you are fitting your curve to two states rather than to one?

T. O. Tiernan: That is always a possibility; little is known about negative ion states. The shoulder is not very pronounced.

Negative ion-molecule reactions of ozone and their implications on the thermochemistry of O_3^-

C. Lifshitz,^{a)} R. L. C. Wu, T. O. Tiernan, and D. T. Terwilliger

The Brehm Laboratory and Department of Chemistry, Wright State University, Dayton, Ohio 45435
(Received 22 August 1977)

An in-line double mass spectrometer has been employed to determine reaction rate coefficients and excitation functions for several types of negative ion reactions involving ozone. The interactions studied include electron transfer reactions, such as $M^- + O_3 \rightarrow M + O_3^-$ (where $M^- = O^-$, OH^- , F^- , Cl^- , Br^- , I^- , S^- , SH^- , Cl_2^- , C_2H^- , NO_2^- , and CO_3^-) and particle transfer reactions, such as $MO^- + O_3 \rightarrow M + O_3$ (where $MO^- = O_2^-$, NO_2^- , NO_3^- , CO_3^-). Translational energy thresholds have been determined for those reactions which are endothermic by applying exact Doppler corrections for the thermal motion of the neutral as well as corrections for the translational energy distribution of the projectile ions. These experiments place a lower limit of $2.26_{-0.06}^{+0.04}$ eV on the electron affinity of ozone. This value is in excellent agreement with the value computed from the bond dissociation energy of O_3^- in its most stable configuration, $D_0^0(O-O_2) = 1.80$ eV, as deduced from measurements of the translational energy thresholds for the collisional dissociation process, $O_3^- + M \rightarrow O^- + O_2 + M$, where $M = He, Ar$. Further implications of these experiments with respect to the structure, thermochemistry, and excited states of O_3^- are discussed.

I. INTRODUCTION

Negative ion-neutral reactions involving ozone have attracted considerable attention owing to their importance in atmospheric chemistry.¹⁻¹⁰ Various experimental techniques have been employed to study these reactions, including flowing afterglow^{1,3,5-7} and static drift tube⁸ methods, as well as ion beam techniques.^{2,4,9} The former have provided reliable rate coefficients for thermal energy ion reactions involving ozone while the latter yielded excitation functions at somewhat higher ion translational energies (>1 eV). In addition, a recently reported study of the reaction between O_3^- and CO_2



was accomplished using flow-drift techniques, in the intermediate range between thermal energy and a few eV.¹⁰ Still, several questions remain to be answered with respect to ozone negative ions, a major uncertainty which persists being the bond dissociation energy of O_3^- . The value of the latter quantity which is calculated from ΔH for Reaction (1) is in disagreement with the value derived from the electron affinity of O_3 which is reported in the literature.¹⁰

Previous determinations of the electron affinity (E. A.) of ozone have been made using photodetachment methods,^{11,12} collisional ionization,¹³ and endothermic charge transfer¹⁴ experiments, and lattice energy¹⁵ and configuration interaction calculations.¹⁶ The reported values of E. A. (O_3) obtained from these studies range from 1.9 to 2.15 eV, with estimated uncertainties as high as 0.4 eV. Among the lowest of these values is that determined by Berkowitz, Chupka, and Gutman¹⁴ from the energy threshold for the I^-/O_3 charge transfer reaction, where the I^- reactant was produced by photon impact (ion pair formation). It is interesting to note that in the same study the latter authors reported a lower limit for

the electron affinity of NO_2 (≈ 2.04 eV) which is considerably lower than the now accepted value, E. A. (NO_2) = 2.36 ± 0.1 eV.¹⁷⁻²⁰ A review of the literature, however, reveals that the first reported investigation which obtained the currently accepted NO_2 electron affinity was that conducted in our laboratory,²¹ and this study was employed endothermic charge transfer measurements, in which Br^- was the projectile ion. At the same time, the lower limit for E. A. (NO_2) which we obtained by similar methods, but using I^- as the projectile ion, was somewhat lower (2.21 eV). This suggested that there might be an inherent difference in the threshold behavior of I^- and Br^- reactants.

Several experiments have recently been reported in which direct dissociation of O_3^- has been observed. Laser photodissociation of O_3^- was shown to yield O^- and O_2 , and this is the major reaction channel at photon energies between 1.8 and 2.7 eV, although photodetachment is also energetically feasible.^{22,23} Collisional dissociation of O_3^- was observed in flow-drift experiments, and it was determined that the bond dissociation energy of O_3^- is lower than that of CO_3^- .¹⁰ However, neither of these experiments has provided an accurate value for the bond dissociation energy $D_0^0(O^-O_2)$, in the O_3^- ion.

The above considerations suggested the desirability of investigating additional endothermic charge transfer reactions of negative ions with ozone. In the experiments reported here, we have employed a tandem mass spectrometer, applied previously for many similar negative ion studies,^{17,21,24-29} and have observed the reactions of some 15 different negative ions with O_3 . In some cases, both electron and particle (O^- and O) transfer reactions have been detected. Energy thresholds for such endothermic charge transfer reactions yield, of course, only lower limits for the electron affinity of the molecular target. However, if a series of projectile ions are employed which indicate a range of electron affinity values, as in the present experiments, then the highest value obtained will be closest to the

^{a)}On sabbatical leave from The Hebrew University of Jerusalem, 1976-77.

true electron affinity; thus, the value of this approach.

In other experiments described in the present paper, translational energy thresholds for collisional dissociation²⁹ of O_3^- have been determined, yielding an accurate value of the bond dissociation energy of O_3^- , in what is believed to be its most stable ground state configuration.

II. EXPERIMENTAL

A. Instrumentation and techniques

An in-line tandem mass spectrometer was utilized in this study. The instrument has been described in detail previously.^{17,24-27,30} Briefly, it is a beam-collision chamber apparatus which provides mass analysis of the product ions. The collection stage is fixed at 0° (LAB) scattering angle. The projectile ion is formed in the electron impact ion source of the first stage mass spectrometer, which produces a mass and energy resolved beam. This beam is then decelerated in a retarding lens and impacted upon the target gas in the field free collision chamber maintained at a constant temperature. Collision chamber temperatures employed in the present studies range from 30 to 170 $^\circ\text{C}$. The energy spread of the projectile ion beam entering the collision cell is ± 0.3 eV (LAB) over the ion energy range 0.3 to about 180 eV (LAB). Product ions are mass analyzed in the second stage mass spectrometer. Pulse counting techniques are used to measure the product ion current.

The gases used in these studies were reagent grade and were obtained from the Matheson Co. Ozone was produced by a Tesla coil discharge through oxygen at low pressure (~ 10 torr) in a vacuum system which was free of hydrocarbon grease or mercury.³¹ The ozone was condensed at -196°C and residual oxygen was removed by pumping on the trapped O_3 . The latter was then vaporized immediately into the ion source of the first stage mass spectrometer or into the collision chamber, as required by the specific reaction studied.

Reactant halide ions were produced by dissociative electron attachment to CH_3F , CCl_4 , CH_3Br , and CH_3I . The CO_3^- reactant was produced in the primary ion source by the ion molecule association reaction, $\text{O}^- + \text{CO}_2 + \text{M} \rightarrow \text{CO}_3^- + \text{M}$. The ions O^- and S^- were produced by dissociative electron capture in N_2O and COS , respectively. The OH^- ion was produced from H_2O by a sequence of reactions involving first, dissociative electron attachment yielding O^- and H^- , followed by the ion molecule reactions, $\text{O}^- (\text{H}_2\text{O}, \text{OH}) \text{OH}^-$, and $\text{H}^- (\text{H}_2\text{O}, \text{H}_2) \text{OH}^-$. The ions NO_2^- and Cl_2^- were formed in mixtures of their parent gases with N_2O , by electron transfer from O^- . The ions SH^- and C_2H^- were produced in mixtures of H_2S or C_2H_2 , respectively, with N_2O , by both direct dissociative electron attachment and by proton transfer to O^- . The projectile ion O_3^- was produced by charge transfer reactions involving O^- or OH^- and O_3 , as discussed in later sections.

The ions are all formed at source pressures ≤ 0.1 torr. It is estimated that they undergo approximately 30 collisions within the source chamber before exiting. If they are initially formed in some excited state, the

rate coefficient for collisional deactivation must be $\leq 10^{-11}$ cm^3/sec in order for the excited species to survive. The transit time required for a projectile ion to reach the collision chamber is such that an excited species must have a lifetime of the order of 10 μsec or longer to survive.

Charge transfer reactions of S^- and SH^- with O_3 were observed by using the low intensity isotopic ions $^{34}\text{S}^-$ and $^{34}\text{SH}^-$ as reactants, in order to distinguish the O_3^- product from the SO^- product which would normally appear at the same nominal mass to charge ratio.

Associative detachment reactions were studied using a method recently developed in our laboratory.²⁷ In these experiments, the target gas in the collision chamber consists of a mixture of the desired neutral reactant and SF_6 . The latter serves as a scavenger for the detached slow electrons which are monitored by measuring the resultant SF_6^- currents.

All charge transfer, particle transfer or collision-induced dissociation reaction rate coefficients (or cross sections) were determined relative to the rate (or cross section) for the reaction $\text{O}^- (\text{NO}_2, \text{O}) \text{NO}_2^-$. Associative detachment reaction rate coefficients (or cross sections) were determined relative to the rate for the reaction $\text{O}^- (\text{NO}, \text{NO}_2) e^-$.

B. Data treatment

The product (secondary) ion intensity $I_s(E_{10})$ is converted to an observed apparent cross section using the relation,^{27,28}

$$\sigma_{\text{app}}^{\text{obs}}(E_{10}) = C[I_s(E_{10})/P_t]/I_p(E_{10}), \quad (2)$$

where $I_p(E_{10})$ is the primary ion intensity, E_{10} is the nominal reactant ion energy in the laboratory frame, P_t is the target gas pressure, and C is a conversion factor. C is determined at $E_{10} = 0.3$ eV using the previously reported cross section of 63 \AA^2 , and the product ion intensity observed in the present study for the charge transfer reaction $\text{O}^- (\text{NO}_2, \text{O}) \text{NO}_2^-$.²⁷

The absolute cross section $\sigma(E_{\text{rel}})$ and its dependence upon the true relative energy of the ionic and neutral reactants (the so-called excitation function) must be deduced from the experimentally observed dependence of $\sigma_{\text{app}}^{\text{obs}}(E_{10})$ on the nominal ion laboratory energy E_{10} . The experimentally obtained excitation function differs from the absolute function owing to two factors, (1) the experimental spread in the incident ion energies and (2) the thermal (Doppler) motion of the neutral target. In earlier treatments of similar data,²⁴ we have neglected the first factor and treated the second by an approximate one-dimensional Maxwellian distribution function due to Bethe and Placzek.³² More recently,²⁸ we have modified the data reduction procedure to take account of both factors (1) and (2), but have still treated Doppler broadening using the Bethe approach. In the present study, we have adopted the exact treatment of the Doppler broadening developed by Chantry,³³ in conjunction with the exact treatment of the incident ion beam energy distribution. In the following, the formulas relating

σ_{app}^{calc} to the absolute cross section, σ , will be developed.

Let m_1 be the mass of the incident ion and m_2 be the mass of the neutral target, and define the quantities,

$$E' = [(m_1 + m_2)/m_2] E_{ion} \quad (3)$$

$$a = m_2/m_1 kT, \quad (4)$$

where T is the temperature of the target molecules. It has been shown previously¹² that, if the incident ion energy distribution is ignored, the calculated apparent cross section is given by the expression,

$$\sigma_{app}^{calc}(E_{ion}) = \int_0^\infty \sigma(E') \left(\frac{E'}{E_{ion}} \right)^{1/2} \left(\frac{a}{4\pi E_{ion}} \right)^{1/2} \{ \exp[-a\{(E')^{1/2} - (E_{ion})^{1/2}\}^2] - \exp[-a\{(E')^{1/2} + (E_{ion})^{1/2}\}^2] \} dE'. \quad (5)$$

Substituting $\epsilon = \sqrt{E'}$ into the above gives,

$$\sigma_{app}^{calc}(E_{ion}) = \frac{1}{E_{ion}} \left(\frac{a}{\pi} \right)^{1/2} \int_0^\infty \{ \exp[-a\{\epsilon - (E_{ion})^{1/2}\}^2] - \exp[-a\{\epsilon + (E_{ion})^{1/2}\}^2] \} \sigma(\epsilon) \epsilon^2 d\epsilon. \quad (6)$$

We assume that the initial ion energy spread can be represented by a Gaussian function. If the nominal beam energy is E_{ion} , then the probability of the ion having energy E'' is given by,

$$P(E'') = \frac{1}{S\sqrt{2\pi}} \exp\left[-\left(\frac{E - E''}{S}\right)^2\right], \quad (7)$$

where S is related to the energy resolution of the instrument and is determined by the requirement that the full width at half-maximum be 0.3 eV ($S = 0.2$ eV).

Substituting Eq. (7) into Eq. (6) then gives,

$$\sigma_{app}^{calc}(E_{ion}) = \frac{(a)^{1/2}}{S\sqrt{2\pi}} \int_0^\infty \int_{-\infty}^\infty \exp\left[-\left(\frac{E_{ion} - E''}{S}\right)^2\right] \{ \exp[-a\{(E'')^{1/2} - \epsilon\}^2] - \exp[-a\{(E'')^{1/2} + \epsilon\}^2] \} \frac{\sigma(\epsilon)\epsilon^2}{E''} dE'' d\epsilon \quad (8)$$

When E_{ion} is large, the second term $\{e^{-a\{(E'')^{1/2} + \epsilon\}^2}\}$ can be neglected, and if the (E'') in the first term is then expanded in a Taylor series about ϵ , the above reduces to,

$$\sigma_{app}^{calc}(E_{ion}) = \frac{(a)^{1/2}}{2S\sqrt{2\pi}} \int_0^\infty \int_{-\infty}^\infty \exp\left\{-\left[\left(\frac{E_{ion} - E''}{S}\right)^2 - \frac{2\gamma}{S}\left(\frac{E_{ion} - E''}{S}\right) + \left(\frac{\gamma^2}{S^2} + \frac{a\gamma^2}{4E''}\right)\right]\right\} d\epsilon \frac{\sigma(E'')}{(E'')^{1/2}} dE'' \quad (9)$$

where

$$\gamma = E'' - E'$$

and

$$\sqrt{E''} = \sqrt{E'} + \gamma/2\sqrt{E'}. \quad (10)$$

Note that ϵ^2 here has been replaced by E' .

This integral is easily evaluated by completing the squares in the exponent giving,

$$\sigma_{app}^{calc}(E_{ion}) = \frac{1}{(2)^{1/2}} \int_0^\infty \left(\frac{1}{S^2 + 4E''/a} \right)^{1/2} \exp\left[-\frac{(E_{ion} - E')^2}{S^2 + 4E''/a}\right] \sigma(E'') dE''. \quad (11)$$

Programs to numerically integrate Eqs. (6) and (12) have been developed in our laboratory for processing by a Hewlett-Packard 2100A computer equipped with a Tektronix 4012 CRT. Since only a single integration is required in Eq. (12), it can be more rapidly computed. Both computer programs display plots of the experimental data, σ_{exp}^{calc} , and the calculated cross sections, σ_{app}^{calc} , as a function of energy on the CRT, and the user can then vary the parameters defining $\sigma(E')$ and visually observe the results of these changes until the best fit is obtained. The $\sigma(E')$ function obtained using Eq. (12) is then used as the starting function for Eq. (6), and further optimized. The functional form used for $\sigma(E')$ is,

$$\sigma(E') = A(E' - E_0^n)/(E')^n, \quad (13)$$

where E_0 , n , m , and the normalization constant A are entered by the user.

The functional form employed for $\sigma(E')$ is related to the threshold behavior of the various types of processes studied. The best fit for endothermic charge transfer was obtained by using a linear-plus-step function, and has also been demonstrated in other cases previously.^{14,15,17} With this function, $m = 0$ and $n = 1$, up to some maximum value of the absolute laboratory energy, E_0' , above which $m = 0$ and $n = 0$. For the endothermic particle transfer reactions, the value $m = 0$ was arbitrarily assigned, and n was varied until a fit was obtained. Collision induced dissociation (CID) processes have previously been treated theoretically,¹¹ and the threshold behavior of the cross section dictates¹² that $m = 1$ and $1.9 < n < 2.2$ for a "direct" CID process.

TABLE I. Translational energy thresholds for endothermic charge transfer reactions of negative ions with O_3 .

Ionic reactant	Electron affinity (eV)	Translational energy threshold (eV)		Lower limit of O_3 electron affinity (eV)
		LAB	CM	
F^-	3.399 ^a	1.9 ^b	1.3 ₆	2.0 ₄
Cl^-	3.615 ^a	2.3 ^c	1.3 ₃	2.2 ₃
Br^-	3.351 ^a	2.9 ^b	1.1 ₆	2.2 ₁
I^-	3.061 ^a	4.0 ^b	1.1 ₆	1.9 ₆
CO_2^-	2.69 ^d	2.7 ^c	1.2	2.7 ^e

^aReference 47.^bThreshold obtained following corrections for Doppler broadening and ion energy distribution (see text).^cThreshold obtained by linear extrapolation of the data points to the noise level; no Doppler correction applied.^dS. P. Hong, S. H. Woo and E. M. Hefmy, Phys. Rev. A 15, 1563 (1977).^eOn the basis of other CO_2 reactions observed in our laboratory with molecules whose electron affinity is known, it is believed that the products of energy transfer are $CO_2 + O$. This calculation of $E_A(O_3)$ therefore takes into account the bond dissociation energy, $D_0(CO_2 - O) = 0.6$ eV (estimate b).

III. RESULTS AND DISCUSSION

A. Charge transfer reactions

1. Translational energy thresholds for endothermic charge transfer reactions of negative ions with O_3

Excitation functions were determined for reactions of e type,



where $M^- = F^-, Cl^-, Br^-, I^-$, and CO_2^- . From the measured excitation function for each reaction, the transla-

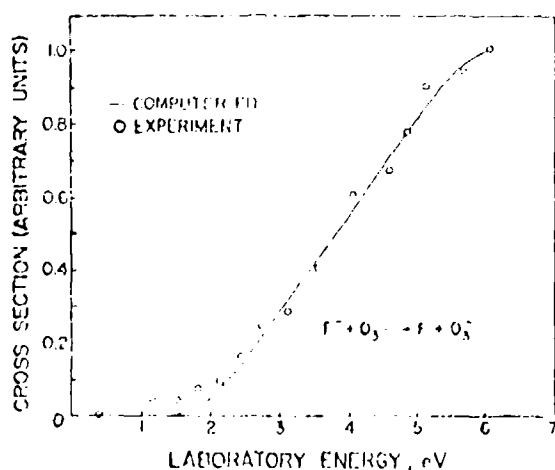


FIG. 1. Cross section for the reaction $F^- + O_3 \rightarrow F + O_3^-$ as a function of translational energy. Points are experimental data at a collision chamber temperature of 300°K; solid line is the calculated "best fit" excitation function derived by convoluting the computed effective energy distribution with the linear-plus-step threshold functions: $\sigma(E') = 0$ for $E' < 1.9$ eV; $\sigma(E') = (E' - 1.9)/3.9$ for $1.9 < E' < 5.8$ eV; and $\sigma(E') = 1.0$ for $E' > 5.8$ eV.

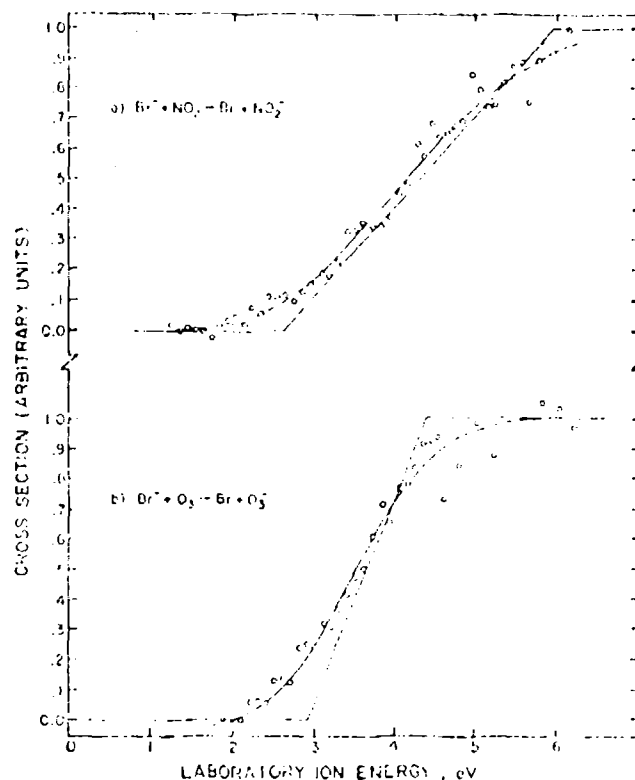


FIG. 2. Translational energy dependence of the cross section for the electron transfer reaction of Br^- with NO_2 and O_3 . Points are experimental data at 125°K; solid lines are the calculated "best fit" threshold functions and the convoluted excitation functions. The linear-plus-step threshold functions are: for NO_2 , $\sigma(E') = 0$ for $E' < 2.6$ eV; $\sigma(E') = (E' - 2.6)/3.3$ for $2.6 < E' < 5.9$ eV; and $\sigma(E') = 1.0$ for $E' > 5.9$ eV; for O_3 , $\sigma(E') = 0$ for $E' < 2.9$ eV; $\sigma(E') = (E' - 2.9)/1.4$ for $2.9 < E' < 4.3$ eV and $\sigma(E') = 1.0$ for $E' > 4.3$ eV.

tional energy threshold E_0 in the center of mass system, was determined. This threshold is equated with the endothermicity of the reaction ΔH_R and the electron affinity of ozone is then calculated from ΔH_R and from the known electron affinity of M , using the thermodynamic relation,

$$E_A(O_3) = E_A(M) - \Delta H_R. \quad (15)$$

The data for Cl^- and CO_2^- demonstrated considerable scatter and were not corrected for the Doppler motion of the neutral target. The F^- , Br^- , and I^- data were treated as explained in the previous section. The translational energy threshold, obtained for all five reactions and the lower limits for the O_3 electron affinity derived from these are summarized in Table I. The experimental data points as well as the computer fitted curves for the excitation functions of the F^- , Br^- , and I^- reactions are shown in Figs. 1, 2, and 3, respectively. In Fig. 2 we have also included similar new data for the reaction,



for comparison. The translational energy threshold for I^- electron transfer to O_3 and the ozone electron affinity deduced from it (Fig. 3 and Table I) are in excellent

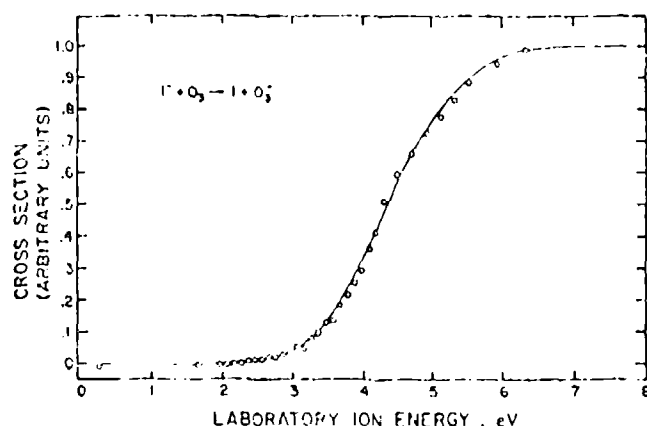


FIG. 3. Cross section for the reaction $I^- + O_3 \rightarrow I + O_3$ as a function of translational energy. Points are experimental data (collision chamber temperature 33°C), solid line is the convoluted "best fit" excitation function. Linear-plus-step threshold function is $\sigma(E) = 0$ for $E' < 4.6$ eV; $\sigma(E) = (E' - 4.6)/0.8$ for $4.6 \leq E' \leq 4.8$ eV and $\sigma(E) = 1.0$ for $E' \geq 4.8$ eV.

agreement with those obtained previously by Berkowitz, Chupia, and Gutman.¹⁵ The Br^- and I^- reactions with O_3 were observed at several different collision chamber temperatures (30, 125, and 170 °C) and the thresholds obtained for reactions of both ions were found to be independent of temperature, within experimental error. However, the Br^- reaction yielded consistently higher values for the electron affinity of ozone than the I^- reaction. Similar behavior was previously observed in our earlier experiments with NO_2 .¹⁷ The presently determined electron affinity for NO_2 (2.40 eV), using Br^- as the projectile ion [Fig. 2(a)], is in excellent agreement with the currently accepted value of 2.36 ± 0.1 eV.²⁰ As we have already noted, electron affinity values derived from threshold measurements of the type described here are considered to be lower limits,^{14,24} since the product ions may be formed with excess internal or translational energies, even at threshold. The present experiments indicate however that the Br^- reaction leaves the electron-transfer product ion with the least amount of excess energy at threshold in the case of both NO_2 and O_3 . Since the excitation function for the Br^-/O_3 reaction (Table I) has been corrected for Doppler motion and ion velocity spread, and since, among the reactions for which threshold corrections could be applied, this reaction gives the highest O_3 electron affinity value, we consider this value to be nearest the true electron affinity. We conclude therefore, that $E.A.(O_3) = 2.26^{+0.05}_{-0.04}$ eV, the error limits reflecting the uncertainties arising from the computer fits.

It is interesting to note that the linear section of the excitation function determined for the Br^-/O_3 reaction [Fig. 2(b)] spans a considerably shorter energy or mass energy range than does that of the I^-/O_3 reaction (Fig. 1). This suggests that, in contrast to the behavior of the I^-/O_3 system, the potential surface of the $[Br^- + O_3]$ reactant pair intersects that of the $[Br + O_3]$ product pair in such a manner that strong interaction occurs only over a very narrow range of internuclear separations

and potential energies. Similar differences in the behavior of various halide ions (for example, I^- as compared to Cl^-) in endothermic electron transfer reactions with the oxygen molecule have been noted in other studies.³² It is also apparent that if the products of the Br^-/O_3 reaction are indeed formed with little or no excess energy at threshold, then the potential surface leading to the $[Br + O_3]$ products must be quite flat from the point at which it intersects the reactant surface to the region of infinite internuclear separation.

2. Observation of exothermic charge transfer reactions at low translational energies which establish limits on the electron affinity of ozone

Negative ion-neutral charge transfer reactions which exhibit large rate coefficients at low relative translational energies can generally be presumed to be exothermic processes. Such exothermic processes are generally characterized by a monotonically decreasing cross section with increasing reactant translational energy. The observation of these reactions therefore provides information concerning the relative electron affinities of the reactant species, and in some cases a series of such observations permits one to bracket the electron affinity of a molecule of interest. For example, observation of the fast electron transfer reaction, $SH^-(NO_2) \rightarrow SH + NO_2^-$, in a previous study,²¹ established that $E.A.(NO_2) > E.A.(SH)$. Similarly, the occurrence of the fast reaction, $NO_2^-(Cl_2) \rightarrow NO_2 + Cl_2^-$,¹⁶ established that $E.A.(NO_2) > E.A.(Cl_2)$. It was thus possible to state that $E.A.(NO_2)$ lies between that of SH and Cl_2 , and since the electron affinities of the latter were known, specific limits for $E.A.(NO_2)$ were established. A similar approach has been applied in the present study of ozone. Charge transfer reactions of selected negative ions with ozone were investigated, and rate coefficients were determined for these at 0.3 eV (LAB) translational energy, as shown in Table II. For comparison purposes, the rate coefficient at 0.3 eV is also shown for the I^-/O_3 charge transfer reaction, which is known to be endothermic. These data clearly indicate that $E.A.(O_3) > E.A.(OH)$, $E.A.(O)$, in agreement with previous findings.¹⁰ These results also show that $E.A.(O_3) > E.A.(Cl)$, $E.A.(C_2H)$. Taken in conjunction with the results discussed in the previous section, then, these observations lead to the conclusion that $2.26^{+0.05}_{-0.04}$ eV, $E.A.(O_3) > 2.46$ eV.

The rate data and excitation function for the S^+ , SH^+ , and NO_2^+ reactions with O_3 (Table II) are somewhat less conclusive with respect to the O_3 electron affinity. While electron transfer from NO_2^+ to O_3 was found to be moderately fast at 0.3 eV ($k = 0.9 \times 10^{-10}$ cm³/molecule sec),



it was observed that the rate coefficient for the reverse reaction (electron transfer from O_3^+ to NO_2) is also reasonably large ($k = 2.0 \times 10^{-11}$ cm³/molecule sec). Moreover, as shown in Fig. 4, the excitation function for both of these processes exhibit behavior which is typical of exothermic processes. This suggests that the electron affinities of O_3 and NO_2 are very nearly

TABLE II. Rate coefficients for charge transfer reactions^a of negative ions with O_3 .

Reactant ion M^-	Electron affinity of M (eV)	$k(10^{-16} \text{ cm}^3 \text{ molecule}^{-1} \text{ sec})^b$
O^-	1.462 ^c	2.0
OH^-	1.825 ^d	5.0
S^-	2.077 ^e	0.9
SH^-	2.519 ^f	0.6
NO_2^-	2.36 ^g	0.9
Cl_2^-	2.46 ^h	0.02
C_2H^-	2.7 ⁱ	0.02
F^-	3.399 ^e	0.0002

^a Measured with reactant ions of ~ 0.3 eV laboratory energy.

^b Determined by normalizing relative rates for all reactions to the absolute value cited for the $O^-(NO_2)$ reaction, $3.5 \pm 1.2 \times 10^{13} \text{ cm}^3 \text{ molecule}^{-1} \text{ sec}$ (see Ref. 3, 60 and C. Litshitz and R. Terwiliger, *Int. J. Mass Spectrom. Ion Phys.*, **12**, 433 (1973)).

^c Reference 47.

^d H. Batop, T. A. Patterson, and W. C. Lineberger, *J. Chem. Phys.*, **60**, 1805 (1974).

^e W. C. Lineberger and E. W. Woodward, *Phys. Rev. Lett.*, **25**, 424 (1970).

^f D. Storer, *J. Chem. Phys.*, **49**, 5607 (1968).

^g Reference 20.

^h Reference 18.

ⁱ D. K. Bohme (Private communication, 1973).

equal. On this basis, however, one would expect that the reaction,



would have a larger rate coefficient, since the electron affinity of S is only 2.077 eV. Also, the excitation function for Reaction (18) is quite flat, not as expected for an exothermic reaction. The observation of an apparently exothermic electron transfer reaction from NO_2^- to O_3 also leads one to expect that the reaction,



will be exothermic, since $E.A. (SH) > E.A. (NO_2)$. In fact, the rate coefficient for the latter reaction is smaller than that for the former, and furthermore, the excitation function for Reaction (19), shown in Fig. 5, clearly exhibits an energy threshold. It is perhaps significant that the cross section for this reaction at the lowest energy accessible in these experiments is considerably larger than that typically observed for highly endothermic reactions. As we have recently reported,³ the major reaction channel for both the S^-/O_3 and SH^-/O_3 interactions is associative detachment,



[the energy dependence of Reaction (21) is also shown in Fig. 5], and the dominance of these reactions in the energy region from ~ 0.5 –1 eV may affect the apparent excitation functions for the electron transfer processes. Other important factors which can affect the electron

transfer reactions discussed above are the lowest energy limit and the energy resolution which can be achieved for the reactant ion beam in the tandem mass spectrometer. Negative ion electron transfer reactions which are only slightly endothermic could be driven by the translational energy of the reactant ion beam, which, as already noted, is 0.3 ± 0.3 eV even at the lowest energy attainable. Thus some slightly endothermic reactions might appear to be exothermic. Similar effects could result if the reactant ions were vibrationally or electronically excited in these experiments. Earlier studies in our laboratory¹¹ suggested the existence of an excited NO_2^- ion formed by negative-ion electron transfer to NO_2 , and a recently reported investigation of the photodestruction of NO_2^- indicates the existence of a long-lived vibrationally excited NO_2^- species.²² Obviously, it is therefore possible that the apparently exothermic NO_2^-/O_3 electron transfer reaction which we observe involves internally excited reactant ions.

B. Particle transfer reactions

Rate coefficients were also measured for a number of exothermic and endothermic particle (O^- and O atom) transfer reactions involving ozone, at a laboratory ion energy of 0.3 eV. The results are summarized in Table III and compared with previously reported data. The first three reactions listed in Table III are exothermic, and the measured rate coefficients for these at 0.3 eV are all lower than the corresponding values obtained for thermal ions using the flowing afterglow technique. In the one case where comparison with an earlier ion beam experiment² is possible [for the reaction $O_2^-(CO_2, O_2)CO_2$] the data from the two experiments are in quite good agreement. The flowing afterglow rate coefficient reported for the reaction, $O_2^-(NO_2, O_2)NO_2$,¹⁶ presumably corresponds to the total disappearance rate coefficient for the O_2^- reactant, and therefore would include the rate coefficient for the electron transfer channel, $O_2^-(NO_2, O_2)NO_2^-$. It was assumed in the earlier study that the particle transfer reactions was more important, contrary to the present results. The rate coefficient for the sum of both channels determined in the present study is $2.1 \times 10^{12} \text{ cm}^3 \text{ molecule}^{-1} \text{ sec}$, only slightly lower than the value obtained previously at 300°K. In studying the reactions just described, it should be noted that the O_2^- reactant was produced by the reaction $O^-(O_2, O)O_2^-$. As will be discussed later, the O_2^- reactant beam produced in this manner is partially in an excited state, and this may, of course, affect the reaction paths observed. The particle transfer reaction channel yielding NO_2^- was found to be of minor importance for both the O^-/NO_2 and the NO_2^-/O_3 interactions in the present experiments. The major reaction in both cases is charge transfer. The NO_2 products account for no more than 5% of the total reaction cross section in each case. The excitation functions obtained for the reaction, $NO_2^-(O_3, O)NO_2$, and $O_2^-(CO_2, O_2)CO_2$ are presented in Fig. 4. The rate coefficients determined for the O^-/CO_2 and O_2^-/NO_2 reactions are plotted as a function of energy in Figs. 6 and 7, respectively. Here, the rate coefficients, k , have been derived from the experimentally measured

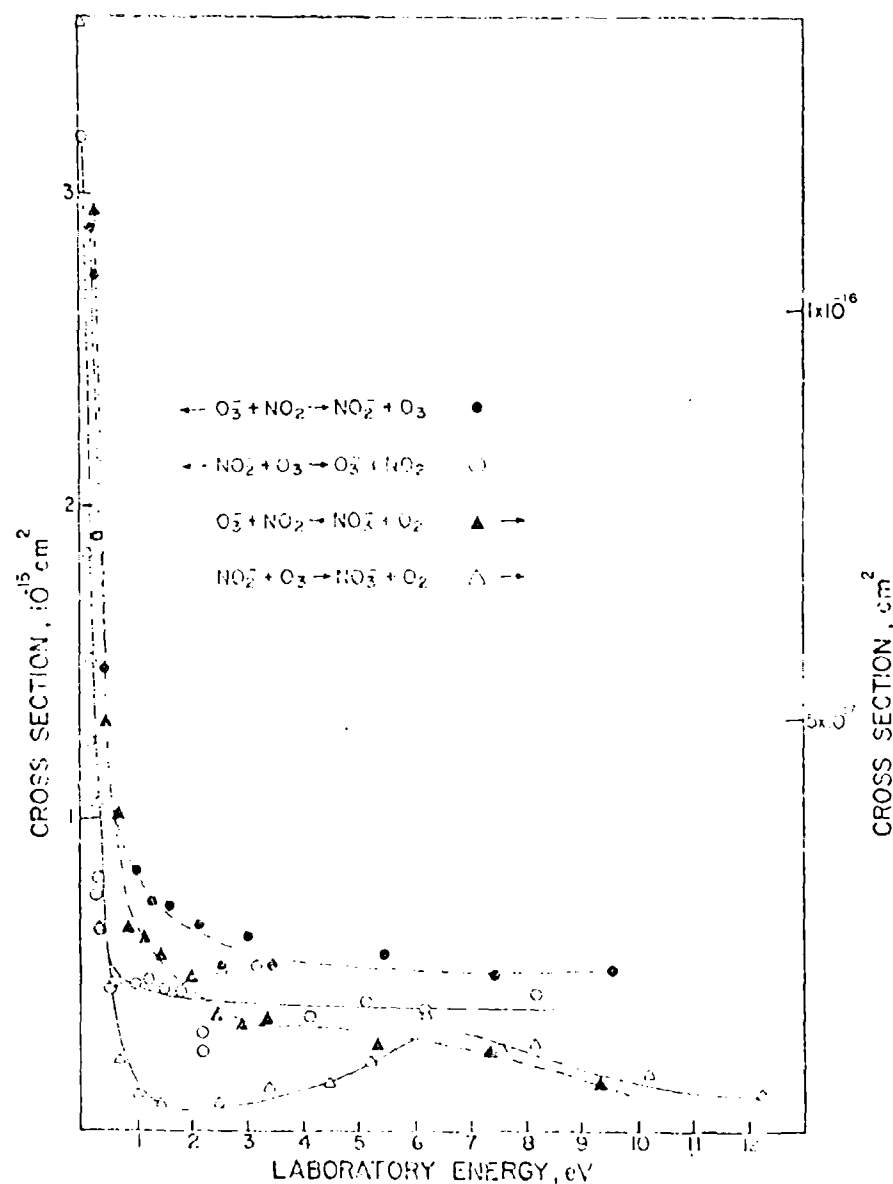


FIG. 4. Translational energy dependence of the cross section for the reactions of NO_2^- with O_3 , and of O_3^- with NO_2 ; note that there are two cross section scales.

cross sections, σ_{exp}^{obs} , using the relation,

$$k = \sigma_{exp}^{obs} \bar{v}, \quad (22)$$

where \bar{v} is the average ion drift velocity at the corresponding laboratory energy employed. The rate coefficients obtained for the O_3^-/O_2 reaction over the energy range up to about 1 eV (e.m.) using the flow-drift method¹⁰ are considerably larger (by an order of magnitude) than those obtained from the beam experiments, both in our laboratory and elsewhere.¹¹ However, the present data for the O_3^-/NO_2 reaction (Fig. 7) are in much better agreement with flow-drift data,¹² for the energy range which is common to both experiments. The rate coefficient for the endothermic process, CO_2^+/O_2 , CO^+/O_2 , as shown in Table III, is larger at 0.3 eV than at 1.09 eV, as expected.

Excitation functions were also determined in the present study for several endothermic O_3^- transfer reactions yielding O_3^- . Several factors make it diffi-

cult to determine accurate translational energy thresholds from the measurements. First, the cross sections for these processes are quite small, which results in considerable scatter in the experimental data points. Secondly, the thresholds exhibit a very gradual onset and there is no *a priori* knowledge with respect to the functional behavior of the excitation function. Still, reasonably good threshold data was obtained for three of the four reactions studied,



The excitation functions measured here for Reaction (23) and (24) are shown in Figs. 8 and 9, respectively. Vost *et al.*¹³ have previously studied Reaction (23) and Paulson and Gale¹⁴ have observed Reaction (24). The

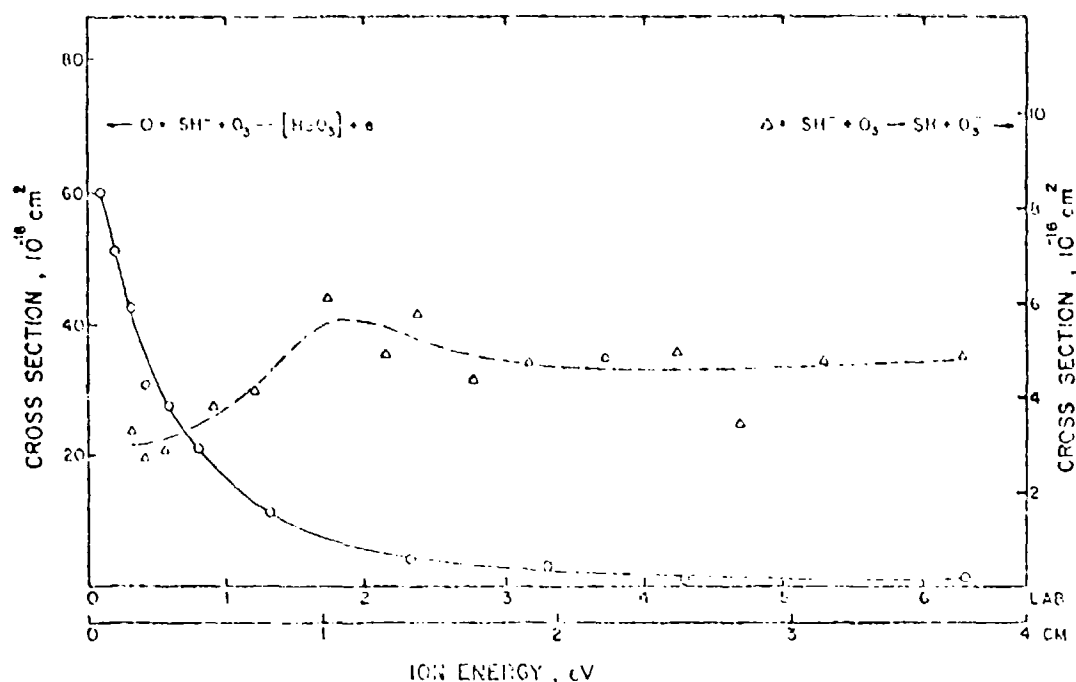


FIG. 5. Translational energy dependence of the cross section for the reaction of SH^+ with O_3 .

present results provide much more accurate data in the threshold region than that obtained previously, however. The energy thresholds determined by treating this data, as explained previously in Sec. II, are summarized in Table IV. The error limits specified for the threshold energies and for the values of the exponent n (Eq. 13) are estimated from the ranges of k_0 and n , respectively, which yield a good fit to the experimental data. If the products are formed with no excess energy at threshold, then the threshold energy in the c.m. sys-

tem can be used in conjunction with other thermochemical data to compute the $\text{O}_2\text{--O}^+$ bond dissociation energy in O_3^+ . It can readily be shown that for the general reaction,



the $\text{O}_2\text{--O}^+$ bond dissociation energy is related to the M--O^+ bond dissociation energy and the energy threshold for the reaction by the expression,

$$D_0^0(\text{O}_2\text{--O}^+) = D_0^0(\text{M--O}^+) - E_{\text{th}} \quad (28)$$

TABLE III. Rate coefficients for particle transfer reactions involving O_3 and O_3^+ .

Reaction	ΔH eV ^a	Present data cm ³ molecule ⁻¹ sec ⁻¹	Other values cm ³ molecule ⁻¹ sec ⁻¹	Method	Reference
$\text{O}_3^+ + \text{CO}_2 \rightarrow \text{O}_3 + \text{CO}_2^+$	-0.2	$(4 \pm 1) \times 10^{-11}$ at 0.3 eV	5×10^{-11} at 0.3 eV	IP	38
			5.5×10^{-12} at 300°K	FA	5
			5.5×10^{-12} at 300°K	SD	8
$\text{O}_3^+ + \text{NO}_2 \rightarrow \text{O}_3 + \text{NO}_2^+$	-0.8	1.2×10^{-11} at 0.3 eV	2.5×10^{-12} at 300°K	FA	18
$\text{NO}_3^+ + \text{O}_3 \rightarrow \text{O}_3 + \text{NO}_3^+$	-2.7	4.4×10^{-12} at 0.3 eV	1.8×10^{-11} at at 500°K	FA	30
$\text{CO}_3^+ + \text{O}_2 \rightarrow \text{CO}_2 + \text{O}_2^+$	$+0.2$	5.7×10^{-14} at 0.3 eV	$< 6 \times 10^{-16}$ at 7 < 600°K	FD	10
$\text{O}_3^+ + \text{O}_2 \rightarrow \text{O} + \text{O}_4^+$	$+2.2$	3.58×10^{-13} at 0.3 eV	—	—	—

^aHeats of reaction calculated using $\Delta H_f^\circ(298^\circ\text{K})$ values.

IP, ion-molecule; FA, flux-area; SD, static-diffusion; FD, flux-diffusion.

^cThe present ion O_3^+ is produced by the reaction $\text{O}^+(\text{O}_2, \text{CO}_2)$ and is reported in its excited state.

The values thus derived, also listed in Table IV, are, in effect, lower limits. We consider the value $D_0(\text{O}_2-\text{O}^+) = 1.8 \pm 0.1$ eV obtained from the threshold for Reaction (23) to be the most accurate of these values because the computer fit near threshold (Fig. 6) is quite good and the bond dissociation energy $D_0(\text{O}-\text{O}^+)$ is very accurately known.⁴¹ Reactions (24) and (25) yield an O_3 bond dissociation energy, which is (within the fairly large error limits) in agreement with that obtained from Reaction (23). However, Reaction (25) obviously produces one or both of the products in excited states at threshold.

An alternative approach in treating the particle transfer reaction excitation functions involves the application of the principle of microscopic reversibility, which gives, for the post-threshold energy dependence of endothermic non-neutral reaction cross sections, the expression,⁴²

$$\sigma = A(E - E_0)^{1/2}/E, \quad (20)$$

This expression yields a temperature dependent rate coefficient of the form,

$$k(T) = k_{\text{coll}} e^{-E_0/kT}, \quad (30)$$

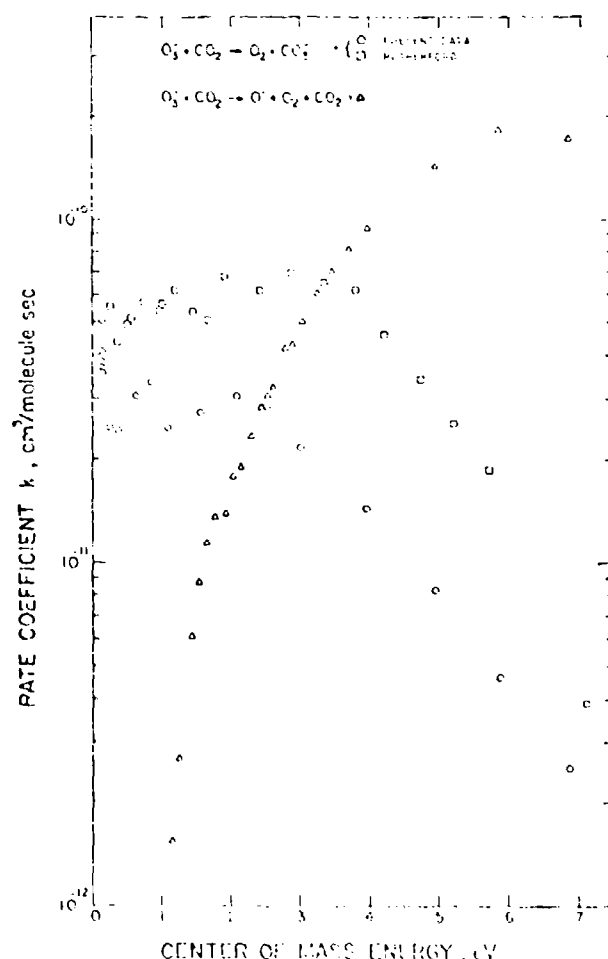


FIG. 6. Rate coefficients for the reactions of O_3 with CO_2 as a function of relative kinetic energy: \circ , $\text{O}_3 + \text{CO}_2 \rightarrow \text{O}_2 + \text{CO}_2$; Δ , $\text{O}_3 + \text{CO}_2 \rightarrow \text{O} + \text{CO}_2 + \text{CO}$. \circ , data of Lifshitz *et al.*¹⁸ for the same reactions (Ref. 18); Δ , $\text{O}_3 + \text{CO}_2 \rightarrow \text{O} + \text{CO}_2 + \text{CO}$.

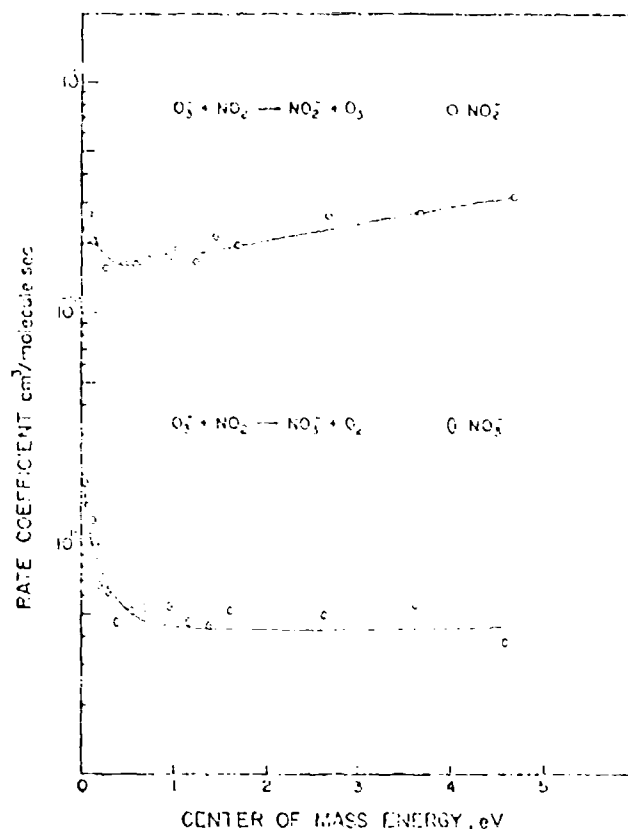


FIG. 7. Rate coefficients for the reactions of O_3^+ with NO_2 as a function of relative kinetic energy: \circ , $\text{O}_3^+ + \text{NO}_2 \rightarrow \text{NO}_2^+ + \text{O}_3$; Δ , $\text{O}_3^+ + \text{NO}_2 \rightarrow \text{NO}_3^+ + \text{O}_2$.

where k_{coll} is the Langevin collision rate coefficient. However, our experimental data could not be fitted to such a threshold function. It is quite possible that the experimental excitation function actually consists of many small concave steps, corresponding to Eq. (20), which are unresolved and give a resultant convex appearance. This could be the case if a large number of

TABLE IV. Translational energy thresholds for endothermic particle transfer reactions. $M(\text{O}-\text{O})$ and $D_0(\text{O}-\text{O})$ bond dissociation energies determined from these.

Reaction	Threshold energy (eV)	k	$D_0(\text{O}-\text{O})$ (eV)	$D_0(\text{O}-\text{O})$ (eV)
$\text{O}_3 + \text{CO}_2 \rightarrow \text{O}_2 + \text{CO}_2$	1.8 ± 0.1	2.4 ± 0.1	1.8 ± 0.1	1.8 ± 0.1
$\text{O}_3 + \text{CO}_2 \rightarrow \text{O} + \text{CO}_2 + \text{CO}$	1.2 ± 0.3	0.42 ± 0.1	1.0 ± 0.1	1.0 ± 0.2
$\text{O}_3 + \text{CO}_2 \rightarrow \text{O} + \text{CO}_2 + \text{CO}$	1.1 ± 0.4	2.1 ± 0.2	1.0 ± 0.1	1.0 ± 0.2
$\text{O}_3 + \text{CO}_2 \rightarrow \text{O} + \text{CO}_2 + \text{CO}$	1.1 ± 0.4	4.1 ± 0.1	1.0 ± 0.1	1.0 ± 0.2

^aReference 41.

^bReference 29.

^cNo curve fitting was attempted in this case because of some unexplained structure near threshold. E_0 was obtained by short range linear extrapolation of the data points.

^dThe bond dissociation energy was computed from $D_0(\text{O}-\text{O}) = D_0(\text{O}-\text{O}) - D_0(\text{O}-\text{O})$.
^eSee Table I, $D_0(\text{O}-\text{O})$ (eV).
^fSee Table I, $D_0(\text{O}-\text{O})$ (eV).
^gSee Table I, $D_0(\text{O}-\text{O})$ (eV).
^hSee Table I, $D_0(\text{O}-\text{O})$ (eV).
ⁱSee Table I, $D_0(\text{O}-\text{O})$ (eV).
^jSee Table I, $D_0(\text{O}-\text{O})$ (eV).
^kSee Table I, $D_0(\text{O}-\text{O})$ (eV).
^lSee Table I, $D_0(\text{O}-\text{O})$ (eV).
^mSee Table I, $D_0(\text{O}-\text{O})$ (eV).
ⁿSee Table I, $D_0(\text{O}-\text{O})$ (eV).
^oSee Table I, $D_0(\text{O}-\text{O})$ (eV).
^pSee Table I, $D_0(\text{O}-\text{O})$ (eV).
^qSee Table I, $D_0(\text{O}-\text{O})$ (eV).
^rSee Table I, $D_0(\text{O}-\text{O})$ (eV).
^sSee Table I, $D_0(\text{O}-\text{O})$ (eV).
^tSee Table I, $D_0(\text{O}-\text{O})$ (eV).
^uSee Table I, $D_0(\text{O}-\text{O})$ (eV).
^vSee Table I, $D_0(\text{O}-\text{O})$ (eV).
^wSee Table I, $D_0(\text{O}-\text{O})$ (eV).
^xSee Table I, $D_0(\text{O}-\text{O})$ (eV).
^ySee Table I, $D_0(\text{O}-\text{O})$ (eV).
^zSee Table I, $D_0(\text{O}-\text{O})$ (eV).

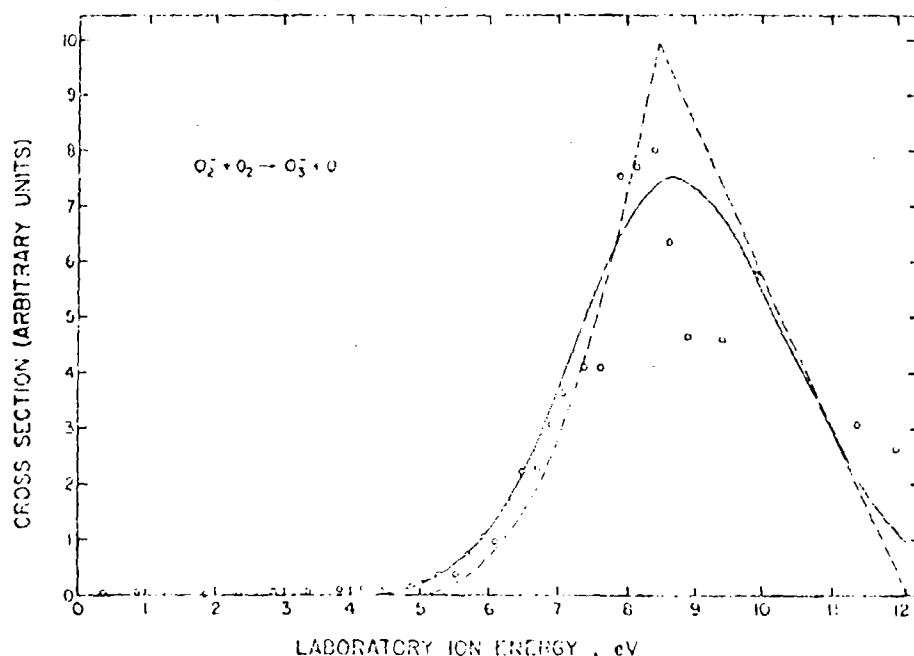


FIG. 8. Relative cross section for the reaction $O_2^+ + O_2 \rightarrow O_3^+ + O$ as a function of translational energy. Points are experimental (170°C) data; the solid line is the convoluted "best fit" excitation function and the dashed line is the assumed threshold function: $\sigma(E') = 0$ for $E' < 4.69$ eV; $\sigma(E') = [(E' - 4.69)^{1/2} / 2.7]^{1.7}$ for $4.69 < E' < 8.3$ eV; $\sigma(E') = (12 - E')^{1.7}$ for $8.3 < E' < 12.0$ eV and $\sigma(E') = 0$ for $E' > 12.0$ eV.

closely-spaced final states is being populated by these particle transfer reactions.

C. Collision induced dissociation (CID) reactions

In a preliminary communication,⁴¹ we recently reported the results of collision-induced dissociation (CID) experiments which indicate the formation of an excited O_3^+ ion as the product of the charge transfer reaction,



This excited ionic state lies ~ 0.64 eV above the ground state O_3^+ . The latter is apparently formed as a product of the reaction,



TABLE V. Best fit values of A , E_0 , and n as obtained by convoluting $\sigma = A(E - E_0)^n$ with the combined ion and neutral translational energy distribution and comparing with $\sigma_{exp}^{(170^\circ C)}$ for the CID reaction $O_3^+ + M \rightarrow O_2 + O_3^+$.

Target gas M	A^a ($\text{cm}^2 \text{eV}^{0.5} \times 10^{14}$)	E_0^a eV	n
A. O_3^+ from CO^+ , OH^+ , or Ar^+ in mixture of N_2O , O_3 in the ion source			
Ar	0.145	1.68	1.9
Ar	0.206	0.96	2.1
CO_2	0.66	6.56	2.0
B. O_3^+ from CO^+ , OH^+ in mixture of H_2O , O_3 in the ion source			
Ar	0.128	1.77	2.1
Ar	0.202	1.82	2.0
C. O_3^+ from CO^+ , OH^+ and OH_2^+ in mixture N_2O , O_3 , H_2O			
N_2	0.64	1.77	2.0

^aValues given are for the combined ion and neutral translational energy.

Figure 10 presents typical experimental results for the CID of O_3^+ on Ar;



here the O_3^+ reactant has been prepared by three different processes. As is evident from the data in Fig. 10, the observed CID threshold is dependent upon the source of O_3^+ . The lowest threshold is obtained for O_3^+ produced from a mixture of N_2O and O_3 , where Reaction (31) probably represents the mode of formation. (The O^+ is formed by dissociative electron attachment to N_2O .) The highest threshold is for O_3^+ produced from a mixture of H_2O and O_3 , where Reaction (32) is the mechanism of production. A threshold intermediate between these two is observed for O_3^+ formed from a mixture of H_2O , N_2O , O_3 , in which the ratio $O^+ : OH^+$ was observed to be $\sim 2/1$. Table V summarizes the CID

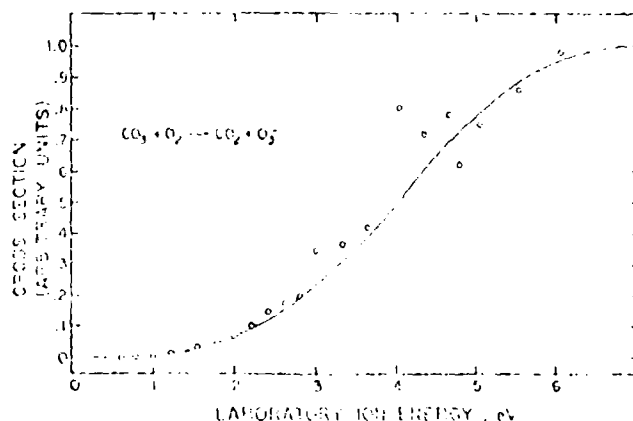


FIG. 9. Relative cross section for the reaction $CO_2^+ + O_2 \rightarrow CO_2 + O_2^+$ as a function of translational energy. Points are experimental (170°C) data; the solid line is the convoluted "best fit" excitation function and the dashed line is the assumed threshold function: $\sigma(E') = 0$ for $E' < 1.2$ eV; $\sigma(E') = [(E' - 1.2)^{1/2} / 1.2]^{1.7}$ for $1.2 < E' < 5.0$ eV and $\sigma(E') = 1$ for $E' > 5.0$ eV.

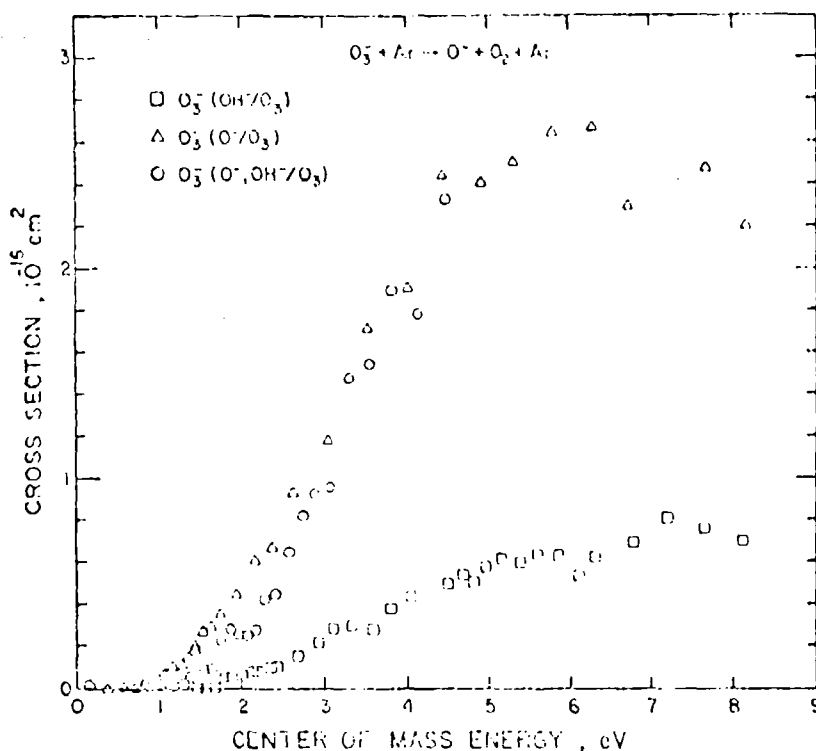


FIG. 10. Cross section for the reaction $O_3^+ + Ar \rightarrow O^+ + O_2 + Ar$ as a function of translational energy. Δ , experimental data for O_3^- produced by the reaction, $O^+(O_2, OH/O_3)$; \square , data for O^+ produced by the reaction, $O^+(O_2, OH/O_3)$; \circ , data for O_3^- from both reactions, $O^+(O_2, OH/O_3)$ and $O^+(O_2, OH/O_3)$.

thresholds derived by treating the measured excitation functions in the manner described earlier in this paper. Also listed are the factors A , E_0 , and n of $r_{1/2}^n$ (13) which correspond to the best computer fit of the experimental data. As expected, it is observed that the threshold for CID of excited O_3^- is lower than for the ground state O_3^- , and in addition, the A factor is higher for the former ion. Parks, Wagner, and Winkler⁴¹ have previously studied the threshold behavior of collision-induced ion-pair formation in thallium halides in some detail, and have determined E_0 , n , and A for a series of such reactions. In their experiments, the dependence of A on internal energy was investigated by varying the reactant temperature, and the value of A was observed to increase with increasing internal energy. In the latter experiments the internal excitation could only be vibrational or rotational excitation. In the present case, however, the excitation in O_3^- can be both vibrational-rotational and electronic excitation. It is also possible that the excited O_3^- represents an isomeric structure, as previously discussed.¹²

In Fig. 11 we have replotted the data for CID of ground state and excited O_3^- on Ar in a different manner, which is suggested by the Levine and Bernstein^{42,43} model. Here, the quantity, $(E_{int}/E_{tr})^{1/2}$, has been plotted as a function of E_{tr} . Since the n values giving the best fit were 2.0 and 2.1 (Table V) an average value of 2.05 was employed for Fig. 11. Then the experimental values for $E_{tr}^{1/2}$, where E_{tr} is the center of mass translational energy, were plotted as a function of the total energy E_{tot} . For the case where O_3^- is derived from the OH/O_3 reaction, $E_{tr} = E_{tot} - E_0$. For the case where O_3^- is formed by $O^+(O_2)$ reaction, $E_{tr} = E_{tot} - 0.84$ eV. Plotting the data in this manner, the two sets of

experimental points (without deconvolution) are observed to extrapolate to the same threshold, $E_0 = 1.8$ eV. Moreover, the slope of the plot, which is equal to $A^{1/2}$, is considerably greater in the case of the excited state reaction than for the ground state reaction, the factors being $A = 0.841 \times 10^{-16}$ and $0.394 \times 10^{-16} \text{ cm}^2 \text{ eV}^{-0.5}$, respectively.

In several previously reported instances,⁴⁴ it has been noted that vibrational energy is more effective than translational energy in promoting CID reactions. This is the case for CID of H_2^+ on He ,⁴⁵ for which a plot similar to that shown in Fig. 11 was presented, (except with $n = 2.5$)⁴⁶ and also for CID of thallium halides.⁴⁷ The present CID results, with respect to the dependence of the A factor on internal energy, suggest to us that the internal excitation of O_3^- formed in Reaction (31) is vibrational energy. These results show that for two reactants having the same total energy, but different proportions of internal and translational excitation, the CID cross section is considerably larger for that reactant having the greater fraction of its energy as internal energy. The intermediate energy threshold obtained here for CID of a mixture of ground state and excited state O_3^- ions may then be due to partially relaxed O_3^- , which again would be consistent with vibrationally excited O_3^- .

As already discussed, the major reaction channel from the O_3^-/CO_2 interaction at low energies is particle transfer. At energies greater than 1 eV (v.i.m.) however, the reaction of O_3^- produced via Reaction (31) with CO_2 also yields an O^+ product. In Fig. 6, we have plotted the rate coefficient k for production of O^+ from this reaction,



J. Chem. Phys., Vol. 63, No. 1, 1 January 1975

- ⁴¹E. K. Parks, A. Wagner, and S. Weston, *J. Chem. Phys.*, **68**, 5502 (1978).
- ⁴²T. O. Tierman and C. Lifshitz, "The role of excited states in ion-neutral collisions," in *The Excited State in Chemical Physics*, edited by J. Wu, McGraw-Hill, Vol. II in the *Advances in Chemical Physics* series, edited by I. Prigogine and S. Rice (Wiley-Interscience, New York, to be published).
- ⁴³W. A. Chapiro, in *Ion-Molecule Reactions*, edited by J. L. Franklin (Plenum, N. Y., 1972), Vol. 1, p. 73.
- ⁴⁴H. H. Gerd and W. C. Lineberger, *J. Phys. Chem. Ref. Data*, **4**, 535 (1975).
- ⁴⁵J. L. Cole and R. N. Zare, *J. Chem. Phys.*, **57**, 5331 (1972).

Excitation Functions of Slow Proton Transfer Reactions Involving Negative Ions

C. Lifshitz,[†] R. L. C. Wu, and T. O. Tieman*

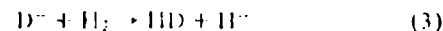
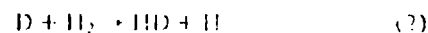
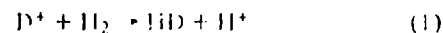
*Contribution from The Beckman Laboratory and Department of Chemistry,
Wright State University, Dayton, Ohio 45435. Received September 1, 1977*

Abstract: Excitation functions were determined for a series of slow proton and deuteron transfer reactions involving negative ions using a tandem mass spectrometer. Some of the reactions observed, for example, $\text{ND}_2^- + \text{D}_2 \rightarrow \text{D}^- + \text{ND}_3$, exhibit translational energy thresholds, even though they are exothermic. Other reactions, such as $\text{CH}_3\text{COCH}_2\text{D} + \text{CD}_3\text{COCD}_2^- \rightarrow \text{CH}_3\text{COCH}_2\text{D} + \text{CD}_3\text{COCD}_2^-$, exhibit a complex functional dependence of the cross section upon relative translational energy, which in turn is quite sensitive to the internal energy of the neutral reactant. Rate coefficients determined for these negative ion reactions in the present investigation are compared with analogous data previously reported for thermal energy reactions. The translational energy thresholds observed for several of the reactions are consistent with the existence of a potential energy barrier in the reaction coordinate between the reactants and products. It is demonstrated that the deconvoluted excitation function for the $\text{ND}_2^- + \text{D}_2$ reaction is of the form $\sigma = (E_{\text{th}} - E_0)^{1/2}/E_{\text{th}}$ as required by theory, and that the translational energy threshold corresponds to the Arrhenius activation energy for this process.

Among the many gas-phase ion-neutral reactions which have been studied, proton transfer processes have perhaps been the subject of greatest interest recently, owing largely to their important role in solution chemistry.^{1,2} Much of the recent research has been concerned with proton transfer to negative ions, and has focused on the determination of rate coefficients for thermal energy reactions, and the application of such data in constructing gas-phase acidity and basicity scales.³ While the rates for many of these reactions are typical of those usually observed for exothermic or thermoneutral reactions, several interesting exceptions have been observed. In particular, certain exothermic proton transfer reactions of amide ions^{4,5} and of larger delocalized negative ions⁶ have been found to be remarkably slow. These observations prompted some tentative conclusions with respect to the dynamics of slow proton transfer reactions of negative ions.^{7,8} Such conclusions, based solely on the magnitude of rate coefficients measured at a single temperature, cannot of course provide a detailed picture of the reaction dynamics, since a low rate coefficient for a particular proton transfer reaction of this type could be explained by either an activation energy barrier (as has been suggested for the amide ion reactions⁵) or by a low entropy factor (as suggested for the delocalized negative ion reac-

tions⁶). Obviously, in some cases, both factors might be operative.

Owing to the limitations of rate data which were just discussed, increasing interest has developed in the determination of translational energy dependences of reactive scattering cross sections (so-called "excitation functions") as a probe of reaction dynamics.^{9,10} Such data can provide considerable information with respect to energy barriers for reactions of interest. This is well illustrated by investigations of the three closely related processes,



which have been discussed by Henchman et al.^{9,10} All three of these are nominally thermoneutral reactions. However, the excitation functions for reactions 2 and 3, which are quite similar, both exhibit translational energy thresholds, whereas reaction 1 exhibits no threshold, and its cross section decreases monotonically with increasing energy.^{9,11} These results are consistent with the calculated potential surfaces on which these reactions proceed, since the surfaces relevant to reactions 2 and 3 show energy barriers between the reactants and products,^{12,13} while the surface relevant to reaction 1 contains a deep basin

[†] On sabbatical leave from Tel. Aviv University of Jerusalem, 1976-1977.

in the reaction coordinate between the reactant and product species.¹⁴

In the present study, we have determined excitation functions for several thermoneutral and exothermic proton transfer reactions of negative ions, for which thermal rate data have been previously reported. It was expected that these measurements would provide additional insight into the dynamics of these gas-phase processes.

Experimental Section

Materials. The chemicals utilized in this work were obtained from commercial sources, and were used without further purification. Acetone (*d*₆, 99.8% D) was obtained from Stohler Isotope Chemicals while HD (98% D) and ND₃ (99% D) were supplied by Merck Sharp and Dohme of Canada, Ltd.

Instrumentation. An in-line tandem mass spectrometer, previously described,¹⁵ was utilized for these studies. Briefly, it is a beam-collision chamber apparatus which provides mass analysis of the product ions. The collection stage is fixed at 0° (LAB) scattering angle. The projectile ion is formed in the electron impact ion source of the first stage mass spectrometer, which produces a mass and energy resolved beam. This beam is then decelerated in a retarding lens and impinged upon the target gas in the field-free collision chamber maintained at a constant temperature and pressure. The energy spread of the projectile ion beam entering the collision cell is 4.0–3 eV (LAB) over the ion energy range 0.2 to about 180 eV (LAB). Collision chamber temperatures and pressures employed range from 30 to 110 °C and from 5×10^{-3} to 20×10^{-3} Torr, respectively. Product ions are mass analyzed in the second stage mass spectrometer. Pulse counting techniques are used to measure the product ion current.

Preparation of Reactant Ions. Reactant ions are produced by dissociative electron attachment using appropriate source molecules, as described previously,¹⁵ or by ion-molecule reactions occurring in the first-stage ion source. D⁺ and ND₃⁺ ions were formed by dissociative electron capture to ND₃. Typical currents of these ions obtained in the tandem mass spectrometer were 1.5×10^{-11} and 1.5×10^{-10} A, respectively. Organic negative ions were produced by proton transfer from selected molecules to O⁻. For example, a mixture of N₂O (which forms O⁻ by dissociative electron capture) and acetone was employed to produce CH₃C(O⁻) + CH₃ (*mp* 52) via the well-known proton transfer reaction from acetone to O⁻.¹⁶

Collection Efficiency. Several experiments were conducted in an effort to assess the degree to which the collection efficiency of the product ions varies with incident ion energy in the reactions studied here. Such variations could be the result of increased momentum transfer at higher velocities and could seriously affect the shapes of the measured excitation functions. The technique used by us to estimate the importance of such effects involves the measurement of "ion beam profiles", and has been described previously.^{15,16} The angular divergence of the product beam as it exits from the collision chamber is estimated by applying a lateral field across two split focusing electrodes immediately following the chamber. The product ion beam can thus be swept across the collector slit and an angular profile obtained. Measurements of this type indicated that there is very little variation in the degree of forward scattering of the product H⁺ ion of reaction 3a for incident D⁺ ion energy is varied. It thus appears that even if a mechanism such as "spectator stripping"¹⁷ sets in as the incident ion energy is increased, this does not affect the product ion, which in this case presumably serves as the "spectator", to which very little momentum is transferred (the reaction being H⁺ stripping). We believe therefore that, although the second stage analyzer of the in-line tandem collects from only a limited angle in the forward scattered product ion beam, the fraction of product ions collected for the reactions studied here is relatively independent of incident ion energy. Thus, the measured excitation functions for negative ion proton transfer reactions reported in the present study should not be seriously distorted by collection efficiency variations.

Data Treatment. The product (secondary) ion intensity $I(U, \theta)$ is converted to an observed apparent cross section, using the relation^{18,19}

$$\sigma_{app}^{+}(U, \theta) = C [I(U, \theta)/P_t] / I_p(U, \theta) \quad (4)$$

where $I_p(U, \theta)$ is the primary ion intensity, I_{lab} is the nominal reactant ion energy in the laboratory frame, P_t is the target gas pressure, and

C is a conversion factor. C is determined at $E_{lab} = 0.3$ eV using the previously reported cross section of 63 Å^2 and the product ion intensity observed in the present study for the charge transfer reaction $O(^1\text{NO}_2)(\text{O})\text{NO}_2^{+}$.¹⁹ Rate coefficients reported in this study were derived from the experimentally measured cross sections, σ_{app}^{+} , using the relation $k = \sigma_{app}^{+} \bar{v}$, where \bar{v} is the average incident ion velocity at the laboratory energy utilized.

The absolute cross section $\sigma(U, \theta)$ and its dependence upon the true relative energy of the ionic and neutral reactants can in principle be deduced from the experimentally observed dependence of $\sigma_{app}^{+}(U, \theta)$ on the nominal ion laboratory energy E_{lab} . The experimentally obtained excitation function differs from the absolute function owing to two factors: (1) the translational energy distribution of the incident ion beam, and (2) the thermal (Doppler) velocity distribution of the neutral target. The second factor (which results in Doppler broadening) is of particular importance for the case in which heavy projectile ions are impacted on light targets. The manner in which the absolute excitation functions are deduced from experimentally observed functions has been described in detail previously.^{15,21}

Results and Discussion

1. D⁺ Reactions. Table I lists the rate coefficients determined in the present study for several proton transfer reactions to D⁺ at a reactant ion translational energy of 0.3 eV (LAB). No previously reported data, with which these values can be directly compared is available. Paulson²² has reported a value of $k = 15 \times 10^{-10} \text{ cm}^3/\text{molecules at } E_{lab} = 0.6 \text{ eV}$ for the D⁺/D₂O proton transfer reaction, an isotopic variant of the D⁺/H₂O reaction studied here. The reactions of D⁺ with H₂O, HCl, C₂H₂, H₂S, and CH₃OH are observed to be very fast (on the order of gas kinetic collision rates). These reactions, as shown in Table I, are all exothermic; that is, the neutral molecules are stronger acids in the gas phase than is HD.^{23,25,29} Betowski et al.²⁶ determined rate coefficients for a series of proton transfer reactions involving both positive and negative ions, and their results indicate that the experimental rate coefficients are generally larger than the Langevin rates by a factor of 3 or 4, in the case of those reactions which are highly exothermic (>30 kcal/mol). This is not surprising since these reactions involved polar molecules, and the permanent dipole moments of the latter lead to increased reactivity. On the other hand, several proton transfer reactions from polar molecules to negative ions which are only slightly exothermic (including the H⁺/H₂O reaction) were found to have experimental rate coefficients which exceed the Langevin rate by a smaller factor. Betowski et al.²⁶ noted that this reduced probability for slightly exothermic proton transfer reactions might be a consequence of the reaction mechanism, or alternatively, could result from a small activation energy barrier. The excitation function determined in the present study for the analogous D⁺/H₂O reaction (and the other fast negative ion proton transfer processes mentioned above) give no indications of energy threshold, for these processes, and therefore any activation barriers for these processes must be smaller than the lower limit of the ion translational energy attainable in our apparatus (~0.3 eV, LAB).

In the studies discussed above, Betowski et al.²⁶ found that the experimental rate coefficients for highly exothermic proton transfer reactions involving polar molecules were in better agreement with the values calculated using the ADK theory than with the Langevin rates. As can be seen from the data in Table I, this does not seem to be the case for the negative ion polar molecule reactions studied here.

Rate coefficients for the reactions of D⁺ with H₂, NH₃, and ND₃ are also shown in Table I, and are seen to be rather small in comparison with those for the reactions just discussed. In addition, the excitation functions for the reactions of D⁺ with H₂, NH₃, and ND₃ were found to exhibit translational energy thresholds, which are indicative of activation barriers for these processes. Figure 1 shows the excitation function measured for

Table I. Rate Coefficients for Various Proton Transfer Reactions to D^- and NH_2^-

XH	$k_{exp}, 10^{-10}$ $cm^3/molecules \cdot s^a$	k_1^c $10^{-10} cm^3/molecules \cdot s$	k_{ADO}^d	k_{exp}/k_{ADO}	$-\Delta H_{298K}^e$ kcal/mol
1. D^- Reactions: $D^- + XH \rightarrow X^- + HD$					
CH_3OH	19	30.7	39.1	0.49	20
H_2O	22	21.0	32.9	0.67	10
HCl	17	27.6	32.2	0.53	67
C_2H_2	19	31.4	31.4	0.60	~ 30
H_2S	26	33.1	36.6	0.71	50
CCl_3H	0.67	48.0	50.8	0.013	f
H_2	0.3	20.8	20.8	0.014	0
NH_3	0.2	26.3	34.8	0.0057	-2.6
ND_3	0.065	26.1	34.6	0.0019	-2.9
2. NH_2^- and ND_2^- Reactions					
$NH_2^- + H_2 \rightarrow H^- + NH_3$	0.18	15.6	15.6	0.012	3.2
$NH_2^- + D_2 \rightarrow D^- + NH_2D$	0.10	11.5	11.5	0.0087	~ 3.0
$NH_2^- + HD \rightarrow D^- + NH_3$	0.17	6.5 ^g	6.5	0.026	2.6
$NH_2^- + HD \rightarrow H^- + NH_2D$	0.17	6.5 ^g	6.5	0.026	~ 3.0
$ND_2^- + D_2 \rightarrow D^- + ND_3$	0.09	11.4	11.4	0.0079	2.9

^a Measured with reactions of 0.3 eV laboratory energy and at a collision chamber temperature of 300 K. ^b Rate coefficients were determined relative to the rate $k = 1.2 \times 10^{-10} cm^3/molecules \cdot s$ for the reaction $O^- + NO_2 \rightarrow NO_2^- + O$. ^c Long-range theory, G. Goumounis and D. P. Stevenson, *J. Chem. Phys.*, **79**, 294 (1983). ^d Average dipole orientation theory, M. T. Bowers and L. Sun in ref. 1, p. 163. Calculated for an effective temperature T such that the center of mass energy $E_{CM} = kT$. ^e Calculated from available heats of formation, electron affinities, and proton affinities, H. M. Rosenstock, K. Dravi, B. W. Steiner, and J. T. Herron, *J. Phys. Chem. Ref. Data*, **1**, 6 (1972); J. L. Beauchamp in ref. 1, p. 413; K. Tanaka, G. I. Mackay, J. D. Payzant, and D. K. Bohme, *Can. J. Chem.*, **54**, 1643 (1976); S. A. Sullivan and J. L. Beauchamp, *J. Am. Chem. Soc.*, **98**, 1160 (1976). ^f Exothermicity uncertain. ^g $k_{forward}$ divided by statistical factor of 2.

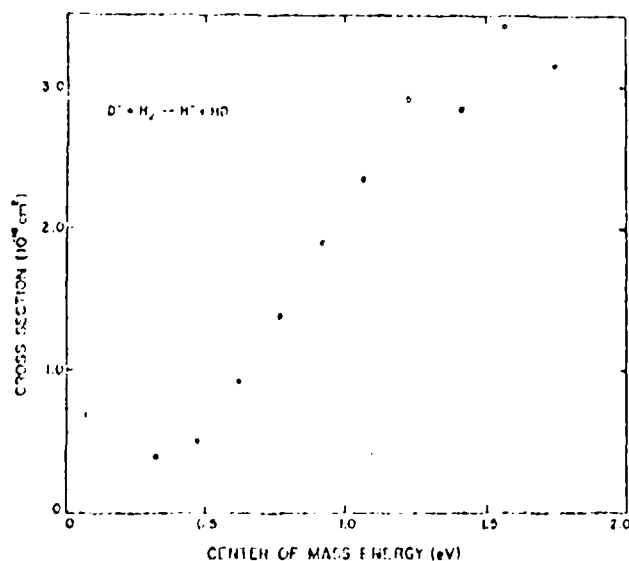
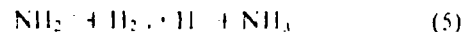


Figure 1. Excitation function for the reaction $D^- + (HD, HD)H_2$; the reaction cross section $\sigma_{rel}^{(1)}$ (see text) is plotted as a function of nominal ion energy (CM).

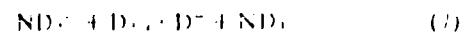
reaction 3 (not corrected for ion translational energy spread and Doppler broadening). These results are in general agreement with Paulson's data⁹⁻¹¹ and the expectations from theory,¹² which were discussed earlier. The rate coefficients for the D^-/NH_3 and D^-/ND_3 reactions (Table I) are somewhat larger than that determined by Bohme et al.¹ for the analogous H^-/NH_3 reaction ($k = 0.009 \times 10^{-10} cm^3/molecules \cdot s$). Because the first state of the tandem mass spectrometer in the present configuration does not transmit H^- ions, we cannot directly observe the latter reaction. In any case, the rate coefficients determined here at an incident ion energy of ~ 0.3 eV are not directly comparable with those measured at thermal energies by Bohme et al.¹ The energy dependence of the cross section for the D^-/NH_3 proton transfer reaction is rather flat over the entire energy range examined ($\sim 0.1-2.4$ eV, in the

center of mass system). This behavior is quite similar to that which we have previously observed in the case of D^-/SiH_4 electron transfer reaction.¹⁷ In both of these cases, a light incident ion is impacted on a heavy target molecule, and the experimental energy resolution in the laboratory system is approximately the same as that in the center of mass system. The resolution attainable (± 0.3 eV) is of the same order of magnitude as the translational energy threshold for the D^-/NH_3 reaction, and it is thus rather difficult to obtain an accurate value for this threshold. The difference in the rate coefficients for the D^-/NH_3 and D^-/ND_3 reactions which are listed in Table I is presumably indicative of kinetic isotope effects.

2. NH_2^- and ND_2^- Reactions. Rate coefficients for amide ion reactions with H_2 , HD, and D_2 are also presented in Table I. As for the D^- reactions with ammonia, interesting kinetic isotope effects are observed. Both the forward and reverse steps of the reaction



were studied in considerable detail by Bohme and co-workers.^{1-4,6,8} Their results indicate that H_2 is a stronger acid in the gas phase than is NH_3 . Bohme et al.¹ reported a rate coefficient of $0.23 \times 10^{-10} cm^3/molecules \cdot s$ at 298 K for the forward step of reaction 5, which may be compared with our value of $0.18 \times 10^{-10} cm^3/molecules \cdot s$, determined at 0.3 eV (Table I). The currently accepted value for the equilibrium constant of reaction 5 is $K_{eq} = 27.1$ at 298 K.¹⁸ This value can be used in conjunction with the computed ΔS^\ddagger for reaction 5 to calculate the difference in the proton affinities of H^- and NH_2^- . The resulting difference is $PA(H^-) - PA(NH_2^-) = -3.2$ kcal/mol. In the present study, we have also observed two isotopic variants of reaction 5, namely,



The equilibrium constants of reactions 6 and 7 have not yet been determined experimentally. They can be derived, however, by the usual thermodynamic relations, for example for

reaction 6, eq 8-11.

$$\Delta H^\circ_{298} - T\Delta S^\circ_{298} = \Delta G^\circ_{298} = -RT \ln K_{eq} \quad (8)$$

$$\Delta H^\circ_{298} = \Delta H^\circ_0 + \int_0^{298} \Delta C_p dT \quad (9)$$

$$\Delta H^\circ_0 = EA(\text{NH}_3) - EA(\text{D}) + D^\circ_0(\text{H-D}) - D^\circ_0(\text{NH}_3\text{H}) \quad (10)$$

$$\Delta S^\circ_{298} = S^\circ_{298}(\text{D}^-) + S^\circ_{298}(\text{NH}_3) - S^\circ_{298}(\text{NH}_2^-) - S^\circ_{298}(\text{HD}) \quad (11)$$

Using the appropriate bond dissociation energies, electron affinities, and standard entropies²⁹ for the species involved in these reactions, one obtains the equilibrium constants $K_{eq,6} = 0.82$ and $K_{eq,7} = 1.8$ at 298 K. (The calculated proton affinity of D^- , 599.8 kcal/mol, is 0.6 kcal/mol higher than that for H^- .) The value used for the bond dissociation energy $D^\circ_0(\text{NH}_3\text{H})$ here is taken from the equilibrium study of reaction 5 by Bohme et al.⁴ There are two alternative thermochemical values,⁴ one higher and one lower than the value obtained from the equilibrium study. Obviously, if one of these alternative values were used in calculating $K_{eq,6}$ and $K_{eq,7}$, the magnitudes of these equilibrium constants would be different, but of course the value of $K_{eq,6}$ cited above would also change, so that the isotope effects on the equilibrium constants would be essentially the same. The computed equilibrium constants may be compared with the ratios of the rate coefficients for the forward and reverse steps of reactions 6 and 7. Using the data shown in Table I, for reaction 6, $k_f/k_r = 0.85$, and for reaction 7, $k_f/k_r = 1.4$. In spite of the fact that the reactant ions in the present case are not translationally thermal, the agreement between the calculated equilibrium constants and the ratios, k_f/k_r , is surprisingly good.

As previously noted, reaction 3, and both the forward and reverse steps of reaction 5 and its various deuterated analogues, are relatively slow reactions. Translational energy thresholds were observed for both the forward and reverse steps of the ammonia-hydrogen reactions. The excitation function for the forward step of reaction 7 is shown in Figure 2. This reaction step is exothermic by 2.55 kcal/mol. Yet the excitation function is obviously typical of that observed for reactions which are endothermic or which have an activation barrier. Because of the large ratio of the projectile ion mass to that of the target molecule, the Doppler broadening effect is severe for this reaction. The Doppler width (Δ), which is the half-width of the probability distribution at $1/e$ of the maximum height, is given by the expression¹⁵

$$\Delta = 2(mF_m kT/M)^{1/2} \quad (12)$$

where m and M are the masses of the ion and neutral, respectively, F_m is the nominal reactant ion energy (1 AB), T is the collision chamber temperature, and k is the Boltzmann constant. For $F_m = 2$ eV and $T = 433$ K, $\Delta = 1.17$ eV for the ND_2^+/D reactant pair. The experimental excitation function must be deconvoluted to correct for the Doppler broadening and the ion translational energy distribution, as noted earlier. Since neither the energy threshold for reaction 7 nor the postthreshold energy dependence of the cross section is known, trial "absolute" excitation functions were tested until a best fit was achieved between the calculated convoluted curve^{15,21} and the experimental data of Figure 2. The excitation function expected from theory¹⁰ for an endothermic ion-molecule reaction has the functional form

$$\sigma(E_{rel}) = \sigma_0 Y(E_{rel})/E_{rel}^2 \quad (13)$$

where the "yield function" is given by

$$Y(E_{rel}) = (S_p/h^2) C^2 S [2(E_{rel} - E_0)/(S + 2)]^{1/2} \exp(-E_{rel}) \quad (14)$$

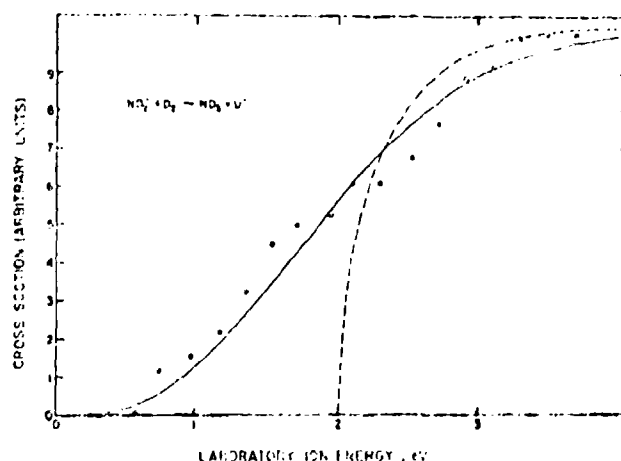


Figure 2. Excitation function for reaction 5D: $\text{ND}_2^+ + \text{D} \rightarrow \text{ND}_3 + \text{D}^+$; points are experimental data for σ_p^+ (in arbitrary units) as a function of the nominal ion energy (1 AB). The experimental cross section at the maximum is $\approx 1.8 \times 10^{-17} \text{ cm}^2$ at a nominal ion energy (CM) of 0.6 eV, and drops at higher energies (not shown). The smooth curve is the computer fit to the data, obtained by convoluting the deuterium-charge representation of the absolute excitation function in the laboratory frame with the reactant translational energy distribution and the Doppler broadening distribution (reaction 6, ref. 21).

and

$$k^2 = (2\mu/h^2) E_{rel} \quad (15)$$

where E_{rel} is the relative translational energy (CM), E_0 is the translational energy threshold (CM), $S = d$, and $C = \alpha e^2/2$ for an ion-induced dipole interaction, α is the polarizability of the neutral, e is the electronic charge, and $h = h/2\pi$, where h is Planck's constant and μ is the reduced mass of the ion-neutral pair. Inserting eq 14 and 15 into eq 13, one obtains

$$\sigma(E_{rel}) = 2\pi(\alpha e^2/2)^{1/2} \frac{(E_{rel} - E_0)^{1/2}}{E_{rel}} \quad (16)$$

Employing this functional form, and treating E_0 as a parameter, the best fit of the computer calculated curve to the experimental data (see Figure 2) corresponds to an energy threshold of $E_0 = 2$ eV (1 AB) or $E_0 = 0.36$ (CM) = 8.4 kcal/mol. We can now consider the relationship between this translational energy threshold, E_0 , and the Arrhenius activation energy, E_a , for the reaction. The temperature-dependent rate coefficient, $k(T)$,^{10,12} is related to the cross section by the expression

$$k(T) = (2/kT)^{1/2} (1/\pi\mu)^{1/2} \times \int_0^\infty \exp(-E_{rel}/kT) \sigma(E_{rel}) E_{rel} dE_{rel} \quad (17)$$

Inserting eq 16 into eq 17, the rate coefficient is then given by

$$k(T) = 2\pi(\alpha/\mu)^{1/2} \exp(-E_0/kT) \quad (18)$$

or, in other terms,

$$k(T) = k_{\infty} \exp(-E_a/kT) \quad (19)$$

where k_{∞} is the Langevin collision rate coefficient. The Arrhenius activation energy is given as usual by¹⁰

$$E_a = -RT^2 d \ln k(T)/dT \quad (20)$$

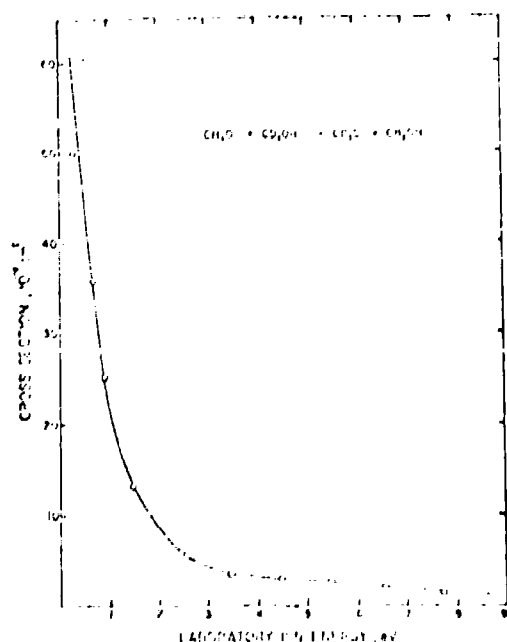
so it is apparent that $E_a = E_0$. In their treatment of similar proton transfer reactions, McLay, Hainsworth, and Bohme⁴ have tentatively assumed that

$$k_{\infty} = k_{\text{Langevin}} \exp(-E_a/kT) \quad (21)$$

Table II. Rate Coefficients for Proton Transfer Reactions to Organic Negative Ions

Reaction	k , 10^{-10} cm ³ /molecules	
	Present ^{a,b}	Values reported previously
$\text{CH}_3\text{O}^- + \text{CD}_3\text{OH} \rightarrow \text{CD}_3\text{O}^- + \text{CH}_3\text{OH}$	6.76	
$\text{CH}_3\text{O}^- + \text{C}_2\text{H}_5\text{CH}_2\text{OH} \rightarrow \text{C}_2\text{H}_5\text{CH}_2\text{O}^- + \text{CH}_3\text{OH}$	6.58	2.0
$\text{CH}_2=\text{CHCH}_2^- + \text{C}_2\text{H}_5\text{OH} \rightarrow \text{CH}_2=\text{CHO}^- + \text{C}_2\text{H}_5$	10.9	2.5 ^c
$\text{CH}_2=\text{CHCH}_2^- + \text{C}_2\text{H}_5\text{CH}_2\text{OH} \rightarrow \text{C}_2\text{H}_5\text{CH}_2\text{O}^- + \text{C}_2\text{H}_4$	≤ 0.005	0.75; ^e ~ 0.1 ^d
$\text{CH}_2=\text{CHCH}_2^- + \text{CD}_3\text{COCD}_3 \rightarrow \text{CD}_3\text{CO}^- + \text{C}_2\text{H}_4\text{D}$	0.018	
$\text{CH}_3\text{C(O)}^- \rightarrow \text{CH}_3 + \text{CD}_3\text{C(O)}^- \text{O}(\text{CD}_3) \rightarrow \text{CD}_3\text{C(O)}^- + \text{CD}_3 + \text{CH}_3\text{C(O)CH}_2\text{D}$	0.032 ^e	
	0.014 ^c	
$\text{CD}_3\text{C(O)}^- \rightarrow \text{CD}_3 + \text{CH}_3\text{C(O)}^- \text{O}(\text{CH}_2\text{CH}_3) \rightarrow \text{CH}_3\text{C(O)}^- + \text{CHCH}_3 + \text{CD}_3\text{C(O)CH}_2\text{H}$	0.1 ^e	0.061 ^e
	0.032 ^c	

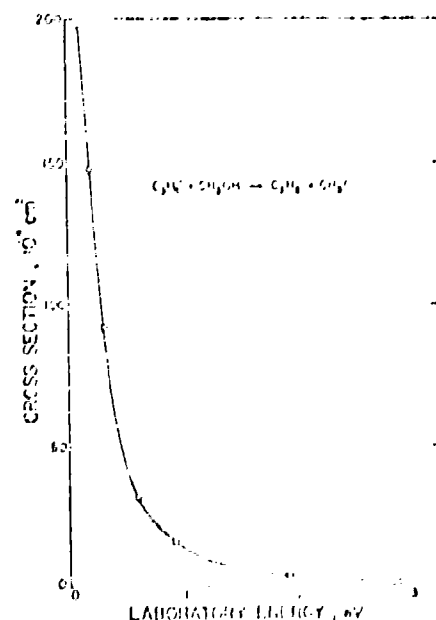
^a Measured with reactant ions of 80.3 eV laboratory energy. ^b Rate coefficients were determined relative to the rate $k = 1.2 \times 10^{-9}$ cm³/molecules for the reaction $\text{O}^- + \text{NO}_2 \rightarrow \text{NO}_2^- + \text{O}$. ^c Measured by the ICR method at 300 K (ref 23). ^d Measured by the flowing afterflow method at 300 K (ref 3a). ^e Collision chamber temperature 300 K. ^f Collision chamber temperature 440 K. ^g Measured by the ICR method at 300 K (ref 6).

Figure 3. Excitation function for the reaction $\text{CH}_3\text{O}^- (\text{CD}_3\text{OH}) \rightarrow \text{CH}_3\text{OH} (\text{CD}_3\text{O}^-)$.

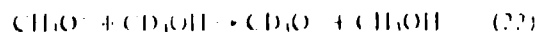
From the above discussion, it is seen that this is equivalent to our assumed excitation function, with $E_{th} = E_0$. Using eq 21 Mackay et al.¹ computed for the forward step of reaction 5 an activation energy $E_a = 2.5$ kcal/mol. This is somewhat lower than the value of 3.4 kcal/mol obtained in the present study for the forward step of reaction 7; the difference being well outside the experimental error limits of the two measurements. Apparently, this difference reflects a true isotope effect, although the activation energy value derived here must be considered as an upper limit. It was observed that other tried excitation functions, which rise less sharply at the threshold, does the function represented by eq 16, could also be fit to the experimental data (up to convolution with the energy distribution), provided that the threshold parameter, E_{th} , was less than 2 eV (in the laboratory system). That is to say, from our results, we can calculate only that $E_{th} < 3.4$ kcal/mol.

The threshold behavior similar to that observed above was also observed for the forward step of reaction 8, and the magnitude of the former seems to be slightly lower than that estimated for the $\text{ND}_3^+/\text{D}_2\text{O}$ reaction.

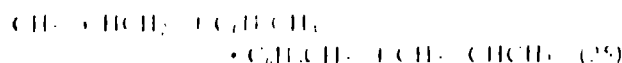
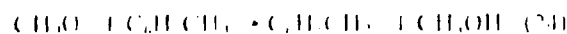
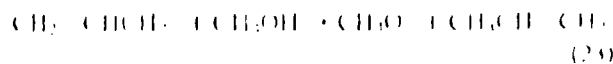
A. Organic Negative Ion Reactions. The rate coefficients measured in the present study for a number of organic negative ion proton transfer reactions are shown in Table II. The rate

Figure 4. Excitation function for the reaction $\text{CH}_2=\text{CHCH}_2^- (\text{C}_2\text{H}_5\text{OH}) \rightarrow \text{CH}_2=\text{CHO}^- (\text{C}_2\text{H}_5)$.

coefficient for the reaction



is approximately half the collision rate constant,¹⁶ which suggests that this reaction involves the formation of a hydrogen-bonded intermediate, which can decompose to give either the oxidized products or the original reactants, with equal probabilities. Such organic ion-molecule reactions involving polyatomic species are now generally considered to proceed at low energies via intermediate complexes which decompose in various ways depending upon energy content.¹⁷⁻¹⁹ The excitation function for reaction 22, shown in Figure 3, is typical for a reaction having no activation barrier. Reactions 23, 24, and 25 were also observed previously²¹ under thermal energy conditions. In these earlier studies, reactions 23 and 24 were found to be fast, while reaction 25 was shown to be slow.



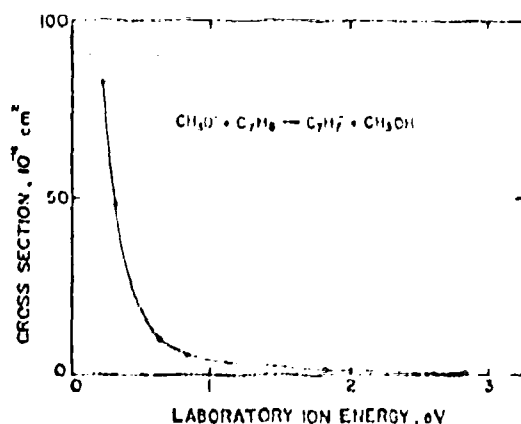


Figure 5. Excitation function for the reaction CH_3O^+ ($\text{C}_6\text{H}_5\text{CH}_2$, CH_3OH) H^+ .

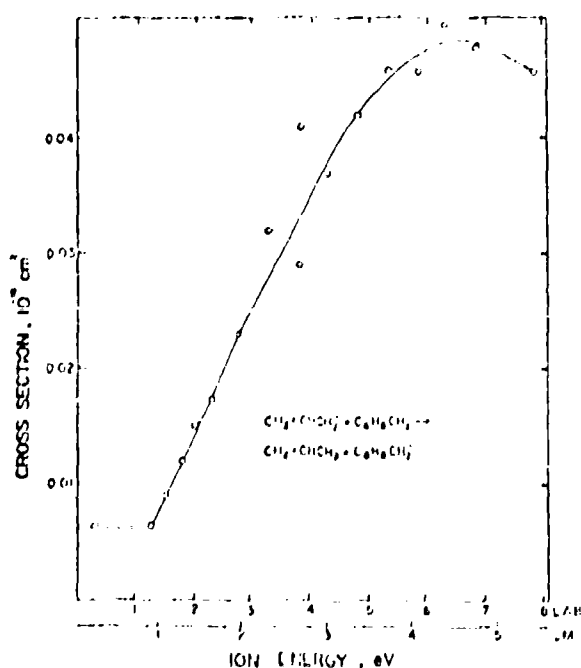
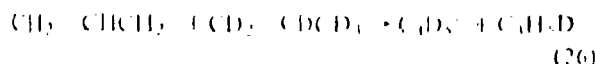


Figure 6. Excitation function for the reaction C_6H_5^+ (C_6H_5 , C_6H_6) H^+ . Note that the plus have not been corrected for Doppler broadening.

These observations lead to the conclusion that in a mixture of these components, the presence of methanol catalyzes the conversion of allyl anion to benzyl anion. Figures 4-6 show the excitation functions measured in the present study for reactions 23, 24, and 25. As shown, these are uncorrected for the Doppler broadening effect. As expected, the reactions 23 and 24 do not exhibit translational energy thresholds. However, although reaction 25 is exothermic, the excitation function for this process clearly indicates a translational energy threshold. Similar threshold behavior is observed (Figure 7) for the nominally thermoneutral reaction



These results indicate the existence of energy or activation barriers in the potential surfaces of some proton transfer reactions to delocalized negative ions. The magnitude of the thresholds is indicative of activation barriers on the order of ~ 10 kcal/mol. There is a surprising disagreement between the rate coefficient measured in the present study for reaction 25

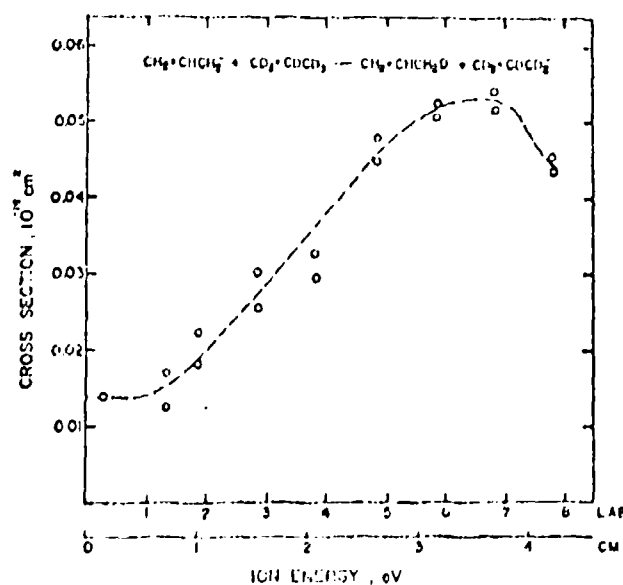


Figure 7. Excitation function for the reaction $(\text{C}_6\text{D}_5)^+$ (C_6D_5 , C_6D_6) D^+ . The data have not been corrected for Doppler broadening.

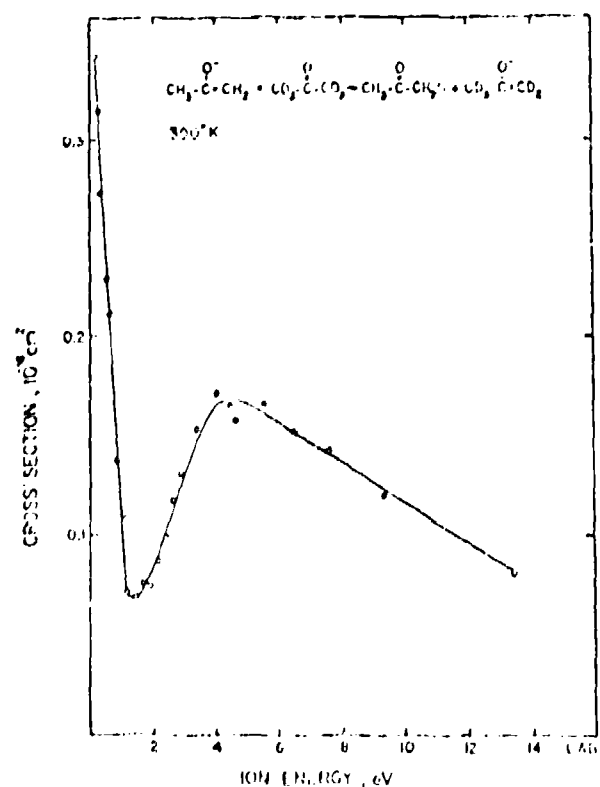


Figure 8. Excitation function for the reaction $\text{CH}_3\text{COH}_2^+$ (C_6D_6 , C_6D_6) CH_3COH_2 (C_6D_6 , C_6D_6) H^+ . Collision chamber temperature is 300 K.

and those previously reported^{15,24} (Table II). We believe, however, that the low rate coefficient which we obtained is consistent with the observation of a high activation barrier. The rate coefficients of reactions 25 and 26 were rather insensitive to the collision chamber temperature (in the range 300-430 K) increasing only slightly at the higher temperature. However, the rate of reaction 25 was observed to be extremely sensitive to the presence of impurities in the collision chamber,

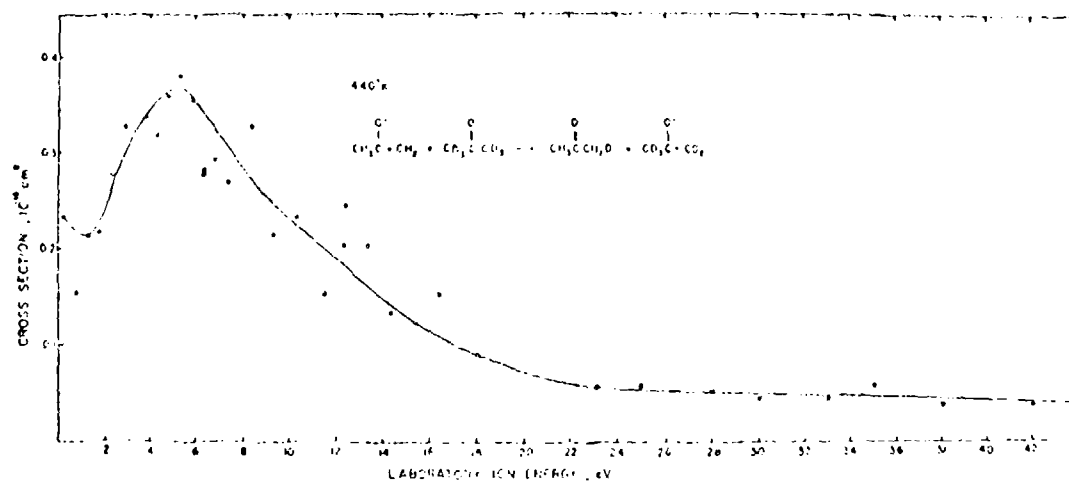


Figure 9. Excitation function for the reaction $\text{CH}_3\text{COCH}_2^- + (\text{CD}_3\text{COCD}_3)_2\text{CH}_3\text{COCH}_2\text{H}_3\text{D}_6$. Collision chamber temperature is 440 K.

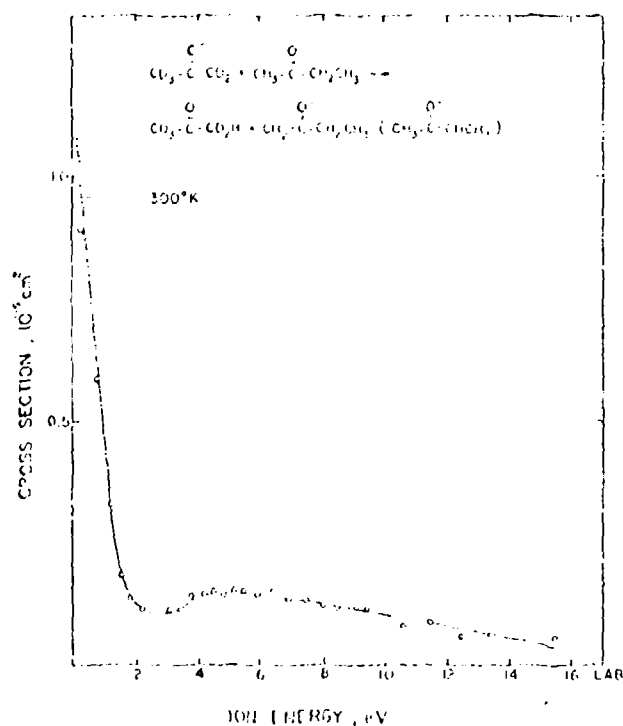


Figure 10. Excitation function for the reaction $\text{CD}_3\text{COCD}_3^- + (\text{CH}_3\text{COCH}_2\text{CH}_2\text{CD}_3\text{COCD}_3)_2\text{H}_5\text{CH}_3\text{COCH}_2\text{CH}_3$. Collision chamber temperature is 300 K.

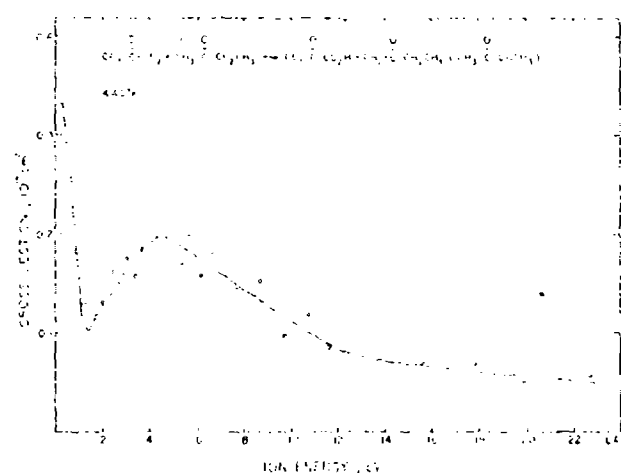
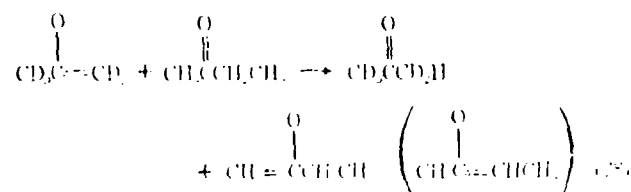
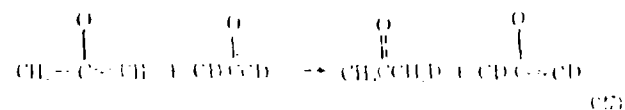


Figure 11. Excitation function for the reaction $\text{CD}_3\text{COCD}_3^- + (\text{CH}_3\text{COCH}_2\text{CH}_2\text{CD}_3\text{COCD}_3)_2\text{H}_5\text{CH}_3\text{COCH}_2\text{CH}_3$. Collision chamber temperature is 440 K.



the rate increasing dramatically in the presence of even trace quantities of methanol, in agreement with the ICR data.²² Thus, realistically, the rate coefficient reported here probably represents at best an upper limit. It seems probable that the values previously reported¹²⁻²³ are also upper limits, since the presence of trace impurities in the afterglow and ICR experiments would have a similarly adverse effect.

Of special interest are the reactions of delocalized enolate anions with aliphatic ketones, such as



Reaction 22 is nominally thermoneutral, while reaction 23 is slightly exothermic (for formation of either ionic product).²⁴ The rate coefficients of these reactions were determined in the present study and are compared with previous data in Table II. Excitation functions were also measured for each reaction at both low (300 K) and high (440 K) collision chamber temperatures. These functions are shown in Figure 8-11 and the corresponding rate coefficients for these reactions are plotted as a function of translational energy in Figures 12 and 13. These excitation functions do not exhibit translational energy thresholds. On the contrary, in the low kinetic energy range, the cross section drops with increasing energy in a manner typical of exothermic reactions, having no activation barrier. The result is consistent with the model suggested by Farnick and Brauman,²⁵ which predicts that there are activation barriers

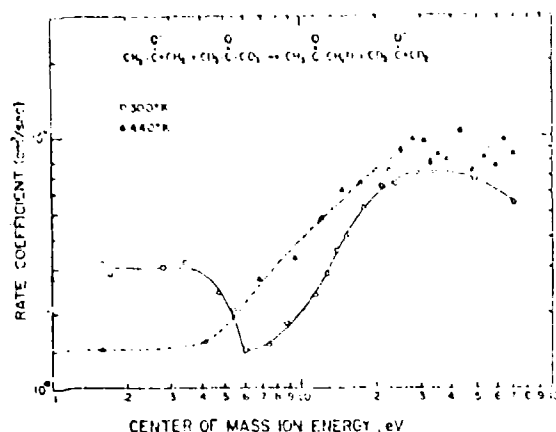


Figure 12. Rate coefficients for the reaction $\text{CH}_3\text{COCH}_3 + (\text{CD}_3\text{CO})^+$ ($\text{CH}_3\text{COCH}_3 + \text{CD}_3\text{CO}^+$) as a function of relative translational energy at the two collision chamber temperatures indicated.

in the potential surfaces appropriate to reactions 27 and 28, but that the height of these barriers is lower than the potential energies of either the separated reactants or products. This barrier corresponds to the symmetrical transition state for proton transfer, the reaction proceeding via a three-step mechanism involving the formation of a nonsymmetrical intermediate, $[\text{AH} \cdots \text{B}]^+$, which lies in a potential well with respect to the reactants, $(\text{AH} + \text{B}^+)$, as well as with respect to the transition state, $(\text{A} \cdots \text{H} \cdots \text{B})^+$. According to this model,⁶ it is the competition between two unimolecular decompositions of the intermediate, the back reaction forming $(\text{AH} + \text{B}^+)$ via a single bond cleavage, and the forward rearrangement reaction, producing the symmetrical transition state, which determines the overall bimolecular rate coefficient at thermal energies. This model is well supported by the present results. We observe that the rate coefficient and its variation with translational energy (Table II and Figures 12 and 13) are strongly dependent on the collision chamber temperature. At low translational energies, it is seen that an increase in the collision chamber temperature decreases the overall rate coefficient. A similar effect has been observed in certain hydride ion transfer reactions of large polyatomic positive ions.³² Increasing the collision chamber temperature results in an increase in the internal energy of the neutral reactant, and in turn, the internal energy of the intermediate, $[\text{AH} \cdots \text{B}]^+$, is increased. The higher internal energy of the intermediate favors the unimolecular channel having a high activation energy and a high entropy factor, that is, the simple bond cleavage, which corresponds to the back reaction yielding the original reactants. An increase in the cross section with increasing translational energy is observed at energies greater than ~ 1.5 eV in the laboratory system. This may reflect a change in the mechanism of the reaction, resulting from the fact that the long-lived intermediate can no longer be formed at the higher interaction energies. It is well known that the mechanism of an ion-neutral reaction can change from one involving formation of a persistent intermediate complex to a direct mechanism as the collision energy is increased.³³ The lifetime of such an intermediate collision complex decreases with increasing internal energy E^+ , and in turn the internal energy increases as the relative energy of the reactants is increased. When the interaction energy increases to the point that the intermediate is no longer formed, back reaction to give reactants can no longer compete effectively with the forward reaction, and an increase in the cross section (and of E^+) with increasing energy is then observed. This is qualitatively further supported by the fact that the point of onset of the rising portion of the plot of E^+ as a function of ion energy shifts to lower relative energies as the

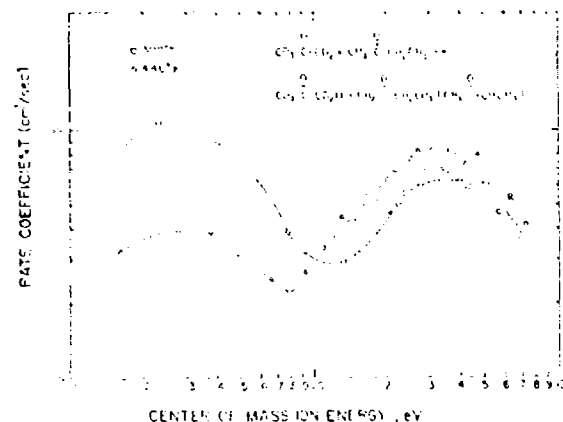


Figure 13. Rate coefficients for the reaction $\text{CD}_3\text{COCH}_3 + (\text{CD}_3\text{CO})^+$ ($\text{CD}_3\text{COCH}_3 + \text{CD}_3\text{CO}^+$) as a function of relative translational energy at the two collision chamber temperatures indicated.

temperature is increased (Figures 12 and 13). This demonstrates the equivalent role of internal and relative translational energy in reducing the lifetime of the intermediate complex. The second decrease in the cross section at still higher energies (Figures 8–11) is consistent with the behavior of many ion-molecule reactions at higher energies and presumably simply reflects a decrease in the collision cross section.

Acknowledgment. This work was supported by the Air Force Office of Scientific Research under Contract F44620-76-C-0007 with Wright State University. The authors are grateful for helpful discussions with Professors D. K. Bohme and J. L. Brauman.

References and Notes

- (1) D. K. Bohme in "Interactions between Ions and Molecules," P. Ausloos, Ed., Plenum Press, New York, 1978, p. 47.
- (2) S. G. Lias and P. Ausloos in "Molecular Ion Chemistry: The Role of Reaction Chemistry," J. H. D. E. J. van der Vliet, D. G. Lias, p. 1.
- (3) See, for example, (a) D. K. Bohme, L. Lee, and J. L. Brauman, *J. Am. Chem. Soc.*, **94**, 5103 (1972); (b) S. A. Saito and J. L. Brauman, *ibid.*, **98**, 1160 (1976); (c) T. P. McMahon and P. Keenleyside, *ibid.*, **96**, 5909 (1974).
- (4) D. K. Bohme, R. S. Hemmings, and H. W. Roesler, *J. Chem. Phys.*, **55**, 17 (1972).
- (5) G. L. Mackay, R. S. Hemmings, and D. K. Bohme, *Chem. J. Chem.*, **54**, 10 (1972).
- (6) W. E. Ferguson and J. L. Brauman, *J. Am. Chem. Soc.*, **90**, 1091 (1968).
- (7) M. E. Carter and R. B. B. Farnham, *J. Chem. Phys.*, **55**, 4541 (1971); M. E. Carter and R. B. Farnham, *ibid.*, **55**, 5134 (1971); R. B. Farnham, *Acc. Chem. Res.*, **6**, 303 (1973).
- (8) See, for example, M. D. Burrows, *The Molecular Ion*, Academic Press, New York, 1972, pp. 101–104.
- (9) J. D. Roberts and M. J. B. Farnham, *Adv. Phys. Chem. Ser. 1*, **9** (1972).
- (10) M. J. B. Farnham, *ibid.*, p. 15.
- (11) J. L. Brauman, *Int. Rev. Phys. Chem.*, **12**, 45 (1972).
- (12) I. Chodura, R. M. Stevens, F. L. Minn, and M. Kapteina, *J. Chem. Phys.*, **45**, 2720 (1966).
- (13) C. D. Burrows and H. F. King, *J. Am. Chem. Soc.*, **90**, 2251 (1968).
- (14) (a) G. C. Papanicolaou, D. L. King, J. C. Papanicolaou, R. B. Farnham, and A. H. E. Ables, *J. Chem. Phys.*, **52**, 6065 (1970); (b) R. B. Farnham and J. C. Papanicolaou, *ibid.*, **57**, 4062 (1973).
- (15) T. G. Farnham, R. M. Stevens, and F. L. Minn, *J. Chem. Phys.*, **55**, 5037 (1971).
- (16) (a) D. L. Farnham and T. O. Tjornheim, *Int. Rev. Phys. Chem.*, **12**, 21 (1972); (b) D. L. Farnham, *ibid.*, **12**, 45 (1972); (c) D. L. Farnham, *ibid.*, **12**, 45 (1972); (d) D. L. Farnham, *ibid.*, **12**, 45 (1972).
- (17) T. O. Tjornheim and D. L. Farnham, *Theoretical and Experimental Molecular Ion Chemistry*, J. L. Brauman, Ed., Plenum Press, New York, 1973, p. 145.
- (18) G. C. Papanicolaou, R. B. Farnham, and J. C. Papanicolaou, *J. Chem. Phys.*, **57**, 4062 (1973).
- (19) T. G. Farnham, R. M. Stevens, and F. L. Minn, *J. Chem. Phys.*, **55**, 5037 (1971).
- (20) J. L. Brauman, *Int. Rev. Phys. Chem.*, **12**, 45 (1972).
- (21) J. L. Brauman, *Int. Rev. Phys. Chem.*, **12**, 45 (1972).
- (22) J. L. Brauman, *Int. Rev. Phys. Chem.*, **12**, 45 (1972).
- (23) J. L. Brauman, *Int. Rev. Phys. Chem.*, **12**, 45 (1972).
- (24) J. L. Brauman, *Int. Rev. Phys. Chem.*, **12**, 45 (1972).
- (25) J. L. Brauman, *Int. Rev. Phys. Chem.*, **12**, 45 (1972).
- (26) J. L. Brauman, *Int. Rev. Phys. Chem.*, **12**, 45 (1972).
- (27) J. L. Brauman, *Int. Rev. Phys. Chem.*, **12**, 45 (1972).
- (28) J. L. Brauman, *Int. Rev. Phys. Chem.*, **12**, 45 (1972).
- (29) J. L. Brauman, *Int. Rev. Phys. Chem.*, **12**, 45 (1972).
- (30) J. L. Brauman, *Int. Rev. Phys. Chem.*, **12**, 45 (1972).
- (31) J. L. Brauman, *Int. Rev. Phys. Chem.*, **12**, 45 (1972).
- (32) J. L. Brauman, *Int. Rev. Phys. Chem.*, **12**, 45 (1972).
- (33) J. L. Brauman, *Int. Rev. Phys. Chem.*, **12**, 45 (1972).

- Press, New York, N.Y., 1972, p. 77.
- (23) J. E. Brauman, C. A. Lueder, and M. J. White, *J. Am. Chem. Soc.*, **95**, 577 (1973).
- (24) D. Lofth, J. L. Beauchamp, and J. R. Eyley, *J. Am. Chem. Soc.*, **92**, 7045 (1970).
- (25) J. L. Beauchamp and L. A. P. 413.
- (26) D. Lofth, J. L. Beauchamp, G. F. Mackay, and D. E. Bohme, *Chem. Phys. Lett.*, **34**, 321 (1975).
- (27) C. L. Yeh, T. O. Therman, and B. M. Hughes, *J. Chem. Phys.*, **59**, 3167 (1973).
- (28) C. E. Young, E. Lindholm, and D. K. Bohme, *Can. J. Chem.*, **49**, 979 (1971).
- (29) *(F¹⁹O₂)* and *(F¹⁸O₂)*, G. Herzberg, *Molecular Spectra and Molecular Structure*, Vol. I, 2nd ed., Van Nostrand, Princeton, N.J. (1945) and *Tables of Molecular Vibrational Frequencies*, Part A, NIST Monograph 16, 1957; *(F¹⁹O₂)* and *(F¹⁸O₂)*, J. W. McKean and R. A. B. Fowles, *J. Chem. Phys.*, **48**, 33 and 46 (1968) respectively; at 298 K, the vibration energy of *(F¹⁹O₂)* was estimated to be 0.018 eV (181).
- (30) K. D. Gonsky and R. D. Pinnell, *J. Chem. Phys.*, **56**, 2201 (1972).
- (31) R. D. Pinnell, *Kinetic Theory of Gases*, McGraw-Hill, New York, N.Y., 1958, Chapter 8.
- (32) E. F. Greene and A. Kuipersmann, *J. Chem. Educ.*, **45**, 561 (1968).
- (33) R. Kuntz, *Chem. Rev.*, **53**, 459 (1963).
- (34) J. J. Salomon, M. Moshier, and F. H. Field, *J. Am. Chem. Soc.*, **96**, 372 (1974).
- (35) (a) R. Wolfgang, *Acc. Chem. Res.*, **3**, 42 (1970). (b) Z. Herman and R. Wolfgang, *Acc. Chem. Res.*, **3**, 42 (1970).

Characterization of the luminescence from low energy He^+/Xe and He^+/Kr reactions*

E. GRANT JONES, B. MASON HUGHES† and THOMAS O. TIERNAN‡

Department of Chemistry and Brehm Laboratory, Wright State University, Dayton, OH 45435, U.S.A.

and

DARRELL C. FEE and DARRELL G. HOPPER‡

Argonne National Laboratory, Argonne, IL 60439, U.S.A.

(Received November 1977; in revised form 11 April 1978)

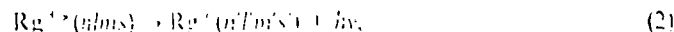
Abstract. The luminescence spectra produced by the reactions of 400-eV helium ions with xenon and krypton gas are reported and analyzed. In this paper spectral observations have been made for the XeII and XeII transitions which produce radiation in the wavelength interval 80–130 nm, and emission cross sections have been determined. Radiative transitions in the 130–800 nm interval have been treated similarly, and the results are available upon request. An important feature of the present work is that the experimental configuration utilized permits the excited products to radiate in the absence of significant perturbation from collisions or from electric or magnetic fields.

INTRODUCTION

THE REACTIONS of ionic helium with the other rare gases, Rg,



produce complex optical emission spectra which result,



from electronically excited products [1–10]. Such ion-neutral reactions are of interest as possible laser pumping mechanisms [11]. The large difference between the recombination energy of the He^+ ion, 24.58 eV, and the atomic ionization potential of both Xe and Kr (12.13 eV and 14.0 eV, respectively) causes many radiating Xe^{+*} or Kr^{+*} ion states to be accessible when translational to internal energy transfer of 5 eV or less occurs. The energetic requirements for the production of various Xe^+ and Xe

* Research supported in part by the United States Air Force Office of Scientific Research under Contract F44620-76-C-0001 with Wright State University and supported in part by the Aerospace Research Laboratories, Wright-Patterson AFB, both in-house and under contract MHPR99-04-000117 with Argonne National Laboratory (USLRDA).

† Present address: Environmental Research Center, University of Utah, Salt Lake City, UT 84112, U.S.A.

‡ NRC-ARL Research Associate, 1972–1974. Present address: Science Applications, Inc., 4124 Linden Ave., Suite 702, Dayton, OH 45422, U.S.A.

- [1] M. FURUKAWA, R. NOVIK and S. TORI, *Phys. Rev. Lett.* **15**, 818 (1965).
- [2] D. JONES, E. J. DE HEER and A. SALON, *Physica*, **36**, 606 (1967).
- [3] H. SCHULSTING, *Z. Naturforsch.*, **23a**, 970 (1968).
- [4] E. J. DE HEER, B. E. J. JONES, D. JONES and E. WATTEBORN, *Mol. Phys.* **41**, 868 (1969).
- [5] R. C. FEE and R. D. NATHAN, *Phys. Rev. Lett.* **25**, 34 (1970).
- [6] S. H. LEE, C. W. WHEAT, S. H. DWORETSEY and L. A. FRENCH, *Phys. Rev. Lett.* **25**, 1284 (1970).
- [7] B. M. HUGHES, E. G. JONES and T. O. TIERNAN, *Abstracts of the VIIIth International Conference on the Physics of Electronic and Atomic Collisions*, Vol. 1, p. 223, Institute of Physics, Bologna (1970).
- [8] B. M. HUGHES, E. G. JONES and T. O. TIERNAN, *Phil. Mag.* **19**, 1561 (1970).
- [9] R. C. FEE, *Phys. Rev. A10*, 117 (1974).
- [10] E. G. JONES, E. M. FROST, D. A. FEE and T. O. TIERNAN, *Phys. Rev. A15*, 616 (1977).
- [11] C. B. COOPER, A. J. COOPER, S. M. GERRY, B. W. JOHNSON and M. SUGIYAMA, *Appl. Phys. Lett.* **24**, 17 (1974).

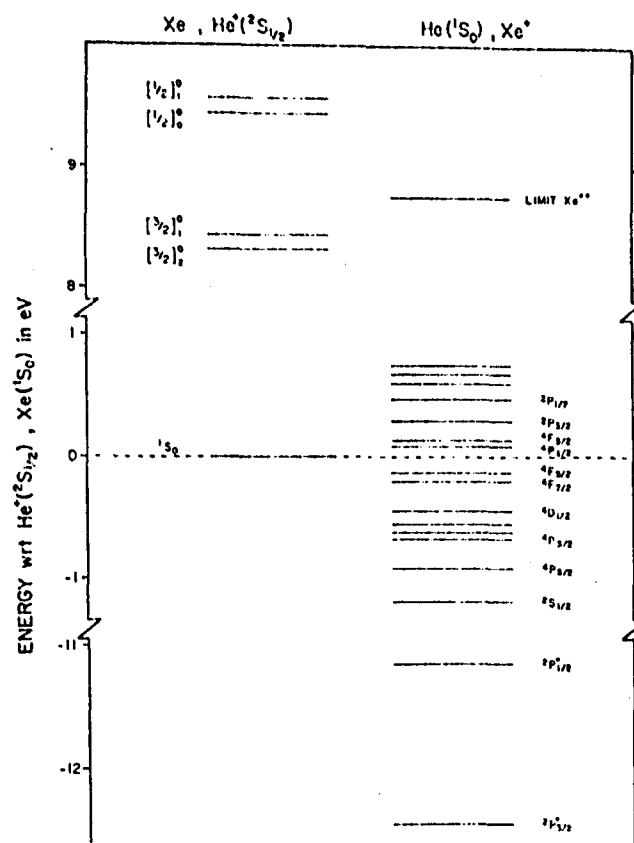
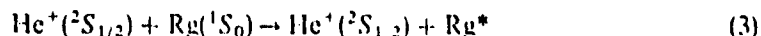


Fig. 1. Energy spectrum of low-lying $(\text{HeXe})^+$ asymptotes with respect to $\text{He}^+(^2S_{1/2}) + \text{Xe}(^1S_0)$.

states are summarized in Fig. 1. The reactions of He^+ with Ne or Ar and inelastic scattering with Ne, Ar, Kr, or Xe.



to produce excited neutral states Rg^* are considerably more endothermic than the reactions of He^+ with Kr or Xe and fewer emission lines are observed at low-to-moderate He^+ translational energies [5, 7, 9]. Thus, the low energy $\text{He}^+ + \text{Xe}$ and $\text{He}^+ + \text{Kr}$ reactions provide an excellent means of populating the low-lying states in Xe^+ and Kr^+ . The intensities of the vacuum u.v. emissions which result from Xe^{+*} or Kr^{+*} product states are reasonably high and there is no apparent interference from neutral Xe^* or Kr^* emissions.

EXPERIMENTAL TECHNIQUES

In order to characterize completely the wavelengths and absolute cross sections of spectral emissions from He^+/Rg collisions, reactions (1) are studied under low-pressure and low-conversion conditions. A mass-selected beam of He^+ ions (1–5 nA) is directed upon xenon or krypton gas at low pressure (4–8 millitorr) in a collision chamber (path length = 0.475 cm). The ion exit slit of the collision chamber is located at the focal point of the 1 m concave grating of a McPherson Model 225 vacuum u.v. spectrometer which is oriented to monitor radiation emitted along the collision axis. A photomultiplier detector and pulse counter are used. The magnetic field in the collision region has been determined to be less than 0.1 Gauss and the electric field is estimated to be less than 0.1 V/cm. The collision-chamber monochromator region is differentially pumped and the pressure in the monochromator housing is maintained at or below 1×10^{-5} torr for the experiments reported here. The detection system incorporates no optical windows for measurements in the region between 50 and 130 nm.

Cross sections for emission of radiation in the 50–130 nm range are calculated from the relation

$$\sigma(\lambda) = I_p(\lambda) [I_{\text{det}}] \quad (4)$$

where $\sigma(\lambda)$ is the cross section for emission of the observed wavelength λ , $I_p(\lambda)$ is the total number of photons produced per second at wavelength λ , n is the number density of atoms in the collision region, l is the collision cell length, and I_a is the He⁺ ion current. The quantity $I_p(\lambda)$ is determined by assuming isotropic photon emission [12]. The transmission function which is used to calculate $I_p(\lambda)$ in the vacuum ultraviolet (v.u.v.) region is established by using estimated grating reflectances [13], assuming literature values for photomultiplier quantum efficiencies [14, 15] and by employing the production by Lyman-alpha radiation in the He⁺/H₂ reaction for calibration [16]. More details on the apparatus are published elsewhere [17]. The uncertainties in the emission cross sections reported here are estimated to be on the order of a factor of three. Relative errors are estimated to be $\pm 25\%$.

CLASSIFICATIONS

The spectral classifications are based upon the energy levels tabulated by MOORE [18] and MINNHAGEN *et al.* [19]. The criteria for each classification are (a) an energy match, (b) the selection rule $\Delta J = 0, \pm 1$, and (c) Laporte's wavefunction parity rule (even \leftrightarrow odd) [20]. The energy selection criterion which is applied is such as to require that the difference between two levels match the observed line to within its experimental uncertainty. The latter quantity varies with wavelength and is reported in the tables with each observed line.

A rigorous, self-consistent classification of all lines observed in He⁺/Xe and He⁺/Kr collisions can be made to transitions between states of Xe⁺ and Kr⁺, respectively. These classifications are provided in Tables 1 and 2 and in [21]. None of the observed lines can be classified with confidence by transitions between excited states of He, Xe, or Kr, although sporadic matches occur, mostly in the visible region [21].

Processes such as reaction (3) which yield excited atomic products have been excluded as possibilities, and all observed lines have been attributed to allowed ionic transitions, for a combination of reasons. First, the endothermicity of such processes is 8–12 eV for collisions which would populate the upper levels for the potentially assignable neutral atomic transitions. The corresponding endothermicity for all transitions contributing appreciably to the total intensity is less than 4 eV if all classifications are made in XeII. Secondly, the allowed v.u.v. transitions from the first few excited neutral states to the ground state are not observed. Even if these excited neutral levels cannot be directly populated in reaction (3), they should be populated by cascading as they are the lower levels of some strong visible transitions which match observed lines. A third reason for excluding excited atomic products is that the sums of intensities of all

- [12] Calibration was based on the techniques outlined by H. J. KOSKOWSKI and R. D. LEE in *Theory and Methods of Optical Pyroacety*, National Bureau of Standards Monograph 41, Washington (1962).
- [13] Values for reflectance were obtained by interpolating the data of T. NAMIOKA and W. R. HUNTER, *Optics Communications* 8, 229 (1973). These numbers were increased by 50% to approximate the increased reflectance of a platinum compared to a gold coated grating.
- [14] K. C. SCHMIDT, Technical Applications Note 9803, Bendix Electro-Optics Division, Ann Arbor, Michigan; M. C. JOHANSSON and J. SVENSSON, Absolute quantum efficiency of a channeltron photomultiplier, Technical Note, Bendix Corp., Research Laboratories Division, Southfield, Mich.
- [15] EMR photoelectric data for calibration of 541F-08-18-03900 photomultiplier-tube that was used in this study.
- [16] The cross section for Lyman-alpha radiation in the He⁺/H₂ reaction determined using the estimated grating reflectance [13] and quantum efficiency [14, 15] at 1216 Å agrees within 30% of the accepted value measured by G. H. DUNN, R. GIBALLE and D. PRETZER, *Phys. Rev.* 128, 2200 (1962).
- [17] B. M. HUGHES, to be submitted to *Rev. Sci. Instrum.*
- [18] C. E. MOORE, *Atomic energy levels*, Vols. I, II and III, National Bureau of Standards, Circular 467, U.S. Dept. of Commerce.
- [19] L. MINNHAGEN, H. STRUHD and B. PETERSSON, *Ark. Fys.* 39, 471 (1969).
- [20] D. G. HOPPER, SEARCH, A FORTRAN IV program for examining energy level tables for matches to observed transitions; D. G. HOPPER, E. G. JONES, D. C. FEE, and K. SIGENHAUER, TABLET: A set of computer-format versions of energy level tables for N and N⁺, N², He, Ne, Kr, Xe, Cl, Br, and I, from various literature sources. The computer program SEARCH, level tables TABLET, and usage documentation are available upon request.
- [21] E. G. JONES, B. M. HUGHES, F. O. TURNER, D. C. FEE, and D. G. HOPPER, Brehm Laboratory Technical Report 10 (1977). Available upon request from Brehm Laboratory, Wright State University, Dayton, OH 45435.

Table 1. Luminescence from the reaction $100\text{eV He}^+ + \text{Xe} \rightarrow \text{He} + \text{Xe}^{*+}$

Line no.	Observed wavelength* λ_0 (nm)	Emission Cross Section† (10^{-18}cm^2)	XeII Transition		$\lambda_1 - \lambda_0^\ddagger$ (nm)	ΔH^\S (eV)
			Lower State	Upper State		
1	71.98 ± 0.4	1.2	$5p^5 2p^0_{3/2}$	$6d^4 F_{5/2}$	-0.09	4.79
			$5p^5 2p^0_{3/2}$	$6d^4 F_{3/2}$	-0.37	4.86
			$5p^5 2p^0_{3/2}$	$20_{1/2}$	0.10	4.74
			$5p^5 2p^0_{1/2}$	$7s^4 D_{3/2}$	-0.18	6.12
2	73.33 ± 0.4	1.0	$5p^5 2p^0_{3/2}$	$6d^4 D_{3/2}$	0.36	4.37
			$5p^5 2p^0_{3/2}$	$16_{3/2}$	-0.08	4.47
			$5p^5 2p^0_{3/2}$	$18_{1/2}$	-0.10	4.47
			$5p^5 2p^0_{3/2}$	$8_{5/2}$	-0.11	4.48
			$5p^5 2p^0_{3/2}$	$10_{5/2}$	-0.19	4.50
			$5p^5 2p^0_{3/2}$	$7s^4 P_{3/2}$	0.33	3.97
3	75.13 ± 0.4	1.0	$5p^5 2p^0_{3/2}$	$7s^4 P_{3/2}$	-0.05	4.06
			$5p^5 2p^0_{3/2}$	$2_{1/2}$	0.11	4.02
			$5p^5 2p^0_{3/2}$	$4_{1/2}$	-0.20	4.09
			$5p^5 2p^0_{3/2}$	$4_{3/2}$	-0.20	4.09
			$5p^5 2p^0_{1/2}$	$6d^4 P_{3/2}$	-0.28	5.41
			$5p^5 2p^0_{1/2}$	$5d^4 S_{1/2}$	-0.10	3.57
			$5p^5 2p^0_{3/2}$	$5d^4 P_{1/2}$	-0.02	3.29
			$5p^5 2p^0_{3/2}$	$5d^4 D_{3/2}$	-0.17	2.77
4	77.47 ± 0.3	0.5	$5p^5 2p^0_{3/2}$	$6s^4 S_{1/2}$	-0.02	2.93
			$5p^5 2p^0_{3/2}$	$5d^4 D_{5/2}$	-0.04	2.31
5	78.75 ± 0.3	2.0	$5p^5 2p^0_{3/2}$	$5d^4 S_{1/2}$	-0.05	3.57
6	80.63 ± 0.2	6.0	$5p^5 2p^0_{3/2}$	$5d^4 P_{3/2}$	-0.02	3.35
7	84.01 ± 0.1	4.9	$5p^5 2p^0_{3/2}$	$5d^4 F_{5/2}$	0.08	1.77
8	84.29 ± 0.1	4.9	$5p^5 2p^0_{1/2}$	$5d^4 D_{5/2}$	-0.06	1.52
9	85.50 ± 0.1	1.4	$5p^5 2p^0_{1/2}$	$5d^4 P_{3/2}$	0.00	1.35
10	87.07 ± 0.1	6.7	$5p^5 2p^0_{3/2}$	$5d^4 D_{5/2}$	0.02	1.13
11	88.79 ± 0.1	5.5	$5p^5 2p^0_{3/2}$	$5d^4 D_{3/2}$	0.09	0.92
12	89.83 ± 0.1	0.7	$5p^5 2p^0_{3/2}$	$6s^4 D_{5/2}$	0.05	0.93
13	91.25 ± 0.1	9.5	$5p^5 2p^0_{3/2}$	$5d^4 P_{3/2}$	0.00	0.86
14	92.58 ± 0.1	15.5	$5p^5 2p^0_{3/2}$	$5d^4 P_{1/2}$	0.02	0.80
15	93.13 ± 0.1	5.2	$5p^5 2p^0_{3/2}$	$5d^4 P_{3/2}$	-0.03	0.73
16	93.52 ± 0.1	7.8	$5p^5 2p^0_{3/2}$	$5d^4 P_{1/2}$	-0.03	0.68
17	93.95 ± 0.1	9.5	$5p^5 2p^0_{3/2}$	$5d^4 P_{3/2}$	-0.03	0.60
18	94.42 ± 0.1	5.4	$5p^5 2p^0_{3/2}$	$6s^4 P_{1/2}$	-0.02	0.47
19	94.98 ± 0.1	9.4	$5p^5 2p^0_{3/2}$	$6s^4 P_{3/2}$	-0.07	0.29
20	95.94 ± 0.1	3.6	$5p^5 2p^0_{3/2}$	$6s^4 D_{3/2}$	-0.03	1.54
21	97.34 ± 0.1	10.4	$5p^5 2p^0_{3/2}$	$6s^4 P_{1/2}$	-0.04	0.09
22	97.70 ± 0.1	7.5	$5p^5 2p^0_{3/2}$	$5d^4 D_{3/2}$	-0.02	1.35
23	98.90 ± 0.1	28.5	$5p^5 2p^0_{3/2}$	$5d^4 D_{3/2}$	-0.02	0.92
24	99.24 ± 0.1	6.5	$5p^5 2p^0_{3/2}$	$5d^4 D_{1/2}$	-0.01	-0.45
25	102.73 ± 0.1	4.7	$5p^5 2p^0_{3/2}$	$5d^4 D_{3/2}$	0.01	0.86
26	103.25 ± 0.2	1.7	$5p^5 2p^0_{3/2}$	$5d^4 P_{1/2}$	-0.04	0.80
27	103.81 ± 0.1	4.7	$5p^5 2p^0_{3/2}$	$5d^4 D_{3/2}$	-0.04	-0.55
28	104.17 ± 0.1	6.0	$5p^5 2p^0_{3/2}$	$5d^4 D_{3/2}$	0.00	-0.63
29	104.83 ± 0.1	25.3	$5p^5 2p^0_{3/2}$	$5d^4 P_{1/2}$	-0.01	0.68
30	105.22 ± 0.1	10.4	$5p^5 2p^0_{3/2}$	$6s^4 P_{3/2}$	-0.03	-0.67
31	106.72 ± 0.1	2.6	$5p^5 2p^0_{3/2}$	$6s^4 P_{1/2}$	-0.01	0.47
32	107.47 ± 0.1	16.5	$5p^5 2p^0_{3/2}$	$6s^4 P_{3/2}$	-0.02	-0.92
33	110.02 ± 0.1	11.1	$5p^5 2p^0_{3/2}$	$5p^6 2S_{1/2}$	0.02	-1.19
34	115.87 ± 0.1	2.5	$5p^5 2p^0_{3/2}$	$5d^4 P_{1/2}$	-0.02	-0.45
35	124.35 ± 0.3	1.5	$5p^5 2p^0_{1/2}$	$5p^6 2S_{1/2}$	0.13	-1.19

* Calculated in vacuum.

† The calculation of these values assumes isotropic photon emission and neglects possible polarization effects.

‡ The wavelength λ_1 corresponding to the classification is calculated from the levels listed in [18] by the search program [20].§ Enthalpy change for the reaction $\text{He}^+ + \text{Xe} \rightarrow \text{He} + \text{Xe}^{*+}$.

transitions populating specific ion levels which are not expected to be directly populated in reaction (1) agree very well with the corresponding sums for transitions depleting those levels, provided that all classifications are made to ionic transitions. Finally, the number of matches of observed lines with excited neutral transitions decreases dramatically for $\text{He}^+ \text{Rg}$ collisions in the sequence $\text{Ne} \rightarrow \text{Ar} \rightarrow \text{Kr} \rightarrow \text{Xe}$, whereas the number of matches with excited ion transitions increases.

Table 2. Luminescence from the Reaction 100 eV He⁺ + Kr → He + Kr⁺*

Line no.	Observed wavelength [*] λ_0 (nm)	Emission cross section [†] (10 ⁻¹⁸ cm ²)	KrII transition		$\lambda_T - \lambda_0^{\ddagger}$ (nm)	ΔH_S (eV)
			Lower state	Upper state		
1	56.24 ± 0.3	0.15	4p ⁵ 2p ⁰ _{3/2}	(³ P)7s ⁴ P _{1/2}	-0.08	11.49
			4p ⁵ 2p ⁰ _{3/2}	(¹ D)5d ² D _{3/2}	-0.16	11.52
			4p ⁵ 2p ⁰ _{3/2}	(¹ D)5d ² P _{3/2}	0.04	11.44
			4p ⁵ 2p ⁰ _{3/2}	(¹ D)5d ² F _{5/2}	-0.03	11.45
			4p ⁵ 2p ⁰ _{3/2}	(³ P)7s ² P _{3/2}	-0.05	11.48
2	58.04 ± 0.3	0.21	4p ⁵ 2p ⁰ _{3/2}	(¹ D)5d ² P _{1/2}	-0.22	11.55
			4p ⁵ 2p ⁰ _{3/2}	(¹ D)6s ² D _{3/2}	0.11	10.73
			4p ⁵ 2p ⁰ _{3/2}	(¹ D)6s ² D _{5/2}	0.08	10.74
			4p ⁵ 2p ⁰ _{1/2}	(³ P)7s ⁴ P _{1/2}	-0.13	11.49
			4p ⁵ 2p ⁰ _{1/2}	(¹ D)5d ² P _{3/2}	-0.01	11.44
3	58.73 ± 0.3	0.1	4p ⁵ 2p ⁰ _{1/2}	(³ P)7s ² P _{3/2}	-0.10	11.48
			4p ⁵ 2p ⁰ _{1/2}	(¹ D)5d ² P _{1/2}	-0.28	11.54
			4p ⁵ 2p ⁰ _{3/2}	(³ P)5d ² D _{3/2}	0.20	10.45
			4p ⁵ 2p ⁰ _{3/2}	(³ P)5d ² D _{5/2}	-0.10	10.56
			4p ⁵ 2p ⁰ _{1/2}	(¹ D)5d ² D _{3/2}	-0.16	11.25
4	59.77 ± 0.3	0.17	4p ⁵ 2p ⁰ _{3/2}	(³ P)5d ⁴ P _{3/2}	0.09	10.12
			4p ⁵ 2p ⁰ _{3/2}	(³ P)5d ² P _{1/2}	0.13	10.11
			4p ⁵ 2p ⁰ _{3/2}	(³ P)5d ⁴ P _{5/2}	-0.08	10.18
			4p ⁵ 2p ⁰ _{3/2}	(³ P)5d ² F _{5/2}	0.11	10.12
			4p ⁵ 2p ⁰ _{3/2}	(³ P)5d ² P _{3/2}	-0.22	10.23
5	60.74 ± 0.3	0.17	4p ⁵ 2p ⁰ _{1/2}	(¹ D)6s ² D _{3/2}	0.23	10.74
			4p ⁵ 2p ⁰ _{3/2}	(³ P)5d ⁴ F _{5/2}	-0.16	9.88
			4p ⁵ 2p ⁰ _{3/2}	(³ P)5d ⁴ P _{1/2}	0.07	9.80
			4p ⁵ 2p ⁰ _{3/2}	(³ P)5d ⁴ F _{3/2}	-0.19	9.89
			4p ⁵ 2p ⁰ _{1/2}	(³ P)5d ² D _{3/2}	-0.21	10.56
6	62.93 ± 0.3	0.42	4p ⁵ 2p ⁰ _{1/2}	(³ P)5d ⁴ P _{1/2}	-0.06	9.80
7	63.45 ± 0.3	0.25	4p ⁵ 2p ⁰ _{3/2}	(³ P)6s ⁴ P _{3/2}	0.21	8.89
			4p ⁵ 2p ⁰ _{3/2}	(³ P)6s ⁴ P _{5/2}	-0.11	8.99
			4p ⁵ 2p ⁰ _{1/2}	(³ P)6s ² P _{1/2}	-0.02	9.63
			4p ⁵ 2p ⁰ _{1/2}	(³ P)5d ⁴ D _{1/2}	0.17	9.57
			4p ⁵ 2p ⁰ _{1/2}	(¹ D)4d ² S _{1/2}	0.14	9.35
8	64.20 ± 0.3	0.29	4p ⁵ 2p ⁰ _{1/2}	(¹ S)4d ² D _{3/2}	-0.11	9.43
			4p ⁵ 2p ⁰ _{1/2}	(³ P)6s ² P _{3/2}	-0.27	9.47
			4p ⁵ 2p ⁰ _{3/2}	(¹ D)4d ² D _{5/2}	-0.02	7.95
			4p ⁵ 2p ⁰ _{3/2}	(¹ S)5s ² S _{1/2}	0.26	7.49
			4p ⁵ 2p ⁰ _{1/2}	(¹ D)4d ² P _{3/2}	-0.05	8.24
9	66.90 ± 0.3	1.03	4p ⁵ 2p ⁰ _{1/2}	(¹ D)4d ² P _{1/2}	-0.21	8.28
10	68.33 ± 0.3	0.30	4p ⁵ 2p ⁰ _{3/2}	(¹ D)4d ² D _{3/2}	0.03	8.03
			4p ⁵ 2p ⁰ _{3/2}	(³ P)4d ² D _{5/2}	-0.05	6.41
			4p ⁵ 2p ⁰ _{3/2}	(³ P)4d ⁴ P _{5/2}	-0.03	6.10
			4p ⁵ 2p ⁰ _{3/2}	(³ P)4d ² D _{3/2}	-0.06	6.10
			4p ⁵ 2p ⁰ _{3/2}	(³ P)4d ⁴ P _{3/2}	0.03	5.90
11	75.18 ± 0.1	1.40	4p ⁵ 2p ⁰ _{3/2}	(³ P)4d ² F _{5/2}	0.02	5.90
			4p ⁵ 2p ⁰ _{3/2}	(³ P)4d ² P _{3/2}	-0.02	5.70
			4p ⁵ 2p ⁰ _{3/2}	(³ P)4d ² P _{1/2}	-0.04	5.64
			4p ⁵ 2p ⁰ _{3/2}	(³ P)4d ⁴ F _{5/2}	0.00	5.49
			4p ⁵ 2p ⁰ _{1/2}	(³ P)4d ² D _{3/2}	-0.03	6.10
12	72.99 ± 0.1	1.26	4p ⁵ 2p ⁰ _{3/2}	(¹ D)5s ² D _{5/2}	-0.03	5.27
13	74.34 ± 0.1	1.01	4p ⁵ 2p ⁰ _{3/2}	(³ P)4d ⁴ F _{3/2}	-0.04	5.59
			4p ⁵ 2p ⁰ _{3/2}	(³ P)4d ⁴ P _{1/2}	-0.03	5.47
			4p ⁵ 2p ⁰ _{1/2}	(¹ D)5s ² D _{3/2}	-0.06	5.23
			4p ⁵ 2p ⁰ _{1/2}	(³ P)5s ² P _{1/2}	-0.01	4.42
			4p ⁵ 2p ⁰ _{3/2}	(³ P)4d ⁴ D _{3/2}	-0.01	4.42
14	76.14 ± 0.1	0.87	4p ⁵ 2p ⁰ _{3/2}	(³ P)4d ⁴ D _{5/2}	-0.00	4.34
15	76.44 ± 0.1	0.29	4p ⁵ 2p ⁰ _{3/2}	(³ P)5s ² P _{3/2}	-0.08	4.10
16	77.10 ± 0.1	0.48	4p ⁵ 2p ⁰ _{3/2}	(³ P)5s ² P _{1/2}	-0.02	4.42
17	77.40 ± 0.3	1.43	4p ⁵ 2p ⁰ _{1/2}	(³ P)4d ⁴ D _{3/2}	-0.02	4.42
18	78.24 ± 0.1	3.69	4p ⁵ 2p ⁰ _{3/2}	(³ P)5s ⁴ P _{3/2}	-0.05	3.40
19	79.95 ± 0.1	0.19	4p ⁵ 2p ⁰ _{1/2}	(³ P)5s ⁴ P _{1/2}	0.00	3.99
20	80.58 ± 0.1	0.24	4p ⁵ 2p ⁰ _{1/2}	4s4p ⁶ ² S _{1/2}	0.00	2.93
21	81.87 ± 0.1	2.13	4p ⁵ 2p ⁰ _{1/2}	4s4p ⁶ ² S _{1/2}	-0.01	2.93
22	82.65 ± 0.1	0.39	4p ⁵ 2p ⁰ _{1/2}			
23	83.04 ± 0.1	0.59	4p ⁵ 2p ⁰ _{3/2}			
24	84.48 ± 0.1	1.24	4p ⁵ 2p ⁰ _{3/2}			
25	86.46 ± 0.1	0.77	4p ⁵ 2p ⁰ _{1/2}			
26	86.91 ± 0.1	1.99	4p ⁵ 2p ⁰ _{3/2}			
27	88.68 ± 0.1	2.77	4p ⁵ 2p ⁰ _{1/2}			
28	89.10 ± 0.1	0.72	4p ⁵ 2p ⁰ _{1/2}			
29	91.74 ± 0.1	1.10	4p ⁵ 2p ⁰ _{3/2}			
30	96.54 ± 0.1	1.55	4p ⁵ 2p ⁰ _{1/2}			
31						

* Calculated in vacuum.

† The calculation of these values assumes isotropic photon emission and neglects possible polarization effects.

‡ The wavelength λ_T corresponding to the classification is calculated from the levels listed in [19] by the search program [20].§ Enthalpy change for the reaction He⁺ + Kr → He + Kr⁺.

RESULTS

Tables 1 and 2 summarize the emission cross sections and classifications for radiation within the interval 50–130 nm from the $\text{He}^+ + \text{Xe}$ and $\text{He}^+ + \text{Kr}$ reactions, respectively. An analysis of emissions observed in the spectral range 130–890 nm has also been completed [21]. In total, 116 lines in He^+/Xe and 84 lines in He^+/Kr systems have been classified and emission cross sections determined. The complete spectra are not presented here due to the volume of these data; they are available upon request [21]. The lines reported here represent about 70% of the total emissions cross section observed from each of the reactions.

CONCLUSIONS

Within the limitations listed above, the data in Tables 1 and 2 provide the basis for determining the relative probability for transition from individual levels to either the $^2P_{1/2}^0$ or $^2P_{3/2}^0$ states of the ion. It should be emphasized that the spectra are obtained under experimental conditions which minimize the perturbing effects of (a) gas collisions, (b) resonance absorption of the emitted radiation [22], and (c) electric and magnetic fields in the reaction region. Consequently, the ratio of the emission cross sections for transitions from each level to the $^2P_{3/2}^0$ and $^2P_{1/2}^0$ electronic ground states should more closely represent the relative transition probabilities than does the corresponding intensity ratio obtained from discharge spectra [23].

It is notable that in some cases the cross section ratio for a given pair of states in KrII is small when the cross section ratio between the analogous states in XeII is large and vice versa. For example, in the KrII spectrum the only observed transition from $5s^4P_{1/2}$ is $^2P_{1/2}^0 \leftarrow 5s^4P_{1/2}$. In the XeII spectrum the corresponding transition $^2P_{1/2}^0 \leftarrow 6s^4P_{1/2}$ is below the detection limit but the transition $^2P_{3/2}^0 \leftarrow 6s^4P_{1/2}$ is the most intense line in the spectrum. For another example, the emission cross section ratios of the first doublets $ns^2np^5\ ^2P_{3/2}^0 \leftarrow nsnp^6\ ^2S_{1/2}/ns^2np^5\ ^2P_{1/2}^0 \leftarrow nsnp^6\ ^2S_{1/2}$ is 1.10/1.55 in KrII but 11.1/1.5 in XeII. It is not presently clear why the ratios of analogous transition pairs differ so markedly from KrII to XeII. However, the effect is also observed in BrI and I spectra [24] taken by the same methods as employed here for KrII and XeII. That is, the cross sections are comparable to a large degree for the spectra of the isoelectronic sequences KrII, BrI and XeII, I. For the reasons given above, we expect that these results for cross section ratios are correct. Obviously, the problem can be viewed in terms of the transition matrix elements. For the present we conclude that (1) in XeII, transitions to the $^2P_J^0$, $J = 3/2$ state are heavily favored over the statistical ratio of 2/1 for $J = 3/2$ and (2) in KrII transitions to the $^2P_J^0$, $J = 1/2$ state are slightly favored relative to the same statistical ratio. The physical reason for this behavior is currently under study in our laboratories.

All of the lines reported in Table 2 for KrII were classifiable [20, 21] as transitions in the level table of MOORE [18] in spite of the critical revisions of the KrII analysis by MINNHAGEN, STRIHD, and PETERSON [19]. It is expected that the same situation will obtain when a revised XeII analysis is employed to reclassify our XeII results. This result is a significant fact for the analysis since the observation of a line by the present technique can serve as a confirmation of the existence of the levels connected with it for $J < 5/2$ [25].

In addition to problems associated with the basic physics of transition processes, the data in Tables 1 and 2 have important connotations to the study of non-resonant

[22] Using He^+ ion beam currents $< 10^{-10}$ A there is less than 10% attenuation in passing through the collision chamber. As a result, the production density is a negligibly small fraction of the neutral atom density.

[23] J. C. BOYCE, *Phys. Rev.* **49**, 730 (1936).

[24] (a) K. F. SIEGELMAYER, Ph.D. thesis, Air Force Institute of Technology (1976).

(b) A comparison of isoelectronic sequences BrI, KrII, I, XeII, is in preparation.

[25] The authors are grateful to the reviewer for this point.

charge-transfer processes. For example, the cross sections for lines in the full XeII spectrum [21] have been utilized to make significant cascading corrections ($\sim 30\%$) to the emission spectrum. By employing such corrections experimental determination of the energy distribution in the reaction products of $100\text{ eV He}^+ + \text{Xe}$ collisions has been made [10, 26].

Acknowledgement We thank JOHN G. DRYDEN for his preparation of the ink drawing for Fig. 1, and Mrs. PATTY SHIVELY for her capable typing of the manuscript.

[26] E. G. JONES, D. C. FEE, T. O. TIERNAN and B. M. HUGHES, Distribution of internal energy in the products of $\text{He}^+ + \text{Xe}$ reactions; to be submitted to *J. Chem. Phys.*

Revised

Distribution Category:
Coal Conversion and
Utilization - MHD
UC-90g

ANL-77-21

ARGONNE NATIONAL LABORATORY
9700 South Cass Avenue
Argonne, Illinois 60439

CONFERENCE ON HIGH TEMPERATURE SCIENCES
RELATED TO OPEN-CYCLE, COAL-FIRED MHD SYSTEMS

at

Argonne National Laboratory
Argonne, Illinois 60439
April 4-6, 1977

Sponsored by Argonne National Laboratory and
the Argonne Universities Association

THERMODYNAMIC PROPERTIES OF GAS PHASE MOLECULAR IONS

R.L.C. Wu, C. Lifshitz[†] and T. O. Tiernan
Department of Chemistry, Wright State University
Dayton, Ohio 45431

INTRODUCTION

Thermochemical properties of gas phase molecular negative ions have been determined from translational energy thresholds for endoergic reactions in which these ions are involved. Excitation functions for these reactions were obtained using a tandem mass spectrometer. Three types of reactions have been studied — charge transfer, particle transfer and collision-induced dissociation. Previously reported experiments conducted in our laboratory [1-8] have shown that reliable values of molecular electron affinities, bond dissociation energies and ionic heats of formation may be obtained from such measurements. New data relating to CO_3^- and O_3^- will be presented in the present paper, and results obtained for several other ions of interest will be reviewed.

EXPERIMENTAL

An in-line tandem mass spectrometer previously described [1-8] was utilized in this study. The projectile ion is formed in the electron-impact ion source of the first stage mass spectrometer which produces a mass and energy analyzed beam which is impacted upon the target gas in the collision chamber. The energy spread of the projectile ion beam entering the collision cell is about ± 0.3 eV (LAB) over the ion energy range, 0.3 to about 180 eV (LAB). Pulse counting techniques are used to measure the product ion current.

Projectile ions are produced by dissociative electron attachment using appropriate source molecules or by ion molecule reactions occurring in the primary ion source. For example, Br^- is produced by the direct electron impact process, $e + \text{CH}_3\text{Br} \rightarrow \text{CH}_3 + \text{Br}^-$, while O_3^- is produced in a mixture of N_2O and O_3 by the sequence of reactions, $e + \text{N}_2\text{O} \rightarrow \text{O}^- + \text{N}_2$, and $\text{O}^- + \text{O}_3 \rightarrow \text{O} + \text{O}_3^-$. Ozone was produced in these studies by a Tesla coil discharge through O_2 , the excess O_2 being removed at -196°C [9]. Grease free, mercury free vacuum lines were employed and the fresh O_3 was directly introduced either into the ion source or into the collision chamber, as required.

Data Treatment and Corrections for Ion Energy Distribution and Doppler Motion

The product ion intensity $I_s(E_{10})$ is converted to an observed apparent cross section [7]

$$\sigma_{\text{app}}^{\text{obs}}(E_{10}) = C[I_s(E_{10})/P_t]/I_p(E_{10}) \quad (1)$$

[†]On sabbatical leave from The Hebrew University of Jerusalem, 1976-77.

where $I_p(E_{10})$ is the primary ion intensity, E_{10} is the nominal reactant ion energy in the laboratory frame, P_t is the target gas pressure, and C is a conversion factor based on the intensity for the reaction O^-/NO_2 , for which the cross section is known.

Corrections for the ion energy distribution and Doppler motion of the neutral were applied as previously described [2,8]. A computer fitted excitation function based on these corrections, calculated using an assumed threshold function was compared in each case with the experimental data. The threshold behavior of the total cross section σ for collision-induced dissociation reactions is known from theoretical considerations [10]. The threshold functions for charge transfer and particle transfer have not been predicted theoretically. A model assuming a linear-plus-step function gave the best fit to most of the charge transfer data described here.

RESULTS AND DISCUSSION

Charge Transfer

Excitation functions were obtained for the charge transfer reactions of the projectile ions O^- , OH^- , S^- , SH^- , F^- , Cl^- , Br^- , I^- , NH^- , C_2H^- , NO_2^- and CO_3^- with O_3 . The experimental data points, as well as the computer fitted curve for the excitation function of the Br^-/O_3 reaction are shown in Fig. 1.

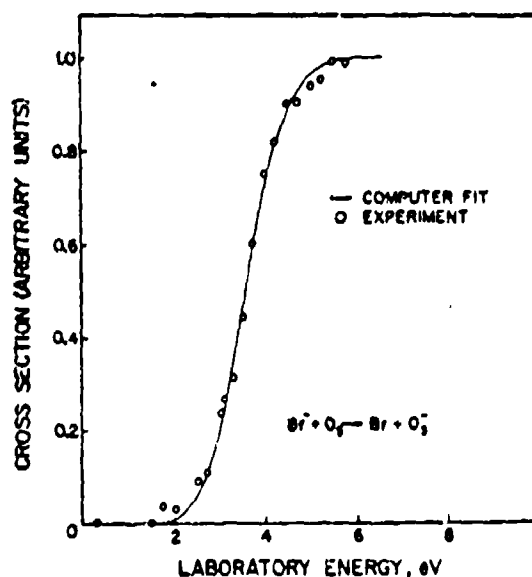


Figure 1. Cross Section for the Reaction $Br^- + O_3 \rightarrow O_3^- + Br$ as a Function of Translational Energy. Points are experimental data. Solid line is the calculated "best-fit" excitation function.

The translational energy threshold of the linear-plus-step function threshold law employed for the computer fit (2.8 eV in the laboratory system), corresponds to an electron affinity of $EA(O_3) = 2.3$ eV. Other projectile ions gave similar results leading to an average value for the electron affinity of ozone of 2.28 ± 0.1 eV.

Particle Transfer

Considerable caution must be exercised when employing translational energy thresholds for particle transfer reactions in order to calculate their endoergicities. Many exoergic and thermoneutral reactions involving negative ions were observed to demonstrate translational energy thresholds due to the presence of energy barriers in their respective potential surfaces. Notable examples are the reactions, $O^-(H_2, H)OH^-$, $NH_2^-(H_2, NH_3)H^-$ and $D^-(H_2, HD)H^-$. The great advantage of beam experiments such as those reported here is the ability to determine excitation functions for both the forward and reverse steps of a particular particle transfer reaction. The non-existence of a translational energy threshold in the exoergic direction ensures that the translational energy threshold in the endoergic direction is equal to the endoergicity. This principle has been applied in studying the ozone system for which the following particle transfer reactions were investigated: $CO_3^-(O_2, CO_2)O_3^-$, $O_2^-(O_2, O)O_3^-$, $NO_2^-(O_2, NO)O_3^-$, $NO_3^-(O_2, NO_2)O_3^-$. The experimental data points and the corresponding computer fitted curve for the CO_3^-/O_2 reaction are shown in Fig. 2. The translational energy threshold yields a bond dissociation energy of $D(O_2 - O^-) = 1.6 \pm 0.1$.

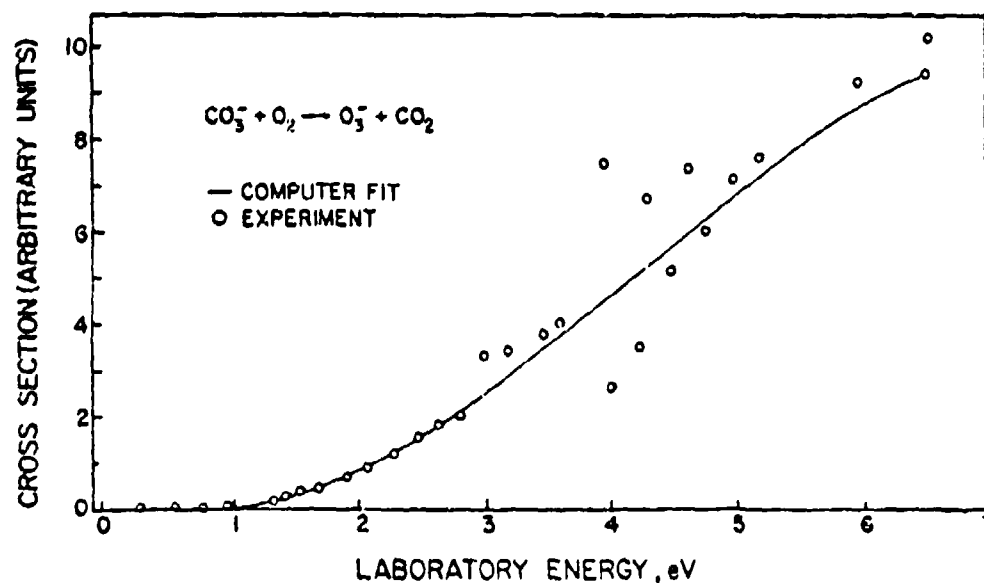


Figure 2. Cross Section for the Reaction $CO_3^- + O_2 \rightarrow O_3^- + CO_2$ as a Function of Translational Energy. Points are experimental data, solid line is the calculated "best-fit" excitation function.

Table I

BOND DISSOCIATION ENERGIES, HEATS OF FORMATION AND MOLECULAR ELECTRON AFFINITIES DERIVED FROM
TRANSLATIONAL ENERGY THRESHOLDS FOR ENDOERGIC NEGATIVE ION REACTIONS

Ion (XO_m^-)	$O^- - XO_{m-1}$ Bond Dissociation Energy (eV)	Heat of Formation		Electron Affinity of	
		XO_m^- (eV)	XO_m^- (eV)	XO_m	XO_m
NO^-	5.0 ± 0.1 (CID)*	0.91 ± 0.1 (CID)		0.02 ± 0.1 (CID); 0.015 ± 0.1 (CT)	
O_2^-	4.1 ± 0.1 (CID)	-0.44 ± 0.1 (CID)		0.44 ± 0.1 (CID); 0.45 ± 0.1 (CT)	
NO_2^-	4.0 ± 0.1 (CID)	-2.0 ± 0.1 (CID)		2.4 ± 0.1 (CID); 2.28 ± 0.1 (CT)	
N_2O^-	0.43 ± 0.1 (CID)	0.62 ± 0.1 (CID)		0.22 ± 0.1 (CID)	
CO_3^-	2.0 ± 0.1 (CID)	-4.98 ± 0.1 (CID)		3.1 ± 0.2 (CID)	
O_3^-	1.8 ± 0.1 (PT)	-0.80 ± 0.1 (CT) -0.74 ± 0.1 (PT)		2.22 ± 0.1 (PT); 2.28 ± 0.1 (CT)	
$OH^-(H_2O)$	1.0 ± 0.1 (CID) $D(OH^- - H_2O)$				

* CID - collision-induced dissociation; CT - charge transfer; PT - particle transfer

Collision-Induced Dissociation

Collisional dissociation thresholds have been measured to obtain the bond dissociation energies and heats of formation of molecular negative ions of O_2^- , NO^- , NO_2^- , N_2O^- , CO_3^- , O_3^- and NO_3^- . Rare gas atoms, diatomic and triatomic molecules served as collision reaction partners in these experiments. The corrected threshold data for CO_3^- yield a dissociation energy, $D(CO_2 - O^-) = 2.0 \pm 0.1$.

Data obtained for various negative ion species using the techniques described are summarized in Table I. These results will be compared with similar data obtained in other ion-beam, flowing afterglow, flow-drift, photodestruction and collisional ionization studies [11-16].

ACKNOWLEDGEMENTS

This work was supported by the Air Force Office of Scientific Research under Contract No. F44620-76-C-0007 with Wright State University. The authors are grateful for the invaluable assistance of C. D. Miller with the tandem mass spectrometer, and for the assistance of Dr. T. Terwilliger in programming the computer fit calculations.

REFERENCES

1. C. Lifshitz, B. M. Hughes and T. O. Tiernan, Chem. Phys. Lett. 7, 469 (1970).
2. T. O. Tiernan, B. M. Hughes and C. Lifshitz, J. Chem. Phys. 55, 5692 (1971).
3. B. M. Hughes, C. Lifshitz and T. O. Tiernan, J. Chem. Phys. 59, 3162 (1973).
4. C. Lifshitz, T. O. Tiernan and B. M. Hughes, J. Chem. Phys. 59, 3182 (1973).
5. T. O. Tiernan and R. P. Clow, Adv. Mass Spectrom. 6, 295 (1974).
6. T. O. Tiernan, in 'Interactions Between Ions and Molecules,' edited by P. Ausloos (Plenum, New York, 1974), pp. 601-604.
7. D. G. Hopper, A. C. Wahl, R. L. C. Wu and T. O. Tiernan, J. Chem. Phys. 65, 5474 (1976).
8. T. O. Tiernan and R. L. C. Wu, Adv. Mass Spectrom. 7, in press.
9. S. Braslavsky and J. Heicklen, Int. J. Chem. Kin. 8, 801 (1976).
10. C. Rebeck and R. D. Levine, J. Chem. Phys. 58, 3942 (1973).
11. J. Berkowitz, W. A. Chupka and D. Gutman, J. Chem. Phys. 55, 2733 (1971).
12. J. A. Rutherford, B. R. Turner and D. A. Vroom, J. Chem. Phys. 58, 5267 (1973).
13. D. Vogt, J. Mischke and W. Dreves, Physics Lett. 59A, 113 (1976).
14. I. Dotan and F. C. Fehsenfeld, to be published.
15. J. P. Moseley, P. C. Cosby, R. A. Bennett and J. R. Peterson, J. Chem. Phys. 65, 2512 (1976).
16. E. W. Rothe, S. Y. Tang and G. P. Reck, J. Chem. Phys. 62, 3829 (1975).

Distribution of internal energy in the products of the reactions of 100 eV He⁺ with Xe

E. Grant Jones and Thomas O. Tiernan

Department of Chemistry and The Brehm Laboratory, Wright State University, Dayton, Ohio 45433

Darrell C. Fee

Department of Chemical Engineering, Argonne National Laboratory, Argonne, Illinois 60439

B. Mason Hughes

Flammability Research Center, University of Utah, Salt Lake City, Utah 84112

(Received 4 January 1979; accepted 11 October 1979)

The luminescence spectrum in the range from 50 to 890 nm which results from collision of a 100 eV beam of ground state He⁺ ions with Xe has been investigated. All observed emissions can be classified as Xe II transitions. Corrections of the spectra for cascading (amounting to about 10% of the total emission cross section) have been made in order to derive cross sections for direct production of Xe⁺ in the bimolecular collision. Comparisons of the cross section for radiative state production with the total cross section for charge transfer indicate that excited Xe⁺ states are formed with high efficiency. The internal energy distribution of Xe⁺ products maximizes at an energy corresponding to the conversion of <1 eV of translational energy into internal energy. For the near-resonant charge transfer reactions studied, a propensity to conserve the projection along the internuclear axis of the total electronic angular momentum is observed. The significance of the distribution of Xe⁺ states and the effects of kinetic energy are discussed.

I. INTRODUCTION

The charge transfer reaction between He⁺ and Xe



has been a subject of interest for many years. Cross sections for total charge transfer at collision energies above 100 eV (Refs. 1 and 2) and below 100 eV (Ref. 3) have been reported, based on measurements of Xe⁺ production ion currents. Studies at thermal⁴ and near-thermal⁵ energies indicate that this reaction has an extremely small cross section. Reports⁶ of extensive optical excitation in Xe⁺ for low relative collision energies (<500 eV) led to further studies of luminescence at energies above 300 eV (Refs. 7 and 8) and more recently below 100 eV.⁹⁻¹²

Comparisons between the cross sections for total charge transfer and for production of luminescence from this reaction indicate that a large fraction of the charge transfer reactions produce optical excitation.⁹⁻¹² The efficiency and specificity of the excitation in reactions of this type may have important implications with respect to the use of charge transfer reactions in laser pumping. However, the optical spectrum in the region 50–890 nm produced at 100 eV impact energy¹³ is a very complex pattern of Xe II emissions, most of which arise from transfer of kinetic into internal electronic energy. The number of states directly populated by the He⁺/Xe charge transfer reaction is much greater than the number of states populated by the corresponding He⁺/Kr, He⁺/Ar, He⁺/Ne, or He⁺/He reactions.¹⁴ Consequently, the probability of forming a given state can more readily be correlated with kinetic to internal energy transfer, and with preferred quantum-mechanical selection rules in a statistically significant manner, for the He⁺/Xe reaction. These correlations permit insights into charge transfer reactions and may facilitate

optimization of charge transfer reactions for laser pumping applications.

The emission spectrum observed from collisions of 100 eV He⁺ ions with Xe,¹³ and a tabulation of the classifications in Xe II and the absolute emission cross sections¹⁴ have been previously reported. In the present paper, we present and discuss the distribution of radiating states of Xe⁺ produced directly by reaction (1) for 100 eV collision energies, on the basis of the previously measured emission cross sections.¹⁴ Corrections of the spectral data for cascading which must be made in order to derive the cross sections for direct production of Xe⁺ in reaction (1), are discussed.

II. EXPERIMENTAL

A. Apparatus

The optical emission apparatus used to obtain the emission spectrum analyzed in the present study has been described elsewhere^{10,12,17} and is shown schematically in Fig. 1. Briefly, the apparatus functions as follows. Projectile He⁺ ions formed by electron impact are mass and energy analyzed and impacted on target Xe atoms located in a collision chamber. Typical experimental conditions for these experiments are summarized in Table I and are appropriate for monitoring predominantly bimolecular ion-neutral events.

Optical emissions produced in the collision chamber are monitored over the spectral interval 50–890 nm in the direction of the ion beam, using a McPherson 1-m vacuum monochromator with interchangeable gratings and detectors.

B. Calibration

The optical system was calibrated for the spectral range, 450–890 nm, using an NBS calibrated strip

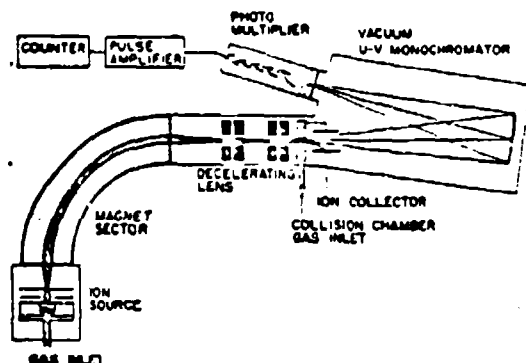


FIG. 1. Schematic representation of the optical emission apparatus.

lamp. In the range 250–450 nm, a relative instrument function was calculated based on the relative grating reflectance and photomultiplier quantum efficiency. This function was then normalized at 450 nm to the absolute value obtained using the calibrated lamp.

In the vacuum ultraviolet (vuv) region, no simple absolute calibration methods are available. Therefore, attempts were made to derive an appropriate calibration function utilizing quantum efficiency data obtained from the detector suppliers,^{14,15} and reflectance were data estimated in the following manner. Namioka and Hunter¹⁶ have reported an absolute reflectance of 4% at 121.6 nm for a gold-coated grating blazed at 90 nm. Sampson¹⁷ has further shown platinum to have a reflectance of about 1.4–1.5 times that of gold. On this basis, and consistent with reports of Zaidel and Shreider,²² we have estimated a reflectance of 6% at 121.6 nm for the grating²³ used in the present experiments. The relative spectral reflectances were interpolated from the data of Namioka and Hunter at 121.6, 58.4, and 30.4 nm. As a check of this overall procedure, the experimental cross section for production of Lyman α radiation from 100 eV He⁺/H₂ collisions²⁴ was determined. The value derived, 0.60×10^{-16} cm² compares favorably with the previously reported value²⁵ of 0.51×10^{-16} cm².

It is estimated that absolute cross sections used in this study are accurate within a factor of 3 and relative cross sections within $\pm 30\%$.

III. APPLICATION OF CASCADING CORRECTIONS TO SPECTRAL DATA

A. Discussion of spectral data and assumptions made in applying cascading corrections

As already mentioned, we have presented in previous reports the emission spectrum¹² and a tabulation of the absolute emission cross sections¹⁴ for radiative products from collisions of 100 eV He⁺ ions with Xe. The spectrum is consistent with transitions in Xe II arising from the radiation of Xe⁺ products formed in the reaction. None of the observed emission lines could be positively classified as transitions in Xe I. As noted in our earlier communication,¹² this is in disagreement with the previous studies of De Heer *et al.*,⁸ who reported Xe I

resonance lines produced from the He⁺/Xe reaction at higher collision energies. More recently we have re-examined emissions from this process in the spectral range from 120–150 nm. We find that at $\lambda = 147$ nm the Xe I resonance line is present, but only under higher collision chamber pressures. In fact, the intensity of this line was observed to vary as the square of the Xe atom concentration over the range from 0.1–7.0 mtorr. It appears that this excitation results from a two-step process involving the formation of fast helium metastables,²⁶ or Xe⁺ metastable ions, which subsequently collide with Xe. These observations confirm the higher-order pressure effects reported by De Heer *et al.*⁸ No effects of resonance absorption were detected over the pressure interval studied.

On the basis of Xe II line classifications¹⁴ and the measured emission cross sections, we have corrected the He⁺/Xe spectral data for cascading, making the following assumptions.

- (1) All optical emissions occur isotropically without polarization.
- (2) Luminescence at wavelengths > 890 nm is not significant under the experimental conditions employed here.
- (3) All excited species formed in the collision have radiated within 10^{-8} s. Ions with lifetimes longer than 10^{-8} s can diffuse out of the viewing region without being detected. Typical measured lifetimes²⁷ of radiating Xe⁺ states are 10^{-8} s.

TABLE I. Experimental conditions and parameters for optical emission experiments.

Reactant ion formation	70 eV (electron impact)
He ⁺ ion energy (lab. eV)	1–170
He ⁺ ion kinetic energy spread (FWHM, eV)	1
Primary He ⁺ current (nA)	1–4
Collision chamber pressure (mTorr)	1–5
Collision gas temperature (K)	300
Ion path length in collision chamber (cm)	0.475
Magnetic fields in collision chamber (G)	< 1
Electric fields in collision chamber (V cm ⁻¹)	< 0.1
Direction of photon detection	In-line with ion beam
Monochromator entrance slit width (mm)	1.0 (low resolution) 0.1 (high resolution)
Photon detection	single-photon counting (SSR 1110) vuv: Bendix Channeltron EMR 541-F, LIF window VIB: RCA C31034A (195 K)
Cross-section detection limit	0.3×10^{-18} cm ²

TABLE II. Total cross sections for emission, cascading, and direct formation for each Xe⁺ level produced from reactions of 100 eV He⁺ with Xe.

Xe II state designation	ΔH^a (eV)	Cross section ^b (10 ⁻¹⁸ cm ²)		
		Total emission (σ_e) _i	Cascading (σ_c) _i	Direct forma- (σ_d) _i
5p ¹ P _{3/2}	-12.46	nonradiative	191.	0
5p ¹ P _{1/2}	-11.15	nonradiative	50	0
5p ¹ S _{1/2}	-1.19	12.6	0	12.6
6s ¹ P _{1/2}	-0.92	16.5	15.1	1.4
6s ¹ P _{3/2}	-0.87	10.4	12.0	-1.6
6s ¹ P _{1/2}	-0.09	28.5	1.2 (0.4)	27.3
5d ¹ D _{3/2}	-0.62	0	2.6	?
5d ¹ D _{1/2}	-0.63	12.7 (12.7) ^d	1.7	11.0
5d ¹ D _{5/2}	-0.55	6.0	1.3 (0.6)	4.7
5d ¹ D _{1/2}	-0.44	3.4 (0.9)	1.8 (0.2)	1.6
5d ¹ F _{5/2}	-0.13	0	5.8	?
5d ¹ F _{7/2}	-0.20	0	1.4	?
5d ¹ F _{3/2}	0.13	0	5.8	?
6s ¹ P _{3/2}	0.29	10.4	3.7 (0.4)	6.7
6s ¹ P _{1/2}	0.47	6.2	0.6	5.6
5d ¹ P _{3/2}	0.60	9.4	0.4 (0.2)	9.0
5d ¹ P _{1/2}	0.68	18.1 (12.7) ^d	0	18.1
5d ¹ P _{3/2}	0.74	9.5	4.6 (3.2)	4.9
5d ¹ P _{1/2}	0.86	6.1 (0.9)	0	6.1
5d ¹ P _{3/2}	0.80	12.5	0.6 (0.6)	11.9
5d ¹ D _{3/2}	0.92	12.5 (7.8) ^e	1.1 (1.1)	11.4
5d ¹ D _{1/2}	1.13	9.5	3.8 (0.3)	5.7
6s ¹ D _{3/2}	0.93	7.8 (7.8) ^e	1.1 (0.3)	6.7
6s ¹ D _{1/2}	1.54	7.5	3.9 (2.6)	3.6
5d ¹ D _{3/2}	1.35	7.2	4.3	2.9
6s ¹ D _{1/2}	1.62	5.5	0.9 (0.6)	4.6
6p ¹ P _{1/2}	1.42	7.4 (0.6)	3.8 (0.3)	3.6
6p ¹ P _{3/2}	1.40	5.5 (0.7)	2.2 (0.5)	3.3
6p ¹ P _{1/2}	1.64	1.8	0.1 (0.1)	1.7
6p ¹ D _{1/2}	1.64	13.3	2.9	10.4
6p ¹ D _{3/2}	1.62	10.3	1.9 (0.1)	8.4
6p ¹ D _{5/2}	2.02	5.7 (0.9)	0.5	5.2
6p ¹ D _{1/2}	2.47	0.4 (0.4)	1.8 (1.8)	-1.4
5d ¹ F _{3/2}	1.77	6.7	3.2 (0.8)	3.5
5d ¹ F _{1/2}	1.79	0	8.4	?
5d ¹ D _{1/2}	2.31	4.9	0.3 (0.3)	4.6
5d ¹ D _{3/2}	2.95	3.0 (3.0)	0.3 (0.3)	2.7
6p ¹ S _{1/2}	2.57	0.5 (0.5)	0.3 (0.1)	0.2
6p ¹ S _{3/2}	2.62	4.0 (4.0)	0.4	3.6
6p ¹ D _{3/2}	2.61	6.7	0.3	6.4
6p ¹ D _{5/2}	2.95	2.4 (1.2)	0.1 (0.1)	2.3

TABLE II (Continued)

Xe II state designation	ΔH^a (eV)	Cross section ^b (10 ⁻¹⁸ cm ²)		
		Total emission (σ_e) _i	Cascading (σ_c) _i	Direct forma- (σ_d) _i
6p ¹ P _{3/2}	2.82	0	0.3	?
6p ¹ P _{1/2}	2.99	0	0.4 (0.4)	?
6s ¹ S _{1/2}	2.92	3.0 (3.0)	0.4	2.6
5d ¹ P _{1/2}	3.29	2.0	0	2.0
5d ¹ P _{3/2}	3.35	1.4	0	1.4
6p ¹ P _{3/2}	3.52	7.5 (2.9)	0	7.5
6p ¹ P _{1/2}	3.67	3.2 (0.7)	1.0	4.2
5d ¹ S _{1/2}	3.57	5.9 (0.5)	0	5.9
6p ¹ P _{3/2}	3.62	1.5 (0.4)	0	1.5
6p ¹ P _{1/2}	4.00	0	0	0
6p ¹ D _{3/2}	3.90	1.4 (0.1)	0	1.4
6p ¹ D _{5/2}	3.93	1.9 (0.8)	0	1.9
7s ¹ P _{1/2}	3.97	4.0 (0.5)	0	4.0
7s ¹ P _{3/2}	4.06	0	0	0
7s ¹ P _{1/2}	4.29	0	0	0
2 _{1/2}	4.02	0	0	0
4 _{1/2}	4.09	0	0	0
4 _{3/2}	4.09	0	0	0
6 _{1/2}	4.16	0	0	0
6d ¹ D _{1/2}	4.34	3.1	0	3.1
6d ¹ D _{3/2}	4.35	0.7 (0.1)	0	0.7
6d ¹ D _{5/2}	4.37	1.5 (0.6)	0	1.5
18 _{3/2}	4.47	0	0	0
18 _{1/2}	4.47	0	0	0
8 _{1/2}	4.47	1.2 (0.7)	0	1.2
6d ¹ F _{1/2}	4.48	2.0 (0.2)	0	2.0
6d ¹ F _{3/2}	4.79	0	0	0
6d ¹ F _{5/2}	4.66	0	0	0
10 _{1/2}	4.49	0	0	0
1 _{1/2}	4.56	0	0	0
4p ¹ G _{3/2}	4.57	2.5	0	2.5
4p ¹ F _{3/2}	4.58	1.3 (0.3)	0	1.3
4p ¹ F _{5/2}	4.59	1.2	0	1.2
12 _{3/2}	4.66	0	0	0
20 _{1/2}	4.74	0	0	0
3 _{1/2}	4.78	0	0	0
5 _{1/2}	4.79	0	0	0
7 _{1/2}	4.80	0	0	0
9 _{1/2}	4.84	0	0	0
11 _{1/2}	4.86	0	0	0
13 _{1/2}	4.90	0	0	0
15 _{1/2}	4.90	2.0 (0.6)	0	2.0
17 _{1/2}	4.92	0	0	0

TABLE II (Continued)

Xe II state designation	ΔH^0 (eV)	Cross section ^b (10 ⁻¹⁸ cm ²)		
		Total emission (σ_e) _i	Cascading (σ_c) _i	Direct forma- (σ_d) _i
6p ³ P _{1/2}	4.93	0	0	0
1s _{1/2}	4.94	0	0	0
6d ¹ P _{1/2}	5.01	1.2 (1.2)	0	1.2
6d ¹ P _{3/2}	5.41	1.5 (1.5)	0	1.5
6d ¹ P _{3/2}	5.32	0	0	0
21s _{1/2}	5.02	0	0	0
7s ¹ P _{1/2}	5.20	0.5 (0.3)	0	0.5
7s ¹ P _{3/2}	5.28	0.7 (0.4)	0	0.7
23s _{1/2}	5.33	0	0	0
6d ¹ D _{1/2}	5.44	0	0	0
6d ¹ D _{3/2}	5.64	0	0	0
6d ¹ P _{1/2}	5.55	0.1 (0.1)	0	0.1
7s ¹ D _{1/2}	5.68	0.1 (0.1)	0	0.1
7s ¹ D _{3/2}	6.11	0	0	0
14s _{1/2}	5.78	0	0	0
25s _{1/2}	5.83	0	0	0
37s _{1/2}	5.84	0	0	0
29s _{1/2}	5.84	0.2 (0.2)	0	0.2
6d ¹ D _{3/2}	5.90	0	0	0
6d ¹ D _{5/2}	6.10	0	0	0
31s _{1/2}	5.94	0	0	0
33s _{1/2}	6.01	0	0	0
35s _{1/2}	6.05	0	0	0
37s _{1/2}	6.10	0	0	0
6d ¹ F _{1/2}	6.64	1.0	0	1.0
39s _{1/2}	6.32	0.7	0	0.7
41s _{1/2}	7.03	0	0	0
Limit [Xe III]		0	0	0

^aEnthalpy change for the reaction He⁺ + Xe → He + Xe⁺.

^bThe symbol 0 under σ_e column indicates that no emission lines from the level were observed in the spectrum. The symbol 0 under σ_c column indicates that no cascade lines into the level were observed in the emission spectrum. Value shown in parenthesis indicates the extent to which the cross section has been estimated. (See Ref. 14.)

^cThe present study provides no direct measurement of this value. Estimates have been made; see text.

^dThere is an uncertainty of ±1.7 in these values because of the unresolved transitions: 6p³P_{1/2} → 3d¹D_{1/2}, 6p³P_{1/2} → 3d¹P_{1/2}, 6p³P_{1/2} → 3d¹P_{3/2}. Tabulated values assume equal contribution from each transition.

^eThere is an uncertainty of ±7.8 in these values because of the unresolved transitions: 6p³P_{1/2} → 3d¹D_{3/2}, 6p³P_{1/2} → 6s¹D_{3/2}. Tabulated values assume equal contribution from each transition.

(4) The radiation observed is adequately resolved and correctly classified.

(5) The cross section for direct formation of level *i*,

(σ_d)_i, the cross section for emission from level *i*, (σ_e)_i, and the cross section for cascading into level *i*, (σ_c)_i, are related by the expression,

$$(\sigma_e)_i = \sum_j \sigma_{j \rightarrow i} - \sum_j \sigma_{i \rightarrow j} = (\sigma_e)_i - (\sigma_c)_i, \quad (2)$$

where $\sigma_{j \rightarrow i}$ is the emission cross section from level *i* to any lower level *j*, and $\sigma_{i \rightarrow j}$ is the cross section for cascading into level *i* from any higher level *k*.

Table II summarizes the values obtained for σ_e , σ_c , and σ_d for the different Xe⁺ levels. The Xe⁺ levels in Table II are denoted by the L-S designation of Moore,²⁰ even though the coupling for Xe II is not pure L-S. Only two selection rules, $\Delta J = 0$ and even — odd, have been used to deduce the line classifications, because these rules are applicable for dipole radiation with J-J and L-S coupling.²¹

The extent to which the cross sections in Table II are uncertain is given in parentheses. This is based on estimates from the emission spectrum.¹⁴ The enthalpy change for reaction (1) which corresponds to formation of the specific product states listed is also in Table II. As can be seen, only the first few states are thermally accessible for collisions occurring at thermal energy.

B. Cases where cross sections for cascading contributions exceed the total emission cross section

Since large errors can arise in taking the difference between numbers of similar magnitude, negative cross sections in Table II are considered to be zero within experimental uncertainties. Two of the most important states¹¹ 6s¹P_{1/2,3/2}, radiating in the vuv are populated mostly via cascading from higher energy states, so the cross sections for direct excitation are nearly zero. This finding agrees with results obtained by De Heer *et al.*,⁸ under different conditions, and it confirms the relative accuracies of our optical calibrations.

Emissions from long-lived states are not efficiently detected under the experimental conditions. For example, five of the states listed in Table II (5d¹D_{1/2}, 5d¹F_{1/2}, 5d¹F_{3/2}, 5d¹F_{5/2}, and 5d¹F_{7/2}) are nonradiative under the present conditions. Radiation from four of these states is electric-dipole forbidden, and radiation from 5d¹F_{3/2} to the ground state is not found in this study.²⁰ Each of these states can be populated by cascading from higher levels, and significant population inversions can occur. These studies provide information about their population by cascade; however, since no information concerning their direct excitation is available the term "?" is used under column σ_e in Table II for these cases.

C. Magnitude and uncertainty of cascading corrections

Corrections to the total observed emission cross sections for σ_c amount to approximately 30%. On the average, states of Xe⁺ with total angular momentum quantum number *J* of $\frac{1}{2}$ and $\frac{3}{2}$ are populated significantly by cascading (>30%), whereas cascading corrections to Xe⁺ (*J* = $\frac{5}{2}$) states are almost negligible (<7%). As a result,

cross sections determined for direct formation of Xe⁺ ($J = \frac{1}{2}$) states closely approximate those measured for total emission from the original spectrum.

The cross section for directly forming Xe⁺ ($J = \frac{1}{2}$) states which have large emission cross sections and very small cascading corrections can be determined with a relative accuracy close to that cited for the emission cross section ($\pm 30\%$). There will be larger uncertainty in most of the other derived direct formation cross sections, however, since each cascading cross section listed in Table II represents the sum of as many as five individual emission cross sections. It is thus difficult to assess the magnitude of the errors for much of the data presented in the last column of Table II.

There are also errors in the reported cross sections for emission and cascading (indicated by the estimated numbers in parentheses) which are due to insufficient optical resolution in the experiments. The latter prevents unambiguous classification of some of the lines in the original spectrum. The two most serious cases are outlined in the footnotes of Table II. In each case the two classifications for the observed lines were assumed to be equally valid, and both transitions were assessed as having equal weight.

IV. RESULTS AND DISCUSSION

A. Comparison of the total reaction cross section with cross section for forming radiative Xe⁺ states

The total cross section for the direct production of radiative Xe⁺ states in reaction (1), for 100 eV He⁺ ions, is 2.7×10^{-16} cm². This represents a lower limit to the total charge transfer cross section because the extent of production of nonradiative excited states in the reaction is unknown. The total charge transfer cross section reported by Maier¹ at the same energy is 10.5×10^{-16} cm², whereas Koopman² has obtained a value of 15×10^{-16} cm². The total cross section for formation of radiative Xe⁺ states is therefore about one-fourth the total charge transfer cross section indicated by Maier's data. For the analogous He⁺-Kr reaction under the same experimental conditions, we have measured a total cross section for radiative Kr⁺ production¹¹ which is also approximately one-quarter to one-third of Maier's value for the total charge transfer reaction.¹ This could be interpreted as indicating that there is a consistent calibration factor difference between our data and those of Maier and that all He⁺ reactions result in excited Xe⁺ state formation. There is evidence that the ground state Xe⁺($5p^2\ ^3P_{2,3}$) and first excited state Xe⁺($5p^2\ ^1P_{1,2}$) are not formed in the reaction at near-threshold energies.¹² For interactions at 100 eV, however, it is not known how much, if any, Xe⁺($5p^2\ ^3P_{2,3}$) is formed in reaction (1). In any case, it can be stated with certainty that a large fraction of the He⁺-Xe reactions produce excited Xe⁺ levels.

Subsequent to direct excitation, most excited states produced in reaction (1) eventually radiate, reaching after a few sequences the Xe⁺($5p^2\ ^3P_{2,3}$) states. The total cascading terms listed in Table II for the ground

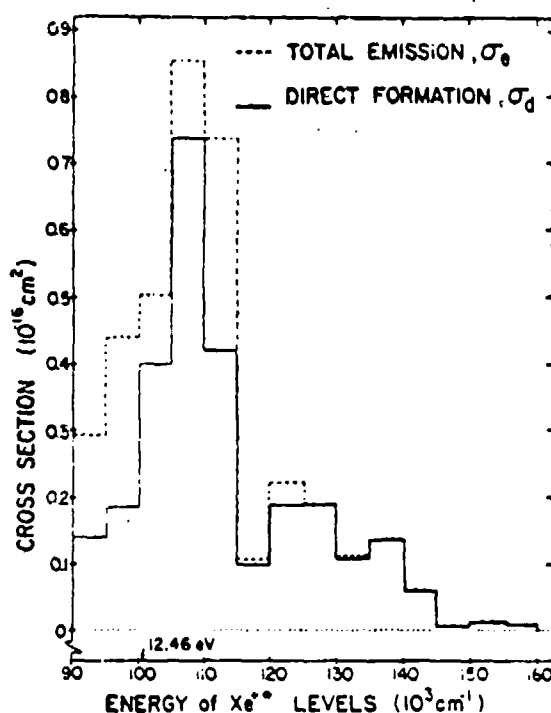
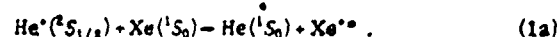


FIG. 2. Dashed line: histogram of the total cross section for emission, σ_e , from Xe⁺ levels lying within 5000-cm⁻¹ intervals, as a function of the energy of the radiating states formed in reaction of 100 eV He⁺ ions with Xe. Solid line: histogram of σ_d , the total cross section for direct production, in 100 eV He⁺/Xe collisions, of Xe⁺ levels lying within 5000-cm⁻¹ intervals, as a function of the energy of the radiating states.

and first excited states indicate that Xe⁺($^3P_{2,3}$) and Xe⁺($^1P_{1,2}$) are populated (after most of the emissions are completed) approximately in the ratio of 4/1.

B. Distribution of the radiative Xe⁺ levels formed

Spectroscopic analysis of the excited products formed in collisions of 100 eV He⁺ ions with Xe shows that the excitation is exclusively in Xe⁺ and that reaction (1), the charge transfer process, is the dominant reaction. As a result of this spectroscopic information, the charge transfer process can be represented more specifically by the reaction



There is the possibility, under 70 V electron impact conditions, of producing He⁺ metastable ions. We do not observe significant spectral changes using 50 V electron impact; hence, we assume that their contribution to the reactant He⁺ ion beam is negligible. In addition, none of the observed luminescence arising from bi-molecular reaction could be positively classified as He I or He II lines. Formation of the metastable 3S_1 state of He, being endothermic by more than 19 eV, is not considered significant.

It is useful to represent the distribution of Xe⁺ levels produced in reaction (1a) by a series of histograms. Such a histogram is presented in Fig. 2, where

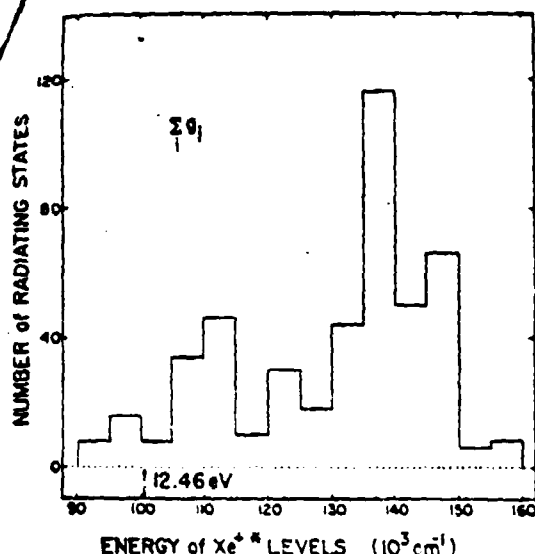


FIG. 3. Histogram of the number of Xe⁺* radiating states (Σg_i) lying within each 5000-cm⁻¹ energy interval as a function of the energy of the radiating states.

$\sigma_e = \Sigma_i(\sigma_{ei})$, the total cross section for emission from states i of Xe⁺* (within a series of arbitrarily selected 5000-cm⁻¹ intervals), is plotted as a function of the energy of the radiating states. The summation is over all radiating states which lie within each 5000-cm⁻¹ interval. Similarly, the total cross section $\sigma_d = \Sigma_i(\sigma_{di})$ for direct population of radiating states of Xe⁺* lying within these energy intervals is also plotted in Fig. 2. The difference between the two histograms, within each energy interval, represents the correction to the total emission cross section arising from cascading contributions. It can be seen that the magnitude of these corrections is a greater fraction of the total emission cross section for the lower-energy states, that is, those radiating in the vuv spectral region. The total cross section for production of states of Xe⁺* lying within the energy region 100 000–115 000 cm⁻¹ in reaction (1a) is obviously large. Hence, the total emission cross section, σ_e , is greatest for states within this interval.

The amount of energy available in reaction (1a) for thermal energy reactants is 12.46 eV (Ref. 32) or 100 500 cm⁻¹ (1 eV = 8068.3 cm⁻¹). This quantity, shown by an arrow in Fig. 2, represents the maximum amount of energy that may be deposited in Xe⁺ in the absence of translational to internal energy conversion. Clearly, formation of the majority of the product Xe⁺* ions observed in the present study requires the conversion of some translational energy into internal energy. The quantity of energy transferred in reaction (1a) at 100 eV impact as shown in Fig. 2 can exceed 50 000 cm⁻¹, i.e., ~6 eV, although the most probable quantity of energy transferred is in the range of 0–1 eV. There is a suggestion in the data shown in Fig. 2 of a second maximum in the vicinity of 120 000–130 000 cm⁻¹, corresponding to the transfer of ~3 eV of energy.

In Fig. 3, the total number of radiating Xe⁺* states,

$\Sigma_i g_i$, where g_i is the degeneracy of the i th level, is plotted as a function of the energy of the radiating states for each of the same intervals selected in Fig. 2. In Fig. 4, the average cross section per radiating state, $\bar{\sigma}_d$, for direct formation of Xe⁺* states is plotted in a similar manner. The latter term is defined by the relation $\bar{\sigma}_d = \Sigma_i(\sigma_{di}) / \Sigma_i g_i$, where g_i is the degeneracy of i th state and the summation over i covers all radiating states within the energy interval (5000 cm⁻¹).¹³ The representation in Fig. 4 takes into account the large variations in the density of states which occur within the energy intervals of the histogram.

By plotting the data as shown in Fig. 4, Xe⁺* states having excitation energies in the range 100 000–105 000 cm⁻¹ are shown to be preferentially formed in reaction (1a). The second maximum in Fig. 2 (which was mentioned above) does not appear in Fig. 4, indicating that it is a consequence of the greater density of Xe⁺* states in that region. The maximum in the distribution occurs in the region of near-resonance (see arrow in Fig. 4). This result is generally consistent with the adiabatic principle¹⁴ which predicts a maximum reaction cross section at low collision energies only for states in the vicinity of resonance (that is, states lying near 100 500 cm⁻¹). As noted earlier, exothermic channels for reaction (1a) can only produce states of Xe⁺* with energy below 100 000 cm⁻¹, and it is quite clear from Fig. 4 that such exothermic channels, although available, are considerably less important than endothermic channels at the reaction energies employed here (100 eV He⁺ impact).

C. Distribution of Xe⁺* quantum states formed

The following observations can be made concerning the distribution of quantum states of Xe⁺* produced in reaction (1a).

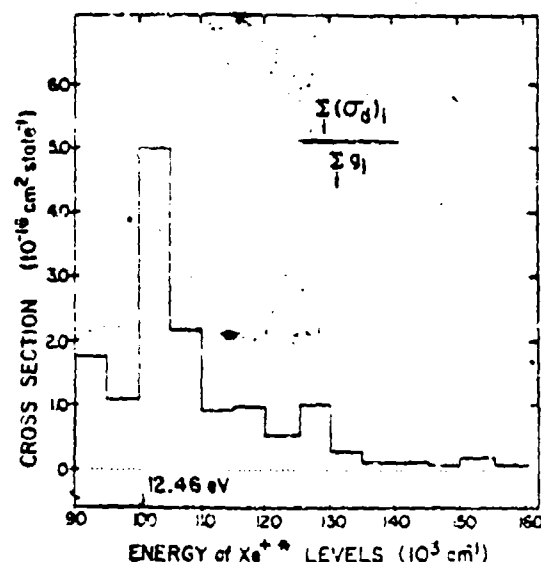


FIG. 4. Histogram of $\bar{\sigma}_d$, the cross section averaged per radiating state for direct production of states of Xe⁺* lying within 5000-cm⁻¹ intervals in reaction of 100 eV He⁺ ions with Xe.

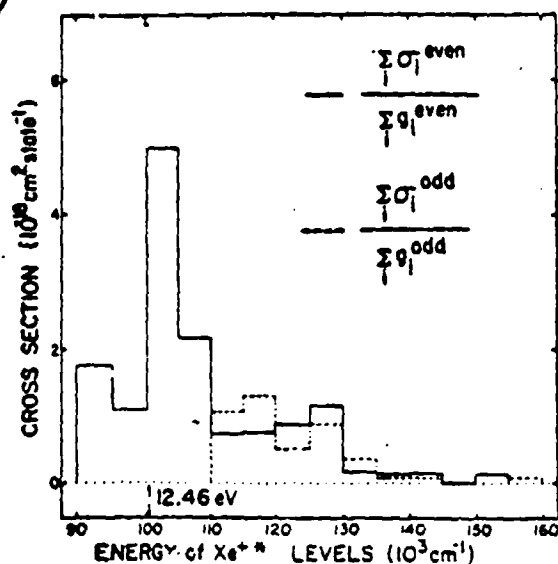


FIG. 5. Histograms of the cross section in reaction of 100 eV He⁺ ions with Xe for producing even- or odd-parity states of Xe⁺ as a function of the energy of the radiating states. The cross section is averaged per radiating state of either even or odd parity within 5 000-cm⁻¹ intervals.

1. Total spin (S) and total electronic angular momentum (L)

For the heavy Xe⁺ ion, neither *S* nor *L* are valid quantum numbers.

2. Parity

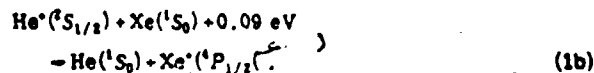
For all levels of Xe⁺, the parity is well defined. A comparison of the distributions of states with even and odd parity is shown in Fig. 5. The comparison is invalid in the interval 90 000–110 000 cm⁻¹ (because there are no odd-parity Xe⁺ levels within this region), but in the intervals where both even-parity and odd-parity states exist, there does not appear to be a preferred reaction channel based on the parity of the Xe⁺ product ions.

3. Total angular momentum (J)

In the vicinity of near-resonance, states of Xe⁺ with total angular momentum quantum number $J = \frac{1}{2}$ are preferentially populated. The cross section, averaged per state, for directly forming, via reaction (1a), levels of Xe⁺ with total angular momentum quantum numbers of $\frac{1}{2}$, $\frac{3}{2}$, and $\frac{5}{2}$, respectively are plotted in the histogram format in Fig. 6. The ordinate for the upper histogram is $\sum_i (\sigma_{i,1/2})_d / \sum_i (g_{i,1/2})_d$, where $(\sigma_{i,1/2})_d$ is the cross section for directly forming the *i*th level having $J = \frac{1}{2}$ in reaction (1a). $(g_{i,1/2})_d$ is the degeneracy of the *i*th level having $J = \frac{1}{2}$, i.e., 2, and the summation is carried out over all radiating states within the interval. States of Xe⁺ with $J = \frac{1}{2}$ which lie in the vicinity of near-resonance for the reaction are formed with relatively higher probabilities than those in other energy regions. States with $J = \frac{1}{2}$ are also formed preferentially in the same energy regions, but there does not appear to be any

such behavior for states with $J = \frac{3}{2}$, $\frac{5}{2}$, and $\frac{7}{2}$, respectively (the latter two are not shown in Fig. 6, but see Table II).

Production of Xe⁺ ($J = \frac{1}{2}$) states near resonance, in which very little (<1 eV) translational to internal energy conversion takes place, is exemplified by the formation of Xe⁺(6s ¹P_{1/2}).



From Table II, it can be seen that reaction (1b) has the largest cross section of any reaction producing luminescence in this system. This reaction channel is only slightly endothermic and is within 0.09 eV of being resonant. It is clear from the data in Table II that under the relatively low pressure collision conditions employed in the present study (which ensure that predominantly bimolecular ion-neutral events occur), charge transfer reactions are highly specific in populating certain levels of Xe⁺. This is in sharp contrast to the behavior observed in afterglows, as indicated by the spectra obtained for He/Xe mixtures at much higher pressures. For example, Shuker *et al.*,¹¹ reported enhanced Xe $\underline{\text{I}}$ emission in afterglow experiments due to

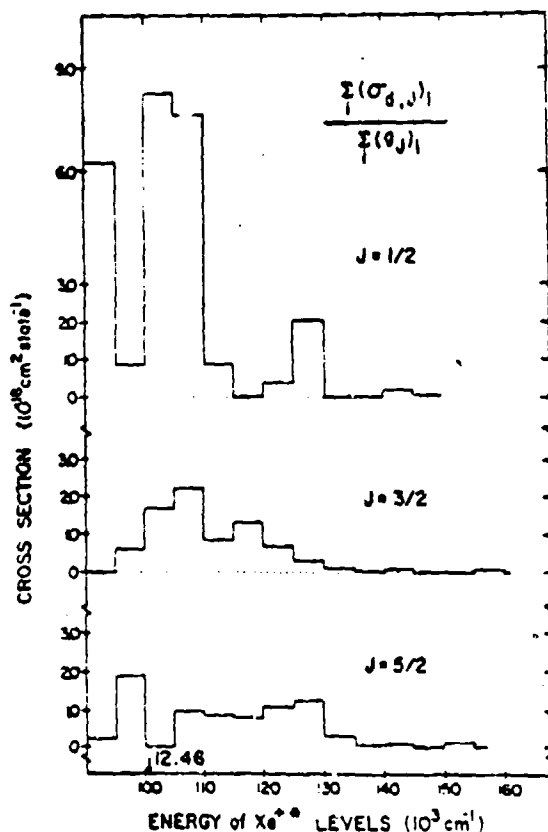


FIG. 6. Histograms of the cross section in reaction of 100 eV He⁺ ions with Xe for producing Xe⁺ ($J = \frac{1}{2}$, $\frac{3}{2}$, $\frac{5}{2}$) as a function of the energy of the radiating states. The cross section is averaged per radiating state with $J = \frac{1}{2}$, $\frac{3}{2}$, or $\frac{5}{2}$ within 5 000-cm⁻¹ intervals.

the presence of He, but the broad, nonspecific enhancement of all Xe²⁺ levels which they observed, led them to conclude that the enhancement did not arise from charge transfer processes.

It should be noted, at this point, that all of the conclusions discussed above are drawn from the cross section data presented in Table II. The inability to spectroscopically resolve some of the transitions, as already mentioned, results in some uncertainty for the cross sections deduced for direct formation of specific states, but the validity of the general conclusions is unaffected.

To summarize then, the conclusions from Figs. 2-6 are as follows. The reaction of He⁺ with Xe at 100 eV tends to populate specific levels of Xe²⁺ near the energy resonance for the charge transfer reaction. The most probable reaction channels involve the transfer of some small (<1 eV) amount of translational energy (*T*) into internal energy (*I*). In the vicinity of near-resonance, states of Xe²⁺ with total angular momentum quantum number $J = \frac{1}{2}$ are preferentially populated.

D. Total production of Xe²⁺ in selected *J* levels

The total cross sections for directly forming Xe²⁺ states with $J = \frac{1}{2}, \frac{3}{2}, \frac{5}{2},$ and $\frac{7}{2}$ are 1.0, 0.7, 0.7, and 0.2 $\times 10^{-18}$ cm², respectively. The larger total cross section for forming $J = \frac{1}{2}$ levels is consistent with the peak near resonance as shown in Fig. 6.

In Fig. 7 the total cross sections divided by the total

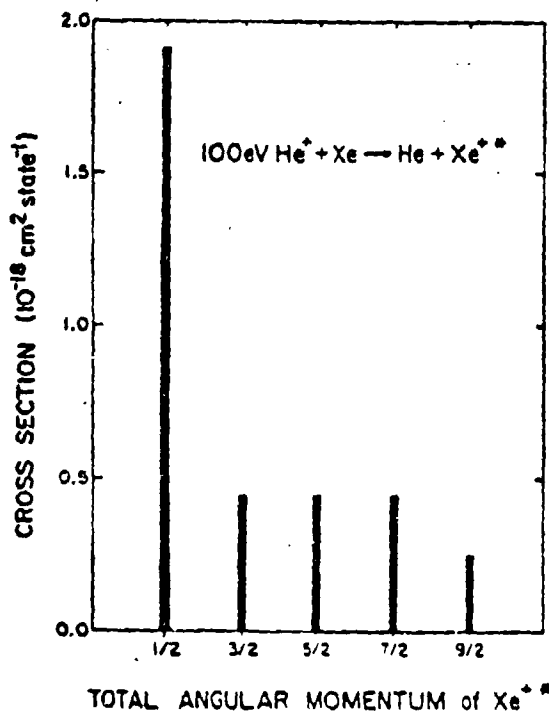


FIG. 7. Total cross section for production of Xe²⁺ ($J = \frac{1}{2}, \frac{3}{2}, \frac{5}{2}, \frac{7}{2}$) in collisions of 100 eV He⁺ ions with Xe. The cross section is averaged per total number of states of each *J*.

number of states of each *J*, are plotted as a function of the total electronic angular momentum, *J*, of Xe²⁺ formed in reaction (1). Figure 7 again indicates that the most probable reaction under 100 eV collisions involves the formation of Xe²⁺ ($J = \frac{1}{2}$). At large internuclear separations, the total electronic angular momentum of the approaching system is given by $(J_{e,100})_i = J_{e,100}(\text{Xe}) + J_{e,100}(\text{He}^+)$. For reaction (1a), this reduces to $(J_{e,100})_i = J_{e,100}(\text{He}^+) = \frac{1}{2}$. Similarly for the separated products, the total electronic angular momentum is given by $(J_{e,100})_f = J_{e,100}(\text{Xe}^+) + J_{e,100}(\text{He})$. For reaction (1a), this reduces to $(J_{e,100})_f = J_{e,100}(\text{Xe}^+)$. For the most probable reactions, particularly near resonance, $J_{e,100}(\text{Xe}^+) = \frac{1}{2}$, or $\Delta J_{e,100} = 0$. That is, there is no change in the total electronic angular momentum quantum number during the collision. According to the selection rules developed by Kronig¹⁴ for radiationless processes such as charge transfer reactions, $\Delta J_{e,100} = 0$ where $J_{e,100}$ is the total angular momentum quantum number of the system. It follows that the production of Xe²⁺ ($J = \frac{1}{2}$) states does not require transfer of angular momentum of the collision into electronic angular momentum of one of the separated products. For collisions of 100 eV He⁺ ions with Xe in a reaction cell, the angular momentum $J_{e,100}$, associated with the collision is not well defined, because processes with a wide range of impact parameters are sampled. However, for the reactants, $J_{e,100}$ is very large compared to $(J_{e,100})_i$. The preponderance of Xe²⁺ ($J = \frac{1}{2}$) product states for near-resonant processes indicates that there is no significant transfer of collisional angular momentum into electronic angular momentum of the product Xe²⁺ ion. This result is consistent with the occurrence of "long-range" processes involving relatively weak interactions and small amounts of translational (*T*) to internal (*I*) energy (*T* → *I*) conversion. It would appear that, although the initial collisional angular momentum can be very large, it is difficult to transfer the latter into internal angular momentum of the atoms within the short time period and at the long interaction range which are characteristic of the collision.

The possibility of transfer of the collisional angular momentum is greatest for low-impact-parameter or short-range processes in which the particles can penetrate to the region where the potential is highly repulsive. In this region, the ion-neutral interactions are strong and the relative velocity of approach becomes small. Under such "short-range" conditions there is a higher probability for transfer of translational into internal energy. The magnitude of energy transfer *T* → *I* for the He⁺/Xe system can be seen in Fig. 8(a), in which reaction probability (per available radiating Xe²⁺ states) is plotted as a function of the extent of kinetic energy transfer. Clearly, the most probable reactions involve a minimum amount of energy transfer. In Fig. 8(b), relative reaction probability is plotted as a function of the extent of angular momentum transfer. It should be noted, however, that the latter histogram is only an approximate representation of angular momentum transfer, since it is assumed that for all collisions, the angular momentum transferred in the collision has a projection along the internuclear axis in the same direction as the projection of *J*(Xe⁺).

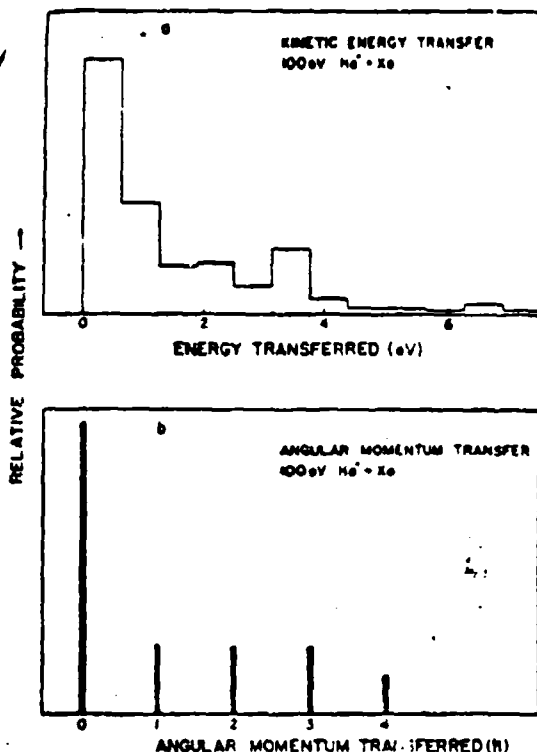


FIG. 8. (a) Reaction probability (per available radiating Xe⁺ state), in collisions of 100 eV He⁺ ions with Xe, as a function of kinetic to internal energy conversion. (b) Data of Fig. 7 represented as reaction probability (per available radiating Xe⁺ state) in collisions of 100 eV He⁺ ions with Xe as a function of collisional to internal angular momentum transfer. This plot is a true representation only if the projection along the internuclear axis of the collisional angular momentum transferred and $J(\text{Xe}^+)$ vectors have the same direction.

There is further experimental evidence from ion-atom reactions which indicates the conservation of J_{tot} . Blom and co-workers found that for the He⁺/Hg system at thermal energies there is essentially equal probability of producing Hg⁺ in the $7p^2P_{3/2}$ and $7p^2P_{1/2}$

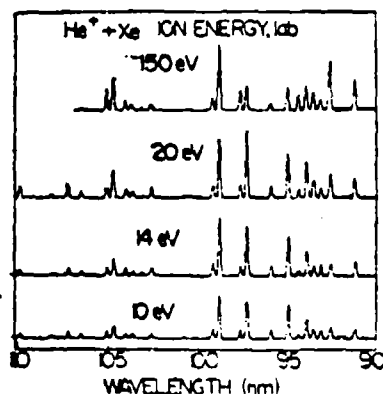


FIG. 9. Luminescence in the vuv spectral region arising from collisions of 10, 14, 20, and 150 eV He⁺ ions with Xe.

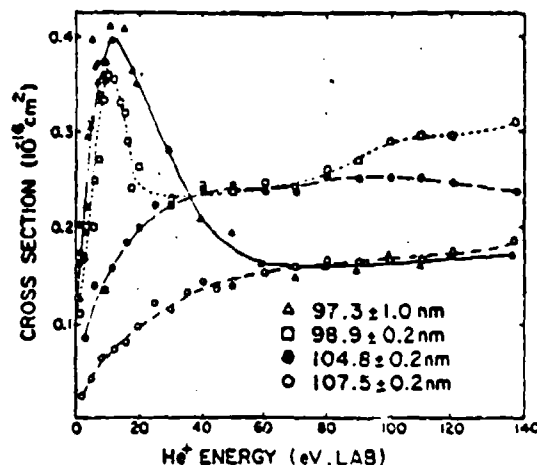


FIG. 10. Kinetic energy dependence of selected Xe II emission lines produced in collisions of He⁺ ions with Xe. 97.3 nm ($5p^2P_{3/2}^o - 6s^2P_{3/2}$), 98.9 nm ($5p^2P_{1/2}^o - 6s^2P_{1/2}$), 104.8 nm ($5p^2P_{3/2}^o - 5d^4D_{3/2}$), 107.5 nm ($5p^2P_{1/2}^o - 6s^2P_{1/2}$).

states, despite the fact that the reaction to produce the latter is almost 0.5 eV less exothermic for ground-state reactants.²⁷ In addition, no other Hg⁺ states with $J > \frac{1}{2}$ were observed in this reaction, at thermal energies, although several exist in the energy region between the $7p^2P_{3/2}$ and $7p^2P_{1/2}$ states of Hg⁺. Apparently this observation is also an indication of the low probability of transferring collisional into electronic angular momentum, similar to that suggested by the results of the present study.

E. Effects of changing collision energy

The product distributions discussed previously pertain to 100 eV He⁺/Xe collisions. Although we have not carried out a complete analysis of the emissions at lower kinetic energies, we have monitored the energy dependence of most of the major lines. Common behavior for all of the observed lines is a low-energy (2 eV) kinetic energy threshold consistent with that indicated by studies of the behavior of the total charge transfer cross section.^{2,4} The results of the kinetic energy dependence experiments are summarized in Figs. 9-11. In Fig. 9,

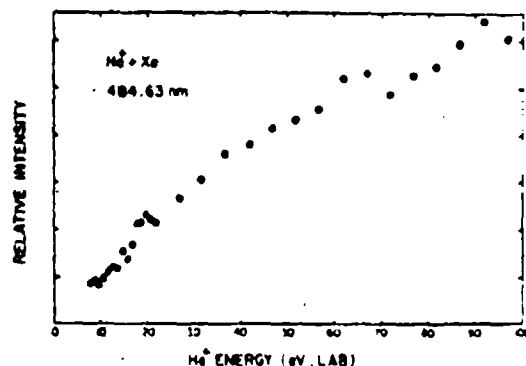


FIG. 11. Kinetic energy dependence of 484.63 nm Xe II line ($6s^2P_{1/2}^o - 6p^4D_{3/2}^o$), produced in collisions of He⁺ ions with Xe.

several vuv-spectral scans at different collision energies are shown. Obviously, the same levels of Xe⁺ are populated at laboratory kinetic energies from 10–150 eV, but the relative distributions of Xe⁺ products change significantly with energy. There is evidence that the total charge transfer cross section⁷ as well as the cross section for light emission^{4,13} maximize at collision energies below 20 eV. We have previously reported¹⁴ that radiation from Xe⁺(6s²P_{1/2}) at 97.3 nm has a pronounced maximum at about 12 eV. This is shown in Fig. 10, along with the energy dependence of several other major lines. The low-energy maxima of the 97.3- and 98.9 nm lines account, in part, for the maximum observed at 10 eV by Lipeles *et al.*,⁶ in the total cross section for light production in the vuv region. The 104.8-nm line due to unresolved radiation from Xe⁺(5d⁴D_{1/2}), level 8 in Table II, and Xe⁺(5d²P_{1/2}), level 17 in Table II, is also shown in Fig. 10. The kinetic energy behavior of this line is characteristic of that observed for many of the spectral lines, that is, it exhibits a low-energy onset, followed by a continuous, slow rise in the cross section up to 150 eV. Other spectral lines were found to exhibit sharp maxima in their cross sections. The total charge transfer cross-section dependence on kinetic energy, as observed by Majer,⁷ represents the summation of the behavior of all of the excited states populated in reaction (1), as well as that of the ground states. Certainly the luminescence results reported in the present study are consistent with the previously measured total cross-section data in that there is a low kinetic energy onset for all emissions and several states are observed with sharply peaking excitation functions that may contribute to the overall energy maximum observed in the total reaction cross section.

The kinetic energy dependences of some of the observed spectral lines are indicative of the probability of directly forming the corresponding radiating states from reaction (1) at particular energies. For example, for each of the lines (97.3, 98.9, and 104.8 nm, Fig. 10) discussed above, cascading effects are quite small for 100 eV collisions.¹⁴ In contrast, the behavior of the 107.5 nm line, which is also shown in Fig. 10, and which is produced by radiation from the Xe⁺(6s²P_{1/2}) state, does not provide any information concerning the direct population of this level in reaction (1). Within the accuracy of the cross section measurements given in Table II, the difference between σ_e and σ_r for Xe⁺(6s²P_{1/2}) is approximately zero, indicating that this level is populated only via cascading from the higher-energy levels. Therefore, the kinetic energy variation of the 107.5-nm line represents the excitation function for the formation of higher Xe⁺ states, namely, 6p²D[°] and 6p²P[°], which have 2–3 eV more energy than Xe⁺(6s²P_{1/2}). The energy variation of the 484.63-nm line (6s²P_{1/2}–6p²D_{3/2}[°]) is shown in Fig. 11. This is the major cascade process which contributes to Xe⁺(6s²P_{1/2}), which explains the similarity of its energy behavior to that of the 107.5 nm line.

In summary, the transfer of translational to internal energy is necessary for the direct formation of Xe⁺ states from the He⁺/Xe reaction. However, in some

instances, kinetic energy alone is not sufficient to promote reaction. The existence of thresholds and pronounced maxima in the excitation functions of several of the Xe⁺ states formed in reaction (1) suggests the occurrence of potential curve-crossing mechanisms, as have been proposed in analogous systems.^{15,16} These will now be discussed further.

F. Reaction mechanism

Several previously reported studies have provided insight into the mechanism of the He⁺/Xe interaction. Elastic scattering of He⁺ in collisions with Xe has been studied by Baudon *et al.*,¹⁷ and by Weise and Mittman.¹⁸ Weise and Mittman conclude that polarization forces are the dominant interaction forces between He⁺ and Xe. By treating their scattering data, using a 12–4 potential, the latter authors have calculated a well depth of 0.28 eV. This minimum is assumed to occur at long range (~3.2 Å which is the sum of the estimated radii for He⁺ and Xe).¹⁸ In other experiments, Tanaka *et al.*¹⁹ have observed weak He/Xe⁺ molecular emissions, excited by electric discharge of binary He/Xe mixtures, at pressures in excess of 1 Torr. These have been ascribed to HeXe⁺ excited states having relatively small dissociation energies. There is no evidence for a strongly bound, stable HeXe⁺ species analogous to those reported for other rare-gas heteronuclear diatomic ions.¹⁴

The present study has also yielded information bearing on the He⁺/Xe reaction mechanism. We have observed a propensity for conserving the total electronic angular momentum of the He⁺/Xe system, particularly for near-resonant processes. We have also observed that a significant fraction of the He⁺/Xe collisions resulting in reaction involve the conversion of small amounts of translational to internal energy, and it is reasonable to identify these collisions as long-range interactions. In addition, He⁺/Xe charge transfer reactions, involving extensive (>2 eV) kinetic energy transfer, were observed in the present experiments, and these also involve the transfer of collisional angular momentum into orbital angular momentum of Xe⁺.¹⁴ Such collisions must involve stronger close-range interactions which occur on the highly repulsive region of the potential curves.

Information from the present study coupled with available literature data permits the construction of a qualitative potential diagram, as shown in Fig. 12, which is useful in the visualization of the He⁺+Xe reaction. The reactant channel, He⁺(¹S_{1/2})+Xe(¹S₀), and the four primary product channels, He(¹S₀)+Xe(⁵D[°]²S_{1/2}), He(¹S₀)+Xe(⁶s²P_{1/2}), He(¹S₀)+Xe(⁵d²P_{1/2}), and He(¹S₀)+Xe(³d⁴P_{1/2}), are depicted in this figure. All of these product channels have cross sections in the range (0.1–0.3)×10⁻¹⁶ cm². All four of these product channels involve Xe⁺ ($J=\frac{1}{2}$) states, so that these reactions are in the category $\Delta J_{\text{elec}}=0$. Using the qualitative diagram depicted in Fig. 12, the following reaction sequence is suggested. Reactants at thermal energy approach along the He⁺(¹S_{1/2})+Xe(¹S₀) curve, pass through the minimum and in the absence of radiation or stabilizing collisions, exit via the same path. These elastically scattered

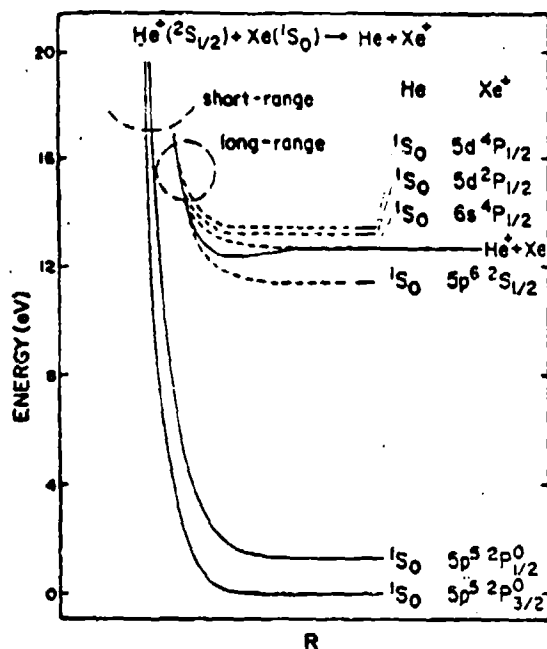


FIG. 12. Schematic representation of a mechanism for producing the four major Xe* states in collisions of 100 eV He⁺ ions with Xe. Relative energy of the HeXe⁺ system is shown with respect to He(1S₀) + Xe(5d⁴P_{1/2}) taken as 0.00 eV. The system approaches along the He(1S₀) + Xe(1S₀) potential curve (solid line) and exits along the dashed potential curves.

• He(²S_{1/2}) ions, which experience no kinetic energy loss ($Q=0$), have been observed by Baudon *et al.*,⁴¹ in studies at somewhat higher energies. Such elastic collisions dominate until the relative kinetic energy of approach nears 0.6 eV (Maier's kinetic energy onset for Xe⁺ ions).¹ At this point the system is at a total energy close to the asymptotic limits for He(1S₀) + Xe(5d⁴P_{1/2}) and He(1S₀) + Xe(5d²P_{1/2}), and a series of near or avoided crossings may occur allowing the system to exit along the product curves. These relatively long-range interactions, involving reactant and product channels within 0.8 eV of resonance, would account for the maxima in the distribution of product Xe* levels having $J = \frac{1}{2}$. Access to the ground and first excited states Xe(²P_{1/2,1/2}) is not available at low relative reaction energies. Presumably, not until relatively high translational energies of approach are achieved can these Xe* states be formed via radiationless transitions.⁴² At this point, however, the density of higher-energy Xe* levels which are accessible as a result of translational to internal energy conversion may reduce the probability of ground-state Xe* formation.

Similar arguments can be made to explain the low-energy maxima of the 97.3 and 98.9 nm lines shown in Fig. 10. The probability of near or avoided crossings occurring at long-range is a maximum at low ion velocities in the region of the crossing. Consequently, the cross sections for products resulting from such crossings should show a sharp increase above the energy threshold, followed by peaking at low energies,

and finally, a decrease as the velocity of the projectile increases. The onset of additional exit channels associated with short-range interactions competes effectively at higher energies, causing a sharp decrease in the excitation functions displayed by the 97.3 and 98.9 nm lines.

Charge transfer reactions involving formation of states of Xe* with $J > \frac{1}{2}$ would occur at much higher energies on the steeply repulsive regions of the potential curves. Presumably, the mechanisms of these reactions also involve curve crossings, but in the strong interaction region, there is considerably more energy and angular momentum transfer. Clearly, there is considerable need for theoretical calculations relevant to the He⁺/Xe system, analogous to those completed for some smaller systems such as He⁺/Ne (Ref. 39) and Na⁺/Li.⁴⁰

V. CONCLUSIONS

In the present study, state-to-state cross sections for charge transfer in the He⁺/Xe system have been presented. Comparison of the total cross section for radiative state formation with the total reaction cross section indicates that a large fraction of the charge transfer reactions produce excited Xe*. The distribution of energy in Xe* indicates that the most probable charge transfer reactions at 100 eV involve the transfer of a small quantity (<1 eV) of translational energy into internal energy of the product Xe* ions. A maximum was observed in the overall distribution of Xe* product states which is due in large part to the relatively high cross section for producing Xe*($J = \frac{1}{2}$) levels within 1-eV of resonance. Although spin is not an important quantum number in this system, the total angular momentum is conserved. At 100 eV collision energy, the most probable reactions in the He⁺/Xe system tend to conserve the total electronic angular momentum. The production of Xe*($J = \frac{1}{2}$) is a manifestation of this conservation law. Formation of Xe*($J > \frac{1}{2}$) states requires the conversion of angular momentum of the collision into electronic angular momentum. The present results indicate that for 100 eV He⁺/Xe collisions, the greater the extent of collisional to internal angular momentum conversion required, the lower the overall reaction probability. Finally, a mechanism has been proposed to explain the near-resonant He⁺/Xe charge transfer reaction, in terms of long-range potential curve crossings.

ACKNOWLEDGMENTS

The authors thank Dr. D. G. Hopper, Dr. D. R. Wood, and Dr. D. T. Terwilliger for many valuable discussions and Dr. W. B. Maier, II, for providing results prior to publication. Technical support of Mr. J. G. Dryden is also gratefully acknowledged. This research was supported by the Air Force Office of Scientific Research (AFSC), United States Air Force, under Contract No. F-44620-76-C-0007.

¹B. H. Stedford and J. B. Hasted, *Proc. R. Soc. London A* **227**, 468 (1955).

JHIV 15 LX 12

Jones, Tiernan, Fee, and Hughes: Reactions of 100 eV He⁺ with Xe

- ¹D. W. Koopman, *Phys. Rev.* **154**, 79 (1967).
- ²W. B. Maier, II, *Phys. Rev. A* **5**, 1256 (1972).
- ³D. K. Bohme, York University, has placed an experimental upper limit of 10^{-11} cm³/molecule⁻¹s⁻¹ for the thermal charge transfer rate (private communication).
- ⁴J. B. Launderslager, Jet Propulsion Lab. (private communication).
- ⁵M. Lipeles, R. Novick, and N. Tolk, *Phys. Rev. Lett.* **18**, 815 (1965).
- ⁶D. Jaacks, F. J. De Heer, and A. Salop, *Physica* **36**, 608 (1967).
- ⁷F. J. De Heer, B. F. J. Luvken, D. Jaacks, and L. Walterbeek Muller, *Physica* **41**, 585 (1969).
- ⁸B. M. Hughes, E. G. Jones, C. D. Miller, and T. O. Tiernan, in *Proceedings of the Twenty-first Conference on Mass Spectroscopy and Allied Topics* (San Francisco, 1973).
- ⁹B. M. Hughes, E. G. Jones, and T. O. Tiernan, *Abstracts of VIII International Conference on the Physics of Electronic and Atomic Collisions*, Institute of Physics, Edinburgh, Yugoslavia, 1973, Vol. 1, p. 223.
- ¹⁰B. M. Hughes, E. G. Jones, and T. O. Tiernan, *Bull. Am. Phys. Soc.* **19**, 156 (1974).
- ¹¹E. G. Jones, D. C. Fee, B. M. Hughes, and T. O. Tiernan, in *Proceedings of the Twenty-second Conference on Mass Spectroscopy and Allied Topics* (Philadelphia, 1974).
- ¹²E. G. Jones, B. M. Hughes, D. C. Fee, and T. O. Tiernan, in *Proceedings of the Twenty-fourth Conference on Mass Spectroscopy and Allied Topics*, San Diego, 1976.
- ¹³(a) E. G. Jones, B. M. Hughes, T. O. Tiernan, D. C. Fee, and D. G. Hopper, Brehm Laboratory Technical Report No. 10, Wright State University, Dayton, Ohio, 1977; (b) E. G. Jones, B. M. Hughes, T. O. Tiernan, D. C. Fee, and D. G. Hopper, *Spectrochim. Acta B* **33**, 757 (1978).
- ¹⁴E. G. Jones, B. M. Hughes, D. C. Fee, and T. O. Tiernan, *Phys. Rev. A* **15**, 1448 (1977).
- ¹⁵E. W. Thomas, *Excitation in Heavy Particle Collisions* (Wiley-Interscience, New York, 1972).
- ¹⁶X. X. Xu, *Rev. Sci. Instrum.* (to be published).
- ¹⁷K. C. Schmidt, Technical Applications Note 9803, Bendix Electro-Optics Division, Ann Arbor, Michigan, 1969; "Absorption Quantum Efficiency of a Channeltron Photomultiplier," M. C. Johnson and J. Svenson, Technical Note, Bendix Corporation, Research Laboratories Division, Southfield, Michigan.
- ¹⁸EMR photoelectric data for calibration of 541F-08-18-03800 photomultiplier-tube that was used in this study.
- ¹⁹T. Namioka and W. R. Hunter, *Optics Commun.* **8**, 229 (1973).
- ²⁰J. A. R. Sampson, *Techniques of Vacuum Ultraviolet Spectroscopy* (Wiley, New York, 1967).
- ²¹A. N. Zaidel and E. Ya. Shreider, *Vacuum Ultraviolet Spectroscopy*, translated by Z. Lerman (Ann Arbor-Humphrey, London, 1970).
- ²²The platinum coated grating is manufactured by Bausch and Lomb with serial no. 2265-57-14-J, 1200 lines mm⁻¹, and blazed at 90 nm.
- ²³E. G. Jones, B. M. Hughes, R. L. C. Wu, T. O. Tiernan, and D. G. Hopper, *J. Chem. Phys.* (to be submitted).
- ²⁴G. H. Dunn, R. Geballe, and D. Preizer, *Phys. Rev.* **188**, 1100 (1965).
- ²⁵G. Lantschner and A. Niehaus, *Chem. Phys. Lett.* **23**, 223 (1973).
- ²⁶M. H. Miller, R. A. Roig, and R. D. Bengston, *Phys. Rev. A* **8**, 480 (1973).
- ²⁷C. E. Moore, *Atomic Energy Levels*, Natl. Bur. Stand. Circ. 467 (U. S. Dept. of Commerce, Washington, DC, 19xx), Vols. I-III.
- ²⁸O. Herzberg, *Atomic Spectra and Atomic Structure*, 2nd ed. (Dover, New York, 1944).
- ²⁹This transition is observed in the isoelectronic Ca II spectrum. See G. L. Epstein and J. Reader, *J. Opt. Soc. Am.* **66**, 590 (1976).
- ³⁰E. G. Jones, B. M. Hughes, T. O. Tiernan, and D. C. Fee (unpublished).
- ³¹The energy defect, viz., recombination energy of He⁺ less the first ionization potential of Xe, is 12.46 eV (see Ref. 28).
- ³²Since the cross section for directly forming nonradiating or long-lived states has not been measured, we do not include the Σ_g contribution from these levels.
- ³³H. S. W. Massey, *Rep. Prog. Phys.* **12**, 248 (1949).
- ³⁴R. Shuker, Y. Staur, and A. Szoke, *Phys. Rev. A* **12**, 515 (1975).
- ³⁵O. Herzberg, *Molecular Spectra and Molecular Structure* (Van Nostrand Reinhold, New York, 1939), Vol. 1, p. 416.
- ³⁶E. Graham, IV, M. A. Diondi, and R. Johnson, *Phys. Rev. A* **13**, 965 (1976).
- ³⁷The effects of cascading for He⁺/Xe collisions have not been investigated at energies below 100 eV; however, all of the major lines monitored in the visible spectral region display kinetic energy behavior as apparent in Fig. 11. Thus we assume that if cascading effects are small for 100-eV collision, they will be small at lower energies.
- ³⁸See M. Barat, J. C. Brenot, D. Dhucq, J. Pommier, V. Sidis, R. E. Olson, E. J. Shipsey, and J. C. Browne, *J. Phys. B* **9**, 269 (1976), and references therein.
- ³⁹N. H. Tolk, J. C. Tully, C. W. White, J. Kraus, A. A. Monge, D. L. Simms, M. F. Robbins, S. H. Neff, and W. Lichten, *Phys. Rev. A* **13**, 969 (1976).
- ⁴⁰J. Etudon, M. Barat, and M. Abignol, *J. Phys. B* **3**, 207 (1970).
- ⁴¹H. P. Weise and H. N. Mittman, *Z. Naturforsch. A* **28**, 714 (1973).
- ⁴²Y. Tanaka, K. Yoshino, and D. E. Freeman, *J. Chem. Phys.* **62**, 4484 (1975).
- ⁴³M. S. B. Munson, J. L. Franklin, and F. H. Field, *J. Phys. Chem.* **67**, 1542 (1963).
- ⁴⁴The transfer of translational to internal energy implies linear momentum transfer. Recently Maier (Ref. 46) has measured the kinetic energy of the ionic products of charge transfer in rare-gas systems and has concluded that there is extensive momentum transfer.
- ⁴⁵W. B. Maier, II *Phys. Rev.* (in preparation).
- ⁴⁶More recently the reaction $\text{Xe}(^1P_{3/2,1/2}) + \text{He}$ has been studied at 100 eV ion impact. No Xe I or Xe II emissions could be identified ($\sigma < 10^{-18}$ cm²) indicating that the potential curves associated with the two lowest energy asymptotes in Fig. 12 do not efficiently cross curves leading to Xe⁺ at regions accessible to 100 eV collision energies.

Ref. 3, 12, 13 your only not available on printed.

"FORMATION AND REACTIONS OF NEGATIVE IONS RELEVANT
TO CHEMICAL IONIZATION MASS SPECTROMETRY. I. CI MASS
SPECTRA OF ORGANIC COMPOUNDS PRODUCED BY F^- REACTIONS"

T. O. Tiernan, C. Chang, and C. C. Cheng
Brehm Laboratory and Department of Chemistry
Wright State University
Dayton, Ohio 45435

ABSTRACT

A systematic study of the negative-ion chemical ionization mass spectra produced by the reaction of F^- with a wide variety of organic compounds has been accomplished. A time-of-flight mass spectrometer fitted with a modified high pressure ion source was employed for these experiments. The F^- reagent ion was generated from CF_3H or NF_3 , typically at an ion source pressure of 100 microns. In pure NF_3 , F^- is the major ion formed and constitutes more than 90% of the total ion intensity. While F^- is also the major primary ion formed in pure CF_3H , it undergoes rapid ion-molecule reactions at elevated source pressures, yielding $(HF)_n F^-$ ($n=1$ to 3) ions, which makes CF_3H less suitable as a chemical ionization reagent gas. Among the organic compounds investigated were carboxylic acids, ketones, aldehydes, esters, alcohols, phenols, halides, nitriles, nitrobenzene, ethers, amines and hydrocarbons. An intense $(M-1)^-$ ion was observed in the F^- chemical ionization mass spectra of carboxylic acids, ketones, aldehydes and phenols. Alcohols yield only $(M+F)^-$ ions upon reaction with F^- . A weaker $(M+F)^-$ ion was also detected in the F^- chemical ionization spectra of carboxylic acids, aldehydes, ketones and nitriles. The F^- chemical ionization mass spectra of esters, halides, nitriles, nitrobenzene and ethers are characterized primarily by the ions, $RCOO^-$, X^- , CN^- , NO_2^- and OR^- , respectively. In addition, esters show a very weak $(M-1)^-$ ion (except formates). In the F^- chemical ionization spectra of some aliphatic alkanes and o-xylene, a very weak $(M+F)^-$

ion was observed. Amines and aliphatic alkenes exhibit only insignificant fragment ions under similar conditions, while aromatic hydrocarbons, such as benzene and toluene are not reactive at all with the F^- ion. The mechanisms of the various reactions mentioned are discussed, and several experimental complications are noted. In still other studies, the effects of varying several experimental parameters, including source pressure, relative proportions of the reagent and analyte, and other ion source parameters, on the observed chemical ionization mass spectra were also investigated. In a mixture of NF_3 and n-butanol, for example, the ratio of the intensities of the ions characteristic of the alcohol to that of the $(HF)_n F^-$ ion was found to decrease with increasing sample pressure, with increasing NF_3 pressure, and with increasing electron energy. No significant effects on the spectra were observed to result from variation of the source repeller field or the source temperature. The addition of argon to the source as a potential moderator did not alter the F^- chemical ionization spectrum significantly, but the use of oxygen appears to inhibit formation of the $(HF)_n F^-$ cluster ion. The advantages of using F^- as a chemical ionization reagent are discussed, and comparisons are made with other reagent ions.

INTRODUCTION

Interest in the development and applications of negative-ion chemical ionization (NICI) mass spectrometry has expanded rapidly in the past ten years, as clearly indicated by the attendance at the present and other recent symposia (1) concerned with this topic. The number of publications appearing in the chemical literature which deal with NICI mass spectrometry has also increased significantly during this time period. Several current comprehensive reviews (2-4) have surveyed these publications. In spite of the increasing activity in this field of research, however, relatively few negative ions have yet been investigated as chemical ionization reagents. This is illustrated by the listing shown in Table 1. This situation is due to the lack of established methods for generating usable quantities of many types of negative ions, and to the uncertainties which currently prevail in the understanding of gas phase negative ion chemistry.

In the present paper, we report the results of a systematic study of the reactions of the fluoride negative ion, F^- , with a variety of organic molecules, which are representative of different functional group classes. The F^- ion was selected for investigation as a NICI reagent ion for several reasons. First, it was expected that F^- could be readily produced in large abundance by electron impact on molecules such as CH_3F and NF_3 . The appearance potential of F^- from NF_3 is very near zero eV (11), and previous experiments in our laboratory have demonstrated that the rate coefficient for attachment of near-thermal electrons to NF_3 , yielding F^- , was very large (12). Also, F^- is the

TABLE 1

NEGATIVE IONS USED AS CHEMICAL IONIZATION MASS SPECTROMETRY REAGENTS

IN STUDIES REPORTED TO DATE

Reagent Ion	Source Gases	Type of Ion Source Used	Typical Total Source Pressure (Torr)	Reference *
H ⁻	H ₂	Electron Impact	1	2
O ⁻	N ₂ O/N ₂	Electron Impact	0.3-0.5	5
O ₂ ⁻	N ₂ O/N ₂ /O ₂	Electron Impact	0.3-0.5	2
O ₂ ⁻	O ₂ , H ₂ /O ₂	Townsend Discharge	1	6,7
O ₂ ⁻	Air	Atmospheric Pressure Ionization	Atmospheric Pressure	8
Cl ⁻	CH ₂ Cl ₂	Electron Impact	1	9
OH ⁻	N ₂ O/H ₂ , N ₂ O/CH ₄	Electron Impact	1-3	10
CH ₃ O ⁻	CH ₃ ONO/CH ₄	Electron Impact	1	7

* Numbers shown correspond to those used in the list of references.

only ionic product observed from ion energy electron attachment to NF_3 . Secondly, the proton affinity of F^- is relatively high, 1548 KJ/mole, which is just between the proton affinities of OH^- , 1632 KJ/mole, and Cl^- , 1393 KJ/mole (2). The anionic nucleophilicity of F^- also lies between that of OH^- and Cl^- , which have previously been utilized in NICI studies (see Table 1). These considerations suggest that F^- should be reactive with a number of organic molecules. Still another feature of F^- as a NICI reagent ion is that fluorine is monoisotopic, so that if F^- associates with a particular molecule, only one $(M + 19)^-$ product ion will be observed, since no isotope peaks can be formed. Thus the F^- NICI mass spectra should be simpler and more readily interpreted than those resulting from reactions of other halide negative ions.

The experimental procedures employed and the results obtained in this investigation are described in the following sections.

EXPERIMENTAL

The instrument utilized for the experiments reported herein is a Bendix Model 12-101 Time-of-Flight Mass Spectrometer equipped with a 100 cm. drift tube. The mass spectrometer is fitted with a specially designed, high pressure ion source, which was developed by Chang and Tiernan (13). Figure 1 shows a schematic diagram of the ion source and the focusing lens system. The source, which was constructed from a solid copper block, is actually an open cylinder with an inside diameter of 1.91 cm and a length of 1 cm. A gas inlet orifice, 0.64 cm in diameter was cut into the side of the block. An electron entrance plate (EEP) and an ion exit plate (IEP) are utilized to seal the top

**Figure 1. Schematic Diagram of High Pressure Ion Source Developed
for a Time-of-Flight Mass Spectrometer.**

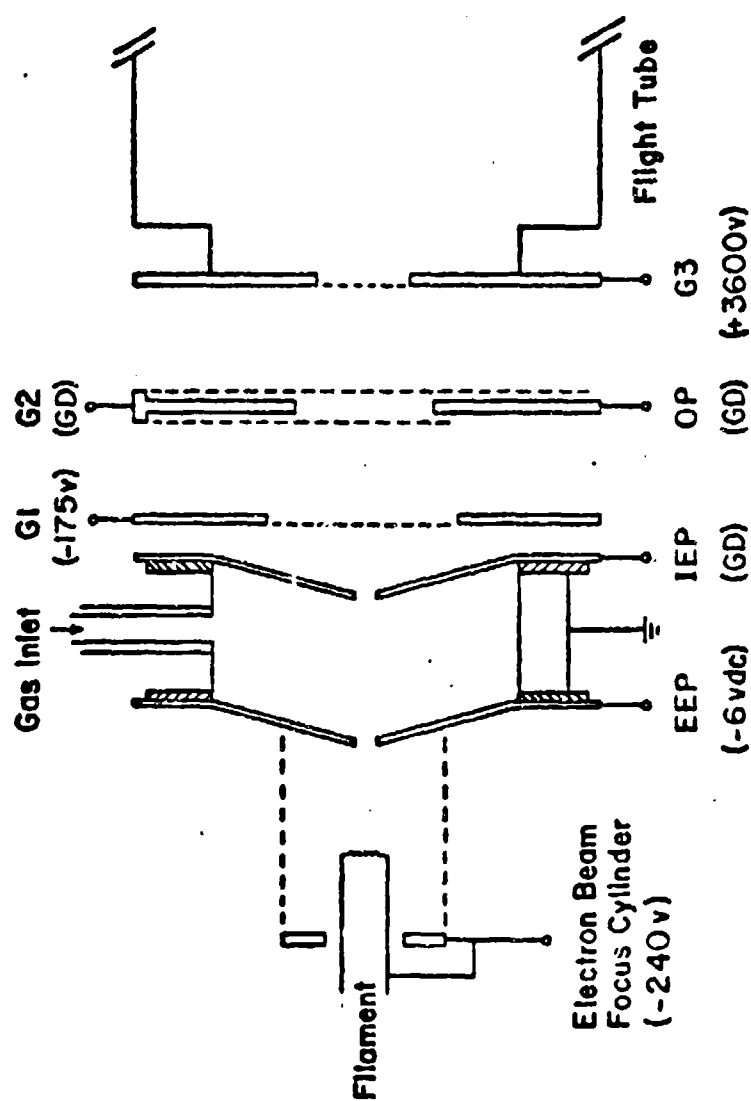


Fig. 1. Schematic Diagram of High Pressure Ion Source Developed for a Time-of-Flight Mass Spectrometer.

and the bottom of the source cylinder. Both plates were identically manufactured from stainless steel, and are cone shaped, with a 0.05 cm diameter orifice at the cone apex. A -6V dc potential is applied continuously to the electron entrance plate as a repeller potential. This facilitates removal of ions from the source. The ion exit plate is maintained at ground potential. Both plates can be used to monitor the electron beam current if desired, by suitable connections. A coiled tungsten wire filament is located about 1 cm from the electron entrance plate. In order to collimate the electron beam, a beam focusing cylinder, which was constructed from 90% transparent rhenium mesh screen, is used to surround the filament. Use of the transparent wire mesh permits efficient pumping of neutral gas from the filament region. This focusing cylinder and one end of the filament are maintained at a negative potential of -240 volts.

The filament is mounted in such a way that the electron beam path coincides with the ion axis. This arrangement differs from that used in most conventional ion sources, in which, the electron beam typically enters the side of the source chamber at an angle of 90 degrees to the direction of ion extraction. With the latter configuration, ions formed in the region just above the ion exit aperture are more likely to be extracted and detected. At lower source pressure this conventional configuration functions well, since ions are formed uniformly along the electron path. However, as the source pressure is increased, the penetrating power of the electron beam decreases rapidly. Thus, only a few ions are formed in the region near the exit aperture. With our new source design, all primary ions are formed along the electron beam path (which is coaxial with the ion extraction path) and

are therefore produced in the region directly adjacent to the ion exit aperture. At higher pressures in the source, these primary ions then react with other molecules in the same region to form the secondary product ions. As noted earlier, a repeller field is applied to drive ions thus formed through the ion exit aperture, which increases the number of ions reaching the detector on any given pulse cycle.

The ion source of the mass spectrometer is housed inside a T-shaped stainless tube which was fabricated for this purpose and which is connected directly to the drift tube of the mass spectrometer. This housing incorporates a high speed pumping port, to which a 4-inch oil diffusion pumping system is directly attached via a flexible 10-cm stainless steel bellows. For the source exit aperture currently used, this is adequate to maintain a pressure differential of about 1000:1 between the source interior and the surrounding region. This differential pumping reduces collisions between ions and neutrals outside the source region to a significant extent. The drift tube region is pumped by the standard pumping system which consists of a 4-inch mercury diffusion pump, a Bendix combined liquid nitrogen trap and Freon-cooled baffle, and a Welch forepump (52). The pressure is monitored by a Philips-type cold-cathode ionization gauge (Veeco) which measures pressures as low as 2×10^{-6} mm of Hg.

The sample inlet system is an all-metal dual reservoir system, containing two 1-liter stainless steel expansion tanks. Each reservoir is connected to the ion source via a variable gas leak, in one case, a Granville-Phillips Series 213 motor-driven variable leak, and in the other, a Granville-Phillips Series 203 manually adjusted leak.

Additions to the sample inlet system were constructed recently to permit introduction of multi-component reagent mixtures and gas samples, and to allow coupling of a gas chromatograph (GC) to the mass spectrometer. These additional inlet sections are also controlled by Granville-Phillips Series 203 manually adjusted leaks, and permit introduction of condensed phase samples from an inlet tube. The latter is a U-shaped 1/4-inch ID glass tube with one end sealed by a septum, and the other end connected to a Whitey SS-2RS4 metric valve, which controls the molecular flow of the sample vapor. This tube was installed near the source-housing flange in order to reduce condensation in the inlet to a minimum. A MKS Baratron pressure sensor head (type 77-H-1) is attached to the source housing to measure the ion source pressure directly. All tubing used for interconnections in this system is 1.27 cm diameter stainless steel tubing. Swagelok tube fittings are used for all couplings. A variety of valves are also used in the system. The sample inlet system and the pressure reference side of the MKS sensor are pumped by means of a CVC type PMCS-2B diffusion pump, backed by a Welch 1400B forepump.

A Hewlett-Packard 2116C computer with 16-bit word length and 24K core memory was used for data acquisition. Since the analog electrometer used for the recording of negative ions is not electrically isolated, the signals from the multiplier cannot be directly input into the computer. Instead, the output signal of the amplifier is further amplified by a Keithley Instrument Type 109 pulse amplifier with 50 ohms input resistance and 20 DB gain. The amplified signal is then transmitted to a scan converter (Pacific Instrument), which is

built into the oscilloscope. The computer directly accepts the signal from the scan converter. This procedure introduces some noise, and reduces detection sensitivity considerably, but permits direct computer acquisition of the data. Four channels are used to establish communication between the computer and the TOF mass spectrometer. The first channel transmits a signal from the Y-axis of the oscilloscope to the computer for the ion intensity. The second channel transmits a signal from the X-axis of the oscilloscope to the computer for a ramp voltage. The third channel transmits the junction voltage of a thermocouple used for temperature measurement. The fourth channel carries a relay message to the computer. These analog signals are converted into digital signals by the A/D converter of the computer. The digital signals are then processed by the computer using previously designed software developed in our laboratory.

Negative ion mass spectra were recorded with the TOF mass spectrometer, normally under the following conditions: accelerating voltage, 3.6 kV; primary electron beam voltage, 240 eV; ion source envelope pressure, approximately 5×10^{-6} mm Hg; source temperature, 70-120 degrees C; and the emission current (which is the current measured at the electron entrance plate) was adjusted to obtain maximum ion intensity. Usually, the latter was varied from several tenths milliampere to about 10 milliamperes. The source pressure was monitored by an MKS Baratron Type 77-H-1 pressure sensor head. The sample pressure was maintained at a constant value, usually between 0.5 and 10 μ and the total pressure was maintained at 100 μ (with the reagent gas added).

Fluoroform used in these studies was obtained from Matheson Gas Products, East Rutherford, N.J., and was specified to be approximately 99.9% pure. NF_3 was obtained from Air Products and Chemicals Inc., Allentown, Pa., with a reported purity of 99.92% minimum. All organic compounds studied were obtained from commercial suppliers and were used without further purification.

RESULTS AND DISCUSSION

A. Formation of the Primary F^- Ion Reactant

1. Using Fluoroform as the Reagent Gas

a. The Spectrum of Pure CHF_3 Under NICI Conditions. In principle, the F^- ion can be produced from several gaseous fluoride compounds by electron impact. The appearance potential of F^- from fluoroform (CHF_3) is about 9.3 eV (11). Thus initially the latter molecule was selected as the reactant source molecule. The NICI mass spectrum of CHF_3 at a pressure of 0.1 Torr and a temperature of 100°C is shown in Table 2. It can be seen that electron impact on CHF_3 at relatively high source pressure yields very small amounts of F^- , and large abundances of various cluster ions. Apparently this is due to the rapid association reaction of the F^- ion with one or more HF molecules, to form cluster ions of the type, $[(\text{HF})_n\text{F}]^-$, where $n=1$ to 3 (14). There are two possible sources for the HF molecules. One possibility is the proton transfer reaction between F^- and the fluoroform molecule, in which CF_3^- is also formed,



TABLE 2

NICI MASS SPECTRUM OF FLUOROFORM OBTAINED AT 100°C AND
0.1 TORR ION SOURCE PRESSURE

<u>m/e</u>	<u>Ion</u>	<u>Relative Intensity (%)</u>
19	F^-	--
39	$(HF)F^-$	19.2
59	$(HF)_2F^-$	100.0
69	CF_3^-	6.9
79	$(HF)_3F^-$	23.8
85	CF_3O^-	24.7
89	$(CHF_3)F^- / (CF_3)^-(HF)$	8.0
105	$(CF_3O)(HF)^-$	8.3
109	$(CHF_3)(HF)F^-$	11.5
128	$(CF_2)(CF_3O)^-$	9.5
135	$C_2F_5O^-$	10.3

The other possibility is a reaction of F radicals, generated in the initial electron impact event, with hydrogen-containing impurities (RH) resident within the ion source.



and



The enthalpy of Reaction 1 is on the order of -56.5 kcal/mole and this process is therefore substantially exothermic. For many RH reactants, Reaction 3 would also be highly exothermic.

Trace quantities of O_2^- or O^- ions inside the source could react with fluoroform molecules to yield the observed m/e 85 peak corresponding to the $(\text{M} - \text{H} + \text{O})^-$ ion in the NICI spectrum shown in Table 2. The m/e 89 ion could be formed either by clustering between fluoroform and F^- , or by clustering between HF and CF_3^- . As shown in Table 2, both the m/e 105 and the m/e 109 ions can be explained on the basis of clustering of HF with the m/e 85 and 89 ions. There are also relatively small amounts of m/e 128 and m/e 135 in the NICI spectrum. It is tentatively assumed that the former ion is $(\text{CF}_2)(\text{CF}_3\text{O})^-$, while the latter ion is apparently $\text{C}_2\text{F}_5\text{O}^-$, which probably arises from HC_2F_5 or other such impurities in the fluoroform.

b. Temperature Effects on the NICI Spectrum of CHF_3 . The relative abundances of ions observed in the fluoroform NICI mass spectrum were found to be temperature dependent. The variation in the relative intensities was studied over a temperature range of 70 to 230°C, at a total source pressure of 0.1 Torr. It was observed that

the relative intensity of m/e 39 increases with increasing source temperature, while the intensities of m/e 59 and 79 decrease, as do those of the m/e 105 and 109 ions. It seems apparent that at higher source temperatures the formation of the larger cluster ions in fluoroform is less favored. This is consistent with the increased relative intensity of the m/e 69 ion as the temperature is increased.

A trace quantity of *n*-butanol (about 0.5 μ) was injected into the ion source which also contained fluoroform at a pressure of 0.1 Torr. Molecular, or quasi-molecular ions, such as $(M-1)^-$ and $(M + F)^-$, were not observed in the NICI spectrum under these conditions. The failure to observe such ions possibly indicates that the reaction rate of F^- with *n*-butanol is much slower than that of F^- with neutrals such as HF.

2. Using NF_3 as the Reagent Gas

a. The Spectrum of Pure NF_3 Under NICI Conditions. Owing to the very low intensity of the primary F^- ion observed in the fluoroform NICI spectrum, a second reagent gas, NF_3 , was tested as a source of F^- . The NICI spectrum of NF_3 at a total pressure of 0.1 Torr shows that the m/e 19, F^- is the major peak, with only a trace quantity of m/e 39, HF_2^- . Again, the HF molecule with which F^- clusters here is probably formed from hydrogen-containing impurities in the source, by a mechanism similar to that described previously.

b. The NICI Spectrum of *n*-Butanol Obtained with NF_3 Reagent Gas. Table 3 shows the NICI spectrum of *n*-butanol obtained with NF_3 reagent gas at a total pressure of 100 μ and at a temperature of 70°C. About 0.5 μ of *n*-butanol was injected into the source with the NF_3 for this experiment. The ions at m/e 19, 39, and 59 are presumably formed as

TABLE 3

NICI SPECTRUM OF n-BUTANOL (0.5 μ) OBTAINED WITH NF₃ REAGENT GAS

AT A TOTAL PRESSURE OF 100 μ

<u>m/e</u>	<u>Ions</u>	<u>Relative Intensity (%)</u>
19	F ⁻	47.7
39	(HF)F ⁻	100.0
59	(HF) ₂ F ⁻	64.5
93	(M + F) ⁻	10.8
113	(HF)(M + F) ⁻	3.2

described earlier. The m/e 93 likely originates from the direct attachment of F^- to the *n*-butanol sample molecule, and the m/e 113 is then formed by clustering of an HF molecule with the $(M + F)^-$ ion. Apparently, F^- undergoes competing reactions with the *n*-butanol and HF molecules. Several additional experiments were therefore conducted in which various experimental parameters were varied, in an attempt to maximize the intensity of the $(M + F)^-$ product.

c. The Effects of Varying Experimental Conditions on the NICI Spectrum of *n*-Butanol Obtained with NF_3 Reagent.

1. Variation of the Total Pressure of NF_3 . At an electron energy of 240 eV, and a source temperature of about 70°C, the relative intensities of m/e 39, $(HF)F^-$, and m/e 93, $(C_4H_9OH)F^-$, in the NICI spectrum of an *n*-butanol- NF_3 mixture were observed at various total ion source pressures over the range from 40 to 120 μ . The observed intensities and the ratio of these are shown in Table 4. The *n*-butanol sample in these experiments was maintained at a constant pressure of 0.5 Torr. It can be seen, from Table 4, that the ratio of the relative intensity of m/e 39 to that of m/e 93 increases as the pressure of NF_3 increases. This indicates that at higher pressures the preferred reaction is the association reaction of F^- with HF. The m/e 93 ion is formed via a second-order reaction, in which F^- ions are first produced from NF_3 , and then cluster with *n*-butanol molecules. The $(HF)F^-$ product ions, on the other hand, are formed by a reaction which is at least third-order. Probably, the F radical, produced by electron impact on NF_3 , abstracts a hydrogen atom from an *n*-butanol molecule or other hydrogen-containing impurities to form an HF molecule.

TABLE 4

RATIO OF RELATIVE INTENSITIES OF m/e 39 TO 93 IN THE NICI SPECTRUM
OF NF₃-n-BUTANOL AT VARIOUS PRESSURES OF NF₃

P_{NF_3} (μ)	Relative Intensity (%)		Ratio I_{39}/I_{93}
	I_{39}	I_{93}	
30	8.4	7.4	1.1
40	25.0	19.9	1.3
60	31.2	8.3	3.8
80	59.8	10.2	5.9
100	100.0	10.8	9.3
120	31.3	2.8	11.2

which then clusters with F^- . Thus, the observed intensity of the $(HF)F^-$ ion varies as the third power of the pressure. At higher pressures, the reaction forming $(HF)F^-$ is thus more favorable than that forming $(M + F)^-$. Thus, in order to observe a distinct quasi-molecular anion in the F^- NICI mass spectrum, such as m/e 93 in this example, the total source pressure has to be kept relatively low. However, the pressure cannot be lower than 30μ , or this product is not observed, owing to the characteristics of the ion source employed in the present studies.

11. Variation of the Electron Energy. The electron energy is another parameter of considerable importance in NICI experiments. When the electron energy was lowered to 40 eV, while all other parameters were kept constant for the present gaseous system, the reaction leading to formation of the $(M + F)^-$ ion was found to be favored. The ratio of m/e 39 to m/e 93 was found to decrease abruptly as the electron energy was reduced from 240 V to 40 V. A possible explanation is that the production of F radicals is enhanced significantly at higher electron energies. The F radicals thus formed react, in turn, with n-butanol to form more HF molecules. Thus, F^- collisions with HF molecules are more probable than collisions with n-butanol molecules at the higher electron energy.

111. Variation of the Repeller Field. By applying a small repeller field to the electron entrance plate of the ion source, (-6 V, d.c.), the residence time of ions inside the source can be reduced. However, the distribution of reaction products was not observed to change significantly as the repeller potential was varied over this

range.

iv. Variation of Source Temperature. Varying the ion source temperature over the range 100° to 190°C, while other parameters are kept constant, resulted in little change in the ratio of relative intensities of m/e 93 to 39. Apparently, the competition between $(HF)F^-$ and $(M + F)^-$ production is rather insensitive to temperature. However, the relative intensities of both the m/e 39 and 93 ions, with respect to m/e 19, decrease markedly as the temperature increases.

v. Variation of Sample Pressure. A series of NF_3 - NICI spectra of n-butanol were obtained at various n-butanol pressures ranging from 1 to 40 μ , at a total pressure of 80 μ and with all other parameters held constant. Listed in Table 5 are the relative intensities of the major ions observed, and the ratios of relative intensities of two successive cluster ions. At higher n-butanol pressures, larger clusters are observed, m/e 79 and 99, which result from successive HF additions. At butanol pressures above 4 μ , a peak is observed at m/e 167. This probably corresponds to an $M(M + F)^-$ ion, which is formed by clustering of another butanol molecule with the $(M + F)^-$ ion. The I_{59}/I_{39} ratio is seen to increase sharply as the sample pressure increases. Moreover, the ratios, I_{79}/I_{59} , I_{99}/I_{79} and I_{113}/I_{93} also increase proportionately with pressure. This indicates that n-butanol plays an important role in the cluster ion formation. It is probable that n-butanol is the most significant source of hydrogen atoms for the reactions yielding HF molecules. With increasing n-butanol pressure, the yield of HF molecules therefore

RELATIVE INTENSITIES OF MAJOR IONS AND RATIOS OF RELATIVE
INTENSITIES OF SUCCESSIVE CLUSTER IONS IN THE NF_3 -NICI SPECTRA OF n-BUTANOL
AT VARIOUS n-BUTANOL PRESSURES*

*The total source pressure was maintained at 80 μ .

increases. These HF molecules then react further with F^- to produce cluster ions of various orders. The ratio, I_{167}/I_{93} , is also observed to increase gradually as the sample pressure increases. This is because at higher concentrations of sample molecules, the formation of the $(2M + F)^-$ ion is enhanced. Finally, as seen in both Table 5, at sample pressures above 4μ , the cluster ion, m/e 59, formed by association of two HF molecules with F^- is preferred to other cluster ions.

vi. Addition of Other Gases to the NF_3 Reagent Gas.

In order to reduce the population of highly energetic electrons in the ion source, certain gases can be added to the reagent gas which act as electron scavengers. Removal of these electrons is desirable because the reaction of high energy electrons with NF_3 is considered to be the major source of F radicals. In the present study, the use of argon as a high-energy electron moderator was investigated. Argon was mixed with the NF_3 gas in different proportions, while maintaining a total ion source pressure of 80μ . The n-butanol sample pressure was maintained at about 0.5μ , while other parameters were kept constant, as before. It was observed that the ratio of relative intensities of m/e 39 to 93 obtained with various pressures of Ar added to the source gas mixture did not decrease, as was expected.

In both solution and gas phase reaction studies, oxygen has been employed as an inhibitor, owing to its ability to scavenge atoms or radicals, thus forming species which are incapable of participating in the chain-propagation steps. It was considered feasible, therefore, that the addition of oxygen to the NF_3 -butanol gas mixture in the ion

source might reduce the population of F radicals. Small quantities of oxygen gas (pressure ranging from 2 to 6 μ) were therefore added to the source, in a series of experiments, in which the total pressure was maintained at 50 μ , the n-butanol pressure was kept constant at 2 μ , and other parameters were not varied. The ratio of the relative intensity of m/e 93 to that of m/e 39 observed in the NICI spectrum was observed to increase by a factor of six, as the pressure of oxygen increased from 0 to 6 μ . Thus, oxygen clearly appears to inhibit the formation of the fluorine radical. However, the overall ion intensities decrease as O₂ pressure increases, and in addition, the lifetime of the tungsten filament is shortened, both of which are undesirable results.

B. Negative Ion Chemical Ionization Mass Spectra from Reactions of F⁻ With Various Organic Compounds

As described in the foregoing sections, impact of electrons on gaseous NF₃ produces a large population of F⁻ ions, which can be used as reactant ions to generate negative chemical ionization mass spectra. Since F⁻ has a large gas phase proton affinity, reactions of this ion with many molecules to produce (M-1)⁻ products by proton transfer are expected to be common. Furthermore, F⁻ is a strong nucleophile, and so bimolecular nucleophilic substitution reactions with this ion are expected to be observed in some cases. The organic compounds, for which F⁻ NICI mass spectra were examined in this study, were selected as representative of a variety of functional group classes. The detailed experimental results obtained for each functional group class are discussed in the following sections. The experimental conditions

TABLE 6

F⁻ NICI MASS SPECTRA OF CARBOXYLIC ACIDS (RCOOH)

<u>Compounds (M)</u>	<u>Mol. Wt.</u>	<u>m/e 19</u>	<u>Rel. Int. [*] (%)</u>		<u>Other ions</u>	
			<u>(M-1)⁻</u>	<u>(M+F)⁻</u>	<u>(2M-1)⁻</u>	<u>m/e (rel. int.) Identity</u>
formic acid (HCOOH)	46	21.2	100	2.4	38.1	42 (5.5) CNO ⁻ 111 (15.0) (HF)(2M-1) ⁻
acetic acid CH ₃ COOH	60	68.7	100	8.0	9.2	42 (5.9) CNO ⁻
isobutyric acid (CH ₃) ₂ CHCOOH	88	94.6	100	14.1	---	57 (46.3) CH ₃ COCH ₂ ⁻
mercaptoacetic acid HSCA ₂ COOH	92	73.4	100	2.7	---	59 (35.2) CH ₃ COO ⁻

^{*} Ions less than 5% relative intensity are omitted except the quasi-molecular ions.

used in obtaining these NICI spectra were selected on the basis of the results obtained in the previously described studies of the effects of pressure, temperature and other experimental parameters.

1. Carboxylic Acids.

The F^- NICI mass spectra of formic, acetic, isobutyric and mercaptoacetic acids are shown in Table 6. It is seen from these data that the most intense ion in the spectra of all these carboxylic acids is the $(M-1)^-$ ion. This ion is formed by the abstraction of a proton, probably from the COOH group. In mercaptoacetic acid, both the SH and the COOH groups contain active hydrogen, but more likely, abstraction occurs preferentially from the COOH group.

F^- attachment to these carboxylic acids to form $(M + F)^-$ ions was also observed, as indicated by the spectra shown in Table 6, but the relative intensities of these ions are much smaller than those of the $(M-1)^-$ products. At higher ion source pressures, the NICI spectra of formic acid and acetic acid show clusters of these molecules with the $(M-1)^-$ ions, that is, $(2M-1)^-$ ions. Cluster ions formed by association of product ions with HF molecules, were also observed in the formic acid NICI mass spectrum. A very weak intensity ion at m/e 42 was observed in the spectra of acetic acid and formic acid. Possibly, this ion is CNO^- , as suggested by Alpin et al (15), or $\begin{array}{c} CH_2-CH_2 \\ \diagdown \quad / \\ :N:- \end{array}$, as postulated by Field (10). The mechanism of formation of this ion is unclear, but it seems more likely that CNO^- would be formed than $\begin{array}{c} CH_2-CH_2 \\ \diagdown \quad / \\ :N:- \end{array}$, because neither formic acid nor acetic acid contains an acetylenic group. Other observed ions having m/e values which do not

correspond to any expected fragments for the compounds undergoing chemical ionization are quite possibly formed from impurities contained in the samples.

2. Carboxylic Acid Esters.

The F^- NICI mass spectra of isopropyl acetate, ethyl acetate, ethyl formate and methyl methacrylate are shown in Table 7. Both isopropyl acetate and ethyl acetate exhibit an intense m/e 59 peak in their F^- NICI spectra, while ethyl formate exhibits an intense m/e 45 peak, and methyl methacrylate is characterized by a strong m/e 85 peak. These peaks correspond to the carboxylate anions from each of these esters, $CH_3CO_2^-$, HCO_2^- and $CH_2=C(CH_3)CO_2^-$, respectively, which are formed by an O-alkyl cleavage, resulting from F^- attack on the alcohol alkyl group and subsequent displacement of carboxylate ions. This can be visualized as a bimolecular nucleophilic substitution reaction.

A weak $(M-1)^-$ ion is also observed in each of the esters studied here, with the exception of ethyl formate. This ion is expected to be primarily formed by abstraction of a relatively acidic hydrogen from the molecule. In isopropyl acetate and ethyl acetate, an alpha hydrogen is available for abstraction by the F^- ion, but in methyl methacrylate, an allylic hydrogen must be abstracted. No $(M-1)^-$ ion is observed in ethyl formate, since this molecule contains no active hydrogen atoms.

Since alkoxide ion, $R'O^-$, is more nucleophilic than F^- (16), the attack of F^- at the carbonyl-carbon center, to release the alkoxide ion, does not occur with this group of ester compounds. This is

TABLE 7

F⁻ NICT MASS SPECTRA OF CARBOXYLIC ACID ESTERS (RCOOR')

Compounds (M)	mol. wt.	m/e 19	Rel. Int. (%) [*]		Other ions m/e (rel. int.) Identity
			m/e 19	RCOO ^{***}	
ethyl acetate CH ₃ COOC ₂ H ₅	88	21.4	100 (m/e 59)	3.4	39 (23.6) (HF)F ⁻
					61 (10.2) ⁻ CH ₂ COF
isopropyl acetate CH ₃ COOCH(CH ₃) ₂	102	20.6	100 (m/e 59)	3.5	39 (18.4) (HF)F ⁻
					57 (6.4) CH ₃ COCH ₂ ⁻
					61 (8.4) ⁻ CH ₂ COF
					79 (5.2) (HF)(RCOO ⁻)
ethyl formate HCOOC ₂ H ₅	74	45.8	100 (m/e 45)		39 (64.3) (HF)F ⁻
					59 (23.6) CH ₃ COO ⁻ or (HF) ₂ F ⁻
					65 (28.9) (HF)(RCOO ⁻)
methyl methacrylate CH ₂ =C(CH ₃)COOCH ₃	100	100	34.2 (m/e 85)	0.4	26 (6.8) CN ⁻
					39 (16.4) (HF)F ⁻
					40 (26.9) ⁻ CH ₂ CN
					45 (8.3) HCOO ⁻
					59 (19.6) CH ₃ COO ⁻ or (HF) ₂ F ⁻

^{*} Ions less than 5% relative intensity are omitted except the quasi-molecular ions.

^{**} R = H in the ethyl formate.

demonstrated by the NICI spectrum of ethyl acetate, since no m/e 45 peak ($C_2H_5O^-$) is observed.

Ions at m/e 26, 42 and 46, having very weak intensities, also appear in the spectra of these compounds. In addition, a low intensity ion at m/e 41 appears in the spectrum of each ester except that of ethyl formate. This ion probably corresponds to the ketene anion, $^-HC=C=O \rightleftharpoons HC\equiv C-O^-$, (15), which is rather commonly observed from oxygen-containing compounds. The ion at m/e 61 in the spectra of ethyl acetate and isopropyl acetate is quite puzzling. It is possible that this ion is $^-CH_2COF$. Two possible mechanisms can be conceived for its formation. One mechanism would involve nucleophilic attack of F^- on the carbonyl carbon, resulting in displacement of the alkoxide ion, yielding an acyl fluoride compound (CH_3COF), followed by abstraction of an alpha hydrogen by F^- . Another possible mechanism would involve addition of an HF molecule to the ketene anion. As mentioned above, nucleophilic displacement reactions involving attack of F^- at the carbonyl carbon apparently do not occur with esters. Therefore, the first mechanism is not probable. Other minor ions observed in the spectra shown in Table 7 are again likely due to impurities.

3. Ketones and Aldehydes.

The F^- NICI mass spectra of acetone, 2-hexanone, 4-heptanone, 2,5-hexadione and cyclopentanone are shown in Table 8. It is seen that the $(M-1)^-$ ion is the predominant ion for all compounds of this type which were examined. The mechanism of formation likely involves abstraction of the active alpha hydrogen in each of these compounds. In addition, $(M + F)^-$ ions, in varying relative abundances (1.2 - 22%),

TABLE 8

F⁻ NICI MASS SPECTRA OF KETONES (RCOR')

<u>Compounds (M)</u>	<u>mol. wt.</u>	<u>m/e 19</u>	<u>Rel. Int. (%)</u> [*]		<u>M⁻</u>	<u>Other ions m/e (rel. int.) identity</u>
			<u>(M - 1)⁻</u>	<u>(M + F)⁻</u>		
acetone CH ₃ COCH ₃	58	79.6	100	1.2	2.0	26 (6.3) CN ⁻
2-hexanone CH ₃ CO(CH ₂) ₃ CH ₃	100	34.0	100	13.0	4.6	26 (11.6) CN ⁻ ; 39 (5.1) (HF)F ⁻
4-heptanone CH ₃ CO(CH ₂) ₄ CH ₃	114	26.3	90.8	11.4	5.1	26 (25.5) CN ⁻ ; 39 (13.4) (HF)F ⁻
2,5-hexadione CH ₃ CO(CH ₂) ₂ COCH ₃	114	42.9	100	22.0	5.8	26 (6.1) CN ⁻
cyclopentanone C ₅ H ₈ O	84	71.0	100	15.4	4.1	26 (30.6) CN ⁻ ; 39 (23.1) HF(F ⁻)

* Ions less than 5% relative intensity are omitted except the quasi-molecular ions.

are also observed in the spectra. These probably are formed by way of tetrahedral intermediates resulting from the attack of the F^- ion at the carbonyl carbon, this being a typical reaction of ketones and aldehydes (17). The molecular anion M^- is also detected in the spectra of these compounds, but in very weak intensity. This ion probably results from resonance electron capture by the molecule. An ion at m/e 26, apparently CN^- , is also observed in each of the ketone spectra.

Similar to the ketones, the F^- NICI mass spectra of aldehydes, including acetaldehyde, propionaldehyde and 2-ethylbutyraldehyde, are all characterized by an intense $(M - 1)^-$ ion, as shown in Table 9. Undoubtedly, the reaction mechanism in these cases also involves abstraction of an active alpha hydrogen from the molecule. The $(M + F)^-$ ion is also a prominent species in the spectra of this group of compounds, and again, formation of these ions probably involves a tetrahedral intermediate. Analytically insignificant ions, such as m/e 26, 39, 42, and 59, are all present in quite high concentrations.

4. Aliphatic Alcohols

The F^- NICI mass spectra of n-butanol, iso-butanol and tert-amyl alcohol are shown in Table 10. All of these compounds exhibit significant $(M + F)^-$ ions. In contrast to the compounds previously discussed, however, aliphatic alcohols show no $(M - 1)^-$ ion in their F^- NICI spectra. This is likely attributable to the fact that aliphatic alcohols are very weak acids, and thus it is relatively difficult to remove a proton from the -OH group.

As discussed earlier, the reactions of F^- with the sample molecule

TABLE 9

F⁻ NICI MASS SPECTRA OF ALDEHYDES (RCHO)

<u>Compounds (M)</u>	<u>mol. wt.</u>	<u>m/e 19</u>	<u>(M - 1)⁻</u>	<u>(M + F)⁻</u>	<u>Other ions m/e (rel. int.) identity</u>
acetaldehyde CH ₃ CHO	44	15.7	100	7.0	26 (42.1) CN ⁻ 39 (15.5) (HF)F ⁻ 42 (6.9) CNO ⁻
propionaldehyde C ₂ H ₅ CHO	58	--	100	19.2	26 (77.9) CN ⁻ 39 (64.3) (HF)F ⁻ 42 (14.7) CNO ⁻ 59 (27.5) (HF) ₂ F ⁻
ethylbutyraldehyde CH ₃ CH(C ₂ H ₅)CH ₂ CHO	100	39.3	14.1	7.7	26 (53.7) CN ⁻ 39 (23.4) (HF)F ⁻ 59 (100) (HF) ₂ F ⁻ 79 (36.8) (HF) ₃ F ⁻

* Ions less than 5% relative intensity are omitted except the quasi-molecular ions.

TABLE 10

F⁻ NICI MASS SPECTRA OF ALIPHATIC ALCOHOLS (ROH)

<u>Compounds (M)</u>	<u>Rel. Int. (%)</u> [*]		<u>Other ions m/e (rel. int.) identity</u>
	<u>mol. wt.</u>	<u>m/e 19 (M + F)⁻</u>	
n-butanol <chem>CH3CH2CH2CH2OH</chem>	74	82.7	58.8
			39 (100) (HF)F ⁻
			59 (11.0) (HF) ₂ F ⁻
			113 (6.9) (HF)(M+F) ⁻
iso-butanol <chem>CH3CH(CH3)CH2OH</chem>	74	77.3	17.1
			39 (47.2) (HF)F ⁻
tert-amyl alcohol <chem>CH3C(CH3)2CH2OH</chem>	88	51.5	17.5
			26 (12.0) CN ⁻
			39 (99.8) (HF)F ⁻
			59 (20.9) (HF) ₂ F ⁻
			93 (19.6) (butanol + F) ⁻

* Ions less than 5% relative intensity are omitted except the quasi-molecular ions.

are in competition with reactions of this ion with HF. It is evident from the data in Table 10, that in the case of the alcohols, formation of $F^-(HF)$ is more favorable than the formation of the $(M + F)^-$ ion. However, F^- NICI may be useful in distinguishing structural isomers of the alcohols. As can be seen by comparing the spectra of n-butanol and iso-butanol, the relative intensities of the $(M + F)^-$ ion in the two spectra are markedly different.

5. Alkyl Chlorides and Halobenzenes

The F^- NICI mass spectra of carbon tetrachloride, chloroform, methylene chloride and 1-chlorobutane are shown in Table 11. All of these compounds exhibit intense m/e 35 and 37 peaks, which correspond to the two isotopes of Cl^- . Formation of these ions apparently occurs via bimolecular nucleophilic substitution reactions. The observation of prominent Cl^- product ions from these reactions supports the conclusion that the nucleophilicity of F^- is greater than that of Cl^- in the gas phase (16).

Since F^- is a stronger Lewis base than Cl^- , it is also possible for F^- to abstract a chloronium ion, Cl^+ , from the CCl_4 molecule to form a CCl_3^- ion, although this product is formed in relatively small amounts (1.4% relative intensity at m/e 117). The characteristic chlorine isotope ratio leads to the observation of CCl_3^- ions at m/e 117, 119 and 121, in the intensity ratio, 3:3:1, which confirms the identity of this ion.

In the F^- NICI mass spectrum of chloroform ($CHCl_3$), an intense CCl_3^- ion is also observed (about 73.4% relative intensity at m/e 117). This is consistent with the expectations of the "inductive" effect in

TABLE 11

F⁻ NICI MASS SPECTRA OF ALKYL CHLORIDES (RCI) AND HALOBENZENE (ArO)

<u>Compounds (M)</u>	<u>mol. wt.</u>	<u>m/e 19</u>	<u>m/e 35^{Cl}-</u>	<u>m/e 37</u>	<u>m/e 79^{Br}-</u>	<u>m/e 81</u>	<u>(M-1)⁻</u>	<u>m/e (rel. int.)</u>	<u>Identity</u>
carbon tetrachloride CCl ₄	152	100	34.2	11.6	--	--	--	117 (1.4) 119 (1.3) 121 (0.6)	CCl ₃ ⁻
chloroform CHCl ₃	118	41.1	100	30.9	--	--	73.4 ^{**} 71.7 ^{**} 22.5 ^{**} 2.8 ^{**}	26 (6.9) 55 (12.2) 57 (3.8) 70 (8.1) 72 (5.2)	CN ⁻ (HF)Cl ⁻ Cl ₂ ⁻
methylene chloride CH ₂ Cl ₂	84	8.0	100	34.4	--	--	0.3	70 (0.4) 105 (0.5) 107 (0.5) 117 (0.6) 119 (0.6) 121 (0.2)	Cl ₂ ⁻ Cl ₃ ⁻ CHCl ₃ ⁻
1-chlorobutane n-C ₄ H ₉ Cl	92	13.7	100	29.4	--	--	--	55 (7.2) 57 (2.4)	(HF)FCI ⁻
chlorobenzene C ₆ H ₅ Cl	112	84.4	100	30.7	--	--	--	39 (40) 55 (24) 57 (8)	(HF)F ⁻ (HF)Cl ⁻

TABLE 11 (cont.)

F⁻ NICI MASS SPECTRA OF ALKYL CHLORIDES (RCI) AND HALOBENZENE (ArO)

<u>Compounds (M)</u>	<u>Rel. Int. (%)</u> [*]				<u>Other ions</u>			
	<u>m/e 19</u>	<u>m/e 35</u>	<u>m/e 37</u>	<u>m/e 79^{Br-}</u>	<u>m/e 81</u>	<u>(M-1)⁺</u>	<u>m/e (rel. int.)</u>	<u>identity</u>
2-chlorophenol C ₆ H ₄ ClOH	100	59.1	17.8	--	--	13.0	55 (10.2)	HFCI ⁺
bromobenzene C ₆ H ₅ Br	156	29.2	--	--	58.9	57.9	39 (100)	(HF)F ⁺
							59 (19.8)	(HF) ₂ F ⁺
							99 (10.0)	[⁺ (HF)Br]
							101 (10.0)	

* Ions less than 5% relative intensity are omitted except the quasi-molecular ions.

** These are isotopic peaks.

this molecule. Chloroform contains three equivalent chlorine atoms located at the methane carbon center, and since chlorine is an electron-withdrawing substituent, the presence of these serves to pull the electron pair, shared by the carbon and hydrogen atoms, away from the hydrogen. This enhances the probability of a proton being released from the molecule upon reaction with F^- . In methylene chloride, the formation of the observed $(M - 1)^-$ ion can be attributed to a similar mechanism. In the latter case, however, the molecule contains only two chlorine atoms, and so the inductive effect should be reduced substantially, and only a very weak $(M - 1)^-$ ion is observed (about 0.3% relative intensity).

Other weak intensity ions, such as the isotopic groups beginning with m/e 70 in the spectra of both chloroform and methylene chloride, and with m/e 105 and 117 in the spectrum of methylene chloride, are also observed. These ions are assumed to be Cl_2^- , Cl_3^- and $CHCl_3^-$, respectively, and are probably produced in subsequent reactions of the chloride ion. However, the 1-chlorobutane spectrum shows no significant ions other than Cl^- .

Ions at m/e 55 and 57, which presumably correspond to the two isotopic ions having the structure, $(HF)Cl^-$, are observed in all of the spectra listed in Table 11, except that of carbon tetrachloride. This again suggests that the HF molecule, which is observed to cluster with ions in many of the F^- NICI spectra, is directly derived from sample molecules which contain hydrogen.

Cl^- is observed to be the most abundant ion in the F^- NICI spectra of chlorobenzene and 2-chlorophenol. Similarly, Br^- is the most

abundant ion in the spectrum of bromobenzene. The Br^- ion is easily identified by the presence of the two isotopic peaks at m/e 79 and 81, which are approximately equal in intensity. Formation of the halide ions can also be visualized as occurring by a mechanism which involves the attack of a nucleophilic reagent upon the ring to form a carbonion intermediate, followed by ejection of the halide ion.

F^- NICI mass spectrometry offers no apparent advantages for either analysis or structural determinations of aliphatic or aromatic halides, since the spectra of all such compounds studied here exhibit halide ion as the only intense product.

6. 2-Chlorophenol and Salicylaldehyde.

The F^- NICI mass spectra of 2-chlorophenol and salicylaldehyde were investigated during this study. As shown in Table 12, the spectrum of 2-chlorophenol exhibits mainly Cl^- ion and a smaller intensity of $(M - 1)^-$ ion. Salicylaldehyde also shows an intense $(M - 1)^-$ ion. Since phenols are rather strong acids, it is relatively easy for the F^- reactant to abstract a proton from the hydroxyl group of these compounds, yielding stable phenoxide ions (ArO^-). Since the 2-chlorophenol molecule contains an active hydrogen atom in the hydroxyl group, it would be expected to complex readily with the F^- ion to form a $(M + \text{F})^-$ product. However, while an abundant $(M + \text{F})^-$ ion appears in the spectrum of salicylaldehyde, no such ion is detected in the 2-chlorophenol spectrum. This may indicate that production of the Cl^- ion is kinetically favored over the addition reaction. At fairly high source pressures the $(M - 1)^-$ ion clusters with another

TABLE 12

F⁻ NICI MASS SPECTRA OF PHENOLS (ArOH)

<u>Compounds (M)</u>	<u>mol. wt.</u>	<u>Rel. Int. (%)[*]</u>		<u>Other ions</u>	
		<u>m/e 19</u>	<u>(M - 1)⁻</u>	<u>(M + F)⁻</u>	<u>m/e (rel. int.) identity</u>
2-chlorophenol C ₆ H ₄ (Cl)OH	128	100	13.0	--	35 (59.1) Cl ⁻
					37 (17.8)
salicylaldehyde C ₆ H ₄ (CHO)OH	122	--	94.3	100	79 (28.8) (HF) ₃ F ⁻
					161 (37.9) (HF)(M+F) ⁻

^{*} Ions less than 5% relative intensity are omitted except the quasi-molecular ions.

molecule of salicylaldehyde to form the $(2M-1)^-$ ion.

7. Nitriles.

The F^- NICI mass spectra of acetonitrile, propionitrile and benzonitrile are shown in Table 13. The spectra of all nitriles studied here are dominated by a very intense CN^- ion peak (m/e 26).

The spectrum of acetonitrile exhibits an $(M - 1)^-$ ion as the major peak. This can be reasonably explained by the fact that the cyano group (CN) is a strongly electron-withdrawing group, which can readily activate the hydrogen atoms attached to the adjacent carbon atom (alpha hydrogen). The reaction of the F^- ion with this molecule in the gas phase thus results in abstraction of a proton, yielding a carbonion, which can be stabilized by electron delocalization. Since benzonitrile does not contain an alpha hydrogen, no significant $(M - 1)^-$ ion is observed in its spectrum. Strangely, the $(M - 1)^-$ ion is also absent in the spectrum of propionitrile, although it does contain an alpha hydrogen. Possibly, this is explained by the electron-donating inductive effect of the methyl group, which reduces the residual electron affinity of the alpha carbon atom, and thus makes removal of the attached hydrogen more difficult.

All of the nitriles investigated here exhibit weak $(M + F)^-$ ions, which are probably formed by a mechanism which involves F^- ion attack on the carbon center adjacent to the cyano group. The F^- NICI spectra of these compounds also display a series of peaks corresponding to C_nN^- ($n=1,3,5$ and 7), which appear at m/e 26, 50, 74 and 98. In the spectrum of acetonitrile, only the peak at m/e 26 is observed. The propionitrile spectrum shows both CN^- and C_3N^- , at m/e 26 and 50, respectively. In the spectrum of benzonitrile, all four peaks at

TABLE 13

F⁻ NICI MASS SPECTRA OF NITRILES (RCN) AND NITROBENZENE

<u>Compounds (M)</u>	<u>mol. wt.</u>	<u>Rel. Int. (%)</u> [*]		<u>(M - 1)⁻</u>	<u>(M + F)⁻</u>	<u>M⁻</u>	<u>Other ions m/e (rel. int.) identity</u>
		<u>m/e 19</u>	<u>CN⁻</u>	<u>NO₂⁻</u>			
acetonitrile CH ₃ CN	41	54.8	11.7	--	100	--	39 (12.8) (HF)F ⁻ 59 (10.1) (HF) ₂ F ⁻
propionitrile C ₂ H ₅ CN	55	100	83.2	--	--	--	39 (40.5) (HF)F ⁻ 50 (5.7) C ₃ N ⁻ 59 (5.0) (HF) ₂ F ⁻
benzonitrile C ₆ H ₅ CN	103	48.3	42.0	--	--	1.2	39 (100) (HF)F ⁻ 50 (23.9) C ₃ N ⁻ 59 (30.1) (HF) ₂ F ⁻ 70 (10.7) (HF)C ₃ N ⁻ 74 (7.1) C ₅ N ⁻ 94 (6.8) (HF)C ₅ N ⁻ 98 (0.9) C ₇ N ⁻
nitrobenzene C ₆ H ₅ NO ₂	123	17.0	--	100	--	1.2	39 (5.3) (HF)F ⁻ 66 (4.02) (HF)NO ₂ ⁻ 86 (13.6) (HF) ₂ NO ₂ ⁻ 93 (14.3) C ₆ H ₅ O ⁻

* Ions less than 5% relative intensity are omitted except the quasi-molecular ions.

m/e 26, 50, 74 and 98 are present. These ions were also observed by Alpin et al (15) in their study of the negative ion mass spectra of these compounds produced by electron impact.

8. Nitrobenzene.

The F^- NICI mass spectrum of nitrobenzene, shown in Table 13, is dominated by a very intense NO_2^- ion peak. Neither the $(M - 1)^-$ ion, nor the $(M + F)^-$ ion is observed in the spectrum of this compound. However, a very weak molecular anion, M^- is observed (1.2% relative intensity). The ion at m/e 93 may be characteristic of this compound, but the mechanism of formation is not clear.

9. Ethers.

Ethers are very weak acids, and the F^- NICI mass spectra of diethyl ether and isopropyl ether, which appear in Table 14, exhibit no $(M - 1)^-$ ions. The oxygen in diethyl ether is apparently not sufficiently electro-negative to activate the hydrogen on neighboring methylene groups, and so abstraction of protons from these groups by F^- does not occur. Although a number of intense peaks of no particular significance are observed in the ether spectra (m/e 26, 42, etc.), the only ions of interest produced from these compounds are those at m/e 45 (possibly $C_2H_5O^-$) and m/e 43 (possibly $C_3H_3O^-$). Apparently, these ions are displaced as a result of nucleophilic attack of F^- at the methylene carbon. The ion at m/e 43 must be formed by loss of H_2 from the $C_2H_5O^-$ ion, yielding an allyl-type structure which is resonance stabilized (10). Similarly, in the spectrum of isopropyl ether, the ions at m/e 59 and 57, which correspond to $(CH_3)_2CHO^-$ and $CH_2=C(CH_3)O^-$, respectively, are the dominant ions in the spectrum. No $(M + F)^-$ ions were observed in

TABLE 14

F⁻ NICI MASS SPECTRA OF ETHERS (ROR)

<u>Compounds (M)</u>	<u>mol. wt.</u>	<u>Rel. Int. (%)[*]</u>		<u>Other ions</u>	
		<u>m/e 19</u>	<u>RO⁻</u>	<u>m/e (rel. int.)</u>	<u>identity</u>
diethylether <chem>C2H5OC2H5</chem>	74	29.2	8.6	26 (100)	CN ⁻
				39 (7.5)	(HF)F ⁻
				42 (60.0)	CNO ⁻
				43 (21.6)	C ₂ H ₃ O ⁻
				62 (7.2)	(HF)CNO ⁻
isopropylether <chem>(CH3)2CHOCH(CH3)2</chem>	102	19.2	9.9	26 (100)	CN ⁻
				39 (6.1)	(HF)F ⁻
				42 (27.3)	CNO ⁻
				57 (6.2)	CH ₂ =C(CH ₃)O ⁻
				62 (6.6)	(HF)CNO ⁻

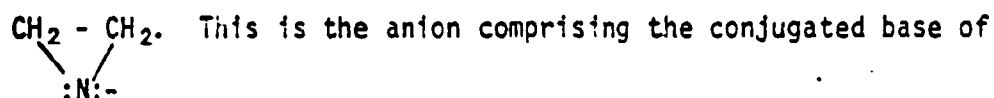
^{*} Ions less than 5% relative intensity are omitted except the quasi-molecular ions.

the spectrum of either ether.

10. Amines.

The F^- NICI mass spectra of diethylamine and n-butylamine are shown in Table 15. Amines are basic, and so no $(M - 1)^-$ ion can be formed by abstraction of a proton from these molecules by the F^- ion. The spectra of the amines are similar to those of the ethers in that they also exhibit several very intense, but analytically insignificant ions (m/e 26, 42, etc.). In contrast to the ethers, however, no larger fragment ions are observed in the amine spectra. This is understandable because the amino group (NH_2) is a stronger nucleophile and does not behave as a good leaving group.

Smit and Field (10) suggested that a possible structure for the ion with m/e 42, which is observed in the spectra of the amines, is



ethylenimine (aziridine). The mechanism of its formation is not yet clear. In the spectrum of diethylamine, a weak $(M + F)^-$ ion, which is probably formed by hydrogen bonding, is also observed. However, no such ion was found in the spectrum of n-butylamine.

11. Hydrocarbons.

a. Aliphatic alkanes and alkenes. The F^- NICI mass spectra of n-pentane, n-hexane, cyclohexane, 1-octene and cyclohexene are shown in Table 16. All of the aliphatic alkanes investigated here exhibit weak $(M + F)^-$ ions in the spectra. The hydrogen atoms in these compounds are not sufficiently acidic to be abstracted by the F^- ion, and thus no $(M - 1)^-$ ion is observed. The F^- NICI spectra of the

TABLE 15

F⁻ NICI MASS SPECTRA OF AMINES

<u>Compounds (M)</u>	<u>mol. wt.</u>	<u>Rel. Int. (%)</u> [*] <u>m/e 19</u>	<u>(M + F)⁻</u>	<u>Other ions</u> <u>m/e (rel. int.)</u> <u>Identity</u>
diethylamine (C ₂ H ₅) ₂ NH	73	100	0.8	26 (33.4) CN ⁻ 39 (17.7) (HF)F ⁻ 42 (7.5) CNO ⁻ or CH ₂ CH ₂ N ⁻
n-butylamine C ₄ H ₉ NH ₂	73	100	--	26 (19.1) CN ⁻ 39 (12.3) (HF)F ⁻ 42 (8.2) CNO ⁻ or CH ₂ CH ₂ N ⁻

* Ions less than 5% relative intensity are omitted except the quasi-molecular ions.

TABLE 16

F⁻ N₂CI MASS SPECTRA OF HYDROCARBONS

<u>Compounds (M)</u>	<u>mol. wt.</u>	<u>Rel. Int. (%)</u> <u>m/e 19</u>	<u>(M + F)⁻</u>	<u>Other ions</u> <u>m/e (rel. int.) identity</u>
n-pentane <chem>CH3(CH2)3CH3</chem>	72	100	1.0	39 (14.8) (HF)F ⁻
n-hexane <chem>CH3(CH2)4CH3</chem>	86	100	1.1	39 (6.4) (HF)F ⁻
cyclohexane	84	100	1.3	39 (8.9) (HF)F ⁻
1-octene <chem>CH2=CH(CH2)5CH3</chem>	112	26.2	--	26 (15.5) CN ⁻ 39 (100) (HF)F ⁻ 59 (17.7) (HF) ₂ F ⁻
cyclohexene	82	100	--	26 (69.9) CN ⁻ 39 (37.8) (HF)F ⁻
benzene <chem>C6H6</chem>	78	100	--	39 (8.5) (HF)F ⁻
toluene <chem>C6H5CH3</chem>	92	100	--	----

TABLE 16 (cont.)

<u>F⁻ NICI MASS SPECTRA OF HYDROCARBONS</u>			
<u>Compounds (M)</u>	<u>mol. wt.</u>	<u>Rel. Int. (%)[*]</u>	<u>m/e 19</u>
o-xylene C ₆ H ₄ (CH ₃) ₂	106		49.3
			39 (69.7) (HF)F ⁻
			59 (6.3) (HF) ₂ F ⁻

^{*} Ions less than 5% relative intensity are omitted except the quasi-molecular ions.

aliphatic alkenes (olefins) show neither $(M - 1)^-$ nor $(M + F)^-$ product ions in their spectra.

b. Aromatic hydrocarbons. The F^- NICI spectra of benzene, toluene and o-xylene are also shown in Table 16. Benzene is not ionized by F^- ion, which indicates that the ring hydrogens are insufficiently acidic to be removed by the F^- ion. The hydrogens in the side chains of the aromatic hydrocarbons examined here are also not sufficiently acidic to facilitate reaction, as indicated by the absence of $(M - 1)^-$ ions in the spectra of toluene and o-xylene. However, o-xylene does produce a very weak $(M + F)^-$ ion.

CONCLUSIONS

A summary of the major product ions observed in the F^- NICI mass spectra of various types of organic compounds studied in the present investigation is given in Table 17. The ability to generate intense quasi-molecular anions, such as $(M - 1)^-$, and/or $(M + F)^-$ ions, from a variety of organic compounds, as was demonstrated to be possible in the present experiments, is certainly of value for analytical applications. The product ions resulting from nucleophilic displacement reactions of F^- are, obviously, of less analytical value, owing to their lower masses. Some of the compounds, examined here, such as carboxylic acids, phenols, aldehydes and alcohols, exhibit both quasi-molecular anions, $(M - 1)^-$, as well as $(M + F)^-$ products, in their F^- NICI mass spectra, and thus two ionic products are available which indicate the molecular weight of the sample species.

F^- NICI mass spectrometry is also potentially applicable for distinguishing chemically similar compounds, such as isomers, as was demonstrated in the case of n-butanol and iso-butanol in the present experiments. For at least some types of compounds with multiple

TABLE 17

MAJOR IONS IN THE F⁻ NICI SPECTRA OF VARIOUS CLASSES OF COMPOUNDS

<u>Major Product Ion</u>	<u>Compound Type</u>
(M - 1) ⁻	Carboxylic Acids Ketones Aldehydes Phenols
(M + F) ⁻	Aliphatic Alcohols Aliphatic Alkanes Cycloalkanes
(CN) ⁻	Nitriles
(NO) ⁻	Nitrobenzene
X ⁻	Halogenated Molecules
RO ⁻	Ethers
RCOO ⁻	Carboxylic Acid Esters
None	Amines Olefins Aromatic Compounds

functional groups, the F^- NICI mass spectra show peaks characteristic of both groups. For example, for 2-chlorophenol, which contains both chloro- and hydroxy- groups, the F^- NICI spectrum exhibits Cl^- ion, and an $(M - 1)^-$ ion.

It seems clear that F^- NICI is a useful technique which is complementary to positive ion CI and electron impact mass spectrometry. F^- NICI mass spectrometry also appears to offer several advantages over NICI mass spectrometry using other reagent ions. Among these advantages are:

- a) Some aliphatic alkanes exhibit small but measurable $(M + F)^-$ ions in their F^- NICI mass spectra, while these compounds are generally unreactive with all other NICI reagent ions for which studies have been reported thus far; b) Since the F^- ion has only one isotope of significant natural abundance, F^- NICI mass spectrometry yields a much simpler and more easily recognizable spectral pattern than that produced by reagent ions such as Cl^- . The $(M + F)^-$ ion can be readily identified since it differs in mass by 19 amu from other ions in the region of the molecular ion. With other typically used NICI reactant ions, product species formed by electron and/or ion attachment processes may sometimes interfere with those produced by chemical ionization; c) In O_2^- NICI mass spectrometry, O_2^- will not react with weaker gas-phase acids such as phenol, chlorophenols and dichlorophenols. The ionization of these compounds by proton transfer reactions with the F^- ion to form $(M - 1)^-$ ions occurs readily in F^- NICI mass spectrometry; and finally, d) F^- NICI mass spectrometry is con-

siderably more sensitive than Cl^- NICI mass spectrometry for some organic compounds, such as aldehydes and ketones.

Investigations are currently in progress in our laboratory to determine the applicability of F^- NICI mass spectrometry for the analyses of more complex molecules, including various pesticides, drugs, and hydrocarbon mixtures.

REFERENCES

1. Symposium on Fundamentals and Applications of Negative Ion Mass Spectrometry. Organized by C. C. Fenselau and T. O. Tiernan. Abstracts of Papers Presented at the 26th Annual Conference on Mass Spectrometry and Allied Topics, St. Louis, Mo., May 31, 1978. American Society for Mass Spectrometry.
2. Jennings, K. R. Negative Ion Chemical Ionization Mass Spectrometry. In: Mass Spectrometry, Vol. 4 of the Specialist Periodical Reports. R. A. W. Johnstone, Ed., The Chemical Society, London, 1977.
3. Bowie, J. H. Reactions of Organic Functional Groups: Positive and Negative Ions. In: Mass Spectrometry, Vol. 4 of the Specialist Periodical Reports. R. A. W. Johnstone, Ed. The Chemical Society, London, 1977.
4. Burlingame, A. L. Shackleton, C. H. L., Howe, I. and Chezhev, O. S. Mass Spectrometry. Anal. Chem. 50, 346R-384R (1978).
5. Bruins, A. P., Ferrer-Correia, A. J., Harrison, A. G., Jennings, K. R., and Mitchum, R. K. Negative Ion Chemical Ionization Mass Spectra of Some Aromatic Compounds Using O^- As The Reagent Ion. In: Advances in Mass Spectrometry, Vol. 7A. N. R. Daly, Ed., Heyden and Son Ltd., London, 1978.
6. Hunt, D. F., McEwen, C. M., and Harvey, T. M. Positive and Negative Chemical Ionization Mass Spectrometry Using a Townsend Discharge Ion Source. Anal. Chem. 47, 1730-1734 (1975).
7. Hunt, D. F., Stafford, Jr., G. D., Crow, F. W., and Russell, J. W. Pulsed Positive-Negative Ion Chemical Ionization Mass Spectrometry. Anal. Chem. 48, 2098-2105 (1976).

8. Dzidic, I., Carroll, D. I., Stillwell, R. N., and Horning, E. C. Gas Phase Reactions. Ionization by Proton Transfer to Superoxide Anions. J. Am. Chem. Soc. 96, 5258-5259 (1974).
9. Tannenbaum, H. P., Roberts, J. D., and Dougherty, R. C. Negative Chemical Ionization Mass Spectrometry--Chloride Attachment Spectra. Anal. Chem. 47, 49-54 (1975).
10. Smit, A. L. C. and Field, F. H. Gaseous Anion Chemistry. Formation and Reactions of OH^- ; Reactions of Anions with N_2O ; OH^- Negative Chemical Ionization. J. Am. Chem. Soc. 99, 6471-6483 (1977).
11. Dillard, J. G. Negative Ion Mass Spectrometry. Chem. Rev. 73, 589-643 (1973).
12. Sides, G. D. and Tiernan, T. O. Dissociative Electron Attachment in Nitrogen Trifluoride. J. Chem. Phys. 67, 2382-2384 (1977).
13. Chang, C. and Tiernan, T. O. Ion Equilibrium Studies in A New Ion Source. Abstracts of Papers Presented at the 22nd Annual Conference on Mass Spectrometry and Allied Topics, Philadelphia, Pa., May 22, 1974, American Society for Mass Spectrometry.
14. Large, R. and Knof, H. A Comparison of Negative and Positive Ion Mass Spectrometry. Org. Mass Spectrom. 11, 582-568 (1976).
15. Alpen, R. T., Budzikiewicz, H. and Djerassi, C. Mass Spectrometry in Structural and Stereochemical Problems. LXXIII. The Negative Ion Mass Spectra of Some Simple Organic Compounds. J. / Chem. Soc. 87, 3180-3186 (1965).
16. Olmstead, W. N. and Brauman, J. I. Gas-Phase Nucleophilic Displacement Reactions. J. Am. Chem. Soc. 99, 4219-4228 (1977).

17. Asubiojo, O. I., Blair, L. K. and Brauman, J. I. Tetrahedral Intermediates in Gas Phase Ionic Displacement Reactions at Carbonyl Carbon. J. Am. Chem. Soc. 97, 6685-6688 (1975).